

Dissertation zur Erlangung des Doktorgrades  
der Fakultät für Chemie und Pharmazie  
der Ludwig-Maximilians-Universität München

# Colloidal Porous Nanoparticles

-

## Synthesis and Functionalization of Nanostructured Aluminosilicates and Silicas

von

Johann Kecht

aus

München

2008



### **Erklärung**

Diese Dissertation wurde im Sinne von § 13 Abs. 3 der Promotionsordnung vom 29. Januar 1998 von Herrn Professor Dr. Thomas Bein betreut.

### **Ehrenwörtliche Versicherung**

Diese Dissertation wurde selbstständig, ohne unerlaubte Hilfe erarbeitet.

München, am 26.07.2008

---

(Unterschrift des Autors)

Dissertation eingereicht am 17.06.2008

1. Gutachter: Prof. Dr. Thomas Bein

2. Gutachter: Prof. Dr. Konstantin Karaghiosoff

Mündliche Prüfung am 21.07.2008



## **Danksagung**

Als erstes möchte ich meinem Doktorvater, Professor Thomas Bein, herzlich für die Aufnahme in seinen Arbeitskreis danken, und für die Möglichkeit in diesem unter besten Bedingungen frei und kreativ arbeiten zu können. Ohne die interessanten Diskussionen, die geistige und finanzielle Unterstützung, und das Vertrauen in meine Arbeit wäre diese nicht möglich gewesen.

Bei Professor Konstantin Karaghiosoff möchte ich mich herzlich für die Übernahme des Zweitgutachtens, sowie für seine angenehme und engagierte Zusammenarbeit und Hilfe in allen Flüssig-NMR-Belangen danken.

Besonderen Dank verdient auch Dr. Svetlana Mintova, welche mir schon früh und geduldig als Mentor im Forschungspraktikum und Diplom die Grundlagen des Schreibens wissenschaftlicher Veröffentlichungen lehrte, und mir auch später aus dem (nicht so) fernen Frankreich immer mit ihrem Expertenwissen über Zeolithe zur Seite stand und mich unterstützt hat.

Natürlich wäre ein Arbeitskreis nichts ohne seine Mitarbeiter, und hier habe ich eindeutig das große Los gezogen. Deshalb ein großes Danke an alle jetzigen und ehemaligen Kollegen und Kolleginnen mit denen ich diese drei interessanten, manchmal anstrengenden, doch immer spaßigen Jahre am Lehrstuhl verbringen konnte. Danke an Johannes und Hendrik (u.a. für die neu gelernten Redewendungen, wie „fett war’s“ / „den kenn ich!“), Camilla (u.a. für das globale Ausbalancieren meines Proteinkonsums), Monika (u.a. für die schokoumhüllten Sonnenblumenkerne), Enrica (u.a. für die Smilies), Lea (u.a. für die Erkenntnis dass man auch in Chemie promovieren kann um dann Rabbi zu werden), Keili (u.a. für die süß-sauer-salzig-scharfen Kerne), Alex (u.a. für seine Hilfe in unserer Super-Kooperation), Stephan (u.a. weil

er nicht nur mein ehemaliger sondern auch mein zukünftiger Kollege ist), Axel (u.a. weil er mein mehr als würdiger Nachfolger ist), Mirjam (u.a. für das Aufhören mit dem Rauchen), Jörg, Valentina, Anderl, Olivier, Gabriela, Barbara, Ralf (Rolf), Markus (danke für die TEMs), Steffen (auch hier danke für die TEMs), Benni, Johann (nicht ich, der andere Johann), Dina, Karin, Changzhu, Shaofeng, und Jürgen, auch wenn er offiziell nicht zum Arbeitskreis gehört (danke für die Bücher!). Besonderen Dank auch an Tina, Regina und Dagmar, ohne deren organisatorische und anderweitige Hilfe der Arbeitskreis längst im Chaos versunken wäre.

Danke an meine guten Freunde Dar, Edi und Gerardo für die mentale Ablenkung nach der Arbeit durch eine Menge sinnvoller und sinnloser Diskussionen und Gespräche.

Der größte Dank gilt meiner Familie, meinen Eltern und meiner Schwester, für Ihre Unterstützung und Ermutigung vor, während, und nach dem Studium.

## **Abstract**

Colloidal porous hosts in the form of microporous aluminosilicate (zeolite) or mesoporous silica nanoparticles are attractive materials for a wide range of potential applications, i.e. controlled release drug delivery systems. However, many fundamental challenges still remain in this relatively young research field. The following work focuses on overcoming some of the present limitations by developing new concepts for the synthesis and functionalization of porous nanoparticles.

The number of zeolite structures available for the synthesis of stable colloidal suspensions is very limited when compared to the large number of known frameworks in bulk materials. A novel class of zeolite templates in the form of metal ammines was developed by taking advantage of the unique synthesis conditions typical in colloidal zeolite systems, i.e. low temperatures and low alkalinity. Square planar copper(II) tetraammine complexes were employed as co-templates in the synthesis of nanosized EDI-type molecular sieves. It was shown that the complexes are the key elements responsible for formation and growth of the zeolite nanoparticles, and their role in the crystallization process was thoroughly investigated. Substitution of the copper complexes by isostructural palladium and platinum species was demonstrated. By employing templates with similar shapes but different effects on the nucleation rate it was possible to drastically decrease the particle size by several factors in comparison to previously known colloidal zeolite systems and to generate stable suspensions of non-agglomerated EDI-type nanocrystals with diameters below 20 nm.

The size and morphology of mesoporous silica nanoparticles was controlled by co-condensation with additives, i.e. phenyltriethoxysilane, and subsequent simultaneous removal of the functional groups and template molecules by oxidation with hydrogen peroxide in a simple one-pot reaction.

Conversion of colloidal mesoporous silica systems with metalorganic reagents was demonstrated. The key step for avoiding particle agglomeration and coalescence processes

involves the removal of water from the mesopores at temperatures below 90 °C either by hydrolysis of triethyl orthoformate or by vapour adsorption from the gas phase.

In a joint project with Alexander Darga from our group, thin films of different phenyl-substituted mesoporous silica nanoparticles were deposited on quartz crystal microbalance chips in order to probe the intrapore surfaces by toluene sorption. It was shown that samples prepared by grafting and co-condensation approaches bearing similar surface densities of functional groups display considerably different toluene heats of adsorption.

Furthermore, a novel concept for the selective functionalization of mesoporous silica nanoparticles was developed. By using a time-delayed co-condensation approach, functional groups can be completely dispersed inside the channels, concentrated in parts of the mesopores, or exclusively placed on the external surface depending on the time of addition. Aminopropyl was used as a representative functionality in order to determine the density of functional groups on the outer surface via zeta potential measurements. Staining with iridium cations and subsequent scanning transmission electron microscopy studies allowed the visualization of metal clusters with different radial distributions depending on the addition time of the organosilane component. In contrast to grafting approaches, it was possible to easily adjust the concentration of functional groups on the outer surface by variation of the organosilane to silane ratio.



# Table of Contents

<b>1 INTRODUCTION.....</b>	<b>1</b>
1.1 PREFACE – THE RENAISSANCE OF POROUS MATERIALS .....	1
1.2 NANOSTRUCTURED POROUS HOSTS .....	4
1.2.1 Introduction .....	4
1.2.2 Zeolites and zeotypes .....	4
1.2.3 Surfactant-templated mesoporous materials .....	7
1.2.4 Crystalline organic-inorganic hybrid frameworks .....	9
1.3 SILICA SOL-GEL AND COLLOID CHEMISTRY .....	11
1.4 ZEOLITE FORMATION.....	13
1.5 ZEOLITE NANOPARTICLE SYNTHESIS .....	15
1.6 MESOPOROUS SILICA FORMATION .....	17
1.7 MESOPOROUS SILICA NANOPARTICLES .....	19
1.8 POROUS SILICATE HOSTS IN DRUG DELIVERY APPLICATIONS .....	21
1.9 GOALS.....	24
1.10 REFERENCES .....	27
<b>2 CHARACTERIZATION.....</b>	<b>37</b>
2.1 DYNAMIC LIGHT SCATTERING .....	37
2.2 ZETA POTENTIAL MEASUREMENT .....	40
2.3 NITROGEN ADSORPTION.....	43
2.4 X-RAY DIFFRACTION.....	47
2.5 INFRARED AND RAMAN SPECTROSCOPY.....	50
2.6 NUCLEAR MAGNETIC RESONANCE.....	52
2.7 SCANNING ELECTRON MICROSCOPY .....	53
2.8 TRANSMISSION ELECTRON MICROSCOPY .....	54
2.7 THERMOGRAVIMETRIC ANALYSIS AND DIFFERENTIAL SCANNING CALORIMETRY.....	55
2.8 REFERENCES .....	56
<b>3 COPPER AMMINE COMPLEXES AS NEW TEMPLATING AGENTS IN ZEOLITE SYNTHESIS .</b>	<b>57</b>
3.1 INTRODUCTION.....	57
3.2 EXPERIMENTAL SECTION .....	58
3.3 CHARACTERIZATION .....	61
3.4 RESULTS AND DISCUSSION .....	62
3.5 CONCLUSIONS .....	82
3.6 REFERENCES .....	83
<b>4 EXTENDING THE TEMPLATING CONCEPT TO OTHER METAL COMPLEXES: EXCEPTIONALLY SMALL ZEOLITE NANOCRYSTALS SYNTHESIZED WITH Pd AND Pt AMMINES.....</b>	<b>85</b>
4.1 INTRODUCTION.....	85
4.2 EXPERIMENTAL SECTION .....	87
4.3 CHARACTERIZATION .....	88
4.4 RESULTS AND DISCUSSION .....	89
4.5 CONCLUSIONS .....	101
4.6 REFERENCES .....	102
<b>5 OXIDATIVE REMOVAL OF TEMPLATE MOLECULES AND ORGANIC FUNCTIONALITIES IN MESOPOROUS SILICA NANOPARTICLES BY H<sub>2</sub>O<sub>2</sub> TREATMENT .....</b>	<b>103</b>
5.1 INTRODUCTION.....	103
5.2 EXPERIMENTAL SECTION .....	104
5.3 CHARACTERIZATION .....	106
5.4 RESULTS AND DISCUSSION .....	107
5.5 CONCLUSIONS .....	125
5.6 REFERENCES .....	126

<b>6 FUNCTIONALIZATION OF COLLOIDAL MESOPOROUS SILICA BY METALORGANIC REAGENTS.....</b>	<b>127</b>
6.1 INTRODUCTION.....	127
6.2 EXPERIMENTAL SECTION .....	129
6.3 CHARACTERIZATION .....	131
6.4 RESULTS AND DISCUSSION .....	132
6.5 CONCLUSION .....	145
6.6 REFERENCES .....	146
<b>7 PROBING THE INTRAPORE SURFACE OF PHENYL-SUBSTITUTED NANOSCALE MESOPOROUS SILICA – PIEZOELECTRIC SORPTION MEASUREMENTS IN THIN FILMS (JOINT PROJECT).....</b>	<b>147</b>
7.1 INTRODUCTION.....	147
7.2 EXPERIMENTAL SECTION .....	151
7.3 CHARACTERIZATION .....	152
7.4 RESULTS AND DISCUSSION .....	155
7.5 CONCLUSIONS .....	170
7.6 REFERENCES .....	171
<b>8 SELECTIVE FUNCTIONALIZATION OF THE OUTER AND INNER SURFACES IN MESOPOROUS SILICA NANOPARTICLES .....</b>	<b>173</b>
8.1 INTRODUCTION.....	173
8.2 EXPERIMENTAL SECTION .....	175
8.3 CHARACTERIZATION .....	179
8.4 RESULTS AND DISCUSSION .....	180
8.5 CONCLUSION .....	201
8.6 REFERENCES .....	202
<b>9 CONCLUSION.....</b>	<b>203</b>
9.1 SUMMARY .....	203
9.2 OUTLOOK .....	205
<b>10 SUPPORTING INFORMATION.....</b>	<b>207</b>
10.1 SUPPLEMENTAL DATA FOR CHAPTER 4 - STRUCTURAL MODELS FOR CU-EDI AND PT-EDI.....	207
10.2 SUPPLEMENTAL DATA FOR CHAPTER 5 – TGA DATA AND <sup>13</sup> C LIQUID STATE NMR.....	209
10.3 SUPPLEMENTAL DATA FOR CHAPTER 6 - TGA DATA AND <sup>13</sup> C SOLID STATE NMR .....	212
10.4 SUPPLEMENTAL DATA FOR CHAPTER 7 – ZETA POTENTIAL CURVES, TG DATA, N <sub>2</sub> ISOTHERMS .....	214
<b>11 CURRICULUM VITAE.....</b>	<b>217</b>
<b>12 PUBLICATIONS AND PRESENTATIONS.....</b>	<b>219</b>
12.1 PUBLICATIONS.....	219
12.2 POSTER PRESENTATIONS .....	220
12.3 ORAL PRESENTATIONS .....	220

## **1 Introduction**

### **1.1 Preface – The Renaissance of porous materials**

Talking about a ‘Renaissance’ of porous hosts in the terms of revival from obsolescence is not entirely correct, as porous materials never stopped being of utmost importance in a variety of fields. However, it can be said that with the advent of several novel materials and advanced applications in recent years, nanoporous media are being used in new ways and thus the scientific interest in investigating porous materials for these tasks has been rekindled and was born anew.

One striking example is the new direction in zeolite science. Zeolites, a species of microporous crystalline aluminosilicates, have been one of the most important porous media in science and industry for many decades. Their application as catalysts, especially in the petrochemical industry,<sup>[1]</sup> as ion exchangers in detergent formulations,<sup>[2]</sup> or as molecular sieves in separation technology<sup>[3]</sup> made them indispensable for many products used in modern everyday life. Correspondingly, zeolites had a big impact in materials science and were a central focus of many academic and industrial investigations, leading to a rising number of publications on this field. In its peak, zeolite science was responsible for up to 3-4% of all newly published materials science publications for over two decades, thus being one of the most dominant topics in this field during the 80s and 90s (Figure 1-1).

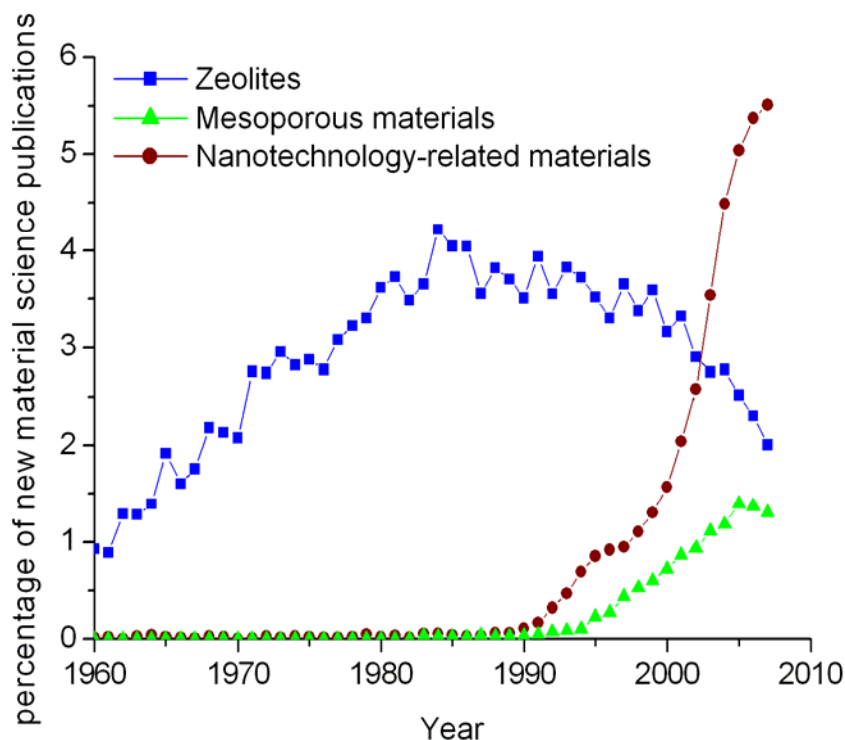


**Figure 1-1.** Ratio of articles focussing on the topics ‘zeolites’, ‘mesoporous’ or ‘nano’ relative to the total number of new materials science publications in each year (raw data source: SciFinder database)

In the following years, however, the relative ratio of new zeolite publications began to decline. This was not surprising. Considering the previously performed high level of investigations in the classic zeolite application areas of catalysis, ion exchange and molecular sieving, it naturally became harder to generate new breakthroughs and novel results. An additional reason was the increasing broadening and diversification inside the field of porous media. The discovery of new classes of porous materials such as ordered mesoporous silicas and metal-organic frameworks offered the community novel perspectives and spurred an increased interest and number of publications, e.g., centered on materials with large pore sizes in the

mesoscale range in order to overcome some of the limitations previously imposed by the smaller zeolite apertures (Figure 1-1).

It therefore happens that in the last few years the field of zeolite research has been redefining itself, slowly receding from the focus on classic industrial applications while steadily shifting into novel areas, including gas storage of hydrogen,<sup>[4, 5]</sup> methane,<sup>[6]</sup> and ammonia,<sup>[7]</sup> sensor devices,<sup>[8, 9]</sup> solar cell technology,<sup>[10, 11]</sup> supercapacitors,<sup>[12, 13]</sup> heat storage,<sup>[14, 15]</sup> biological carriers,<sup>[16, 17]</sup> medical technology,<sup>[18, 19]</sup> nanocluster host materials,<sup>[20, 21]</sup> and many others.

The catalyst for all these changes was the advent of nanotechnology, which led to an explosion of scientific interest for materials with controlled structures in the nanosize regime (Figure 1-1). Being inherently nanostructured scaffolds in the size range of about 0.5 to 1 nm, the unique properties of zeolites provide ample opportunities, i.e., to limit growth processes and confine matter on the nanoscale. Likewise, mesoporous materials can be used in a complementary way for tasks requiring porous materials with more open space, i.e., host-guest chemistry with large biological molecules such as enzymes,<sup>[22]</sup> surface functionalization by attachment of organic moieties inside the channel system,<sup>[23]</sup> or controlled growth of nanoscale wires.<sup>[24]</sup>

Many new applications also first became possible after achieving further control at the nanolevel, i.e., by limiting the particle size of the porous hosts from micrometer-sized bulk materials to nanoparticles with sizes between 50 – 100 nm. As with all forms of matter, such a drastic decrease in size leads to fundamental changes in many physical aspects of the porous hosts, including colloidal stability, optical properties, and diffusion path lengths. It also permits the preparation of hierarchical materials, thin films, membranes, composite materials, and stable suspensions, thus offering pathways to novel applications and research areas.<sup>[25-28]</sup>

It is due to these profound changes that this ‘Renaissance’ takes place, in other words, that zeolites, mesoporous hosts and other porous media become more and more important in areas and applications not previously associated with these materials. However, this ongoing

development is still underway. Each new discovery raises new questions and many of the potential new applications are still in their infancy or even wait to be created.

The following work tries to advance this exciting field by contributing a few stones to the expanding mosaic of nanosized porous host chemistry, by investigating new fundamental aspects of colloidal zeolite synthesis, novel functionalization methods for mesoporous silica nanoparticles, and first steps leading these materials to future applications.

## **1.2 Nanostructured porous hosts**

### *1.2.1 Introduction*

The following summary will give a short overview over different types of common nanostructured porous hosts such that the materials used in this work can be broadly categorized. According to IUPAC, porous hosts can be classified by their pore size as micro- (< 2 nm), meso- (2 – 50 nm) and macroporous (> 50 nm) materials.<sup>[29]</sup>

The summary focuses on ordered materials with defined pore sizes in contrast to disordered porous hosts, e.g., porous silica gel, alumina and polymers exhibiting porosity but with random pore size distributions. Special emphasis is given to zeolites and mesoporous silica.

### *1.2.2 Zeolites and zeotypes*

Apart from some exceptions such as stishovite, a high-pressure SiO<sub>2</sub>-modification with [SiO<sub>6</sub>] octahedrons,<sup>[30]</sup> most oxosilicates are composed of [SiO<sub>4</sub>] tetrahedrons as building blocks. In the case of aluminosilicates, some of these are replaced by [AlO<sub>4</sub>]<sup>-</sup> tetrahedrons, resulting in a negative framework charge which is compensated by counter ions inside the structure.

Zeolites are crystalline aluminosilicates with framework-type structures and defined pores and cavities in the range of 3 – 15 Å.<sup>[31]</sup>

The Si/Al ratio may go as low as unity, in which case each silicon is connected to one aluminium via an oxide bridge. Lower values are prohibited by the so-called ‘Löwenstein rule’ due to unfavourable electrostatic interactions of neighbouring aluminium tetrahedrons bearing a negative charge. Rising Si/Al ratios lead to a decrease of negative charge in the framework and thus of charge-balancing counter ions. At a Si/Al ratio of infinity so-called pure silica zeolites are obtained which do not possess ion-exchange properties but instead exhibit preferred absorption of apolar molecules and hydrophobic properties.

The history of zeolites began with the discovery of the natural mineral stilbite by the Swedish mineralogist Axel Fredrik Cronstedt in 1756.<sup>[32]</sup> Zeolites were soon classified as a new class of hydrated aluminosilicates. As the crystals released evaporating water and began to ‘dance’ upon rapid heating, Cronstedt termed the mineral a ‘zeolite’ based on the greek words ‘zein’ (‘to boil’) and ‘lithos’ (‘a stone’).

Following their first characterization, several key properties were discovered by investigation of natural zeolite minerals, e.g., reversible dehydration without morphology change in 1840 by Damour,<sup>[33]</sup> reversible ion exchange in 1858 by Eichhorn,<sup>[34]</sup> and first molecular sieve effects in 1925 by Weigel and Steinhoff.<sup>[35]</sup>

Following the first zeolite structure determinations in 1930 by Taylor and Pauling,<sup>[36, 37]</sup> the preparation of synthetic zeolite analogues succeeded in 1948 through the pioneering work of Barrer.<sup>[38]</sup> Several commercially important zeolite analogues followed, i.e., the synthesis of zeolites A, X and Y between 1949 and 1954 by Milton and Breck.<sup>[39]</sup> Important industrial applications at this time included the use as molecular sieve for paraffin isomer separation in 1959 by Union Carbide and the use of synthetic zeolite X as a cracking catalyst in 1962 by Mobil Oil.<sup>[39]</sup>

The first zeolites produced in the 40's to early 50's exhibited low Si/Al ratios and were synthesized only from inorganic compounds. Starting in the 60's, the use of organic compounds in zeolite synthesis increased, in particular the application of quaternary ammonium salts as so-called templates or structure directing agents (SDA).<sup>[40, 41]</sup> Due to the decreased charge density and increased steric requirements in comparison to alkali cations, the zeolites incorporating such organic cations as charge-balancing cations in general display much higher Si/Al ratios. Furthermore, the size and shape of the template molecules can be used to direct and control the crystallization of specific framework types.<sup>[42, 43]</sup> A prominent example for the template-directed synthesis of high-silica zeolites is the generation of zeolite  $\beta$  with tetraethylammonium cations discovered in 1967.<sup>[41]</sup> The first all-silica zeolites appeared in the late 70's, e.g. silicalite-1 in 1978.<sup>[44]</sup>

The science of synthetic zeolites and related materials continues to flourish, and while currently 48 natural occurring zeolite minerals are known, the number of available synthetic zeolite structure frameworks is well over 150.<sup>[39, 45]</sup>

While classical zeolites are aluminosilicates, the scientific community soon discovered that open frameworks with partial or full substitution by heteroelements are possible, thus leading to the discovery of so-called zeotypes.

One prominent example are the  $\text{AlPO}_n$ -materials, a series of microporous crystalline aluminophosphate molecular sieves that were first described in 1982 by Wilson et al. at Union Carbide.<sup>[46]</sup> Related materials are the families of silicoaluminophosphate (SAPO)<sup>[47]</sup> and metal aluminophosphate<sup>[39]</sup> (MeAPO) molecular sieves. Furthermore, several metal phosphate open frameworks are known, including phosphates of gallium,<sup>[48]</sup> indium,<sup>[49]</sup> tin,<sup>[50]</sup> antimony,<sup>[51]</sup> molybdenum,<sup>[52]</sup> vanadium,<sup>[53]</sup> iron,<sup>[54]</sup> cobalt,<sup>[55]</sup> manganese,<sup>[56]</sup> copper,<sup>[57]</sup> nickel,<sup>[58]</sup> zirconium,<sup>[59]</sup> and titanium.<sup>[60]</sup>



Moreover, a large selection of metasilicates has been discovered, including among others borosilicates, gallosilicates, titanosilicates and ferrisilicates. In total over 35 elements of the periodic table have been found to be suitable for generation of open framework structures.<sup>[61]</sup>

These new zeotype materials offered greater flexibility in bond lengths, bond angles and coordination numbers, thus enabling new framework structures previously unknown in classical zeolite chemistry. Special interest was given to materials exhibiting large ring sizes, for example the 18 T-atom ring in aluminophosphate VPI-5 in 1988<sup>[62]</sup> or the 20-membered rings of the gallophosphate cloverite<sup>[63]</sup> and aluminophosphate JDF-20.<sup>[64, 65]</sup>

Apart from oxides, there is also an increasing number of nitride,<sup>[66]</sup> sulfide<sup>[67]</sup> and halide<sup>[68]</sup> open frameworks.

### *1.2.3 Surfactant-templated mesoporous materials*

The synthesis of ordered mesoporous silicas by cooperative self-assembly of organic surfactants and inorganic species was first reported in the early 90's by Beck et al.<sup>[69, 70]</sup> An alternative approach was separately developed by Yanigawa et al. at approximately the same time, involving the intercalation of surfactant molecules into kanemite, a layered silicate precursor.<sup>[71-73]</sup> Interestingly, patent literature in 1969 already described a synthesis pathway that, while unrecognized at that time, apparently yields ordered mesoporous materials.<sup>[74, 75]</sup>

By using quaternary ammonium surfactants, it is possible to generate supramolecular assemblies in the form of micelles, which exhibit drastically larger size scales than typical molecular templates previously applied in microporous material syntheses. By applying hydrothermal synthesis in basic media, the scientists at Mobil Oil succeeded in generating a new class of mesoporous materials possessing large uniform pore systems with narrow pore size distributions and pore diameters above 4 nm surrounded by an amorphous silica framework.

Prominent examples of these first so-called M41S materials include MCM-41, with a 2D hexagonal arrangement of cylindrical pores, MCM-48 with a 3D cubic pore system, and MCM-50 with a 1D array of layered sheets (in these names MCM stands for ‘Mobile Composition of Matter’).<sup>[70]</sup> Correspondingly, the silicates and aluminosilicates similar to MCM-41 obtained by the kanemite intercalation approach were termed FSM-n (Folded Sheet mesoporous Materials-n), where n denotes the carbon atoms of the surfactant alkyl chain.

Preparation of mesoporous silicas by co-operative self-assembly using non-ionic organic-inorganic interactions, i.e. hydrogen bonding, and neutral surfactants was reported by Pinnavaia et al. in 1994.<sup>[76, 77]</sup> Materials templated by primary amines, i.e., HMS materials (Hexagonal Mesoporous Silica) and by poly(ethylene oxides), i.e. MSU materials (Michigan State University materials), were reported. In comparison to the strong electrostatic forces between quaternary ammonium cations and the negatively charged silica framework, these neutral surfactants were found to be less strongly bound and thus easily recoverable, i.e., by washing in ethanol and other media.<sup>[76, 78]</sup>

Similarly, syntheses in strongly acidic media were found to be possible by using triblock co-polymers as non-ionic surfactants. Pluronics are a family of triblock co-polymers consisting of poly(ethylene oxide)<sub>x</sub>-poly(propylene oxide)<sub>y</sub>-poly(ethylene oxide)<sub>x</sub> units with variable chain lengths x and y, commonly used for the preparation of such mesoporous silicas.<sup>[79, 80]</sup> The resulting SBA materials (Santa Barbara materials) exhibit several interesting features, i.e., thicker pore walls leading to increased thermal and hydrothermal stability,<sup>[81]</sup> very large obtainable pore diameters,<sup>[80]</sup> large morphological variety,<sup>[82]</sup> and additional microporosity inside the mesopore walls after calcination caused by the partial embedding of poly(ethylene oxide) side chains.<sup>[83]</sup>

By using different inorganic sol-gel precursors, ordered mesoporous oxide systems were synthesized by similar self-assembly approaches, i.e., yielding mesoporous alumina, aluminosilicate, titania, zirconia, tantalum oxides, and wolframates, among others.<sup>[84-87]</sup>

Furthermore, non-oxidic mesoporous systems with different compositions, including metal sulfides,<sup>[88-90]</sup> metals,<sup>[91-93]</sup> and other materials<sup>[94-97]</sup> have been generated using various approaches.

Periodic mesoporous organosilicas (PMOs), i.e., inorganic-organic hybrid materials featuring organic functionalities as integral part of the framework structure, were prepared by using bridged multipodal alkoxysilane precursors.<sup>[98]</sup>

Completely organic mesoporous hosts were prepared by using different mesostructured silicas as hard templates for ‘nanocasting’, followed by subsequent leaching of the siliceous framework in order to generate negative carbon replicas of the pore systems referred to as CMK-n materials (Carbon Mesostructured by KAIST).<sup>[99]</sup> A different class of mesoporous carbons was prepared using a self-assembly approach involving the polymerization of phenol and formaldehyde around triblock copolymer templates.<sup>[100]</sup>

#### *1.2.4 Crystalline organic-inorganic hybrid frameworks*

Porous hybrid solids began drawing academic attention in the late 80’s followed by a continued increase in interest for this new class of materials.<sup>[101-103]</sup> After the pioneering work of Yaghi et al. in 1995,<sup>[104]</sup> the term “metal organic frameworks” (MOFs) was coined for the new microporous materials emerging from the modular concept of combining inorganic metal centers and organic linkers for the formation of three-dimensional hybrid frameworks.

Typical MOF frameworks consist of di-, tri-, or tetravalent metal centers connected by organic linkers incorporating appropriate functional groups for bonding or chelating, i.e., carboxylates, phosphonates, sulfonates, and nitrogen derivatives such as pyridines and imidazoles, among others.<sup>[102, 105]</sup> For the carbon backbone, often rigid species such as aromatic groups are applied. Furthermore, recent investigations focus on chiral ligands<sup>[106-108]</sup> and biologically relevant molecules including amino acids and peptides.<sup>[109-113]</sup> Given the

additional possibility of functionalizing the carbon subnetwork, i.e. with halogeno-, alkyl-, or amino groups, it becomes evident that MOFs offer an exceptionally high versatility in structure, composition and functionality of their frameworks.

In certain cases, their modular design based on distinct molecular units allows the creation of so-called ‘isorecticular’ frameworks (IRMOFs) by exchanging the functionalized linker against larger groups, while retaining the connectivity of the framework in the final structure.<sup>[114]</sup> This permits the systematic variation of a given structure type in order to increase pore sizes or allow the insertion of different functionalities in the cavities. Using a similar approach known as ‘scale chemistry’, the metal centers may also be exchanged for larger inorganic secondary building units such as hexameric clusters, thus resulting in considerably larger frameworks.<sup>[115]</sup> In such materials pore sizes can exceed 2 nm, effectively generating a class of crystalline hybrid mesoporous solids with highly defined pore sizes, e. g., MIL-101<sup>[116]</sup> and MIL-102<sup>[117]</sup> (Materials of Institute Lavoisier).

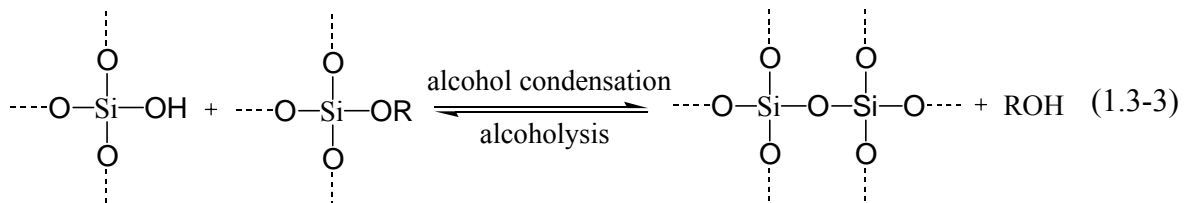
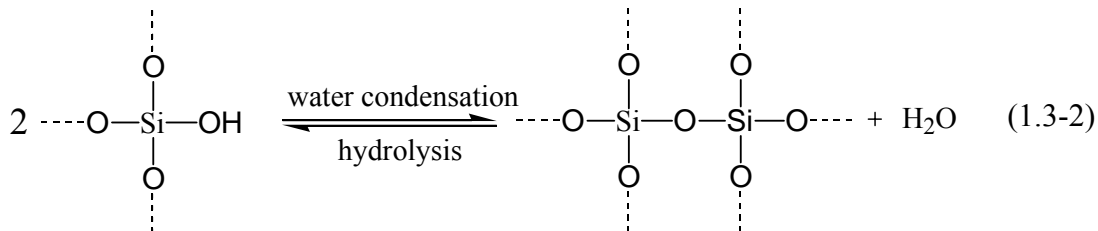
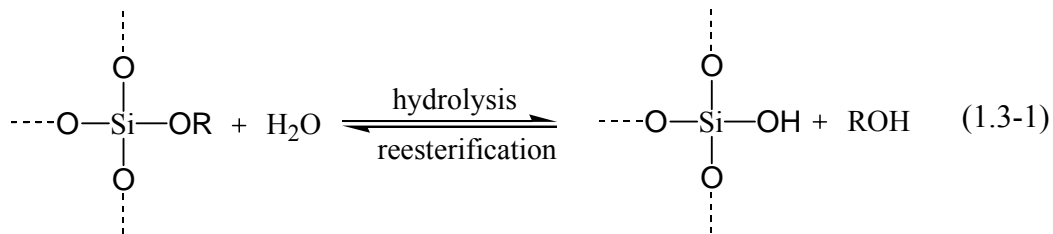
A different class of porous hybrid materials was introduced by Yaghi et al. in 2005.<sup>[118]</sup> Covalent organic frameworks (COFs) were obtained by condensation of organoboronic acids, which present a more covalent bonding in comparison to the ionic nature of metal-ligand interactions in MOFs.<sup>[119]</sup>

Furthermore, Yamamoto et al. first introduced short organic bridging units into zeolite frameworks, replacing oxygen through the generation of so-called ZOLs (Zeolites containing Organic groups as Lattice) and ZOFs (Zeolite Organic Frameworks).<sup>[120-122]</sup>

### 1.3 Silica Sol-gel and colloid chemistry

A colloid is defined as a mixture of two phases with the dimensions of the dispersed phase being in the range of 1-1000 nm. In the case of a dispersion of solid particles in a liquid medium, such a colloidal suspension is referred to as sol. Sol-gel chemistry deals with the formation of inorganic networks, typically from silicon or metal oxide monomer precursors, by formation of colloidal particles and subsequent gelation processes.<sup>[123]</sup>

In the case of silica, sol-gel chemistry typically involves the hydrolysis of alkoxysilanes in basic or acid media. The condensation process can be described by three basic reaction steps:



Reaction conditions including temperature, time, pH, reactant ratios, concentrations, presence of catalysts and homogenizing agents can influence the development of the sol-gel process. The polymerization process is particularly dependent on pH levels, and the complete and rapid hydrolysis is usually achieved by addition of acid or base catalysts. However, the acid-catalyzed condensation mechanism involves protonated silanol species, and thus leads to a

preferential reaction of the more basic silanolates, i.e. monomers and weakly branched oligomers.<sup>[123]</sup> On the other hand, in basic media the preferential condensation between highly condensed oligomers is observed.<sup>[123, 124]</sup> Acid-catalyzed condensation reactions therefore primarily lead to more weakly connected and flexible primarily linear or randomly branched polymer networks, while base-catalyzed reactions generate highly branched isolated clusters (Figure 1.3-1). Gelation in acidic systems occurs due to entanglement and formation of further branches, while under basic conditions gelation commences by agglomeration of discrete particulate entities.

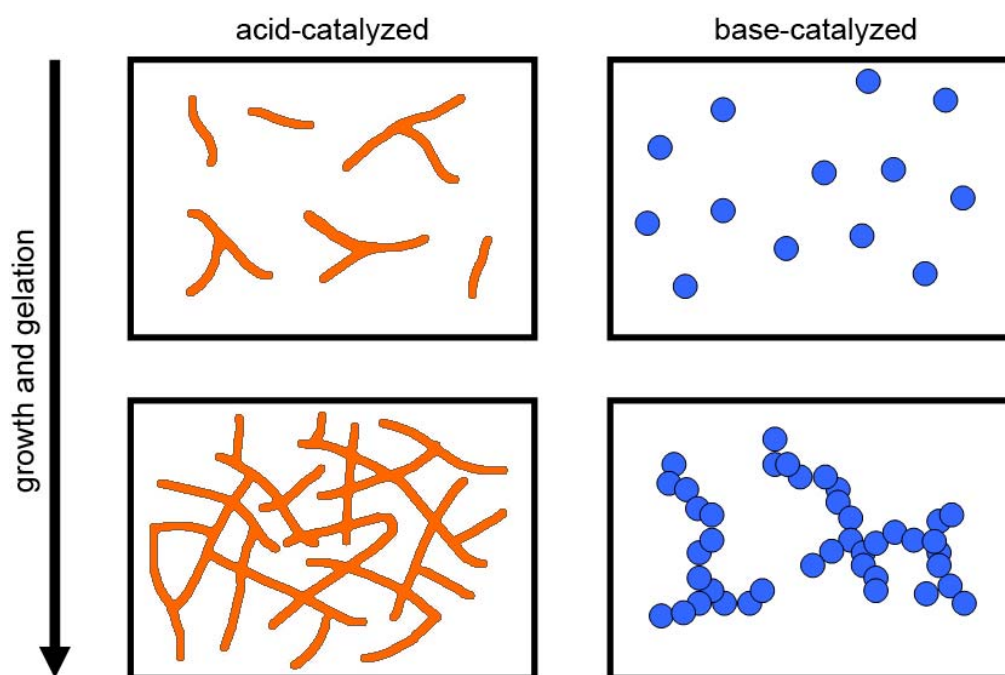


**Figure 1.3-1.** The different pathways of silica condensation by acidic and basic catalysis.

## 1.4 Zeolite formation

The mechanistic aspects of hydrothermal zeolite synthesis have always been one of the focal points in zeolite research.<sup>[125]</sup> Transformation of amorphous aluminosilicate reagents into crystalline molecular sieves usually encompasses multiple reaction stages, i.e. induction period, nucleation, and crystal growth, which are governed by different aspects including constitution of the growth species, template-framework interactions, and zeolite solubility.

A typical hydrothermal zeolite synthesis consists of the following steps:

- Generation of an amorphous precursor gel by mixing of the silica source, alumina source, mineralizer, template, and solvent (water)
- After a potential aging step, the mixture is heated in a sealed autoclave (for temperatures above 100 °C)
- During the induction period, the reactants remain amorphous after raising the synthesis temperature
- Crystal growth converts essentially all amorphous material into zeolite

Several principal proposals for the mechanism of this conversion from reactant gels to crystalline molecular sieves have been advanced in the course of the last 50 years.<sup>[125]</sup> In a first approach, Barrer et al.<sup>[126, 127]</sup> suggested a condensation polymerization of polygonal and polyhedral anions. This was followed by the early works of Breck and Flanigen<sup>[31]</sup> concerning rearrangement and linkage of polyhedra mainly from the solid phase. In contrast, Kerr<sup>[128]</sup> emphasized the crystal growth from solution species, followed by the proposal of Zhdanov<sup>[129]</sup> focussing on solid/liquid solubility equilibria, nuclei from condensation reactions and solution-mediated crystal growth. Several sophisticated concepts followed, including models combining liquid ion phase transportation and solid hydrogel transformation pathways,<sup>[130-133]</sup> nuclei generation by ordering of embryonic clathrate units,<sup>[134]</sup> pre-organized inorganic-

organic composites followed by aggregation-induced nucleation and layer-by-layer crystal growth,<sup>[135-137]</sup> and a ‘nanoslab’ theory, in which growth proceeds via aggregation of brick-like precursor units.<sup>[138-144]</sup> Recent theories propose a solution-mediation model based on crystal growth by localised construction from small, mobile species ordered by the participating cations, stating that the common presence of mobile species renders the distinction between ‘gel rearrangement’ and ‘solid-phase transformation’ mechanism unnecessary (Figure 1.4-1).<sup>[125]</sup>

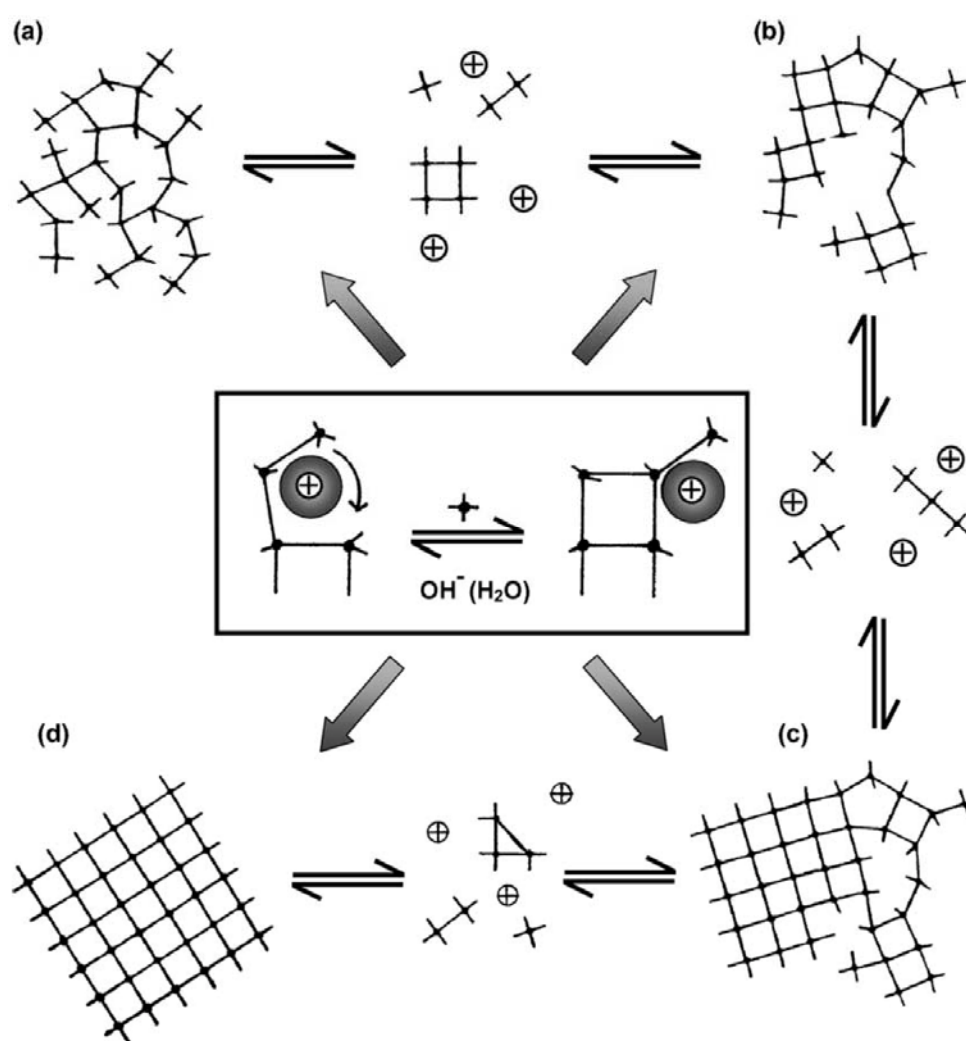


**Figure 1.4-1.** A generalized mechanism for zeolite synthesis featuring amorphous domains (a), elements of local order (b), nucleation by forming of localized periodic structures (c), and dissolution of amorphous areas during crystal growth (d).<sup>[125]</sup>



In this model, fundamental importance is given to the ‘mobility’ resulting from the generation of small reactive species by the mineralizing component, i.e., by hydroxide or fluoride anions. Amorphous domains equilibrate with solution species (Figure 1.4-1a). The resulting building units are ordered and assembled at the growth site by participating cations, which provide a ‘blueprint’ of the spatial architecture by coordinating water molecules, silicate anions and other polar species (Figure 1.4-1b). Nucleation occurs by continuation of such equilibration processes until periodic structures emerge in areas of sufficient order, followed by further growth of the nucleus under gradual dissolution of the amorphous areas (Figure 1.4-1c,d).

The transformation processes are based on equilibria with solution species in the liquid phase, and their self-assembly directed by solvated cations acting as templates and coordination centers. While these reactions usually take place in bulk solution phases, it should be noted that the concept may be extended to apparent solid-phase transformations as long as a solvated layer exists at the solid interface. Examples for such alternative pathways to classic hydrothermal zeolite synthesis include the steam assisted conversion, vapour phase transport, and dry gel conversion techniques.<sup>[145, 146]</sup> Here, part of the reaction components are supplied from the vapour phase in form of water steam or volatile amines, leading to the crystallization of dried precursor materials.

### **1.5 Zeolite nanoparticle synthesis**

Bulk zeolites are typically synthesized under hydrothermal conditions from highly alkaline aluminosilicate gels at temperatures between 100 and 200 °C. However, such standard zeolite syntheses mostly yield micrometer-sized agglomerations of individual crystalline domains. In order to obtain colloidal zeolite nanoparticles, i.e., stable suspensions of discrete zeolite

crystals with sizes under 100 nm and narrow particle size distributions, different synthesis conditions have to be chosen.<sup>[147]</sup>

Most nanozeolite syntheses are performed using clear homogeneous solutions, prepared from colloidal or molecular reactant sources. Given a constant amount of educts, higher nucleation rates will result in smaller particles. Factors that can favour nucleation over growth are low crystallization temperatures (typically 25 - 100 °C) and high levels of supersaturation.<sup>[148, 149]</sup> Another important factor is the steric stabilization of the proto-nuclei, which is often achieved by low alkali contents and abundant addition of organic templates. These bulky quaternary ammonium cations can absorb on the surfaces of the growing particles and prevent further agglomeration. The organic cations also act as structure-directing agents, thus directing the growth of certain zeolite framework types by being incorporated into the channels and cages. By choosing suitable compositions and reactants, it is possible to prepare clear homogeneous solutions containing colloidal or subcolloidal amorphous particles which transform into discrete zeolite nanocrystals after hydrothermal treatment, as compared to the initial aluminosilicate gels yielding agglomerated or polycrystalline materials in standard zeolite syntheses.

Compared to the wide array of different bulk zeolite structures, the scope of available nanosized zeolites is rather limited, although ever-growing. Syntheses of zeolite colloids were first reported in the mid-90's for zeolites ZSM-2, ZSM-5, LTL, and silicalite-1.<sup>[150-153]</sup> In the following years, several other low-silica (LTA, FAU, GIS, SOD, OFF),<sup>[154-158]</sup> high-silica / pure silica (MFI, MEL, BEA),<sup>[151, 153, 159, 160]</sup> and aluminophosphate (AFI, AEL, AEI)<sup>[161-163]</sup> colloidal molecular sieves were discovered. A recent addition to the pool of available colloidal low-silica zeolites are the metal ammine-templated EDI nanoparticles presented in this work.<sup>[164, 165]</sup>

## 1.6 Mesoporous silica formation

As discussed previously, different mesostructured materials can be obtained by variation of the surfactant type and synthesis conditions. Generally, a typical synthesis mixture consists of templating species, i.e., quaternary ammonium surfactants, an inorganic precursor, i.e., tetraethyl orthosilicate, an acid or base catalyst and water as solvent. Depending on the chosen reactants and framework-template interactions a number of different synthesis routes have been described.<sup>[166-168]</sup> The most common routes are the  $S^+I^-$  pathway (S: surfactant, I: inorganic species) for cationic surfactants and anionic silicate species in basic media, the  $S^0I^0$  pathway for nonionic surfactants, and the  $S^+X^-I^+$  /  $S^0H^+X^-I^+$  pathways (X: mediator ion, usually a halide) for cationic and protonated non-ionic surfactants in acidic media, respectively. Although less frequently used, several other denominations exist for routes employing charged surfactants, non-silica materials, and various bonding interactions.<sup>[166]</sup>

Two different formation mechanisms can be used to describe the synthesis of mesoporous silicas: cooperative self-assembly and ‘true’ liquid crystal templating (TLCT, Figure 1.6-1).

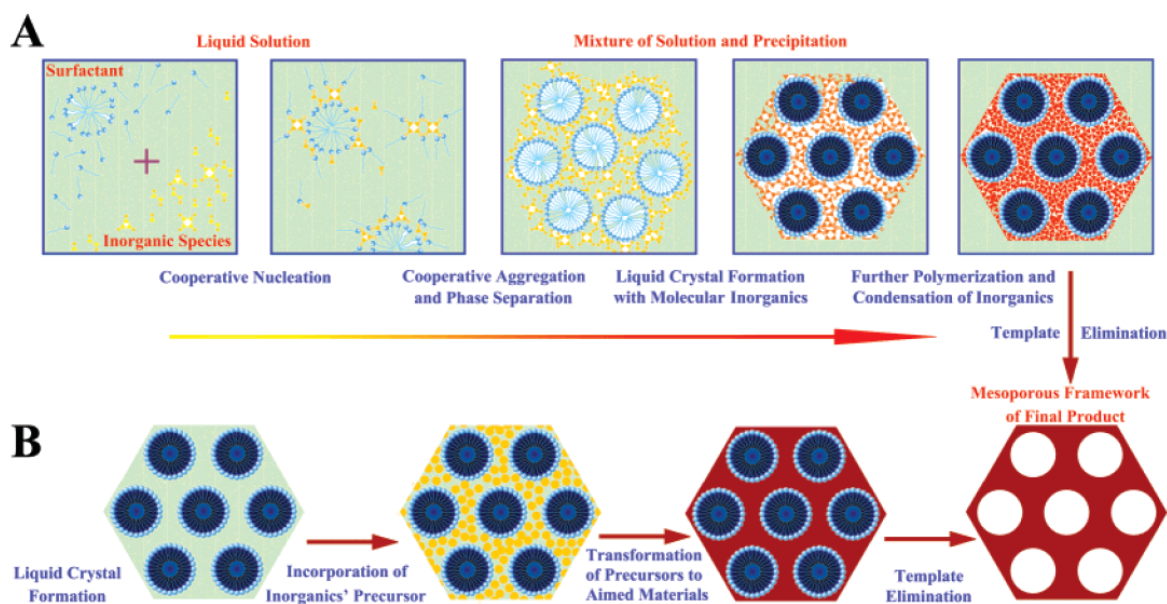


**Figure 1.6-1.** Mesoporous silica formation mechanisms: cooperative self-assembly (A) and ‘true’ liquid-crystal templating (B).<sup>[166]</sup>

In TLCT, a lyotropic liquid-crystalline phase is already present at the chosen reaction conditions before addition and subsequent polymerization of the inorganic precursor.<sup>[169]</sup> However, most syntheses follow the cooperative self-assembly approach, where no initial liquid-crystalline phase is necessary. Instead, the assembly of the ordered mesostructured phase is directed by the electrostatic interactions between the surfactant and silica species during condensation.<sup>[167, 168, 170]</sup> In the case of a  $S^+I^-$  mechanism, Coulomb forces will cause the silicate polyanions to assemble at the positively charged cationic headgroups of the surfactants. This interaction will change the charge density at the interface, allowing the surfactant to form and assemble micelles depending on the reaction conditions. Variations in charge density proceed by continued crosslinking and polymerization of the silicate species, thus directing the assembly of the final mesophase structure with the lowest interface energy. Examples of different mesostructures, i.e., MCM-41 (2D hexagonal, space group  $p6mm$ ), MCM-48 (cubic, space group  $Im\bar{3}d$ ), and MCM-50 (lamellar, space group  $p2$ ), obtained by variation of the synthesis conditions in a cetyltrimethylammonium surfactant-based system are given in Figure 1.6-2.

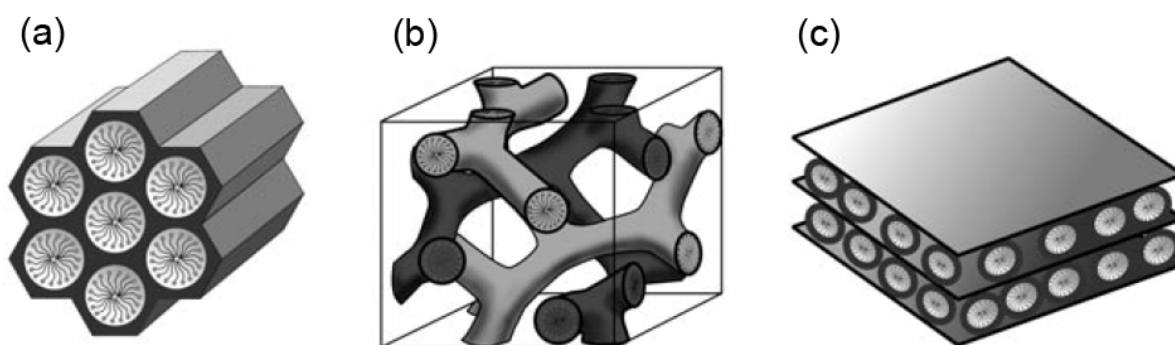


**Figure 1.6-2.** Structures of MCM-41 (a), MCM-48 (b) and MCM-50 (c).<sup>[98]</sup>

By subsequent removal of the template via calcination or extraction approaches, the mesostructured solids may be converted into mesoporous materials. Introduction of organic functionalities onto the mesoporous silica surfaces is commonly achieved either by in-situ co-

condensation of organosilanes during synthesis, or by post-synthesis attachment via grafting approaches.<sup>[98]</sup> In this way, it is possible to alter the surface properties of the mesoporous host material depending on the desired application.

### 1.7 Mesoporous silica nanoparticles

Mesoporous silica can be synthesized in different shapes and morphologies, including films, fibers, and particles in various forms and sizes.<sup>[171, 172]</sup> Bulk mesoporous silica syntheses typically yield particles in the micrometer range. However, several approaches are known to reduce particle size, i.e., for generation of nanoparticles below 100 nm. In the following, these approaches will be briefly outlined:

- (1) stopping particle growth at early stages
- (2) encapsulation by a second surfactant system
- (3) aerosol-based processes
- (4) confined space synthesis
- (5) reduced condensation speeds

Limitation of the particle size by stopping the reaction at early stages of growth, i.e., by quenching via strong dilution, is a viable means to obtain nanosized colloidal entities. However, the obtained yields tend to be small, and the low concentration of the resulting highly diluted suspensions make isolation of significant amounts of product difficult.<sup>[173, 174]</sup> Similar problems arise when slow particle growth is achieved by starting the synthesis from highly diluted reaction mixtures.<sup>[175, 176]</sup>

A different approach to limit particle growth is the application of complementary immiscible surfactant systems. In this case one surfactant acts as supramolecular template for generation

of the mesostructure and the second surfactant acts as size-limiter by surrounding the growing silica particles. Examples for such approaches include CTAB/Pluronic F127 and various triblock-copolymer/fluorocarbon surfactant systems.<sup>[177-179]</sup> In the latter case a great variety of different pore structures and pore sizes was achieved.<sup>[179]</sup> However, removal of the second surfactant system without calcination is often difficult, and partial interparticle aggregation prevents the preparation of monomodal and stable colloidal suspensions.

Aerosol-based processes have been applied for industrial large-scale preparation of various oxidic nanoparticles.<sup>[180, 181]</sup> Similar techniques based on surfactant-containing systems enable the preparation of nanosized porous materials.<sup>[182]</sup> As the resulting products are obtained as dry powders, redispersion as stable suspensions is difficult.

A different route for nanoparticle generation is the so-called confined space synthesis, where particle growth is performed inside the open spaces of a surrounding hard template which is subsequently removed, i.e., by dissolution or calcination. Shape and size of the resulting particles are thus restricted by the dimensions of the host material. Examples include the generation of nanosized mesoporous silica spheres in inversed opals.<sup>[183]</sup> Furthermore, colloidal crystal templating allows for interesting variations of the particle morphology, i.e., the generation of mesoporous silica nanocubes.<sup>[184]</sup>

Adjustment of particle size can also be achieved by precise control of the silica condensation processes. Reducing the condensation rate is possible by adjustment of the reaction conditions,<sup>[185, 186]</sup> or by using complexation agents such as triethanolamine.<sup>[187-189]</sup> In the latter case, the polyalcohol is supposed to generate silatrane chelates in solution, thus stabilizing the silica against further condensation steps.<sup>[190, 191]</sup>

The above triethanolamine-based approach also used in this work offers several advantages, i.e., high yields by allowing concentrated reaction mixtures and the generation of monomodal colloidal suspensions of non-agglomerated particles with narrow size distributions.

### 1.8 Porous silicate hosts in drug delivery applications

Drug delivery systems featuring controlled release and precise time-release dosage are one of the most promising new developments in biomedical materials sciences.<sup>[192-195]</sup> Contrary to traditional administration methods, which result in a saw-tooth curve of drug concentration in the plasma, such systems would allow a near-constant plasma level of pharmaceutical agents during the therapy. Furthermore, additional refinements such as enhanced selectivity and triggered release mechanisms could enable the targeting of specific body areas and cell types. The ordered porosity and excellent biocompatibility<sup>[196-198]</sup> of porous silicates make these materials attractive candidates for the development of controlled release systems.

Due to their versatile framework structures and ion-exchange capabilities, zeolites are ideal host systems for the controlled delivery of small molecules and cations. While their limited apertures inhibit the loading of most large drugs and proteins, zeolites have been shown to be efficient carriers for different pharmaceutical agents including metal cations<sup>[199]</sup> and nitric oxide.<sup>[200, 201]</sup> For example, zinc-containing zeolites have been implemented in baby care products for the treatment of diaper rash.<sup>[202]</sup> On the other hand, large-pore zeolites such as FAU are also capable of incorporating mid-sized drug molecules and have been successfully applied for the controlled release of ibuprofen and doxorubicin in vitro,<sup>[203]</sup> as well as for the in vivo administration of different anthelmintic drugs to rats and pigs for the efficient curing of worm infestations due to their slow release profile.<sup>[204]</sup> Furthermore, the mechanical stability of zeolites allows the formation of microneedles able to pierce human skin for transdermal drug delivery through the permeable zeolite wall.<sup>[205, 206]</sup>

The possibility to efficiently produce zeolites on large industrial scales makes these materials interesting for commercial applications, thus leading to a large number of zeolite-related drug delivery patents.<sup>[199, 200, 202, 206-209]</sup>

In comparison to zeolites, mesoporous silicas offer much larger pore diameters suitable for the uptake of enzymes, polypeptides, large drug molecules, and nucleic acid sequences.<sup>[22, 210]</sup>

They offer ordered porosity with high surface areas, large pore volumes, and well-defined tunable pore sizes. Moreover, the silica surface-drug interactions can be tailored for different applications by functionalization of the pore walls. The benefits of this versatile material class thus make mesoporous silica an ideal research subject for investigations centering on sophisticated controlled release and drug delivery approaches.<sup>[185, 211, 212]</sup>

The drug uptake and release properties of different mesoporous silicas were extensively studied using ibuprofen as a model drug, investigating, among others, the influence of different particle morphologies, pore sizes, and pore architectures on the release rate.<sup>[213-218]</sup> Furthermore, modification of the release profile by functionalization of the pore walls has been demonstrated.<sup>[218-224]</sup>

Recent approaches center on stimuli-responsive controlled release by using various gating mechanisms in order to suppress free diffusion out of the pore system. By exhibiting a ‘zero release’ profile before reaching the target cells and tissues, such site-selective systems allow the administration of highly toxic drugs, i.e., for tumor therapy. Depending on the mechanism, various environmental or external stimuli can be applied for the triggered release, including excitation by UV light and changes in pH, temperature and chemical environment.

Examples for pH-controlled release systems include ionic interactions between polycations and carboxylic acids grafted to SBA-15, in which the polycations assemble around fewer deprotonated acid groups at low pH, thus contracting and triggering the release of vancomycin drug molecules.<sup>[225]</sup> A different charge-controlled approach is based on the mutual electrostatic repulsion of attached protonated polyamine chains, leading to the obstruction of the pore entrances by forcing the chains further apart.<sup>[226]</sup> Capping was also achieved by taking advantage of the pH-dependant polypseudorotaxane formation between polyethyleneimine and different cyclodextrines, blocking the pores by increased complexation at basic pH.<sup>[227]</sup> Furthermore, it is possible to control the diffusion through the mesoporous



silica shell of a hollow vesicle reservoir by enclosing the particles in polyelectrolyte layers with pH dependant swelling characteristics.<sup>[228]</sup>

Thermoresponsive mesoporous silica systems have been developed using temperature-induced phase-changes in polymers, i.e. poly(N-isopropylacryl amide).<sup>[229, 230]</sup>

A series of cap systems based on chemically cleavable disulfide linkages was developed, thus physically blocking the pores by attachment of organic dendrimers<sup>[231]</sup> and cyclodextrines,<sup>[232]</sup> or inorganic nanoparticles of cadmium sulphide,<sup>[233]</sup> iron oxide,<sup>[234]</sup> and gold.<sup>[235]</sup> The release is triggered by exposition to reducing agents such as dihydrolipoic acid or dithiothreitol, i.e., conditions similar to the reductive environment in tumor cells.

A more sophisticated system based on pseudorotaxanes was developed, allowing the redox chemistry-dependant reversible opening and closing of a supramolecular nanovalve.<sup>[236-239]</sup>

Variations of this nanovalve system were created, which feature a similar architecture and respond to different stimuli, including changes in pH,<sup>[240, 241]</sup> light irradiation,<sup>[201, 242]</sup> competitive binding,<sup>[243]</sup> and the presence of specific enzymes.<sup>[244]</sup>

The photocontrolled release of guest molecules was demonstrated by UV irradiation of coumarine-modified MCM-41, causing a reversible pore blocking and opening due to intermolecular dimerization and cleavage of the coumarin units by exposure to light with different wavelengths.<sup>[245-247]</sup>

Many of the studies presented here employ mesoporous silica nanoparticles instead of bulk materials, as applications involving the targeted delivery of pharmaceutical agents into cells require limited sizes for transport to the target area and successful endocytosis. The interactions between cells and mesoporous silica nanoparticles with different sizes, morphologies, and functionalities have been extensively investigated.<sup>[248-250]</sup>

## 1.9 Goals

As stated previously, colloidal porous hosts offer several interesting opportunities for new applications, i.e., in nanotechnology and life sciences. However, many fundamental aspects in the synthesis and processing of such materials are still not well understood. The following work contributes to the solution of this problem by investigating novel approaches for the synthesis and modification of colloidal porous nanoparticles with regard to future applications, particularly the development of sophisticated mesoporous-silica-based drug delivery systems.

In the case of colloidal zeolites, applications would vastly profit from a higher number of available framework structure types, as well as smaller particle sizes (Figure 1.9-1a). However, the required structure-directing ability and simultaneous increase in nucleation rates would require new templating species having both different shapes as well as more powerful electrostatic interactions with silicate species in comparison to classic quaternary amines. In order to overcome these obstacles, metal ammine complexes were investigated as a novel class of zeolite templates displaying high charge densities and uncommon geometries.

On the other hand, several shortcomings in the current synthetic knowledge of mesoporous silica nanoparticles limit the possibilities to generate complex delivery systems such as the one shown in Figure 1.9-1b. For example, one of the key points for the construction of such multifunctional carriers is the control between selective functionalization of the outer particle surface and the inner mesopore system, i.e., in order to avoid pore blocking by incorporation of large moieties inside the mesopore channels and fine-tune the host-guest chemistry without influencing colloidal stability.

Furthermore, the scope of available organosilanes for classical surface functionalization of silica materials is rather limited, especially in respect to biological applications. One possible pathway to overcome this restriction is surface grafting of metalorganic reagents, an extremely versatile class of compounds widely used in synthetic organic chemistry. However,

the sensitive nature of the nanosized colloidal system in comparison to bulk materials increases the challenge as it does not permit a simple transfer of already known procedures.

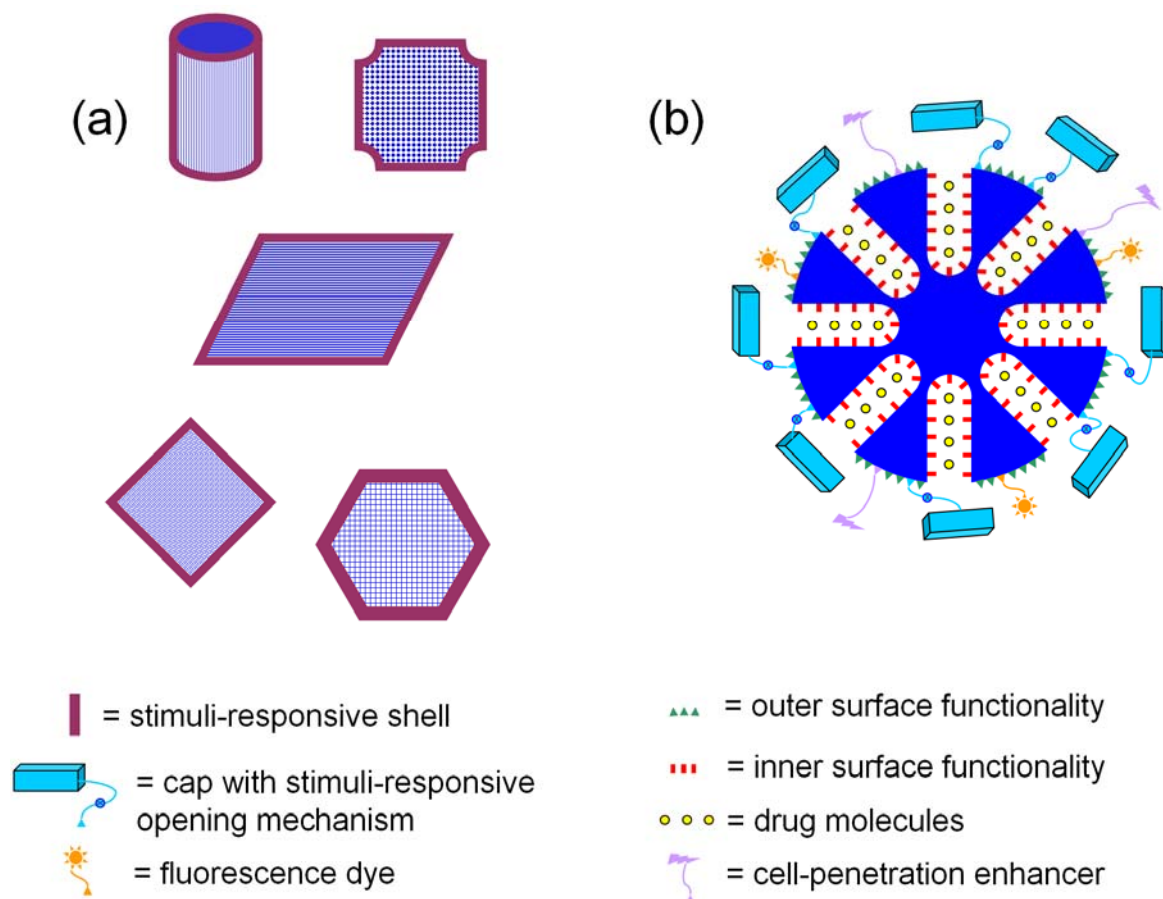


**Figure 1.9-1.** Potential drug delivery vehicles in the form of (a) colloidal zeolite nanocrystals with different framework structures featuring a stimuli-responsive shell for diffusion control, and (b) capped mesoporous silica nanoparticles bearing multiple functionalities allowing tailor-made surface interactions between the environment (cell uptake, colloidal stability, biorecognition, ...) and the guest molecules (pore surface affinity, diffusion rates, ...)

Moreover, size and morphology of the mesoporous silica nanoparticles have to be controlled, preferentially without introduction of unneeded functionalities and under retention of the original surface properties. It is known that co-condensation with certain organosilanes can

promote uniform spherical morphologies, decrease particle size, and increase the monodispersity of the resulting suspensions, among others. However, they also induce drastic changes in surface affinity, i.e., by introduction of hydrophobic surface groups in high amounts, which may be detrimental for the selected field of application. A conceivable solution would be the removal of these organic moieties in an oxidative post-synthesis step, ideally in combination with removal of the organic template, thus simplifying the workup by substitution of the multistep template extraction procedure.

In a joint project with Alexander Darga from our group, piezoelectric sorption measurements by a quartz crystal microbalance were investigated as a potentially powerful tool for the determination of molecule-surface interactions in thin films of functionalized mesoporous silica nanoparticles. A better understanding and new insights on fundamental aspects, such as the impact of different functionalization approaches on the surface affinity in these nanostructured materials, are a crucial factor for later applications.

Solving the aforementioned problems in the synthesis, modification, and characterization of colloidal porous hosts would remove some of the most limiting obstacles for the realization of highly complex and sophisticated porous nanosystems.

## 1.10 References

- [1] P. B. Venuto, *Fluid Catalytic Cracking with Zeolite Catalysts*, Marcel Dekker Inc., New York, **1979**.
- [2] C. J. Adams, A. Araya, S. W. Carr, A. P. Chapple, K. R. Franklin, P. Graham, A. R. Minihan, T. J. Osinga, J. A. Stuart, *Studies in Surface Science and Catalysis* **1997**, *105B*, 1667.
- [3] C. G. Coe, *Gas Separation Technology*, Elsevier, **1990**.
- [4] M. G. Nijkamp, J. E. M. J. Raaymakers, A. J. Van Dillen, K. P. De Jong, *Applied Physics A: Materials Science & Processing* **2001**, *72*, 619.
- [5] V. B. Kazansky, V. Y. Borovkov, A. Serich, H. G. Karge, *Microporous and Mesoporous Materials* **1998**, *22*, 251.
- [6] T. Dueren, L. Sarkisov, O. M. Yaghi, R. Q. Snurr, *Langmuir* **2004**, *20*, 2683.
- [7] C. Y. Liu, K.-i. Aika, *Journal of the Japan Petroleum Institute* **2003**, *46*, 301.
- [8] S. Mintova, S. Mo, T. Bein, *Chemistry of Materials* **2001**, *13*, 901.
- [9] A. R. Pradhan, S. Uppili, J. Shailaja, J. Sivaguru, V. Ramamurthy, *Chemical Communications* **2002**, 596.
- [10] A. Z. Ruiz, H. Li, G. Calzaferri, *Angewandte Chemie, International Edition* **2006**, *45*, 5282.
- [11] M. Alvaro, E. Carbonell, P. Atienzar, H. Garcia, *ChemPhysChem* **2006**, *7*, 1996.
- [12] L. Cao, F. Xu, Y.-Y. Liang, H.-L. Li, *Advanced Material* **2004**, *16*, 1853.
- [13] L. Cao, L.-B. Kong, Y.-Y. Liang, H.-L. Li, *Chemical Communications* **2004**, 1646.
- [14] M. Tather, A. Erdem-Senatalar, *Applied Thermal Engineering* **1999**, *19*, 1157.
- [15] J. Jaenchen, D. Ackermann, H. Stach, W. Broesicke, *Solar Energy* **2004**, *76*, 339.
- [16] H. Chiku, M. Matsui, S. Murakami, Y. Kiyozumi, F. Mizukami, K. Sakaguchi, *Analytical Biochemistry* **2003**, *318*, 80.
- [17] G. Cerri, M. de' Gennaro, M. C. Bonferoni, C. Caramella, *Applied Clay Science* **2004**, *27*, 141.
- [18] C. Platas-Iglesias, L. Vander Elst, W. Zhou, R. N. Muller, C. F. G. C. Geraldies, T. Maschmeyer, J. A. Peters, *Chemistry--A European Journal* **2002**, *8*, 5121.
- [19] K. Kubo, M. Ichikawa, K. Yoshikawa, Y. Koyama, T. Niidome, T. Yamaoka, S.-I. M. Nomura, *Applied Physics Letters* **2003**, *83*, 2468.
- [20] J. E. Mac Dougall, H. Eckert, G. D. Stucky, N. Herron, Y. Wang, K. Moller, T. Bein, D. Cox, *Journal of the American Chemical Society* **1989**, *111*, 8006.
- [21] Y. S. Park, Y. S. Lee, K. B. Yoon, *Journal of the American Chemical Society* **1993**, *115*, 12220.
- [22] Y. Fukushima, T. Kajino, T. Itoh, *Current Nanoscience* **2006**, *2*, 211.
- [23] A. Vinu, K. Z. Hossain, K. Ariga, *Journal of Nanoscience and Nanotechnology* **2005**, *5*, 347.
- [24] J. D. Holmes, M. A. Morris, K. M. Ryan, *Self-Assembly* **2003**, 175.
- [25] B. Zhang, S. A. Davis, S. Mann, N. H. Mendelson, *Chemical Communications* **2000**, 781.
- [26] S. Mintova, T. Bein, *Advanced Materials* **2001**, *13*, 1880.
- [27] J. Kobler, K. Möller, T. Bein, *ACS Nano*, *2*, 791.
- [28] M. A. Snyder, M. Tsapatsis, *Angewandte Chemie, International Edition* **2007**, *46*, 7560.
- [29] K. S. W. Sing, D. H. Everett, R. A. W. Haul, L. Moscou, R. A. Pierotti, J. Rouquerol, T. Siemieniewska, *Pure and Applied Chemistry* **1985**, *57*, 603.
- [30] A. Preisinger, *Naturwissenschaften* **1962**, *49*, 345.
- [31] C. S. Cundy, P. A. Cox, *Chemical Reviews* **2003**, *103*, 663.
- [32] A. F. Cronstedt, *Akad. Handl. Stockholm* **1756**, *18*, 120.

- [33] A. Damour, *Ann. Mines.* **1840**, 17, 191.
- [34] H. Eichhorn, *Poggendorf Ann. Phys. Chem.* **1858**, 105, 126.
- [35] O. Weigel, E. Steinhoff, *Zeitschrift fuer Kristallographie, Kristallgeometrie, Kristallphysik, Kristallchemie* **1925**, 61, 125.
- [36] W. H. Taylor, *Zeitschrift fuer Kristallographie, Kristallgeometrie, Kristallphysik, Kristallchemie* **1930**, 74, 1.
- [37] L. Pauling, *Zeitschrift fuer Kristallographie, Kristallgeometrie, Kristallphysik, Kristallchemie* **1930**, 74, 213.
- [38] R. M. Barrer, *Journal of the Chemical Society* **1948**, 2158.
- [39] E. M. Flanigen, *Introduction to zeolite science and practice*, Elsevier, Amsterdam, **1991**.
- [40] G. T. Kerr, (Mobil Oil Corp.), US 3314752, **1967**.
- [41] R. L. Wadlinger, G. T. Kerr, E. J. Rosinski, (Mobil Oil Corp.), US 3308069, **1967**.
- [42] B. M. Lok, T. R. Cannan, C. A. Messina, *Zeolites* **1983**, 3, 282.
- [43] E. Moretti, S. Contessa, M. Padovan, *Chimica e l'Industria* **1985**, 67, 21.
- [44] E. M. Flanigen, J. M. Bennett, R. W. Grose, J. P. Cohen, R. L. Patton, R. M. Kirchner, J. V. Smith, *Nature* **1978**, 271, 512.
- [45] <http://www.iza-online.org/>.
- [46] S. T. Wilson, B. M. Lok, C. A. Messina, T. R. Cannan, E. M. Flanigen, *Journal of the American Chemical Society* **1982**, 104, 1146.
- [47] B. M. Lok, C. A. Messina, R. L. Patton, R. T. Gajek, T. R. Cannan, E. M. Flanigen, *Journal of the American Chemical Society* **1984**, 106, 6092.
- [48] J. B. Parise, *Inorganic Chemistry* **1985**, 24, 4312.
- [49] S. S. Dhingra, R. C. Haushalter, *Journal of the Chemical Society, Chemical Communications* **1993**, 1665.
- [50] S. Natarajan, M. P. Attfield, A. K. Cheetham, *Angewandte Chemie, International Edition* **1997**, 36, 978.
- [51] B. A. Adair, G. D. De Delgado, J. M. Delgado, A. K. Cheetham, *Angewandte Chemie, International Edition* **2000**, 39, 745.
- [52] R. C. Haushalter, L. A. Mundi, *Chemistry of Materials* **1992**, 4, 31.
- [53] V. Soghomonian, Q. Chen, R. C. Haushalter, J. Zubieta, C. J. O'Connor, *Science* **1993**, 259, 1596.
- [54] M. Cavelllec, D. Riou, C. Ninclaus, J.-M. Greneche, G. Ferey, *Zeolites* **1996**, 17, 250.
- [55] J. Chen, R. H. Jones, S. Natarajan, M. B. Hursthouse, J. M. Thomas, *Angewandte Chemie* **1994**, 106, 667.
- [56] S. Neeraj, M. L. Noy, A. K. Cheetham, *Solid State Sciences* **2002**, 4, 397.
- [57] Q. Huang, M. Ulutagay, P. A. Michener, S.-J. Hwu, *Journal of the American Chemical Society* **1999**, 121, 10323.
- [58] N. Guillou, Q. Gao, M. Nogues, R. E. Morris, M. Hervieu, G. Ferey, A. K. Cheetham, *Comptes Rendus de l'Academie des Sciences, Serie IIc: Chimie* **1999**, 2, 387.
- [59] E. Kemnitz, M. Wloka, S. Trojanov, A. Stiewe, *Angewandte Chemie, International Edition* **1996**, 35, 2677.
- [60] A. I. Bortun, S. A. Khainakov, L. N. Bortun, D. M. Poojary, J. Rodriguez, J. R. Garcia, A. Clearfield, *Chemistry of Materials* **1997**, 9, 1805.
- [61] A. K. Cheetham, P. M. Forster, *The Chemistry of Nanomaterials: Synthesis, Properties and Applications, Volume 2*, WILEY-VCH Verlag GmbH & Co. KGaA, Weinheim, **2004**.
- [62] M. E. Davis, C. Saldarriaga, C. Montes, J. Garces, C. Crowder, *Nature* **1988**, 331, 698.
- [63] M. Estermann, L. B. McCusker, C. Baerlocher, A. Merrouche, H. Kessler, *Nature* **1991**, 352, 320.

- [64] Q. Huo, R. Xu, S. Li, Z. Ma, J. M. Thomas, R. H. Jones, A. M. Chippindale, *Journal of the Chemical Society, Chemical Communications* **1992**, 875.
- [65] R. H. Jones, J. M. Thomas, J. Chen, R. Xu, Q. Huo, S. Li, Z. Ma, A. M. Chippindale, *Journal of Solid State Chemistry* **1993**, 102, 204.
- [66] S. Horstmann, E. Irran, W. Schnick, *Angewandte Chemie, International Edition* **1997**, 36, 1992.
- [67] J. B. Parise, *Science* **1991**, 251, 293.
- [68] J. D. Martin, K. B. Greenwood, *Angewandte Chemie, International Edition* **1997**, 36, 2072.
- [69] C. T. Kresge, M. E. Leonowicz, W. J. Roth, J. C. Vartuli, J. S. Beck, *Nature* **1992**, 359, 710.
- [70] J. S. Beck, J. C. Vartuli, W. J. Roth, M. E. Leonowicz, C. T. Kresge, K. D. Schmitt, C. T. W. Chu, D. H. Olson, E. W. Sheppard, et al., *Journal of the American Chemical Society* **1992**, 114, 10834.
- [71] T. Yanagisawa, T. Shimizu, K. Kuroda, C. Kato, *Bulletin of the Chemical Society of Japan* **1990**, 63, 988.
- [72] S. Inagaki, Y. Fukushima, K. Kuroda, *Journal of the Chemical Society, Chemical Communications* **1993**, 680.
- [73] S. Inagaki, A. Koiwai, N. Suzuki, Y. Fukushima, K. Kuroda, *Bulletin of the Chemical Society of Japan* **1996**, 69, 1449.
- [74] V. Chiola, J. E. Ritsko, C. D. Vanderpool, (Sylvania Electric Products Inc.), US 69-802628 3556725, **1971**.  
US, **1971**, p. 3 pp.
- [75] F. Di Renzo, H. Cambon, R. Dutartre, *Microporous Materials* **1997**, 10, 283.
- [76] P. T. Tanev, T. J. Pinnavaia, *Science* **1995**, 267, 865.
- [77] S. A. Bagshaw, E. Prouzet, T. J. Pinnavaia, *Science* **1995**, 269, 1242.
- [78] K. Cassiers, P. van der Voort, E. F. Vansant, *Chemical Communications* **2000**, 2489.
- [79] D. Zhao, Q. Huo, J. Feng, B. F. Chmelka, G. D. Stucky, *Journal of the American Chemical Society* **1998**, 120, 6024.
- [80] D. Zhao, J. Feng, Q. Huo, N. Melosh, G. H. Frederickson, B. F. Chmelka, G. D. Stucky, *Science* **1998**, 279, 548.
- [81] A. Taguchi, F. Schueth, *Microporous and Mesoporous Materials* **2004**, 77, 1.
- [82] D. Zhao, J. Sun, Q. Li, G. D. Stucky, *Chemistry of Materials* **2000**, 12, 275.
- [83] M. Imperor-Clerc, P. Davidson, A. Davidson, *Journal of the American Chemical Society* **2000**, 122, 11925.
- [84] S. A. Bagshaw, T. J. Pinnavaia, *Angewandte Chemie, International Edition* **1996**, 35, 1102.
- [85] P. Yang, D. Zhao, D. I. Margolese, B. F. Chmelka, G. D. Stucky, *Nature* **1998**, 396, 152.
- [86] B. Lee, D. Lu, J. N. Kondo, K. Domen, *Chemical Communications* **2001**, 2118.
- [87] D. M. Antonelli, J. Y. Ying, *Angewandte Chemie, International Edition* **1996**, 35, 426.
- [88] M. J. MacLachlan, N. Coombs, G. A. Ozin, *Nature* **1999**, 397, 681.
- [89] P. V. Braun, P. Osenar, S. I. Stupp, *Nature* **1996**, 380, 325.
- [90] P. N. Trikalitis, K. K. Rangan, T. Bakas, M. G. Kanatzidis, *Nature* **2001**, 410, 671.
- [91] G. S. Attard, P. N. Bartlett, N. R. B. Coleman, J. M. Elliott, J. R. Owen, J. H. Wang, *Science* **1997**, 278, 838.
- [92] G. S. Armatas, M. G. Kanatzidis, *Nature* **2006**, 441, 1122.
- [93] D. Sun, A. E. Riley, A. J. Cadby, E. K. Richman, S. D. Korlann, S. H. Tolbert, *Nature* **2006**, 441, 1126.
- [94] B. Rushton, R. Mokaya, *Journal of Materials Chemistry* **2008**, 18, 235.

- [95] X. Roy, L. K. Thompson, N. Coombs, M. J. MacLachlan, *Angewandte Chemie, International Edition* **2008**, 47, 511.
- [96] S. Kaskel, P. Krawiec, *Studies in Surface Science and Catalysis* **2007**, 170B, 1770.
- [97] Y. Shi, Y. Wan, B. Tu, D. Zhao, *Journal of Physical Chemistry C* **2008**, 112, 112.
- [98] F. Hoffmann, M. Cornelius, J. Morell, M. Froeba, *Angewandte Chemie, International Edition* **2006**, 45, 3216.
- [99] R. Ryoo, S. H. Joo, S. Jun, *Journal of Physical Chemistry B* **1999**, 103, 7743.
- [100] Y. Meng, D. Gu, F. Zhang, Y. Shi, H. Yang, Z. Li, C. Yu, B. Tu, D. Zhao, *Angewandte Chemie, International Edition* **2005**, 44, 7053.
- [101] B. F. Hoskins, R. Robson, *Journal of the American Chemical Society* **1989**, 111, 5962.
- [102] S. Kitagawa, R. Kitaura, S.-i. Noro, *Angewandte Chemie, International Edition* **2004**, 43, 2334.
- [103] G. Ferey, *Chemical Society Reviews* **2008**, 37, 191.
- [104] O. M. Yaghi, G. Li, H. Li, *Nature* **1995**, 378, 703.
- [105] C. N. R. Rao, S. Natarajan, R. Vaidhyanathan, *Angewandte Chemie, International Edition* **2004**, 43, 1466.
- [106] N. G. Pschirer, D. M. Ciurtin, M. D. Smith, U. H. F. Bunz, H.-C. zur Loye, *Angewandte Chemie, International Edition* **2002**, 41, 583.
- [107] Y. Cui, H. L. Ngo, W. Lin, *Chemical Communications* **2003**, 1388.
- [108] R.-G. Xiong, X.-Z. You, B. F. Abrahams, Z. Xue, C.-M. Che, *Angewandte Chemie, International Edition* **2001**, 40, 4422.
- [109] L. E. Gordon, W. T. A. Harrison, *Inorganic Chemistry* **2004**, 43, 1808.
- [110] H. Ratajczak, J. Barycki, A. Pietraszko, J. Baran, S. Debrus, M. May, J. Venturini, *Journal of Molecular Structure* **2000**, 526, 269.
- [111] J. Fan, C. Slebodnick, R. Angel, B. E. Hanson, *Inorganic Chemistry* **2005**, 44, 552.
- [112] Y. Zhang, M. K. Saha, I. Bernal, *CrystEngComm* **2003**, 5, 34.
- [113] M. Mizutani, N. Maejima, K. Jitsukawa, H. Masuda, H. Einaga, *Inorganica Chimica Acta* **1998**, 283, 105.
- [114] M. Eddaoudi, J. Kim, N. Rosi, D. Vodak, J. Wachter, M. O'Keeffe, M. Yaghi Omar, *Science* **2002**, 295, 469.
- [115] G. Ferey, *Journal of Solid State Chemistry* **2000**, 152, 37.
- [116] G. Ferey, C. Serre, C. Mellot-Draznieks, F. Millange, S. Surble, J. Dutour, I. Margiolaki, *Angewandte Chemie, International Edition* **2004**, 43, 6296.
- [117] G. Ferey, C. Mellot-Draznieks, C. Serre, F. Millange, J. Dutour, S. Surble, I. Margiolaki, *Science* **2005**, 309, 2040.
- [118] A. P. Cote, A. I. Benin, N. W. Ockwig, M. O'Keeffe, A. J. Matzger, O. M. Yaghi, *Science* **2005**, 310, 1166.
- [119] M. Mastalerz, *Angewandte Chemie, International Edition* **2008**, 47, 445.
- [120] K. Yamamoto, T. Tatsumi, *Chemistry of Materials* **2008**, 20, 972.
- [121] K. Yamamoto, Y. Sakata, Y. Nohara, Y. Takahashi, T. Tatsumi, *Science* **2003**, 300, 470.
- [122] B. L. Su, M. Roussel, K. Vause, X. Y. Yang, F. Gilles, L. Shi, E. Leonova, M. Eden, X. Zou, *Microporous and Mesoporous Materials* **2007**, 105, 49.
- [123] C. J. Brinker, G. W. Scherer, *Sol-Gel Science*, Academic Press, Boston, **1990**.
- [124] R. K. Iler, *The Chemistry of Silica - Solubility, Polymerization, Colloid and Surface Properties, and Biochemistry*, John Wiley & Sons, New York, **1979**.
- [125] C. S. Cundy, P. A. Cox, *Microporous and Mesoporous Materials* **2005**, 82, 1.
- [126] R. M. Barrer, J. W. Baynham, F. W. Bultitude, W. M. Meier, *Journal of the Chemical Society* **1959**, 195.
- [127] R. M. Barrer, *Chem. Brit.* **1966**, 2, 380.
- [128] G. T. Kerr, *Journal of Physical Chemistry* **1966**, 70, 1047.



- [129] S. P. Zhdanov, *Molecular Sieve Zeolites - I, Vol. 101*, ACS, **1971**.
- [130] E. G. Derouane, S. Detremmerie, Z. Gabelica, N. Blom, *Applied Catalysis* **1981**, *1*, 201.
- [131] Z. Gabelica, E. G. Derouane, N. Blom, *Applied Catalysis* **1983**, *5*, 109.
- [132] Z. Gabelica, N. Blom, E. G. Derouane, *Applied Catalysis* **1983**, *5*, 227.
- [133] P. Bodart, J. B. Nagy, Z. Gabelica, E. G. Derouane, *Journal de Chimie Physique et de Physico-Chimie Biologique* **1986**, *83*, 777.
- [134] C. D. Chang, A. T. Bell, *Catalysis Letters* **1991**, *8*, 305.
- [135] S. L. Burkett, M. E. Davis, *Journal of Physical Chemistry* **1994**, *98*, 4647.
- [136] S. L. Burkett, M. E. Davis, *Chemistry of Materials* **1995**, *7*, 920.
- [137] S. L. Burkett, M. E. Davis, *Chemistry of Materials* **1995**, *7*, 1453.
- [138] R. Ravishankar, C. Kirschhock, B. J. Schoeman, P. Vanoppen, P. J. Grobet, S. Storck, W. F. Maier, J. A. Martens, F. C. De Schryver, P. A. Jacobs, *Journal of Physical Chemistry B* **1998**, *102*, 2633.
- [139] R. Ravishankar, C. E. A. Kirschhock, P.-P. Knops-Gerrits, E. J. P. Feijen, P. J. Grobet, P. Vanoppen, F. C. De Schryver, G. Miehe, H. Fuess, B. J. Schoeman, P. A. Jacobs, J. A. Martens, *Journal of Physical Chemistry B* **1999**, *103*, 4960.
- [140] C. E. A. Kirschhock, R. Ravishankar, F. Verspeurt, P. J. Grobet, P. A. Jacobs, J. A. Martens, *Journal of Physical Chemistry B* **1999**, *103*, 4965.
- [141] C. E. A. Kirschhock, R. Ravishankar, L. Van Looveren, P. A. Jacobs, J. A. Martens, *Journal of Physical Chemistry B* **1999**, *103*, 4972.
- [142] C. E. A. Kirschhock, R. Ravishankar, P. A. Jacobs, J. A. Martens, *Journal of Physical Chemistry B* **1999**, *103*, 11021.
- [143] C. E. A. Kirschhock, V. Buschmann, S. Kremer, R. Ravishankar, C. J. Y. Houssin, B. L. Mojet, R. A. van Santen, P. J. Grobet, P. A. Jacobs, J. A. Martens, *Angewandte Chemie, International Edition* **2001**, *40*, 2637.
- [144] C. E. A. Kirschhock, S. P. B. Kremer, P. J. Grobet, P. A. Jacobs, J. A. Martens, *Journal of Physical Chemistry B* **2002**, *106*, 4897.
- [145] W. Xu, J. Dong, J. Li, J. Li, F. Wu, *Journal of the Chemical Society, Chemical Communications* **1990**, 755.
- [146] M. Matsukata, M. Ogura, T. Osaki, P. Raja, H. P. Rao, M. Nomura, E. Kikuchi, *Topics in Catalysis* **1999**, *9*, 77.
- [147] L. Tosheva, V. P. Valtchev, *Chemistry of Materials* **2005**, *17*, 2494.
- [148] N. N. Feoktistova, S. P. Zhdanov, W. Lutz, M. Buelow, *Zeolites* **1989**, *9*, 136.
- [149] S. Mintova, V. Valchev, *Zeolites* **1993**, *13*, 299.
- [150] B. J. Schoeman, J. Sterte, J.-E. Otterstedt, *Journal of Colloid and Interface Science* **1995**, *170*, 449.
- [151] A. E. Persson, B. J. Schoeman, J. Sterte, J. E. Otterstedt, *Zeolites* **1995**, *15*, 611.
- [152] M. Tsapatsis, M. Lovallo, T. Okubo, M. E. Davis, M. Sadakata, *Chemistry of Materials* **1995**, *7*, 1734.
- [153] A. E. Persson, B. J. Schoeman, J. Sterte, J. E. Otterstedt, *Zeolites* **1994**, *14*, 557.
- [154] S. Mintova, N. H. Olson, V. Valtchev, T. Bein, *Science* **1999**, *283*, 958.
- [155] B.-Z. Zhan, M. A. White, M. Lumsden, J. Mueller-Neuhaus, K. N. Robertson, T. S. Cameron, M. Gharghouri, *Chemistry of Materials* **2002**, *14*, 3636.
- [156] J. Kecht, B. Mihailova, K. Karaghiosoff, S. Mintova, T. Bein, *Langmuir* **2004**, *20*, 5271.
- [157] J. Yao, H. Wang, K. R. Ratinac, S. P. Ringer, *Chemistry of Materials* **2006**, *18*, 1394.
- [158] J. Hedlund, E. Kurpan, *Studies in Surface Science and Catalysis* **2001**, *135*, 224.
- [159] S. Mintova, N. Petkov, K. Karaghiosoff, T. Bein, *Microporous and Mesoporous Materials* **2001**, *50*, 121.

- [160] M. A. Camblor, A. Corma, A. Mifsud, J. Perez-Pariente, S. Valencia, *Studies in Surface Science and Catalysis* **1997**, 105A, 341.
- [161] H. Du, M. Fang, W. Xu, X. Meng, W. Pang, *Journal of Materials Chemistry* **1997**, 7, 551.
- [162] S. Mintova, S. Mo, T. Bein, *Chemistry of Materials* **1998**, 10, 4030.
- [163] G. Zhu, S. Qiu, F. Gao, G. Wu, R. Wang, B. Li, Q. Fang, Y. Li, B. Gao, X. Xu, O. Terasaki, *Microporous and Mesoporous Materials* **2001**, 50, 129.
- [164] J. Kecht, S. Mintova, T. Bein, *Chemistry of Materials* **2007**, 19, 1203.
- [165] J. Kecht, S. Mintova, T. Bein, *Langmuir* **2008**, 24, 4310.
- [166] Y. Wan, D. Zhao, *Chemical Reviews* **2007**, 107, 2821.
- [167] Q. Huo, D. I. Margolese, U. Ciesla, P. Feng, T. E. Gier, P. Sieger, R. Leon, P. M. Petroff, F. Schueth, G. D. Stucky, *Nature* **1994**, 368, 317.
- [168] Q. Huo, D. I. Margolese, U. Ciesla, D. G. Demuth, P. Feng, T. E. Gier, P. Sieger, A. Firouzi, B. F. Chmelka, et al., *Chemistry of Materials* **1994**, 6, 1176.
- [169] G. S. Attard, J. C. Glyde, C. G. Goltner, *Nature* **1995**, 378, 366.
- [170] A. Monnier, F. Schuth, Q. Huo, D. Kumar, D. Margolese, R. S. Maxwell, G. D. Stucky, M. Krishnamurty, P. Petroff, et al., *Science* **1993**, 261, 1299.
- [171] S. Pevzner, O. Regev, R. Yerushalmi-Rozen, *Current Opinion in Colloid & Interface Science* **2000**, 4, 420.
- [172] C.-Y. Mou, H.-P. Lin, *Pure and Applied Chemistry* **2000**, 72, 137.
- [173] C. E. Fowler, D. Khushalani, B. Lebeau, S. Mann, *Advanced Materials* **2001**, 13, 649.
- [174] Q. Cai, Z.-S. Luo, W.-Q. Pang, Y.-W. Fan, X.-H. Chen, F.-Z. Cui, *Chemistry of Materials* **2001**, 13, 258.
- [175] J. Rathousky, M. Zukalova, P. J. Kooyman, A. Zukal, *Colloids and Surfaces, A: Physicochemical and Engineering Aspects* **2004**, 241, 81.
- [176] R. I. Nooney, D. Thirunavukkarasu, Y. Chen, R. Josephs, A. E. Ostafin, *Chemistry of Materials* **2002**, 14, 4721.
- [177] K. Suzuki, K. Ikari, H. Imai, *Journal of the American Chemical Society* **2004**, 126, 462.
- [178] K. Ikari, K. Suzuki, H. Imai, *Langmuir* **2006**, 22, 802.
- [179] Y. Han, J. Y. Ying, *Angewandte Chemie, International Edition* **2005**, 44, 288.
- [180] H. Muhlenweg, *Speciality Chemicals Magazine* **2005**, 25, 34.
- [181] R. Golchert, H. Mangold, T. Scharfe, (Degussa AG, Germany), EP 2000-107817 1148026, **2001**.
- [182] Y. Lu, H. Fan, A. Stump, T. L. Ward, T. Rieker, C. J. Brinker, *Nature* **1999**, 398, 223.
- [183] W.-S. Chae, P. V. Braun, *Chemistry of Materials* **2007**, 19, 5593.
- [184] F. Li, Z. Wang, A. Stein, *Angewandte Chemie, International Edition* **2007**, 46, 1885.
- [185] B. G. Trewyn, I. I. Slowing, S. Giri, H.-T. Chen, V. S. Y. Lin, *Accounts of Chemical Research* **2007**, 40, 846.
- [186] A. Berggren, A. E. C. Palmqvist, *Journal of Physical Chemistry C* **2008**, 112, 732.
- [187] J. El Haskouri, D. Ortiz de Zarate, C. Guillem, A. Beltran-Porter, M. Caldes, M. D. Marcos, D. Beltran-Porter, J. Latorre, P. Amoros, *Chemistry of Materials* **2002**, 14, 4502.
- [188] K. Möller, J. Kobler, T. Bein, *Advanced Functional Materials* **2007**, 17, 605.
- [189] K. Möller, J. Kobler, T. Bein, *Journal of Materials Chemistry* **2007**, 17, 624.
- [190] J. G. Verkade, *Accounts of Chemical Research* **1993**, 26, 483.
- [191] S. Cabrera, J. El Haskouri, C. Guillem, J. Latorre, A. Beltran-Porter, D. Beltran-Porter, M. D. Marcos, P. Amoros, *Solid State Sciences* **2000**, 2, 405.
- [192] P. Torchilin Vladimir, *Nature reviews. Drug discovery* **2005**, 4, 145.
- [193] J.-W. Yoo, C. H. Lee, *Journal of Controlled Release* **2006**, 112, 1.
- [194] M. Malmsten, *Soft Matter* **2006**, 2, 760.

- [195] M. Vallet-Regi, *Chemistry--A European Journal* **2006**, *12*, 5934.
- [196] P. Korteso, M. Ahola, S. Karlsson, I. Kangasniemi, A. Yli-Urpo, J. Kiesvaara, *Biomaterial* **2000**, *21*, 193.
- [197] S. Chia, J. Urano, F. Tamanoi, B. Dunn, J. I. Zink, *Journal of the American Chemical Society* **2000**, *122*, 6488.
- [198] S. Radin, G. El-Bassyouni, J. Vresilovic Edward, E. Schepers, P. Ducheyne, *Biomaterials* **2005**, *26*, 1043.
- [199] R. D. Ries, K. E. Cobian, (Medtronic, Inc., USA), WO 2004-US8467 2004084955, **2004**.
- [200] R. E. Morris, P. S. Wheatley, A. R. Butler, (The University Court of the University of St. Andrews, UK), WO 2004-GB2905 2005003032, **2005**.
- [201] T. D. Nguyen, K. C. F. Leung, M. Liong, Y. Liu, F. Stoddart, J. I. Zink, *Advanced Functional Materials* **2007**, *17*, 2101.
- [202] S. K. Gupta, (Bioderm Research, USA), US 2007-760466 2007237834, **2007**.
- [203] P. Horcajada, C. Marquez-Alvarez, A. Ramila, J. Perez-Pariente, M. Vallet-Regi, *Solid State Sciences* **2006**, *8*, 1459.
- [204] A. Dyer, S. Morgan, P. Wells, C. Williams, *Journal of Helminthology* **2000**, *74*, 137.
- [205] L. W. Wong, W. Q. Sun, N. W. Chan, W. Y. Lai, W. K. Leung, J. C. Tsang, Y. H. Wong, K. L. Yeung, *Studies in Surface Science and Catalysis* **2007**, *170A*, 525.
- [206] K.-L. Yeung, L.-W. Wong, W. Sun, W.-K. Leung, W.-Y. Lai, N.-W. Chan, (The Hong Kong University of Science and Technology, Peop. Rep. China), WO 2007-CN584 2007095859, **2007**.
- [207] R. Francis, (Medtronic Vascular, Inc., USA)US 2006-381823 2007259017, **2007**.
- [208] S. K. Gupta, (Bioderm Research, USA), US 2006-307824 2006127430, **2006**.
- [209] M. De Gennaro, G. Cerri, C. M. Caramella, M. C. Bonferoni, (Universita' Degli Studi di Napoli "Federico II", Italy; Universita' Degli Studi di Pavia), WO 2002-EP6275 2002100420, **2002**.
- [210] M. Fujiwara, F. Yamamoto, K. Okamoto, K. Shiokawa, R. Nomura, *Analytical Chemistry* **2005**, *77*, 8138.
- [211] M. Vallet-Regi, F. Balas, D. Arcos, *Angewandte Chemie, International Edition* **2007**, *46*, 7548.
- [212] B. G. Trewyn, S. Giri, I. I. Slowing, V. S. Y. Lin, *Chemical Communications* **2007**, 3236.
- [213] F. Qu, G. Zhu, H. Lin, W. Zhang, J. Sun, S. Li, S. Qiu, *Journal of Solid State Chemistry* **2006**, *179*, 2027.
- [214] J. Andersson, J. Rosenholm, S. Areva, M. Linden, *Chemistry of Materials* **2004**, *16*, 4160.
- [215] P. Horcajada, A. Ramila, J. Perez-Pariente, M. Vallet-Regi, *Microporous and Mesoporous Materials* **2004**, *68*, 105.
- [216] C. Charnay, S. Begu, C. Tourne-Peteilh, L. Nicole, D. A. Lerner, J. M. Devoisselle, *European Journal of Pharmaceutics and Biopharmaceutics* **2004**, *57*, 533.
- [217] B. Munoz, A. Ramila, J. Perez-Pariente, I. Diaz, M. Vallet-Regi, *Chemistry of Materials* **2003**, *15*, 500.
- [218] M. Vallet-Regi, A. Ramila, R. P. del Real, J. Perez-Pariente, *Chemistry of Materials* **2001**, *13*, 308.
- [219] W. Zeng, X.-F. Qian, J. Yin, Z.-K. Zhu, *Materials Chemistry and Physics* **2006**, *97*, 437.
- [220] C. Tourne-Peteilh, D. Brunel, S. Begu, B. Chiche, F. Fajula, D. A. Lerner, J.-M. Devoisselle, *New Journal of Chemistry* **2003**, *27*, 1415.
- [221] F. Babonneau, L. Yeung, N. Steunou, C. Gervais, A. Ramila, M. Vallet-Regi, *Journal of Sol-Gel Science and Technology* **2004**, *31*, 219.

- [222] V. S. Y. Lin, C.-Y. Lai, J. Huang, S.-A. Song, S. Xu, *Journal of the American Chemical Society* **2001**, *123*, 11510.
- [223] S. W. Song, K. Hidajat, S. Kawi, *Langmuir* **2005**, *21*, 9568.
- [224] W. Zeng, X.-F. Qian, Y.-B. Zhang, J. Yin, Z.-K. Zhu, *Materials Research Bulletin* **2005**, *40*, 766.
- [225] Q. Yang, S. Wang, P. Fan, L. Wang, Y. Di, K. Lin, F.-S. Xiao, *Chemistry of Materials* **2005**, *17*, 5999.
- [226] R. Casasus, M. D. Marcos, R. Martinez-Manez, J. V. Ros-Lis, J. Soto, L. A. Villaescusa, P. Amoros, D. Beltran, C. Guillem, J. Latorre, *Journal of the American Chemical Society* **2004**, *126*, 8612.
- [227] C. Park, K. Oh, S. C. Lee, C. Kim, *Angewandte Chemie, International Edition* **2007**, *46*, 1455.
- [228] Y. Zhu, J. Shi, W. Shen, X. Dong, J. Feng, M. Ruan, Y. Li, *Angewandte Chemie, International Edition* **2005**, *44*, 5083.
- [229] J. H. Chang, C. H. Shim, B. J. Kim, Y. Shin, G. J. Exarhos, K. J. Kim, *Advanced Materials* **2005**, *17*, 634.
- [230] S. Zhu, Z. Zhou, D. Zhang, C. Jin, Z. Li, *Microporous and Mesoporous Materials* **2007**, *106*, 56.
- [231] D. R. Radu, C.-Y. Lai, K. Jeftinija, E. W. Rowe, S. Jeftinija, V. S. Y. Lin, *Journal of the American Chemical Society* **2004**, *126*, 13216.
- [232] J. L. Vivero-Escoto, V. S. Y. Lin, *Abstracts of Papers, 233rd ACS National Meeting, Chicago, IL, United States, March 25-29, 2007* **2007**.
- [233] C.-Y. Lai, B. G. Trewyn, D. M. Jeftinija, K. Jeftinija, S. Xu, S. Jeftinija, V. S. Y. Lin, *Journal of the American Chemical Society* **2003**, *125*, 4451.
- [234] S. Giri, B. G. Trewyn, M. P. Stellmaker, V. S. Y. Lin, *Angewandte Chemie, International Edition* **2005**, *44*, 5038.
- [235] F. Torney, B. G. Trewyn, V. S. Y. Lin, K. Wang, *Nature Nanotechnology* **2007**, *2*, 295.
- [236] R. Hernandez, H.-R. Tseng, J. W. Wong, J. F. Stoddart, J. I. Zink, *Journal of the American Chemical Society* **2004**, *126*, 3370.
- [237] T. D. Nguyen, H.-R. Tseng, P. C. Celestre, A. H. Flood, Y. Liu, J. F. Stoddart, J. I. Zink, *Proceedings of the National Academy of Sciences of the United States of America* **2005**, *102*, 10029.
- [238] T. D. Nguyen, Y. Liu, S. Saha, K. C. F. Leung, J. F. Stoddart, J. I. Zink, *Journal of the American Chemical Society* **2007**, *129*, 626.
- [239] S. Saha, K. C. F. Leung, T. D. Nguyen, J. F. Stoddart, J. I. Zink, *Advanced Functional Materials* **2007**, *17*, 685.
- [240] T. D. Nguyen, K. C. F. Leung, M. Liong, C. D. Pentecost, J. F. Stoddart, J. I. Zink, *Organic Letters* **2006**, *8*, 3363.
- [241] S. Angelos, Y.-W. Yang, K. Patel, J. F. Stoddart, J. I. Zink, *Angewandte Chemie, International Edition* **2008**, *47*, 2222.
- [242] S. Angelos, E. Johansson, J. F. Stoddart, J. I. Zink, *Advanced Functional Materials* **2007**, *17*, 2261.
- [243] K. C. F. Leung, T. D. Nguyen, J. F. Stoddart, J. I. Zink, *Chemistry of Materials* **2006**, *18*, 5919.
- [244] K. Patel, S. Angelos, W. R. Dichtel, A. Coskun, Y.-W. Yang, J. I. Zink, J. F. Stoddart, *Journal of the American Chemical Society* **2008**, *130*, 2382.
- [245] N. K. Mal, M. Fujiwara, Y. Tanaka, T. Taguchi, M. Matsukata, *Chemistry of Materials* **2003**, *15*, 3385.
- [246] N. K. Mal, M. Fujiwara, Y. Tanaka, *Nature* **2003**, *421*, 350.
- [247] M. Fujiwara, N. K. Mal, Y. Tanaka, (National Institute of Advanced Industrial Science and Technology, Japan), US 2004-761407 2004213996, **2004**.

- [248] D.-M. Huang, Y. Hung, B.-S. Ko, S.-C. Hsu, W.-H. Chen, C.-L. Chien, C.-P. Tsai, C.-T. Kuo, J.-C. Kang, C.-S. Yang, C.-Y. Mou, Y.-C. Chen, *FASEB Journal* **2005**, *19*, 2014.
- [249] I. Slowing, B. G. Trewyn, V. S. Y. Lin, *Journal of the American Chemical Society* **2006**, *128*, 14792.
- [250] Y.-S. Lin, C.-P. Tsai, H.-Y. Huang, C.-T. Kuo, Y. Hung, D.-M. Huang, Y.-C. Chen, C.-Y. Mou, *Chemistry of Materials* **2005**, *17*, 4570.



## 2 Characterization

### 2.1 Dynamic Light Scattering

Dynamic Light Scattering (DLS)<sup>[1, 2]</sup> is also known as Quasi Elastic Light Scattering and Photon Correlation Spectroscopy. It is a non-invasive technique for the determination of hydrodynamic particle diameters in colloidal solutions by measuring the intensity fluctuations caused by interference of scattered laser light from different particles. The temporal evolution of the fluctuations depends on the particle movement by Brownian motion, and is thus correlated to particle size.

Coherent laser light scattered from small particles suspended in a liquid will result in a speckle pattern on a detector area due to the constructive and destructive interference of the light resulting from particles at different positions. If the particles would remain stationary, the speckle pattern would also remain unchanged. However, as the particles are constantly moving due to Brownian motion, i.e., the random collisions with molecules from the liquid surrounding the particle, the intensity distribution of the speckle pattern changes over time. In DLS, these fluctuations in the scattering intensity are correlated across microsecond time scales by an autocorrelation function, i.e., a function that describes how a given measurement relates to itself in a time-dependent manner. The second order autocorrelation curve can be directly derived from the intensity trace according to equation 2.1-1.

$$g^2(q; \tau) = \frac{\langle I(t)I(t + \tau) \rangle}{\langle I(t)^2 \rangle} \quad (2.1-1)$$

$q$  : wave vector

$\tau$  : delay time

$I$  : intensity

The normalized scattered electric field autocorrelation function, i.e., the first order autocorrelation curve, is related to the second order autocorrelation curve by the Siegert equation (2.1-2).

$$g^2(q; \tau) = 1 + \beta [g^1(q; \tau)]^2 \quad (2.1-2)$$

$q$  : wave vector

$\tau$  : delay time

$\beta$  : correcting factor

The first order autocorrelation curve can be fitted by a number of mathematical approaches (i.e. cumulant method, CONTIN algorithm, and others) in order to yield sums of single exponential decays related to the translational diffusion coefficients of the different particle size classes in polydisperse samples. In case of a completely monodisperse sample, a single exponential function (2.1-3; 2.1-4) is obtained for the decay of the autocorrelation function.

$$g^1(q; \tau) = e^{-\Gamma \tau} \quad (2.1-3)$$

$$\Gamma = \frac{D}{\left( \frac{4n_0\pi}{\lambda} \sin\left(\frac{\theta}{2}\right) \right)^2} \quad (2.1-4)$$

$D$  : diffusion coefficient

$n_0$  : refractive index of the solution

$\lambda$  : wavelength of the laser

$\theta$  : angle of the scattering measurement

Under defined experimental conditions, the diffusion coefficient  $D$  of the particles can be measured from the exponent of the fitted curves. The hydrodynamic radius of an equivalent sphere is calculated using the Stokes-Einstein equation (2.1-5).



$$D = \frac{kT}{3\pi\eta d} \quad (2.1-5)$$

$D$  : diffusion coefficient

$k$  : Boltzmann constant

$T$  : temperature

$\eta$  : solvent viscosity

$d$  : hydrodynamic diameter

In cases where samples display broad or polymodal particle size distributions, the interpretation of data based on the particle scattering intensity, as obtained in DLS, can be misleading. Mie theory has to be applied in order to accurately describe the scattering of particles similar or larger than the wavelength of the incoming light. However, the scattering intensity of small particles in a beam of unpolarized light can be sufficiently described by Rayleigh scattering (2.1-6).

$$I = I_0 \frac{1 + \cos^2 \theta}{2R^2} \left( \frac{2\pi}{\lambda} \right)^4 \left( \frac{n^2 - 1}{n^2 + 2} \right)^2 \left( \frac{d}{2} \right)^6 \quad (2.1-6)$$

$I$  : Intensity of the scattered light

$I_0$  : Intensity of the incoming light

$\theta$  : scattering angle

$R$  : distance to the particle

$\lambda$  : wavelength of the incoming light

$n$  : refractive index of the particle

$d$  : particle diameter

As the scattering intensity is proportional to  $d^6$ , a small amount of aggregates or larger particles can dominate the distribution curve. It is therefore common in a lot of applications to

give the volume-weighted and number-weighted size distributions instead, which are proportional to  $d^3$  and  $d$ , respectively. A schematic comparison between the intensity, volume, and number distributions of a suspension containing an identical number of 10 nm and 100 nm particles is shown in Figure 2.1-1.

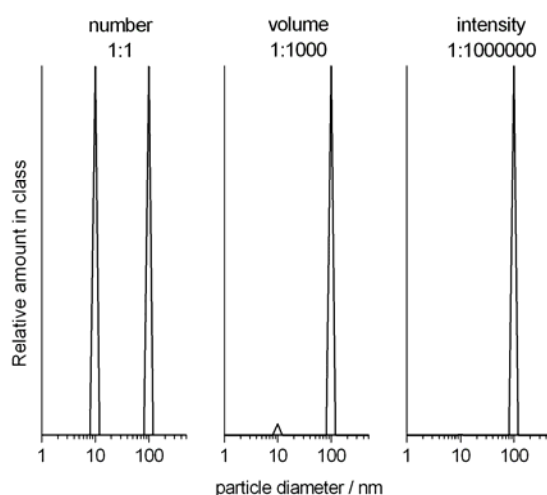


**Figure 2.1-1.** Schematic comparison between the number, volume and intensity distributions of two different particle size classes in DLS.

## 2.2 Zeta potential measurement

The zeta potential<sup>[3]</sup> denotes the electrostatic potential at the interfacial double layer of a colloid or other surface as compared to that of the bulk fluid. Also known as electrokinetic potential, it is widely used in colloid chemistry to determine the stability of dispersions by electrostatic repulsion of the particles, i.e., in relation to the pH value of aqueous systems.

A charged surface affects the distribution of ions in the surrounding interfacial region, thus resulting in a concentration increase of oppositely charged counter ions. Colloidal particles will therefore form an electric double layer when dispersed in an ion-containing solution. The liquid layer surrounding the particle can be divided into two parts. An inner region with

strongly bound ions called the Stern layer, as well as an outer region with less firmly attached and more diffuse ions. While the first few layers of ions and solvent molecules near the particle can be assumed to remain relatively fixed, the liquid further away from the surface will be free to move with respect to the particle. The outer diffuse layer can therefore be further divided by a notional boundary. During particle motion, ions and solvent molecules within the boundary will move with it and follow the particle, while the solvent outside of the boundary remains stationary. This boundary is called the surface of hydrodynamic shear or slipping plane. The term zeta potential is defined as the electrostatic potential at the slipping plane in relation to that of the surrounding bulk liquid at an infinite distance (see Figure 2.2-1).

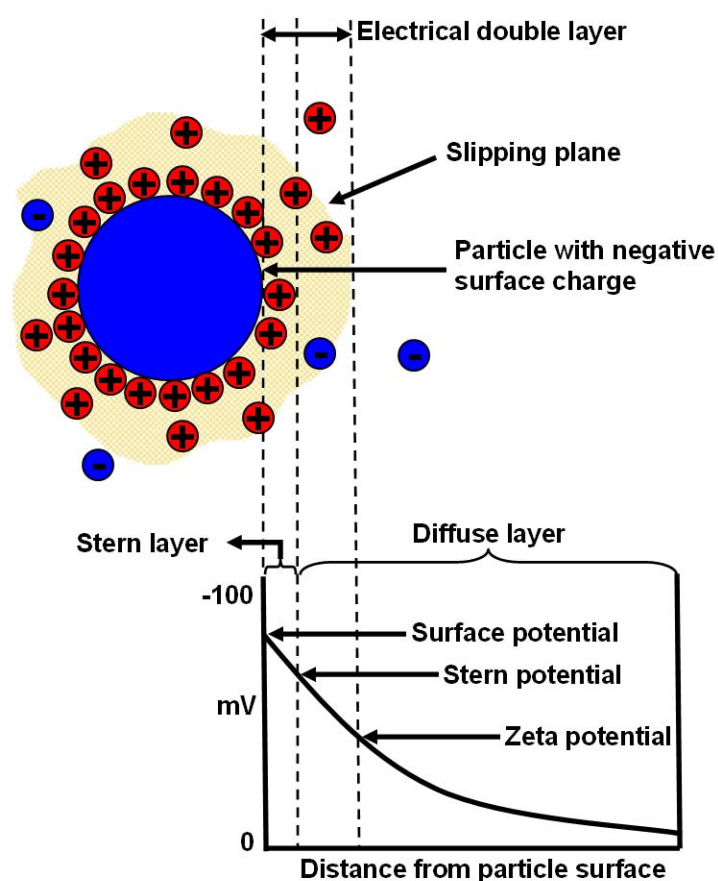


**Figure 2.2-1.** Scheme of the electric double layer around a negatively charged colloid.

Depending on the investigated system, the zeta potential can be determined by a number of different processes collectively called electrokinetic effects: electrophoresis, electroosmosis, streaming potential, and sedimentation potential, among others. For investigations of colloids, one of the most commonly applied techniques is electrophoresis, i.e., measuring the speed of the particles inside an electric field. Charged particles suspended in an electrolyte will move towards the electrode of opposite charge, while being opposed by viscous forces of the surrounding medium. After reaching equilibrium between those two forces, the particles will move with a constant velocity, i.e., their electrophoretic mobility. The zeta potential is related to electrophoretic mobility via the Henry equation (2.2-1).

$$U_E = \frac{2\varepsilon \cdot z \cdot f(Ka)}{3\eta} \quad (2.2-1)$$

$U_E$  : Electrophoretic mobility

$\varepsilon$  : Dielectric constant

$z$  : Zeta potential

$f(Ka)$  : Henry's function

$\eta$  : Viscosity

The value of Henry's function  $f(Ka)$  is usually determined by one of two approximations. For systems containing large particles in aqueous media at moderate salt concentrations usually the Smoluchowski approximation,  $f(Ka) = 1.5$ , is applied. This relation is valid when the electric double layer is very thin compared with the particle radius. Smoluchowski is therefore a good approximation for particles larger than about 200 nm dispersed in electrolytes containing more than  $10^{-3}$  molar salt. On the other hand, the behaviour of systems containing small particles in dilute salt concentrations where the double layer is relatively thick in relation to the particle radii is better approximated by the Hückel equation, i.e. using  $f(Ka) =$

1.0 as a value. The Hückel approximation is also valid for most non-aqueous measurements, i.e., dispersions in organic media.

Electrophoretic mobility of nanoparticles can be measured by Laser Doppler Velocimetry (LDV).<sup>[4]</sup> Laser light scattered from the moving particles is interfered with the reference beam resulting in a fluctuating intensity signal due to the Doppler shift. As the Doppler shift corresponds to the velocity of the particles, the resulting frequency difference forms beat signals proportional to the speed of the particles between the electrodes in a measurement cell.

### 2.3 Nitrogen Adsorption

Analyzing the adsorption of gas molecules, e.g., nitrogen, on solid surfaces is a widespread technique for the characterization of porous bodies.<sup>[5, 6]</sup> By recording the adsorption and desorption isotherms, fundamental data including the surface area, pore size distribution and accessible pore volume of a given material can be obtained.

The process of adsorption, i.e., the enrichment of one or more components in an interfacial layer, occurs when a solid material is exposed to a gas. In this case, the solid is referred to as ‘adsorbent’, the adsorbed gas molecules as ‘adsorbate’ and the gas in equilibrium with the adsorbate as ‘adsorptive’. The following discussion will center on physisorption, i.e., the case where the adsorbate is bound to the surface by van der Waals forces such as dipole-dipole, London forces or hydrogen bonding, in contrast to adsorption via strong covalent chemical bonds in chemisorption.

The two principal methods for the determination of adsorption isotherms are volumetric and gravimetric techniques. In both cases, the adsorbent is held at a constant temperature which is usually at or near the boiling point of the adsorptive, i.e., by cooling with liquid nitrogen in the case of nitrogen sorption. By step-wise increase of the adsorptive pressure followed by

equilibration of the system, the increase in the amount of adsorbed molecules can be measured. In gravimetric systems, this is achieved by detecting the mass gain after each step, while in volumetric systems the adsorbed gas volumes are usually calculated by comparison of the actual pressure change with the expected pressure change in absence of the adsorbent.

In a typical isotherm, the amount of adsorbed material is plotted against the partial pressure of the adsorptive. Adsorption isotherms can be classified as one of six types according to the IUPAC<sup>[7]</sup> (Figure 2.3-1), each type being a characteristic for certain material types (see Table 2.3-1).

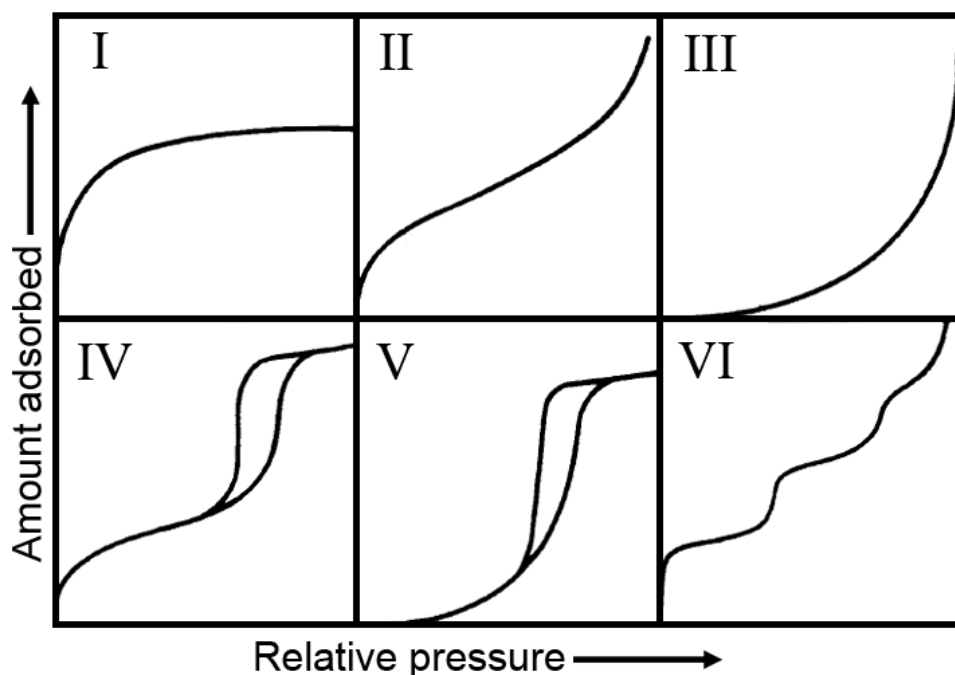


**Figure 2.3-1.** Type I to Type VI adsorption isotherms

**Table 2.3-1.** Classifications of adsorption isotherms

Type	Interpretation
<b>I</b>	Chemisorption isotherms or physisorption in microporous materials, where a plateau is reached after filling of the micropores
<b>II</b>	Nonporous and macroporous materials with high energies of adsorption
<b>III</b>	Nonporous and macroporous materials with low energies of adsorption
<b>IV</b>	Mesoporous materials with high energies of adsorption, often contain hysteresis loops attributed to mesoporosity
<b>V</b>	Mesoporous materials with low energies of adsorption, often contain hysteresis loops attributed to mesoporosity
<b>VI</b>	Several possibilities, including multiple pores sizes and multiple distinct energies of adsorption

Adsorption isotherms can be described by several different models. The two principal methods currently applied in the study of porous materials are the Brunauer-Emmett-Teller (BET) theory and the density functional theory (DFT).

The BET theory is based on a number of simplifying assumptions in order to extend the Langmuir model<sup>[5]</sup> to multilayer adsorption. For low partial pressures ( $p/p_0 < 0.3$ ) the BET equation can be expressed in a linear form (equation 2.3-1).

$$\frac{p/p^0}{n(1-p/p^0)} = \frac{1}{n_m C} + \frac{C-1}{n_m C} (p/p^0) \quad (2.3-1)$$

$p/p^0$ : relative pressure;  $p^0$  is the saturation pressure of the adsorptive

$n$ : amount of adsorbate

$n_m$ : monolayer capacity

$C$ : BET constant

Thus, the BET plot of  $(p/p^0)/[n(1-p/p^0)]$  versus  $p/p^0$  gives a linear correlation with a slope of  $(C-1)/n_m C$  and intercept  $1/n_m C$ . Based on these data and the cross-sectional area of an adsorbate molecule, the specific surface area of the adsorbent can be calculated. It should be noted that the specific  $p/p^0$  range of the linear region in the BET plot is dependent on the system and operation temperature.

While it is possible to calculate pore diameters using a model developed by Barret, Joyner and Halenda (BJH) based on the Kelvin equation,<sup>[5,6]</sup> it was shown that the obtained pore sizes are not exact for small pores. For mesoporous systems with pores in the range of 4 nm, pore diameters calculated by the BJH method are typically decreased by about 1 nm in comparison to values obtained by alternative techniques such as TEM. This deviation is due to the assumption of certain pore-filling mechanisms and pore condensation phenomena which do not accurately describe the behaviour of micropores and small mesopores.

In contrast to these macroscopic approaches, there are several microscopic models including molecular simulations (Monte Carlo simulations), molecular dynamics, statistical mechanic techniques, and density functional theory (DFT), which yield more realistic results. As a drawback, specific knowledge about the structure and surface atoms of the investigated materials is required in order to correctly calculate the forces and input parameters of these models. Therefore, such approaches cannot be applied to unknown surfaces, and the macroscopic theories are still frequently employed.



DFT techniques model the adsorption behaviour by including assumptions about the site-wise attractions between the surface atoms and the adsorbate molecules, and the adsorbate-adsorbate attractions among others. The configuration of the adsorbate molecules is then adjusted in order to obtain a minimum in the system's overall free energy, primarily by changing the number density as a function of distance from the surface. Furthermore, one should distinguish between the local and the non-local density functional theory (NLDFT). In the former, the fluid is assumed to be structureless for calculating the long-range interactions between adsorbate particles. However, this assumption cannot be made for surface adsorption with strongly interacting boundaries. In such cases calculation by the NLDFT becomes necessary, as the solid walls have a considerable influence on the number density.

## 2.4 X-ray Diffraction

X-ray diffraction (XRD)<sup>[8]</sup> is a characterization method that can be applied for the identification of crystalline phases and the determination of certain structural properties, i.e., atom arrangement, grain size, preferred orientation, and defect structure, among others.

The conventional method to produce X-rays is to bombard a target with high-energy electrons. When the electrons are slowed down by interaction with the target, part of their energy is radiated as a continuous background spectrum termed 'Bremsstrahlung'. Depending on the elemental composition of the target, there also exist characteristic narrow lines in the spectrum resulting from X-ray fluorescence. In this process the impact of primary electrons creates a hole in a lower shell of an atom. Electrons residing in upper shells can now fill this vacancy and the surplus energy is released as X-ray photons. By applying blocking filters, a single energy spike can be isolated resulting in fairly monochromatic X-ray radiation. The wavelengths of such photons lie in the Ångström range, which is the same order of magnitude

as the distances between atoms in solid matter. The ordered lattice of a crystal allows one to gain structural information by observing the diffraction patterns caused by constructive and destructive interference of X-rays scattered by the lattice planes (Figure 2.4-1).

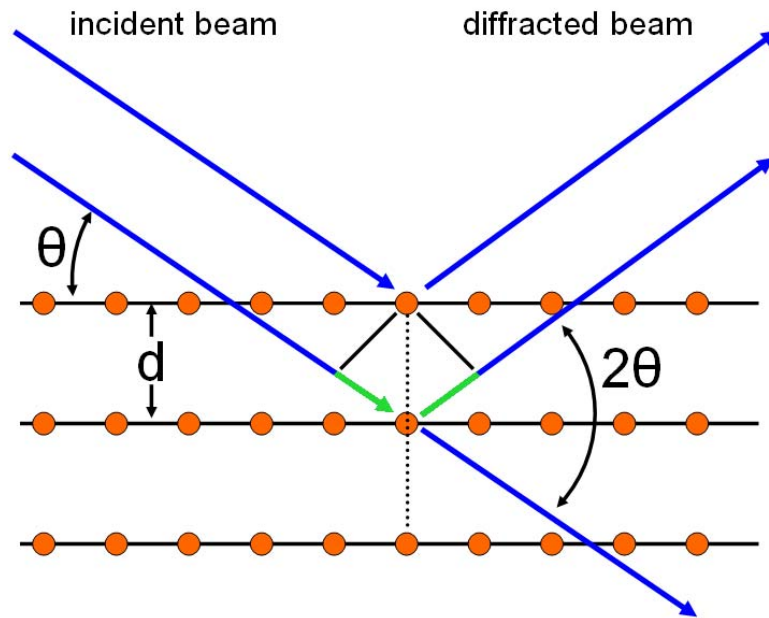


**Figure 2.4-1.** Scheme illustrating the Bragg relation. Constructive interference is achieved when the path difference (marked in green), is a multiple integer of the X-ray wavelength.

The conditions at which constructive interference can be observed are given by Bragg's law (equation 2.4-1).

$$n\lambda = 2d \sin \theta \quad (2.4-1)$$

$n$ : order of interference

$\lambda$ : X-ray wavelength

$d$ : lattice spacing

$\theta$ : angle of incidence

As powder samples contain a large number of randomly oriented crystallites, the resulting diffraction patterns are formed by a set of cones from all planes that satisfy the Bragg conditions. Powder diffraction patterns allow quick identification of crystalline phases by comparison with sample libraries.

Furthermore, the observed half-width of the reflexes gives information about the mean crystalline domain size. For small crystalline domains, reflex broadening is caused by incomplete destructive interference of the out-of-phase X-rays. The mean size of the crystalline domains can be calculated using the Debye-Scherrer formula (equation 2.4-2). As the results are volume-based, it should be noted that small amounts of larger particles will greatly influence the average size.

$$D = \frac{K \lambda}{\beta \cos(\theta)} \quad (2.4-2)$$

$D$ : crystalline domain size

$K$ : Scherrer constant, in general set to 0.9

$\lambda$ : wavelength

$\beta$ : full width at half maximum in radians

$\theta$ : angle of incidence

## 2.5 Infrared and Raman Spectroscopy

Infrared (IR)<sup>[9]</sup> and Raman<sup>[10]</sup> spectroscopy are applied to study the chemical bonding in a material via excitation of vibrational modes. In a basic IR experiment, the intensity of a beam of electromagnetic radiation, usually in the range of 200 - 4000  $\text{cm}^{-1}$ , is measured after interaction with the sample. This mid-IR radiation is capable of inducing transitions between molecular vibrational energy levels, thus providing information about the chemical bonding in the sample. A general selection rule for photon absorption in IR spectroscopy is the change in the dipole moment of the molecule during the vibration. The molecule itself, however, does not need to have a permanent dipole.

In contrast to IR spectroscopy, where the spectra are obtained by direct coupling between the incident radiation and the electronic structure of the chemical bond, Raman spectroscopy relies on the inelastic scattering of monochromatic light by interaction with the electron clouds surrounding the chemical bonds. As both IR and Raman use different physical processes to measure the vibrational spectra, they also display different selection rules for the observable vibrational states and are thus complementary characterization techniques. The general selection rule for Raman scattering is a change in bond polarizability during the vibration, i.e. the signal intensity is determined by the amount of deformation of the electron cloud.

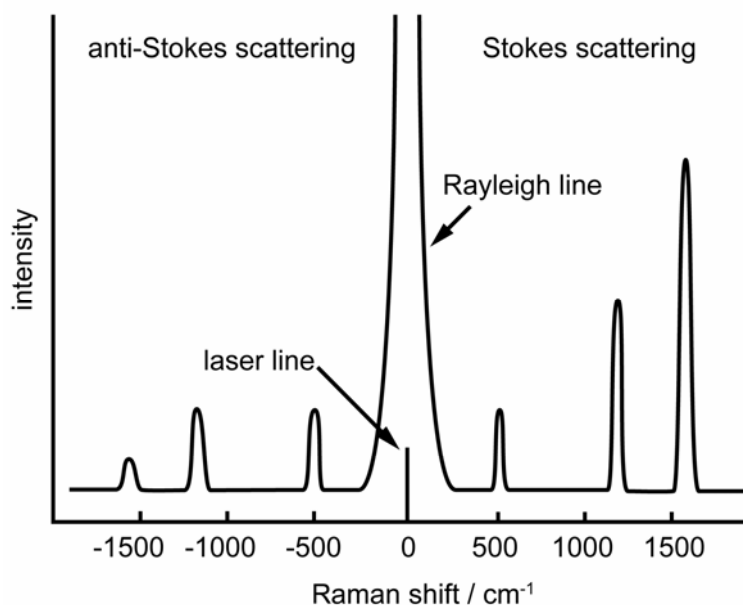


**Figure 2.5-1.** Schematic Raman spectrum

An incident photon is able to excite the system from a given vibrational state into a virtual energy state, from which the photon is re-radiated in all directions after relaxation. Most of the scattered light is released at the same frequency as the incident exciting light, i.e., as Rayleigh scattering (Figure 2.5-1). However, if the excited system was in an energetically low vibrational state, i.e., the ground state, and relaxes back into higher vibrational states, the energy difference is deducted from the scattered photons. This so-called Stokes scattering generates the weak side bands appearing in the spectrum at lower frequencies. Likewise, excitation from higher vibrational states and relaxation into energetically lower states causes lines at higher frequencies by anti-Stokes scattering. Raman lines from both Stokes and anti-Stokes scattering can be used to measure the vibrational frequencies of chemical bonds. Due to the requirement of excited vibrational states, anti-Stokes scattering is strongly temperature dependant and less intensive than the corresponding Stokes lines. It is therefore rarely measured except for specialized techniques such as coherent anti-Stokes Raman spectroscopy (CARS).<sup>[11]</sup> Accordingly, standard sample characterization by Raman spectroscopy is almost exclusively performed via detection of the higher intensity Stokes scattering.

## 2.6 Nuclear Magnetic Resonance

Nuclear magnetic resonance (NMR)<sup>[12]</sup> spectroscopy can be applied to investigate the chemical environment of certain nuclear isotopes, i.e., their coordination numbers, local symmetry and connectivity. For nuclei possessing a permanent magnetic dipole, the orientations of their magnetic moments are limited to discrete quantum states relative to an external magnetic field. By applying electromagnetic waves in the radiofrequency region, transitions between these states can be induced when the resonance condition is met (equation 2.6-1).

$$\omega = \gamma B_{loc} = \gamma(B_0 + B_{int}) \quad (2.6-1)$$

$\omega$  : frequency of the electromagnetic radiation at resonance condition

$\gamma$  : gyromagnetic ratio

$B_{loc}$  : magnetic field strength at the nuclei

$B_0$  : externally applied magnetic field

$B_{int}$  : internal field arising from electronic environments and surrounding magnetic moments

The measured difference between the local magnetic field strength and the applied external field gives insight about the electronic and chemical environment of the nuclei. In the case of solids, dipole-dipole interactions between the magnetic moments of nearby nuclei lead to line broadening in the spectra. One common technique to eliminate this anisotropic effect is the fast rotation of the sample at an angle of 54.7° relative to the electric field, i.e. magic angle spinning nuclear magnetic resonance (MAS-NMR). The mobility of the nuclei in liquid samples also creates an averaging process, leading to an intrinsic elimination of the line broadening related to dipole-dipole interactions.

## 2.7 Scanning Electron Microscopy

Scanning Electron Microscopy (SEM)<sup>[13]</sup> is a technique offering superior spatial resolution and depth of focus as compared to optical microscopy. Instead of interaction with visible light, a focused electron beam is generated under vacuum and rastered over the sample surface. Depending on the size of the electron spot and the interaction volume, resolutions between few nm and less than one nm can be achieved. As the electron beam penetrates the surface, a number of interactions can occur which result in the emission of secondary electrons or photons. Depending on the desired analysis, the resulting species are detected and evaluated.

The amounts of secondary and backscattered electrons are dependent on the acceleration voltage of the primary electron beam. However, they are also dependent upon the sample morphology and will increase with a decreasing glancing angle of incidence as more scattering occurs close to the surface. This change of detected electrons and thus signal intensity depending on the change in surface slope of the sample is responsible for the high topological contrast in SEM.

In addition, collisions of primary electrons with core electrons from atoms in the sample result in excited atomic states. After decaying to their ground state, the atoms in the sample emit X-ray photons with characteristic wavelength distributions for different elements.

In this way, SEM allows one to obtain topographical information as well as elemental composition and spatial distribution near surface regions of the investigated sample.

## 2.8 Transmission Electron Microscopy

Transmission Electron Microscopy (TEM)<sup>[14]</sup> is a standard characterization technique in materials science. By using a focused electron beam on a thin (typically less than 200 nm) sample, micrographs with a high lateral spatial resolution can be achieved. Presently, modern microscopes allow resolutions down to 0.05-0.1 nm if the amount of image distortion is reduced by aberration correctors.<sup>[15, 16]</sup> It is possible to obtain both image and diffraction information from a single sample by TEM. Furthermore, the interactions of the sample matter with the highly energetic electron beam produce characteristic radiation and particles for further materials characterization.

Electrons for TEM imaging are generated either by thermoionic emission from a tungsten filament or by field emission. The resulting electrons are accelerated by an electric potential and focused into a beam by a series of electrostatic and magnetic lenses. Undeflected as well as deflected electrons penetrating the sample can be used for signal detection, resulting in techniques called Bright Field and Dark field imaging, respectively. In both modes, the electron scattering information is projected onto a two-dimensional detector, i.e., a fluorescent screen or CCD array. This projection results in limited depth resolution and superimposition of structural data on the image plane in TEM studies.

Highly charged atomic nuclei scatter electrons more effectively and to higher angles of deflection than those of light atoms. Therefore heavy elements exhibit a higher contrast in TEM imaging. In High Resolution Transmission Electron Microscopy (HRTEM), structures can also be investigated by phase contrast imaging, i.e. the phase differences of scattered electrons in the sample are used to visualize Bragg diffracting planes as periodic fringes.

Scanning Transmission Electron Microscopy (STEM)<sup>[17]</sup> is a technique where the TEM high-energy electron beam is rastered along the specimen, in a similar way to the rastering of the electron beam in SEM. By using a high-angle detector, i.e., in annular dark-field imaging (ADF) it is possible to obtain high-resolution micrographs where single atoms can be



distinguished. Contrary to the phase-contrast in HRTEM that often needs simulations for correct interpretation of the data, the Z-contrast in STEM-ADF is directly related to the squared atomic number  $Z^2$ .

## **2.7 Thermogravimetric Analysis and Differential Scanning Calorimetry**

Thermogravimetric analysis (TGA) relates the change in sample weight to the change in temperature during a heating ramp. Depending on the desired information, the heating can be performed under gas flow of reactive or inert atmospheres, i.e., to control or prevent combustion via oxidative processes.

As a complementary technique, Differential Scanning Calorimetry (DSC) can be performed during TGA by measuring the difference of heat needed to hold the sample and an inert reference at the same temperature. DSC yields information about exothermic and endothermic processes occurring in the sample during heating, i.e. combustion steps, phase transitions and evaporation of absorbed molecules.

## 2.8 References

- [1] N. C. Santos, M. A. R. B. Castanho, *Biophysical Journal* **1996**, 71, 1641.
- [2] *Malvern Instruments Homepage*, <http://www.malvern.de/>.
- [3] J. R. Hunter, *Introduction to Modern Colloid Science*, Oxford University Press, Oxford, **1993**.
- [4] *Malvern Instruments, Zetasizer Nano Series - User Manual*, **2003**.
- [5] F. Rouquerol, J. Rouquerol, K. Sing, *Adsorption by Powders & Porous Solids - Principles, Methodology and Application*, Academic Press, San Diego, **1999**.
- [6] J. B. Condon, *Surface Area and Porosity Determinations by Physisorption - Measurements and Theory*, Elsevier, Amsterdam, **2006**.
- [7] K. S. W. Sing, D. H. Everett, R. A. W. Haul, L. Moscou, R. A. Pierotti, J. Rouquerol, T. Siemieniewska, *Pure and Applied Chemistry* **1985**, 57, 603.
- [8] M. F. Toney, *Encyclopedia of Materials Characterization - Surfaces, Interfaces, Thin Films; XRD - X-Ray Diffraction*, Manning Publications, Greenwich, **1992**.
- [9] J. N. Cox, *Encyclopedia of Materials Characterization - Surfaces, Interfaces, Thin Films; FTIR - Fourier Transform Infrared Spectroscopy*, Manning Publications, Greenwich, **1992**.
- [10] W. B. White, *Encyclopedia of Materials Characterization - Surfaces, Interfaces, Thin Films; Raman Spectroscopy*, Manning Publications, Greenwich, **1992**.
- [11] W. M. Tolles, R. D. Turner, *Applied Spectroscopy* **1977**, 31, 96.
- [12] H. Eckert, *Encyclopedia of Materials Characterization - Surfaces, Interfaces, Thin Films; - Solid State Nuclear Magnetic Resonance*, Manning Publications, Greenwich, **1992**.
- [13] J. B. Bindell, *Encyclopedia of Materials Characterization - Surfaces, Interfaces, Thin Films; SEM - Scanning Electron Microscopy*, Manning Publications, Greenwich, **1992**.
- [14] K. E. Sickafus, *Encyclopedia of Materials Characterization - Surfaces, Interfaces, Thin Films; TEM - Transmission Electron Microscopy*, Manning Publications, Greenwich, **1992**.
- [15] *Transmission Electron Abberation-corrected Microscope - the TEAM project*, <http://ncem.lbl.gov/TEAM-project/>.
- [16] M. A. O'Keefe, S.-H. Yang, *Microscopy and Microanalysis* **2004**, 10, 86.
- [17] C. E. Lyman, *Encyclopedia of Materials Characterization - Surfaces, Interfaces, Thin Films; STEM - Scanning Transmission Electron Microscopy*, Manning Publications, Greenwich, **1992**.

### 3 Copper ammine complexes as new templating agents in zeolite synthesis\*

#### 3.1 Introduction

Organic molecules containing quaternary ammonium groups are widely used as structure directing agents for the stabilization of certain framework type structures.<sup>[1, 2]</sup> On one side the control and stabilization of specific molecular sieves can be achieved, and on the other side the organic additives/templates alter the degree of saturation in the precursor solutions and direct the formation of nanocrystallites that can be further stabilized in colloidal suspensions.<sup>[3]</sup> The need for new nanomaterials with improved surface and bulk properties for the purpose of advanced applications became more pronounced, especially in the fabrication of devices with nano-to-micron-sized dimensions.<sup>[4-6]</sup> One of the standard approaches used for preparation of nanocrystals is based on a substantial excess of organic template or additives. Thus the size of the growing crystals is controlled by achieving a high degree of supersaturation at moderate alkalinity. At these conditions a complete dissolution of the inorganic compounds, particularly silica and alumina sources is achieved. In addition to the common tetraalkyl ammonium templates of microporous nanocrystals, the preparation of molecular sieves using metal complexes in the form of metallocenes has been reported.<sup>[7, 8]</sup> Besides, it was demonstrated that metal amine complexes can serve as structure directing agent for the preparation of microporous aluminophosphates (AlPO<sub>n</sub>).<sup>[9, 10]</sup>

Metal amines are attractive candidates for the role of structure directing agents in zeolite synthesis. The metal centers allow high charge densities, which are supposed to increase the electrostatic interactions with the anionic silicate species during build-up of the zeolitic framework. Furthermore, geometric shapes that are uncommon for classic quaternary ammonium templates are readily available, i.e. square planar or octahedral species.

One striking disadvantage of using metal complexes in bulk zeolite synthesis is their low stability in highly alkaline media at elevated temperatures, resulting in decomposition of the

\* J. Kecht, S. Mintova, T. Bein, *Chem. Mater.* **2007**, 19, 1203-1205.; J. Kecht, S. Mintova, T. Bein, *Micropor. Mesopor. Mater.* **2008**, DOI=10.1016/j.micromeso.2008.04.010.

complexes and formation of metal oxides or hydroxides. However, colloidal zeolites are typically synthesized at temperatures below 100 °C and from clear precursor solutions exhibiting lower alkalinities than the aluminosilicate gels used in bulk zeolite synthesis. Thus, incorporation of metal complexes as structure directing agents could become a viable approach in such systems.

Tetramethyl ammonium (TMA) aluminosilicate solutions have been found to be a very fruitful system for the generation of various colloidal molecular sieves. Colloidal suspensions containing microporous nanosized crystals with FAU,<sup>[13]</sup> LTA,<sup>[14]</sup> OFF,<sup>[15]</sup> and GIS<sup>[16]</sup> framework type structures were synthesized from different precursor solutions containing TMA cations. It is stated that the TMA provides steric stabilization of the proto-nuclei formed in the precursor suspensions by generating a high level of supersaturation and preventing agglomeration of the nanocrystals. Thus leading to a large number of nucleation centers, which yield monodisperse colloidal suspensions of zeolite nanocrystals.<sup>[3]</sup>

Square-planar copper(II) tetraammine  $[\text{Cu}(\text{NH}_3)_4]^{2+}$  was chosen as a model complex due to several advantages, including high stability and charge density, interesting geometry, and the simple and preferential in-situ formation in aqueous solutions in the presence of both copper cations and ammonia.

### 3.2 Experimental Section

A typical precursor solution used for preparation colloidal zeolite had the following chemical composition: 2.37 (TMA)<sub>2</sub>O : 0.05 Na<sub>2</sub>O : 1.00 Al<sub>2</sub>O<sub>3</sub> : 4.16 SiO<sub>2</sub> : 244 H<sub>2</sub>O: 0.50 CuO : 15 NH<sub>3</sub> (sample Cu1-N1). The chemical reactants copper nitrate trihydrate (139 mg, 0.58 mmol), double distilled water (2.80 g, 155 mmol), concentrated ammonium hydroxide solution (1.0 g, 28 wt.% NH<sub>3</sub>, 16 mmol), and tetramethylammonium hydroxide pentahydrate (0.98 g, 5.9 mmol) were mixed in a polypropylene bottle at ambient condition. After complete dissolution

of these reactants, aluminium isopropoxide (468 mg, 2.3 mmol) and Ludox HS-30 colloidal silica (0.96 g, 30 wt.% SiO<sub>2</sub>, 4.8 mmol) were added, and then the reaction mixture was stirred for 30 minutes, resulting in a blue-colored transparent solution. This solution was aged at room temperature without stirring for 3 days, and then transferred in a Teflon-lined stainless steel autoclave for hydrothermal treatment at 100 °C for 3 days. After complete transformation of the amorphous into crystalline phase, the resulting nanocrystals were purified by multi-step high-speed centrifugation and subsequently re-dispersed in double-distilled water. Finally, the crystalline zeolite samples with deep blue color were stabilized in aqueous suspensions at pH = 10.6 and a concentration of solid particles of about 5 wt. %.

Additionally, numerous samples from different precursor solutions (see Table 3-1) were prepared. Furthermore, the precursor solutions with the same chemical composition were subjected to variable synthesis conditions including aging, synthesis temperature and time of hydrothermal treatment (see Table 3-2).

**Table 3-1.** Chemical composition of precursor solutions used for synthesis of nanosized molecular sieves.

Sample*	(TMA) <sub>2</sub> O	Na <sub>2</sub> O	Al <sub>2</sub> O <sub>3</sub>	SiO <sub>2</sub>	H <sub>2</sub> O	CuO	NH <sub>3</sub>
Cu1-N1	2.37	0.05	1.00	4.16	244	0.50	15
Cu0-N0	2.37	0.05	1.00	4.16	244	<b>0</b>	<b>0</b>
Cu1-N0	2.37	0.05	1.00	4.16	244	0.50	<b>0</b>
Cu1-N0.5	2.37	0.05	1.00	4.16	244	0.50	<b>7.5</b>
Cu1-N2	2.37	0.05	1.00	4.16	244	0.50	<b>30</b>
Cu0-N1	2.37	0.05	1.00	4.16	244	<b>0</b>	15
Cu0.1-N1	2.37	0.05	1.00	4.16	244	<b>0.05</b>	15
Cu0.5-N1	2.37	0.05	1.00	4.16	244	<b>0.25</b>	15
Cu2-N1	2.37	0.05	1.00	4.16	244	<b>1</b>	15
Al-0.5	2.37	0.05	<b>0.5</b>	4.16	244	0.50	15
Al-2	2.37	0.05	<b>2</b>	4.16	244	0.50	15
T-0.33	<b>0.79</b>	0.05	1.00	4.16	244	0.50	15
T-0.66	<b>1.58</b>	0.05	1.00	4.16	244	0.50	15
T-1.33	<b>3.15</b>	0.05	1.00	4.16	244	0.50	15
H-0.56	2.37	0.05	1.00	4.16	<b>137</b>	0.50	15
H-2.2	2.37	0.05	1.00	4.16	<b>537</b>	0.50	15

\* All samples were aged for 72 h and treated at 100 °C for 72 h.

**Table 3-2.** Conditions for preparation of molecular sieves from colloidal precursor suspensions.

Sample	Aging [d]	Synthesis temperature [°C]	HT treatment time [h]
CuI-N1	3	100	72
Age-0d	<b>0</b>	100	72
Age-1d	<b>1</b>	100	72
Age-7d	<b>7</b>	100	72
Age-180d	<b>180</b>	100	72
HT-0h	3	-	<b>0</b>
HT-3h	3	100	<b>3</b>
HT-8h	3	100	<b>8</b>
TE-60°C	3	<b>60</b>	72
TE-150°C	3	<b>150</b>	72

### 3.3 Characterization

The crystallinity of the samples was proven by X-ray diffraction (XRD) study performed on a Stoe powder diffractometer in transmission geometry (Cu-K $\alpha$ ,  $\lambda=1.5406$  Å). The size of the crystalline domains in the zeolite samples was determined based on the Scherrer equation, using the line broadening of several Bragg reflections (the fitting of the diffraction patterns was carried out with WinXPOW Size/Strain1.02, STOE & Cie GmbH). The instrumental peak broadening was resolved by measuring lanthanum hexaboride as a reference material (Aldrich). Besides, the colloidal suspensions containing EDI-type nanozeolites were

characterized by dynamic light scattering (DLS) with a Malvern Zetasizer-Nano instrument equipped with a 4 mW He-Ne laser (633 nm) and avalanche photodiode detector.

The chemical composition of the dried zeolite samples was determined by inductively coupled plasma atomic emission spectroscopy (ICP-AES, VARIAN-VISTA). Thermogravimetric analyses (TGA) were performed on a Netzsch STA 440 C TG/DSC (heating rate of 10 K/min in a stream of synthetic air of ~25 mL/min). Transmission electron microscopic (TEM) images were recorded using a JEOL JEM 2011 microscope operating at 200 kV. IR spectra were measured on a Bruker Equinox 55 under diffuse reflectance conditions (samples were mixed with KBr, spectra are background subtracted). Raman spectra were recorded on a Jobin Yvon Horiba HR800 UV Raman microscope using a HeNe laser emitting at 632.8 nm.

### 3.4 Results and Discussion

In order to elucidate the role of the  $[\text{Cu}(\text{NH}_3)_4]^{2+}$  complexes in the formation of EDI-type molecular sieves, two series of precursor solutions consisting of different concentrations of copper and ammonia were prepared, respectively (Table 3-1). The sample Cu1-N1 was chosen as a reference. Samples with a constant concentration of ammonia and different amounts of copper are designated as Cu0-N1, Cu0.1-N1, Cu0.5-N1, and Cu2-N1. Besides, samples with a constant concentration of copper and different amounts of ammonia were prepared and abbreviated as Cu1-N0, Cu1-N0.5 and Cu1-N2. The chemical composition and the XRD data of the final crystalline products are summarized in Table 3-3 and Figures 3-1 and 3-2, respectively.



**Table 3-3.** Type of crystalline phase based on XRD (a) and chemical composition of samples determined by ICP-AES elemental analysis (b).

Sample	Phase <sup>a</sup>	Cu/Al <sup>b</sup>	Na/Al <sup>b</sup>	Si/Al <sup>b</sup>
Cu0-N1	FAU/LTA	-	0.39	1.71
Cu0.1-N1	FAU/EDI	0.20	0.21	1.76
Cu0.5-N1	EDI/FAU	0.45	0.16	1.39
Cu1-N1	EDI	0.39	0.08	1.37
Cu2-N1	EDI	0.44	0.10	1.32
Cu0-N0	FAU	-	0.43	1.70
Cu1-N0	FAU	0.24	0.43	1.90
Cu1-N0.5	FAU/Cu(OH) <sub>2</sub>	1.91	0.32	1.98
Cu1-N2	EDI	0.34	0.10	1.37

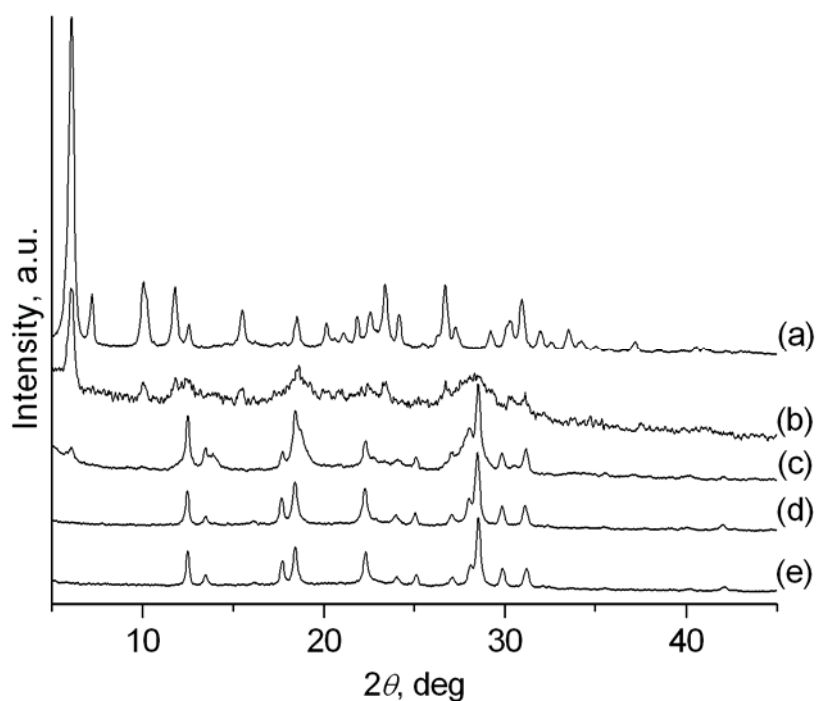


**Figure 3-1.** XRD patterns of samples prepared with constant ammonia content and different amounts of copper: Cu0-N1 (a), Cu0.1-N1 (b), Cu0.5-N1 (c), Cu1-N1 (d), and Cu2-N1 (e).

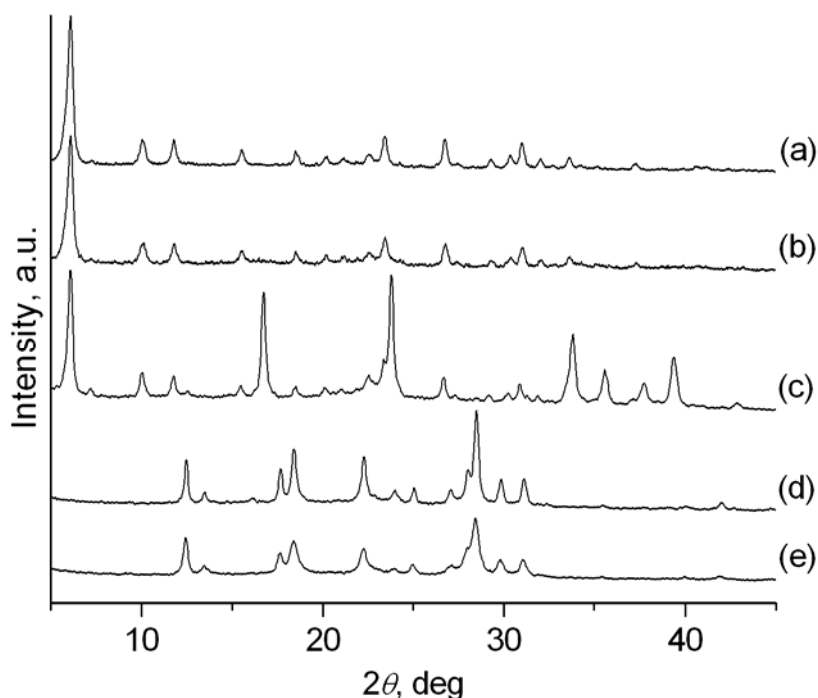


**Figure 3-2.** XRD patterns of sample Cu0-N0 prepared without copper and ammonia (a) and with constant copper content and different amounts of ammonia: Cu1-N0 (b), Cu1-N0.5 (c), Cu1-N1 (d), and Cu1-N2 (e).

As can be seen, the precursor solution with no addition of copper and  $\text{NH}_3$  (Cu0-N0) was transformed into pure FAU nanosized crystals (Figure 2a). The same crystallites were obtained from the solutions containing ammonia (Cu0-N1) and copper (Cu1-N0) only (Figure 3-1a, 3-2b). In the case of sample Cu0-N1, the formation of nanosized LTA crystals as a side phase was stimulated; the reflections corresponding to the LTA phase at  $7.2^\circ$ ,  $12.5^\circ$ , and  $21.8^\circ$   $2\theta$  are presented in the XRD patterns (Figure 3-1a). By combining copper and ammonia in different ratios the formation of crystalline products with variable framework structures was possible. In the presence of ammonia and at low copper concentrations (Cu0.1-N1), the crystallization of the FAU-type zeolite is inhibited, and a second set of reflections corresponding to the EDI-type molecular sieve are occurring in the pattern, but with low intensity and high peak broadening (Figure 3-1b). Furthermore, by increasing the copper

concentration in the precursor solutions (Cu0.5-N1) and keeping the ammonia constant, this effect is enhanced, thus resulting in the formation of only small amounts of FAU-type zeolite, and predominantly EDI type zeolite is formed. By further increasing the copper concentration (Cu1-N1, Cu2-N1), discrete EDI nanocrystals were synthesized as a pure phase with a high degree of crystallinity (Figures 3-1d and 3-1e). A similar development in the crystalline pathway is observed at constant copper amounts by variation of the ammonia concentrations. The single addition of copper without ammonia (Cu1-N0) is resulting in the formation of FAU-type phase (Figure 3-2b). Low  $\text{NH}_3$  concentration (Cu1-N0.5) is not sufficient for the formation of  $[\text{Cu}(\text{NH}_3)_4]^{2+}$  complexes in the highly basic reaction media and leads to the generation of copper hydroxide as a side phase: the reflections at  $16.7^\circ$ ,  $23.8^\circ$  and  $33.8^\circ$   $2\theta$  correspond to copper hydroxide (Figure 3-2c). When both copper and ammonia with sufficient concentrations are present in the precursor solutions, the formation of  $[\text{Cu}(\text{NH}_3)_4]^{2+}$  complexes is enabled, resulting in pure EDI-type phase. A slight peak broadening is observed for the sample synthesized with very high ammonia concentrations (Cu1-N2, Figure 3-2e), which is related with the size of the individual grains. The position of the Bragg reflections for all EDI samples match well with Na-exchanged zeolite K-F (EDI-type),<sup>[17]</sup> however considerable broadening which is a signature of nanocrystallites is observed.

The size of the particles was determined based on the Scherrer equation. The mean size of the crystallites of pure FAU synthesized from solutions Cu0-N0 and Cu0-N1 is about 80 nm, while in sample Cu1-N0, a slight increase in the particle size to 90 nm was measured. In the EDI material (sample Cu1-N1), smaller crystallites of 50 nm are obtained. In order to gain further information on the particle size distributions (PSDs) and morphology, all samples were investigated by dynamic light scattering (DLS) and transmission electron microscopy (TEM) (Figures 3-3, 3-4, 3-5).

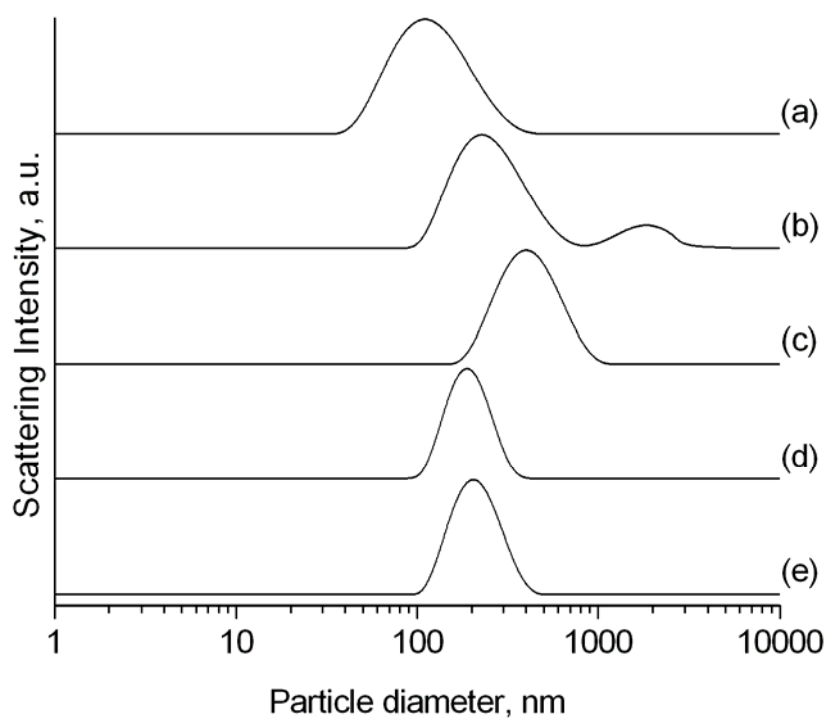


**Figure 3-3.** DLS curves of suspensions containing crystalline samples Cu0-N1 (a), Cu0.1-N1 (b), Cu0.5-N1 (c), Cu1-N1 (d), and Cu2-N1 (e).

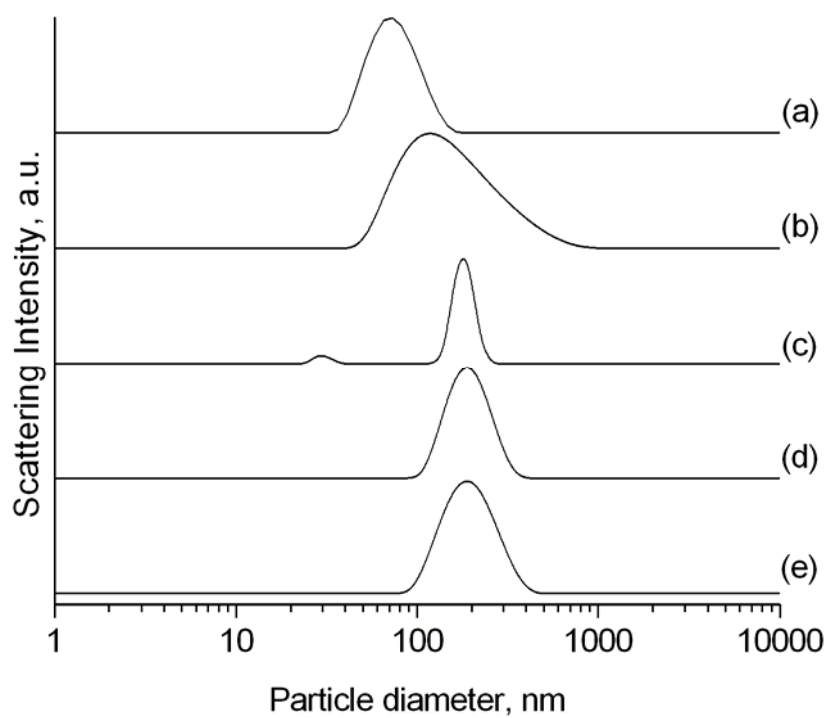


**Figure 3-4.** DLS curves of suspensions containing crystalline samples Cu0-N0 (a), Cu1-N0 (b), Cu1-N0.5 (c), Cu1-N1 (d), and Cu1-N2 (e).

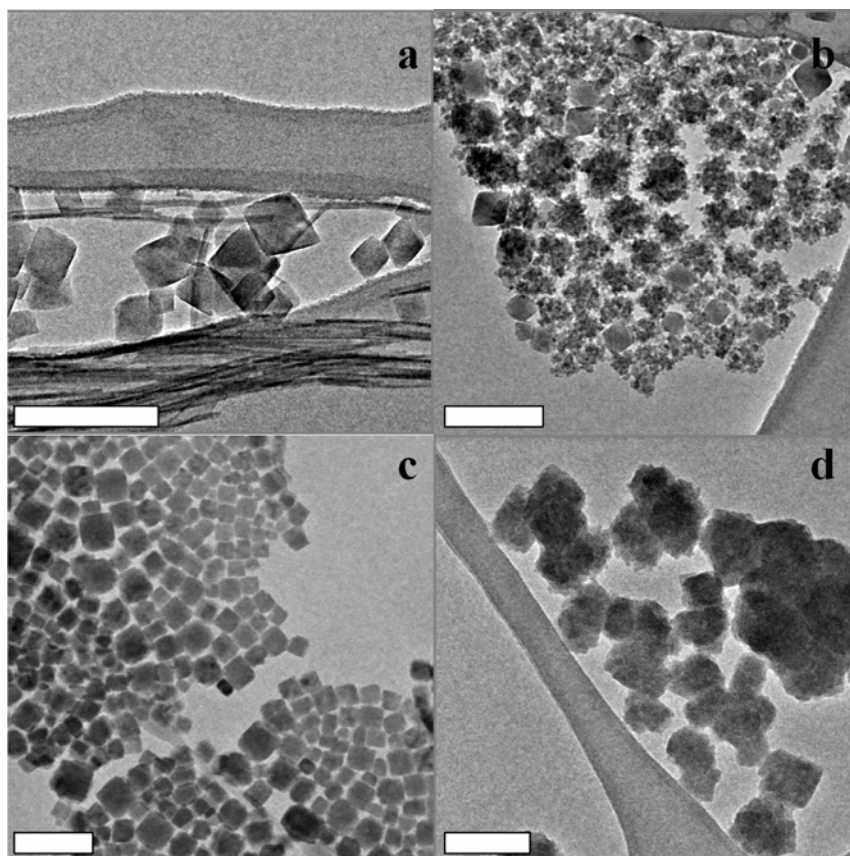


**Figure 3-5.** TEM micrographs of samples Cu1-N0 (a), Cu0.1-N1 (b), Cu1-N1 (c) and Cu1-N2 (d). (scale bar = 200 nm)

The size ranges of the particles determined from the DLS curves are in a good accordance with the values calculated by the Scherrer equation. The PSD curves of samples prepared by single addition of ammonia (sample Cu0-N1, Figure 3-3a) are broader in comparison to the sample without ammonia (Cu0-N0, Figure 3-4a). This is most likely caused by agglomeration of particles with different sizes (see sample Cu0-N1).

For sample Cu0.1-N1, a polymodal PSD curve is measured (Figure 3 b), which coincides with the existence of a mixture of two phases as detected by XRD, i.e. FAU and EDI types zeolites. Supporting information is provided by TEM, showing a mixture of orthorhombic FAU-type nanocrystals and flake-shaped particles assigned as precursors of EDI-type zeolite (Figure 3-5 b). By further increasing the copper content in sample Cu0.5-N1, the amount of FAU crystalline particles is greatly reduced, but still a great degree of agglomeration leading to

broader PSD curves starting at 100 nm and ending at about 1  $\mu\text{m}$  is measured (Figure 3-3c). Only at certain amounts of copper a pure and well crystalline EDI-type phase with comparatively narrow and monomodal PSDs was obtained (sample Cu1-N1, Figure 3-3d). The corresponding TEM micrographs show that the pure EDI crystals exhibit perfect cubic shape (Figure 3-5c) in contrast to the sample containing both EDI and FAU particles. Moreover, further increasing the amount of copper in sample Cu2-N1 (Figure 3-3e) does not have any effects on either particle size distribution or degree of crystallinity as proven by XRD.

Similar DLS results are obtained for the samples synthesized with different amounts of ammonia and constant copper (Figure 3-4). In the case of copper addition without ammonia (Cu1-N0), a very broad PSD curve is measured (Figure 3-4b). No secondary phase is identified in the XRD pattern, while TEM reveals the generation of needle-shaped particles with large aspect ratios in addition to the orthorhombic FAU nanocrystals. Most likely these particles are constructed of copper hydroxide or copper silicate species (Figure 3-5a). For sample Cu1-N0.5, a polymodal PSD curve is measured, which is in accordance to the phase mixture detected by XRD. Finally, the PSD curves of samples Cu1-N1 and Cu1-N2 have a slight broadening (Figure 3-4d,e). The sample Cu1-N2 shows a high degree of intergrowth of crystals and less symmetric morphologies in the TEM picture (Figure 3-5d) in comparison to the regular cubes obtained in sample Cu1-N1.

In conclusion, the presence of copper ammine complexes is necessary for the continuous growth of pure EDI-type nanocrystals. The single addition of copper cations or ammonia leads to crystallization of nanosized FAU zeolite as the main crystalline phase, whereas the combination of both compounds generates EDI-type microporous material. When the amount of one of the components is less and not sufficient (sample Cu0.1-N1), only a partial crystallization of the EDI-type phase is achieved. Most likely the incorporation of  $[\text{Cu}(\text{NH}_3)_4]^{2+}$  as a templating agent during zeolite growth led to a partial depletion of the

complexes and subsequent nucleation of FAU phase as well. In this case, the flake-shaped EDI precursor was not completely transferred into a crystalline material and an amorphous phase remained.

In order to elucidate the type and amount of copper complexes incorporated in the samples, IR/Raman spectroscopy and TG analysis on samples prepared at different concentrations were performed. The first striking difference in the IR spectra is the appearance of a band at  $1275\text{ cm}^{-1}$ , which corresponds to the symmetric deformation of  $\text{NH}_3$  coordinated to  $\text{Cu}^{2+}$ , and is specific for copper-ammine complexes.<sup>[18]</sup> This band appears only in the samples with Cu and  $\text{NH}_3$  being used simultaneously in the synthesis (Figure 3-6). As can be expected, the band is most prominent in sample Cu1-N1 (Figure 3-6e) and less intense in sample Cu0.1-N1 (Figure 3-6d), with the lowest amount of  $[\text{Cu}(\text{NH}_3)_4]^{2+}$ . Correspondingly, the band at  $1620\text{ cm}^{-1}$  in EDI-type material is caused by the doubly degenerate anti-symmetrical deformation vibration of  $\text{NH}_3$  (Figure 3-6e,d). The TMA cations present in the zeolite structures give rise to the bands at  $1490\text{ cm}^{-1}$  (asymmetric deformation mode of the  $\text{CH}_3$  groups),  $1420\text{ cm}^{-1}$  (N- $\text{CH}_3$  rocking modes) and  $950\text{ cm}^{-1}$  (C-N asymmetric stretching vibrations).<sup>[19]</sup> The first band at  $1490\text{ cm}^{-1}$  is not obstructed by others and it is the most intense, thus being clearly visible in the spectra. The highest intensity of the bands is for pure FAU samples, where the TMA is the only one template in use (Figure 3-6a,b,c). However, in the dually templated EDI zeolite the amount of incorporated TMA is less and therefore the intensity of this band is lower (Figure 3-6e). In the low wavenumber region variations in the intensity of the IR bands associated with the secondary building units of zeolites are also observed ( $650\text{-}400\text{ cm}^{-1}$ ).<sup>[20]</sup> The band at  $567\text{ cm}^{-1}$  caused by vibration of the double-six-ring (D6R) units in the FAU structure disappears in EDI-type samples and is replaced by a vibration at  $615\text{ cm}^{-1}$ . Furthermore, changes in band intensities of the two zeolite structures can be observed at  $420\text{ cm}^{-1}$  and  $466\text{ cm}^{-1}$ .

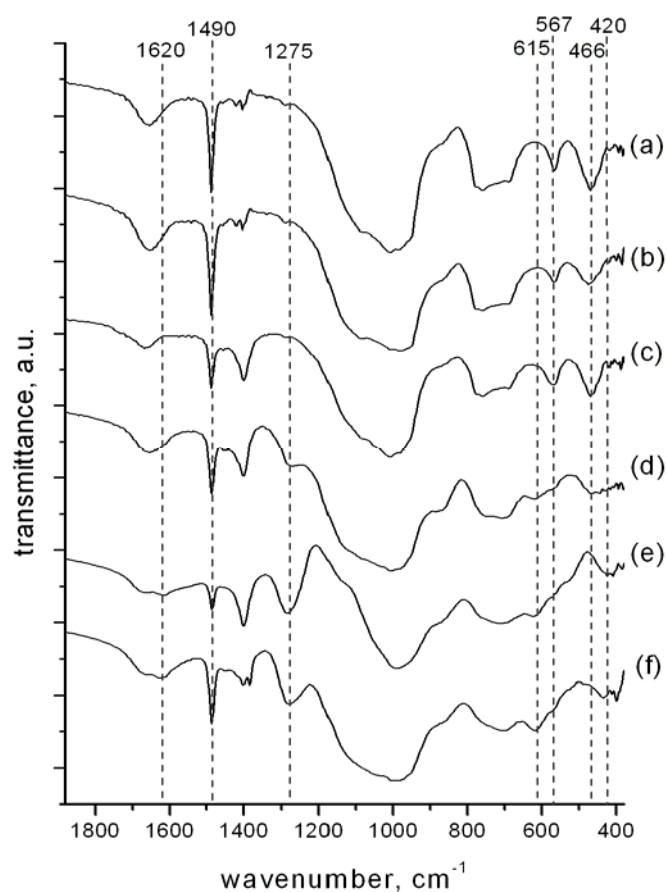


**Figure 3-6.** IR spectra of samples Cu0-N0 (a), Cu1-N0 (b), Cu0-N1 (c), Cu0.1-N1 (d), Cu1-N1 (e), and Cu1-N2 (f).

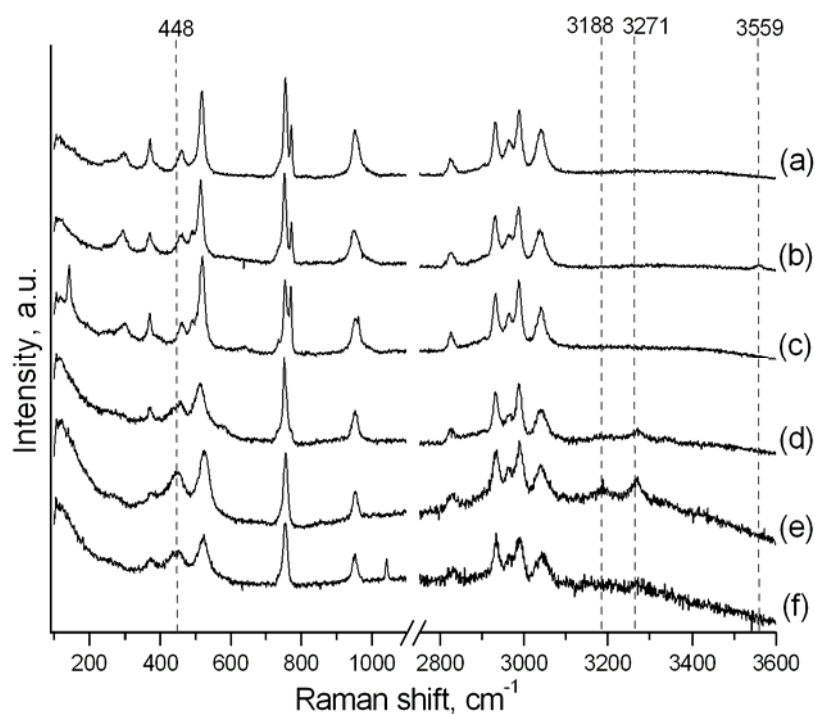


**Figure 3-7.** Raman spectra of samples Cu0-N0 (a), Cu1-N0 (b), Cu0-N1 (c), Cu0.1-N1 (d), Cu1-N1 (e), and Cu1-N2 (f).



The presence of  $[\text{Cu}(\text{NH}_3)_4]^{2+}$  complexes in zeolite crystals is demonstrated by the appearance of a band at  $448\text{ cm}^{-1}$  related with the  $\nu(\text{Cu-N})$  ( $A_{1g}$ ) vibration in the Raman spectra of EDI samples (Figure 3-7). Additionally, the signals at  $3188\text{ cm}^{-1}$  and  $3271\text{ cm}^{-1}$  corresponding to the  $\nu_{\text{as}}(\text{N-H})$  ( $B_{2g}$ ,  $E_g$ ) and  $\nu_s(\text{N-H})$  ( $A_{1g}$ ) vibrations were observed, respectively (Figure 3-7d,e,f).<sup>[21, 22]</sup> The structure-sensitive band related to the motion of an oxygen atom in a plane perpendicular to the T-O-T bonds can be found at  $517\text{ cm}^{-1}$  for the FAU samples, and is shifted slightly to  $525\text{ cm}^{-1}$  for the EDI material. This is in good accordance with the observations made for zeolite structures containing exclusively even-numbered rings (FAU and EDI), where the band occurs at around  $500\text{ cm}^{-1}$ .<sup>[23]</sup> In the FAU samples, a splitting of the symmetrical  $\text{NC}_4$  stretch of the TMA cations is observed at  $755$  and  $772\text{ cm}^{-1}$  (Figure 3-7a,b,c). This was attributed previously to the close fit of the TMA cation in the sodalite cages of the FAU framework.<sup>[24]</sup> In the EDI samples no such shift is detected (Figure 3-7d,e,f). Only in the Cu1-N0 sample a band with relatively low intensity at  $3559\text{ cm}^{-1}$ , was observed, which is attributed to the CuO-H stretch vibration, indicating the presence of copper hydroxide species (Figure 3-7b).

The amount of  $[\text{Cu}(\text{NH}_3)_4]^{2+}$  complex incorporated in the microporous inorganic matrix is determined by TG/DSC and elemental analysis (Figure 3-8, Table 3-3). The pure EDI-type zeolite is an aluminium-rich material with a Si/Al ratio of 1.37 (sample Cu1-N1, see Table 3). The amount of Cu in EDI type material is higher in comparison with FAU zeolite, i.e. a Cu/Al ratio of 0.39 is obtained for sample Cu1-N1 vs. 0.24 for sample Cu1-N0, and the amount of sodium decreases from FAU to EDI-type samples, accordingly.

**Table 3-3.** Type of crystalline phase based on XRD (a) and chemical composition of samples determined by ICP-AES elemental analysis (b).

Sample	Phase <sup>a</sup>	Cu/Al <sup>b</sup>	Na/Al <sup>b</sup>	Si/Al <sup>b</sup>
Cu0-N1	FAU/LTA	-	0.39	1.71
Cu0.1-N1	FAU/EDI	0.20	0.21	1.76
Cu0.5-N1	EDI/FAU	0.45	0.16	1.39
Cu1-N1	EDI	0.39	0.08	1.37
Cu2-N1	EDI	0.44	0.10	1.32
Cu0-N0	FAU	-	0.43	1.70
Cu1-N0	FAU	0.24	0.43	1.90
Cu1-N0.5	FAU/Cu(OH) <sub>2</sub>	1.91	0.32	1.98
Cu1-N2	EDI	0.34	0.10	1.37

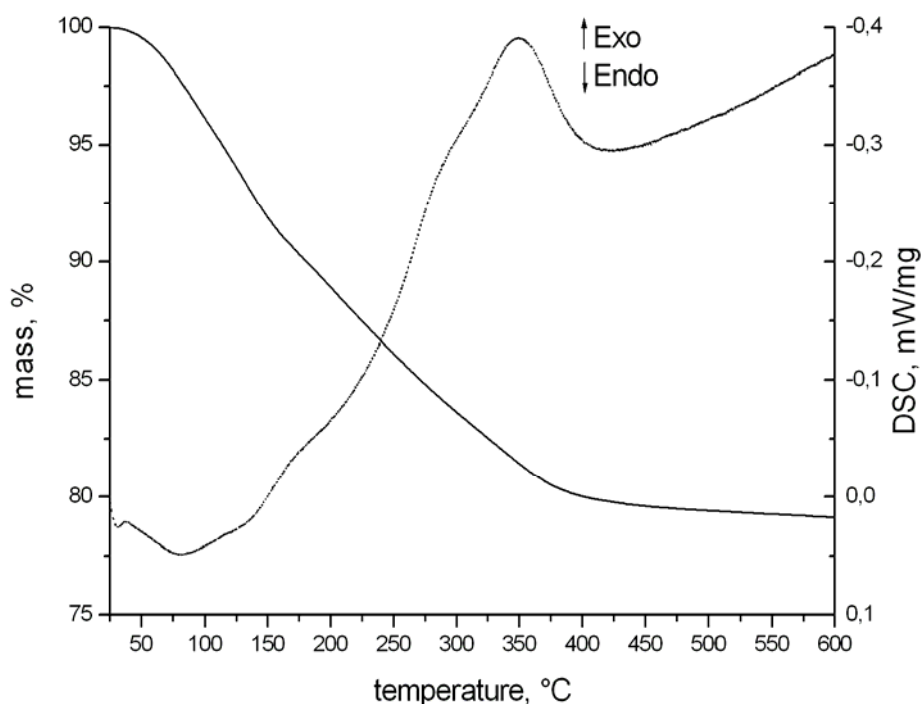


**Figure 3-8.** TG (solid black line) and DSC (dashed grey line) curves of sample Cu1-N1.

The TG curve of sample Cu1-N1 contains one endo- and one exo- peak due to the release of water and decomposition of TMA and the copper complex, respectively (Figure 3-8). Under the assumption that the zeolitic water is removed from the pores at temperatures up to 100 °C (4 %), the remaining exothermic effect from 100 °C to 600 °C (~17 %) is attributed to the combined decomposition of TMA and the copper complex. Taking into account the amount of copper and sodium determined from elemental analysis, it can be calculated that the TMA/Al ratio needed for charge balancing of the zeolitic framework is 0.14, which is expected to be about a 5 % weight loss. The remaining weight loss of 12 % can be attributed to the release of copper-bound ammonia from the aluminosilicate structure. The calculated  $\text{NH}_3/\text{Cu}$  ratio of 3.8 is in good accordance to the expected stoichiometry of 4 in the square planar  $[\text{Cu}(\text{NH}_3)_4]^{2+}$  complex. Thus it can be concluded that the amount of  $[\text{Cu}(\text{NH}_3)_4]^{2+}$  incorporated in the EDI material is very high, and around 82 % of the channel intersections are filled by the

$[\text{Cu}(\text{NH}_3)_4]^{2+}$  complex in sample Cu1-N1 (0.39 Cu per 2.37 T-atoms). This can be used as an indication that the copper ammine complexes have a structural directing instead of a pore filling role.

The crystallization process for pure crystalline EDI phase was subjected to further optimization, where many parameters such as amount of aluminum, TMA, sodium and water were varied (see Table 3-1). The corresponding XRD patterns and DLS curves of this series of samples are given in Figures 3-9 and 3-10.

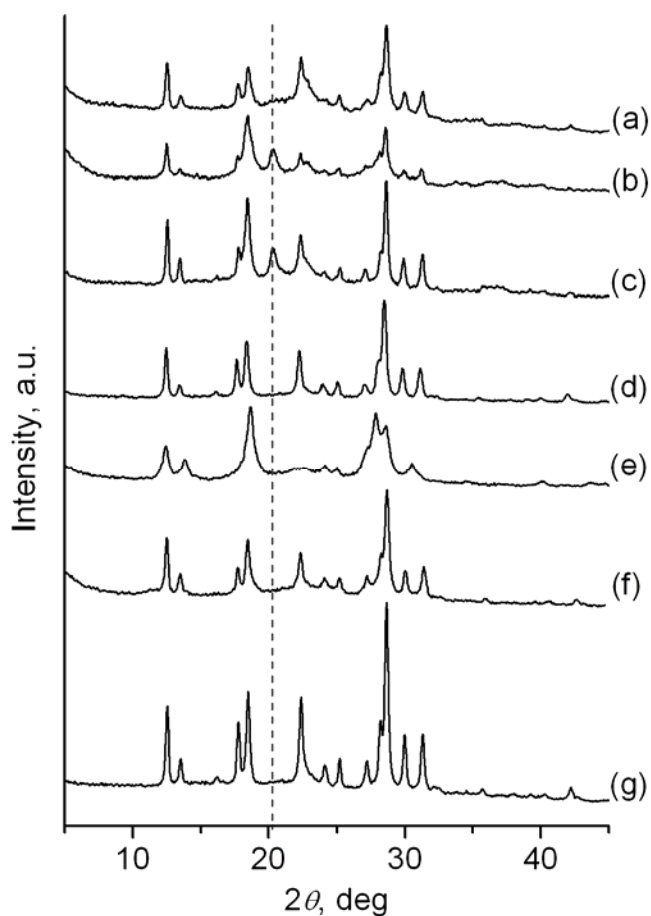


**Figure 3-9.** XRD patterns of samples Al-0.5 (a), Al-2 (b), T-0.33 (c), T-0.66 (d), T-1.33 (e), H-0.56 (f), and H-2.2 (g).

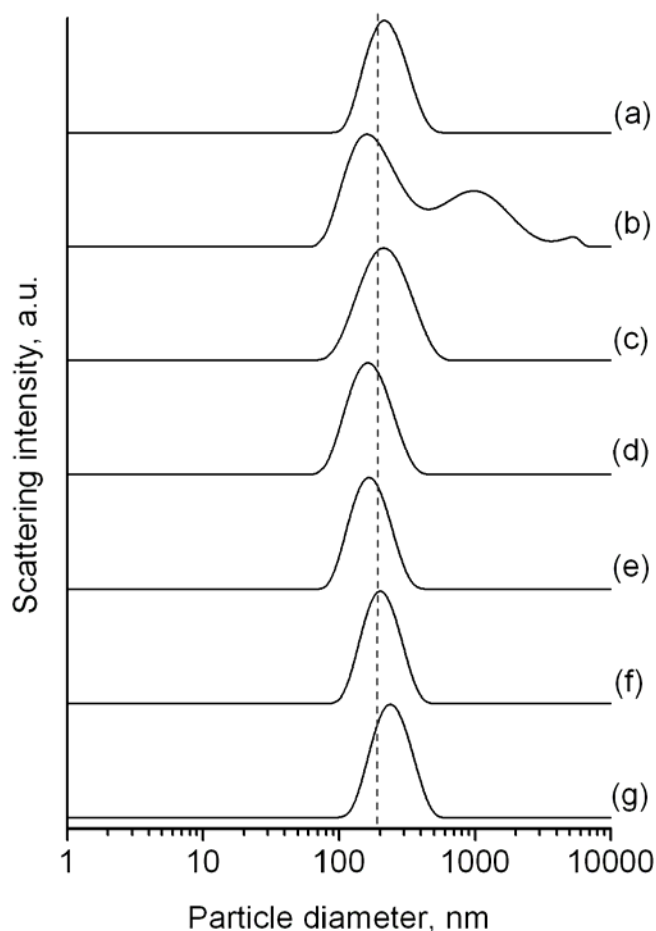


**Figure 10.** DLS curves of suspensions containing crystalline samples Al-0.5 (a), Al-2 (b), T-0.33 (c), T-0.66 (d), T-1.33 (e), H-0.56 (f), and H-2.2 (g); the dashed line marks the scattering maximum of sample Cu1-N1.

As can be seen, in the presence of both copper and ammonia, the EDI phase was obtained from suspensions with different initial compositions. The decrease (sample Al-0.5, Figure 3-9a) and the increase (sample Al-2, Figure 3-9b) of aluminum in the synthesis mixture yield less crystalline products in comparison to sample Cu1-N1 considered as a reference (Figure 3-2d). Also the particle size is increased in the case of sample Al-0.5, and a high polymodal particle size distribution is measured for sample Al-2 (Figure 3-10b). The micrometer-sized particles present in sample Al-2 most likely consist of non-reacted aluminum oxide/hydroxide species. This is also indicated by the presence of an additional reflection at  $20^\circ 2\theta$  in the X-

ray patterns (see Figure 3-9b,c), which is the strongest reflection of  $\text{Al}(\text{OH})_3$  phase. The same reflection is also found in the XRD pattern of sample T-0.33, where low pH resulting from the strong decrease of the organic base led to an incomplete dissolution of the aluminum species (Figure 3-9b). However, no additional reflection is observed in sample T-0.66, which is indicating the presence of pure EDI-type phase. Furthermore, the hydrodynamic diameter of the crystallites is decreased in comparison to sample Cu1-N1 (Figure 3-10d). If the TMA content is increased in the precursor suspension, then the generation of a sodalite phase is observed (sample T-1.33, Figure 3-9e). Additionally, the water content in the precursor solutions is changed and the crystallization process is followed. No decrease in particle size in the systems with lower water content was detected; while at higher water content (see sample H-2.2) the mean particle diameters and degree of crystallinity are increased (Figures 3-9g and 3-10g).

Apart from the chemical composition, the physical parameters such as the aging time, the time of hydrothermal treatment and the synthesis temperature were altered. Precursor solutions with the same chemical composition as for sample Cu1-N1 were subjected to hydrothermal treatment after different times of aging. The generation of EDI-type material proceeds very quickly and the crystallization was completed in less than 8 hours (Figure 3-11). It is important to note that the initial precursor solution obtained after mixing of all reactants was transparent but deep blue. However, after several hours of aging, small amounts of a bright precipitate, which was identified as  $\text{Cu}(\text{OH})_2$  was formed (Figure 3-11a). During the hydrothermal treatment, these copper hydroxide species redissolve, thus the reflections corresponding to copper hydroxide species greatly diminish after 3 hours of hydrothermal treatment at 100 °C (Figure 3-11b). The transformation of the amorphous matter to crystalline material is completed after 8 hours (Figure 3-11c), and no significant differences in the crystallinity and particle size were observed if the samples were treated longer than 72 hours.

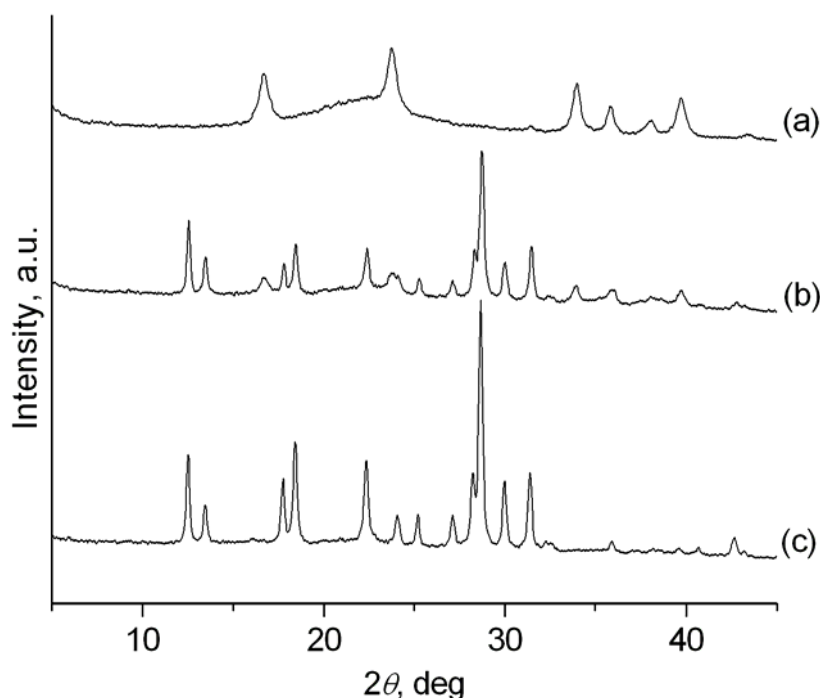


**Figure 3-11.** XRD patterns of samples HT-0h (a), HT-3h (b), and HT-8h (c).

Aging is an important stage for the synthesis of nanozeolites; it is expected to result in the formation of a great number of small particles during the hydrothermal treatment. Moreover, the aging period is vital for incorporation and stabilization of the copper ammine complexes inside the inorganic aluminosilicate matrix prior hydrothermal treatment. Preliminary experiments showed that a precursor solution having the same composition as sample Cu1-N1 without silica and alumina is not stable at room temperature and decomposes by forming a black precipitate of copper oxide. However, after adding silica and alumina sources, the same suspension at similar alkalinity (pH = 13.79 without Al/Si and 13.78 with Al/Si; measured with a gel electrode 1.5 hours after mixing of all reactants) was found to be stable against decomposition even after 6 months of storage at room temperature. Therefore this effect was attributed to the interaction of negatively charged aluminosilicate species with the cationic  $[\text{Cu}(\text{NH}_3)_4]^{2+}$  complexes, thus shielding them and stabilizing against the attacking hydroxide. This effect was confirmed with zeolite samples aged for different times prior to the

hydrothermal treatment. The clear precursor solution of sample Age-0d was subjected to hydrothermal treatment without aging except stirring at room temperature (1.5 hours) to ensure dissolution of all alumina species. The resulting products are presented in Figures 3-12 and 3-13.

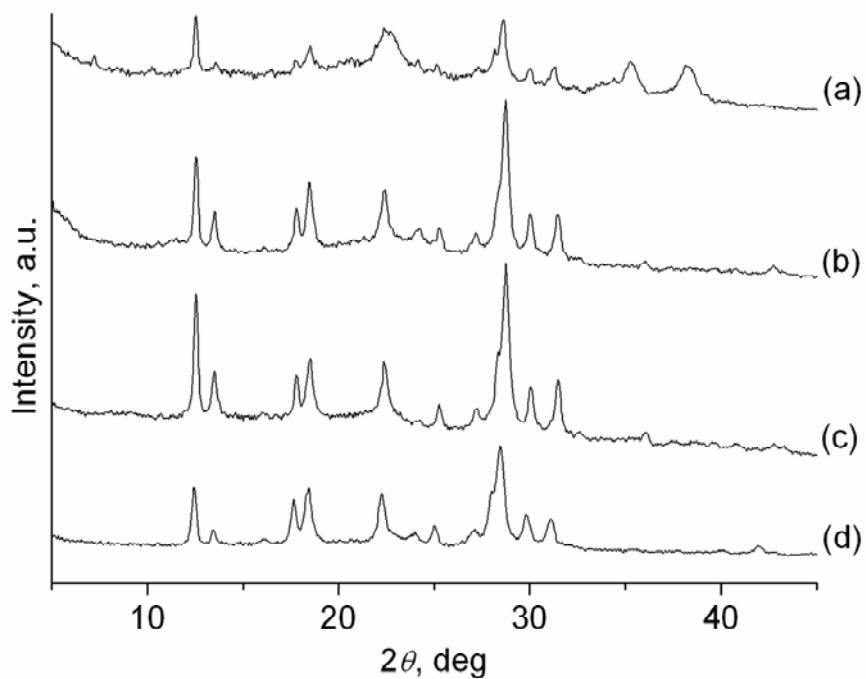


**Figure 3-12.** XRD patterns of samples Age-0d (a), Age-1d (b), Age-7d (c), and Age-180d (d).

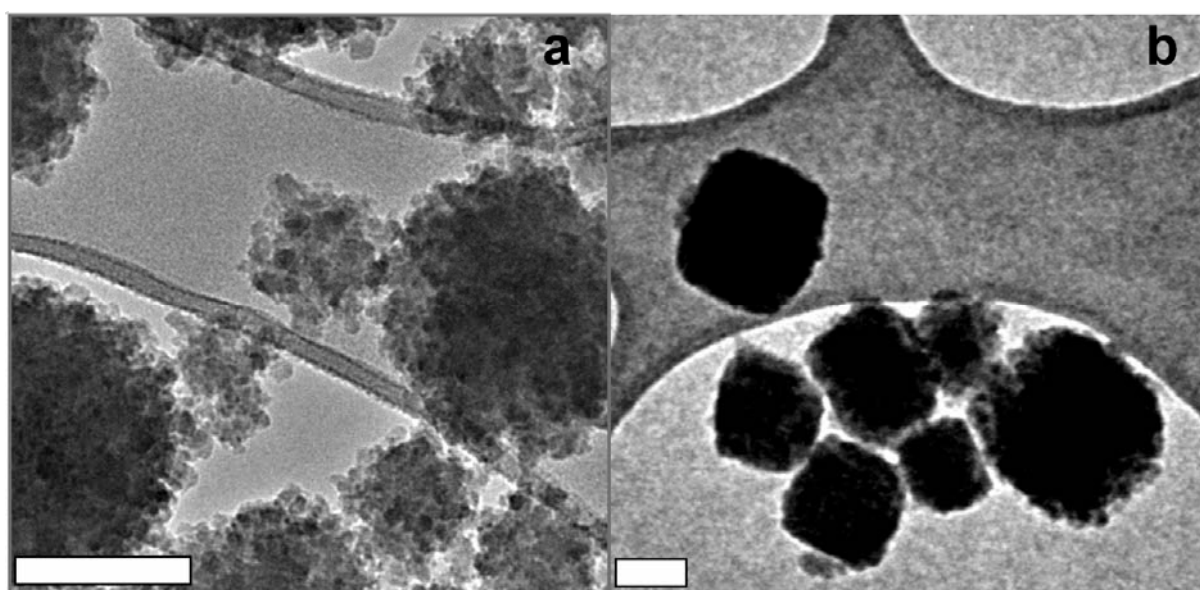


**Figure 3-13.** TEM micrographs of samples Age-0d (a) and Age-7d (b) (scale bar = 100 nm).



As can be seen, sample Age-0d shows a low crystallinity, which is confirmed by the TEM displaying irregular flake-like particles instead of the regular cubes that are found in the aged samples (Figure 3-13). The reflections at  $35^\circ$  and  $38^\circ$  and  $7.2^\circ 2\theta$  correspond to copper oxide and FAU, respectively. These data prove that without aging only a part of the  $[\text{Cu}(\text{NH}_3)_4]^{2+}$  can be incorporated in the aluminosilicate matrix to stabilize the growth of pure EDI-type material. The non-stabilized complexes are decomposed during the hydrothermal treatment leading to the formation of copper oxide as a side phase. Moreover, the low amount of copper ammine complexes causes the incomplete crystallization of EDI and the formation of FAU material as a side phase. Besides, similar materials were obtained from precursor solutions containing low amounts of copper (see Figure 3-1 for samples Cu0.1-N1 and Cu0.5-N1). The IR-band at  $1275\text{ cm}^{-1}$  assigned to the symmetric deformation vibration of  $\text{Cu-NH}_3$  confirms that despite the formation of large amounts of copper oxide in sample Age-0d, part of the  $[\text{Cu}(\text{NH}_3)_4]^{2+}$  was stabilized and did not decompose (Figure 3-14c).

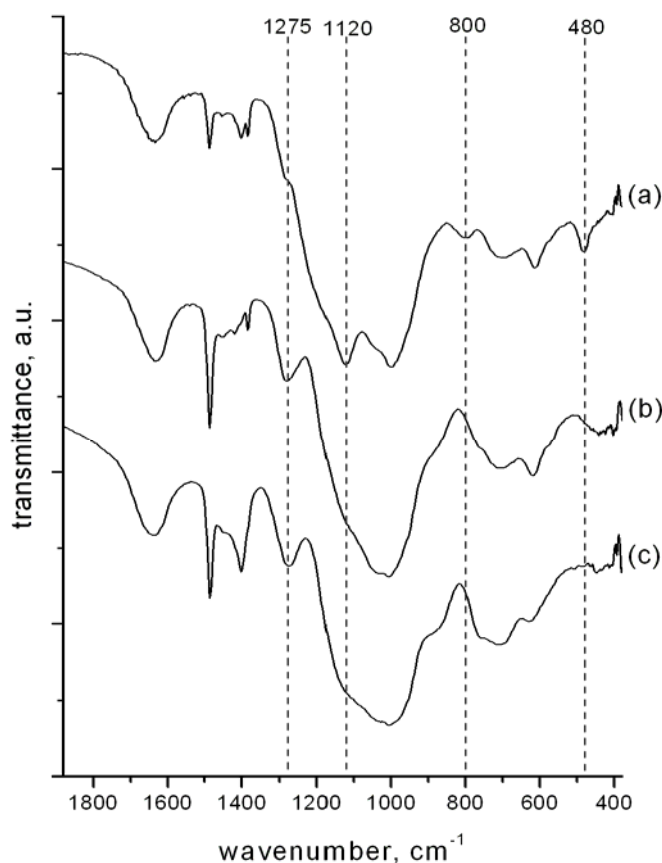


**Figure 3-14.** IR spectra of samples TE-60 °C (a), TE-150°C (b), and Age-0d (c).

The amount of incorporated and stabilized copper complexes is expected to increase with aging time. A relatively high crystallinity and absence of copper oxide are observed for sample Age-1d, thus suggesting that most copper complexes have been stabilized (Figure 3-12b). However, the copper oxide is still present in amounts below the XRD detection limit ( $\sim 5\%$ ), and the formation of a black color side phase was observed. This copper oxide was reduced after aging of the suspensions (2 days), and further pure EDI phase was obtained after 3 days of aging. Consequently, the aging process influences both the crystallinity and morphology of EDI zeolite. After 7 days of aging a change in the morphology of the cube-shaped particles is visible (Figure 3-13b).

The influence of the temperature for hydrothermal treatment on the stability of the copper ammine complexes was also studied. The sample Cu1-N1 aged for 3 days was subjected to treatment at  $60\text{ }^{\circ}\text{C}$  and  $150\text{ }^{\circ}\text{C}$  for 72 hours. The XRD patterns and the corresponding TEM micrographs of the samples obtained under these conditions are shown in Figure 3-15.

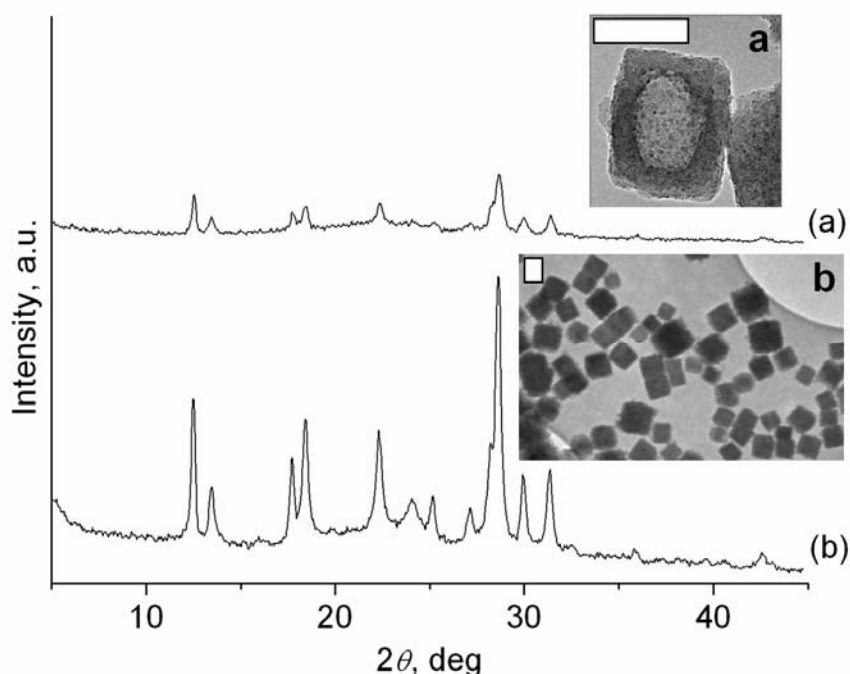


**Figure 3-15.** XRD patterns of samples TE-60 °C (a) and TE-150 °C (b). The insets show TEM images of the corresponding samples. (scale bar = 100 nm)

As can be seen, sample TE-60 °C has low crystallinity, which is explained with the slower growth process at the low temperature (60 °C). The existence of core-shell particles is visible in the TEM micrograph (see inset of Figure 3-15a). The presence of amorphous highly siliceous parts in the core-shell crystals is also proved by the emerging of additional bands at  $1120\text{ cm}^{-1}$ ,  $800\text{ cm}^{-1}$  and  $480\text{ cm}^{-1}$  in the IR spectrum of sample TE-60 °C (Figure 3-14a).<sup>[25, 26]</sup> This is also supported by the ICP chemical analysis data, where sample TE-60°C has higher Si/Al ratio (1.90) in comparison to the crystalline EDI samples (1.37) (see Table 3-4). No core-shell type particles are identified in samples treated at higher temperatures (sample TE-150 °C, Figure 3-15b). Most of the particles have a well-defined cube-shaped morphology with sharp edges and high crystallinity according to the XRD. Once the  $[\text{Cu}(\text{NH}_3)_4]^{2+}$  complexes are incorporated in the amorphous matrix during the aging period, they are stable even after the hydrothermal treatment in a basic media at 150 °C. This study demonstrated that the EDI nanoparticles are crystallized at different temperatures, however the conversion rate from amorphous into crystalline phase is varied.

**Table 3-4.** Chemical composition of samples determined by ICP-AES.

Sample	Cu/Al	Na/Al	Si/Al
TE-60°C	0.43	0.12	1.90
TE-150°C	0.42	0.11	1.53

### 3.5 Conclusions

The crystallization of nanosized EDI type zeolite is shown to be directed by square planar  $[\text{Cu}(\text{NH}_3)_4]^{2+}$  complexes used as co-templating species to the tetramethylammonium cations. Besides, the single addition of copper cations or ammonia leads to the crystallization of pure nanosized FAU type zeolite, whereas the combination of both generates EDI type microporous material. If a sufficient amount of copper ammine complexes is added to the precursor solution, then the EDI phase is crystallized from a wide range of solutions with different initial compositions. Incorporation of the copper complexes during the aging period was found to be a key step in the crystallization pathway. In contrast to the pure  $[\text{Cu}(\text{NH}_3)_4]^{2+}$  complexes, which decompose at room temperature in highly basic media, their incorporation into the sol-gel matrix leads to a stabilization of the metal ammine species even at harsh conditions, such as hydrothermal treatment at 150 °C for several days.

The new templating approach opens up the possibility to prepare new or well-known zeolites in colloidal form by using the versatile class of metal-ammine templates. Metal ammine complexes are promising templates for zeolite synthesis as they carry a high positive charge density for interaction with the anionic silicate species and offer new shapes such as square planar or linear, which are not common for classical quaternary ammonium templates.

### 3.6 References

- [1] C. S. Cundy, P. A. Cox, *Microporous and Mesoporous Materials* **2005**, 82, 1.
- [2] S. Mintova, *Collection of Czechoslovak Chemical Communications* **2003**, 68, 2032.
- [3] L. Tosheva, V. P. Valtchev, *Chemistry of Materials* **2005**, 17, 2494.
- [4] T. Bein, K. Brown, G. C. Frye, C. J. Brinker, *Journal of the American Chemical Society* **1989**, 111, 7640.
- [5] W. Shan, T. Yu, B. Wang, J. Hu, Y. Zhang, X. Wang, Y. Tang, *Chemistry of Materials* **2006**, 18, 3169.
- [6] J. Zhang, J. Dong, M. Luo, H. Xiao, S. Murad, R. A. Normann, *Langmuir* **2005**, 21, 8609.
- [7] C. C. Freyhardt, M. Tsapatsis, R. F. Lobo, K. J. Balkus, Jr., M. E. Davis, *Nature* **1996**, 381, 295.
- [8] P. Behrens, C. Panz, V. Hufnagel, B. Lindlar, C. Freyhardt, G. van de Goor, *Solid State Ionics* **1997**, 101-103, 229.
- [9] R. Garcia, T. D. Coombs, M. J. Maple, W. Zhou, I. J. Shannon, P. A. Cox, P. A. Wright, *Studies in Surface Science and Catalysis* **2004**, 154A, 993.
- [10] N. Rajic, *Journal of the Serbian Chemical Society* **2005**, 70, 371.
- [11] J. Kecht, S. Mintova, T. Bein, *Chemistry of Materials* **2007**, 19, 1203.
- [12] J. Kecht, S. Mintova, T. Bein, *Langmuir* **2008**, 24, 4310-4315.
- [13] B. J. Schoeman, J. Sterte, J. E. Otterstedt, *Zeolites* **1994**, 14, 110.
- [14] S. Mintova, N. H. Olson, V. Valtchev, T. Bein, *Science* **1999**, 283, 958.
- [15] J. Hedlund, E. Kurpan, *Studies in Surface Science and Catalysis* **2001**, 135, 224.
- [16] J. Kecht, B. Mihailova, K. Karaghiosoff, S. Mintova, T. Bein, *Langmuir* **2004**, 20, 5271.
- [17] M. Treacy, J. Higgins, R. von Ballmoos, *Zeolites* **1996**, 16, 330.
- [18] D. R. Flentge, J. H. Lunsford, P. A. Jacobs, J. B. Uytterhoeven, *Journal of Physical Chemistry* **1975**, 79, 354.
- [19] G. Socrates, *Infrared and Raman Characteristic Group Frequencies*, Third ed., John Wiley & Sons Ltd, Chichester, **2001**.
- [20] H. G. Karge, *Microporous and Mesoporous Materials* **1998**, 22, 547.
- [21] P. K. Dutta, R. E. Zaykoski, *Inorganic Chemistry* **1985**, 24, 3490.
- [22] L. Kotai, K. K. Banerji, I. Sajo, J. Kristof, B. Sreedhar, S. Holly, G. Keresztury, A. Rockenbauer, *Helvetica Chimica Acta* **2002**, 85, 2316.
- [23] P.-P. Knops-Gerrits, D. E. De Vos, E. J. P. Feijen, P. A. Jacobs, *Microporous Materials* **1997**, 8, 3.
- [24] B. Mihailova, S. Mintova, K. Karaghiosoff, T. Metzger, T. Bein, *Journal of Physical Chemistry B* **2005**, 109, 17060.
- [25] E. Geidel, H. Lechert, J. Dobler, H. Jobic, G. Calzaferri, F. Bauer, *Microporous and Mesoporous Materials* **2003**, 65, 31.
- [26] T. C. Sheng, S. Lang, B. A. Morrow, I. D. Gay, *Journal of Catalysis* **1994**, 148, 341.



## **4 Extending the templating concept to other metal complexes: Exceptionally small zeolite nanocrystals synthesized with Pd and Pt amines\***

### **4.1 Introduction**

Colloidal suspensions of nanosized molecular sieves with narrow particle size distributions and diameters below 200 nm have attracted considerable attention in the last few years.<sup>[1]</sup> The development of nanotechnology and the requirements for synthesizing nanoscale multifunctional materials present new fascinating goals to the modern solid-state chemistry of nanosized porous systems. Particularly the miniaturization of advanced devices requires molecular sieve crystals in an appropriate form, namely nanocrystals with controlled size, morphology and monomodal particle size distribution. To accomplish these requirements of modern technologies, new innovative approaches in the synthesis and processing of porous solids are required.

Zeolite nanocrystals have been used for the generation of films and membranes, and as precursors for preparation of catalysts and structures with hierarchical porosity.<sup>[2-6]</sup> Actual and new applications of nanosized molecular sieves often utilize the unique spatial structuring of zeolite channel systems for novel concepts such as the stabilization of nanoscale forms of matter,<sup>[7]</sup> size-selective chemical sensing,<sup>[8]</sup> medical diagnostics,<sup>[9]</sup> etc.<sup>[10-12]</sup> Furthermore, a number of forthcoming applications depend not only on the control of the pore structure and intra-zeolite chemistry, but also on the ability to control the external features and morphology of the crystals.<sup>[2, 13]</sup>

However, the generation of very small non-aggregated nanozeolites with sizes below 50 nm poses great synthetic challenges. Some zeolite syntheses can yield crystallite sizes in this range after hydrothermal treatment of clear precursor solutions, i.e. in the case of MFI,<sup>[14]</sup> LTL<sup>[15]</sup> and BEA framework zeolites,<sup>[16]</sup> among others. Although the products can often be recovered in the form of colloidal suspensions, these small secondary crystallites tend to agglomerate into larger particles with sizes of 50 to 200 nm.

\* J. Kecht, S. Mintova, T. Bein, *Langmuir* **2008**, 24, 4310-4315.

A different approach for the generation of small crystallites with sizes of 7-30 nm is based on the confined space synthesis, where an inert mesoporous carbon matrix limits the growth of the zeolite particles.<sup>[17-20]</sup> Due to the calcination necessary for removing the matrix, the final zeolite nanoparticles are irreversibly agglomerated and display broad size distributions, which makes them unsuitable for the preparation of colloidal suspensions.

A possible solution to this problem is the development of highly active nucleation agents, which would induce a high amount of simultaneously growing proto-nuclei. As shown before, copper ammine complexes are highly effective templates for the preparation of nanozeolites at temperatures lower than 100°C, thus avoiding the decomposition of thermally unstable complexes. By replacing the copper species with isosteric square planar complexes  $[\text{Pd}(\text{NH}_3)_4]^{2+}$  and  $[\text{Pt}(\text{NH}_3)_4]^{2+}$  as templates, a similar structure-directing behaviour is expected due to the same geometry of the compounds. However, the variation in size, electronic configuration, and complexation behaviour by employing different metal centers is supposed to change the interactions with the anionic silica species and thus alter the nucleation rate. The resulting suspensions resulting from copper, palladium and platinum complexes are therefore expected to generate the same framework structure but to show different particle size distributions.

As will be shown, the heavy metal centers induce a drastic decrease in particle size, allowing for the first time the synthesis of stable monomodal suspensions containing high amounts of colloidal zeolite single crystals below 20 nm.



## 4.2 Experimental Section

All chemicals were supplied by Aldrich and used as received without further purification for preparation of the initial colloidal solutions. The chemical composition of the precursor solutions is as follows:

2.37 (TMA)<sub>2</sub>O : 0.05 Na<sub>2</sub>O : 1.00 Al<sub>2</sub>O<sub>3</sub> : 4.16 SiO<sub>2</sub> : 244 H<sub>2</sub>O : 0.50 (TM)O : 15 NH<sub>3</sub>, where TM is the transition metal, i.e. Cu, Pd or Pt. Copper(II) nitrate trihydrate (93 mg, 0.38 mmol), tetraamminepalladium(II) nitrate solution (10 % in H<sub>2</sub>O; 1.152 g, 0.38 mmol), or tetraammineplatinum(II) chloride (129 mg, 0.38 mmol) were dissolved in double distilled water (2.02 g, 112 mmol for Pd samples; 2.14 g, 119 mmol for Cu and Pt samples). Concentrated ammonium hydroxide solution (28 wt. % NH<sub>3</sub>; 0.70 g, 11.5 mmol for Cu samples; 0.61 g, 10 mmol for Pd/Pt samples) and tetramethylammonium hydroxide pentahydrate (TMAOH, 0.65 g, 3.62 mmol) were mixed in a polypropylene bottle. After complete dissolution of the TMAOH, aluminium isopropoxide (312 mg, 1.52 mmol) and Ludox HS-30 colloidal silica (30 wt. % SiO<sub>2</sub>; 635 mg, 3.17 mmol) were added, and the mixture was stirred for 30 minutes. The precursor solution is aged at room temperature without stirring for 3 days and transferred in a Teflon-lined stainless steel autoclave. After hydrothermal treatment at 100 °C for 3 days (samples Cu-100, Pd-100, Pt-100) or at 60 °C for 7 days (samples Cu-60, Pd-60, Pt-60), the resulting zeolite nanocrystals were recovered by multi-step centrifugation and washed with double-distilled water. Alternatively, sample Pt-60-dia was purified by dialysis in a Medicell International dialysis tubing (size 10). Furthermore, two samples with mixed metal contents were prepared from precursor solutions with the molar ratios of CuO : PdO = 0.25 : 0.25 (sample CuPd-a) and CuO : PdO = 0.45 : 0.05 (sample CuPd-b). After hydrothermal treatment, all solutions were purified and stabilized in aqueous suspensions at pH = 9.2 – 9.8; a concentration of solid particles of 1 - 3 wt. % was kept in all colloidal suspensions.

### 4.3 Characterization

X-ray diffraction (XRD) measurements were performed on a Stoe powder diffractometer in transmission geometry (Cu-K $_{\alpha 1}$ ,  $\lambda=1.5406$  Å) and a Scintag Inc. XDS 2000 in theta-theta geometry (Cu-K $_{\alpha 1}$ ,  $\lambda=1.5406$  Å; Cu-K $_{\alpha 2}$ ,  $\lambda=1.5444$  Å) to confirm the type of the crystalline phase synthesized from the precursor colloidal system. The size of the crystalline domains in the zeolite samples was determined based on the Scherrer equation, using the line broadening of the Bragg reflections in the range of 10 - 35 °2 $\theta$  (the fitting of the diffraction patterns was carried out with WinXPOW Size/Strain1.02, STOE & Cie GmbH). Prior to the size determination, the instrumental peak broadening was resolved by measuring lanthanum hexaboride as a reference material (Aldrich). In addition, dynamic light scattering (DLS) measurements in colloidal suspensions were performed with a Malvern Zetasizer-Nano instrument equipped with a 4 mW He-Ne laser (633 nm) and avalanche photodiode detector. The chemical composition of the dried zeolite samples was determined by inductively coupled plasma atomic emission spectroscopy (ICP-AES, VARIAN-VISTA).

All samples were subjected to thermogravimetric analyses (TGA) performed on a Netzsch STA 440 C TG/DSC (heating rate of 10 K/min in a stream of synthetic air of ~25 mL/ min). Transmission electron microscopic (TEM) images were recorded using a JEOL JEM 2011 microscope operating at 200 kV.

The spectroscopic studies including IR and Raman were carried out on purified solid samples after freeze-drying. The IR spectra were measured on a Bruker Equinox 55 under diffuse reflectance conditions (samples were mixed with KBr, spectra are background subtracted). Raman spectra were recorded on a Jobin Yvon Horiba HR800 UV Raman microscope using a HeNe laser emitting at 632.8 nm.

#### 4.4 Results and Discussion

Colloidal suspensions containing nanosized EDI-type zeolite crystals were prepared by hydrothermal treatment of precursor solutions containing Cu-, Pd-, and Pt- tetraammine complexes at 60 °C and 100 °C (samples Cu-60, Pd-60, Pt-60, Cu-100, Pd-100, Pt-100). Depending on the templating metal species, the kinetics of the crystallization process are varied, thus resulting in different types of zeolite materials (Figures 4-1, 4-2; positions of the Bragg reflections match with Na-exchanged zeolite K-F (EDI-type), see reference <sup>[21]</sup>). The copper based system readily crystallizes at 100 °C, while at 60 °C the sample contains both crystalline and amorphous phases (Figures 4-1a,b). This observation is combined with an increase of the hydrodynamic diameter of the final colloidal particles (Figures 4-2a, b).

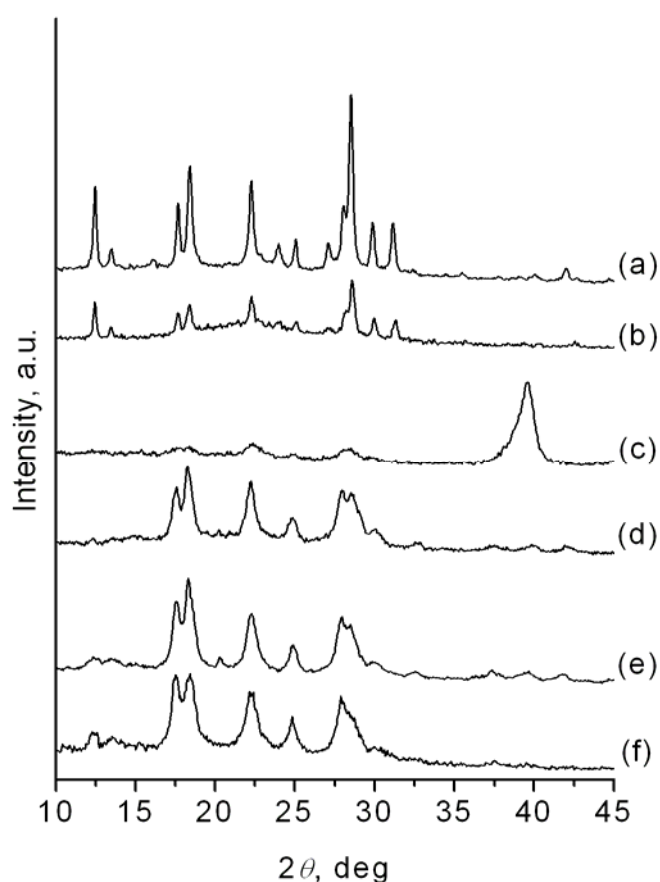


**Figure 4-1.** XRD patterns of samples Cu-100 (a), Cu-60 (b), Pd-100 (c), Pd-60 (d), Pt-100 (e), and Pt-60 (f).

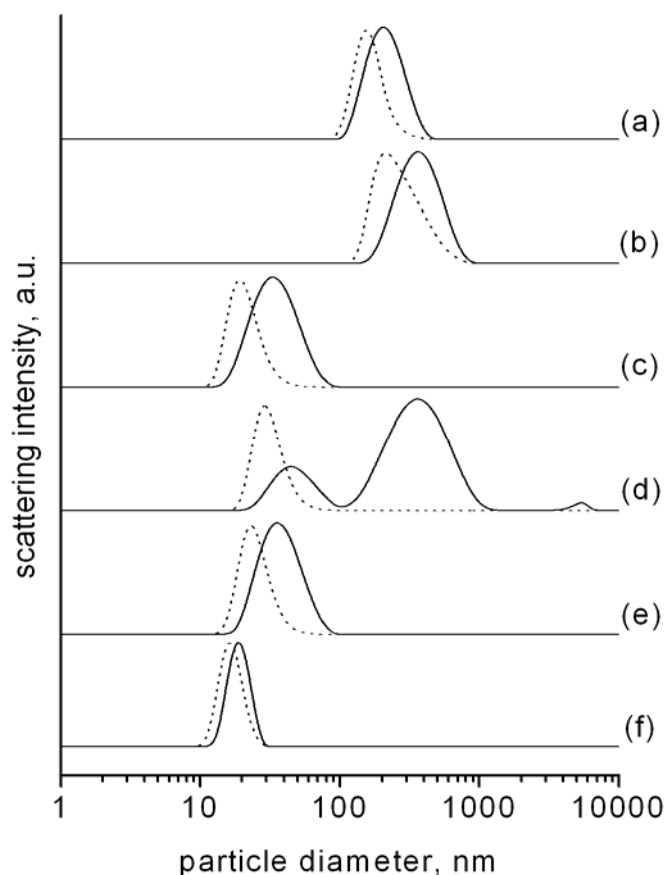


**Figure 4-2.** Unweighted (full line) and number weighted (dotted line) DLS curves of samples Cu-100 (a), Cu-60 (b), Pd-60 (c), Pt-100 (d), Pt-60 (e), and Pt-60-dia (f).

As discussed previously, the increase in the particle size for Cu-EDI at low temperatures is likely caused by the partial generation of core-shell zeolite particles containing amorphous silica, which are observed by TEM (Figure 4-3a, b). This behaviour has been attributed to the different growth and dissolution kinetics of the zeolite phase and intermediate silica species, respectively. The crystallization process of EDI type zeolite with Cu at low temperature is not completed. Probably the crystallization starts at the solid-liquid interfaces going from the periphery to the core of the particles. The growing outer zeolite shell also further limits the dissolution and recrystallization of the silica core. It should be noted that in contrast to conventional zeolite materials, all metal-ammine containing samples were found to be highly

electron beam sensitive, leading to amorphization and formation of metal clusters in TEM after few seconds of irradiation.

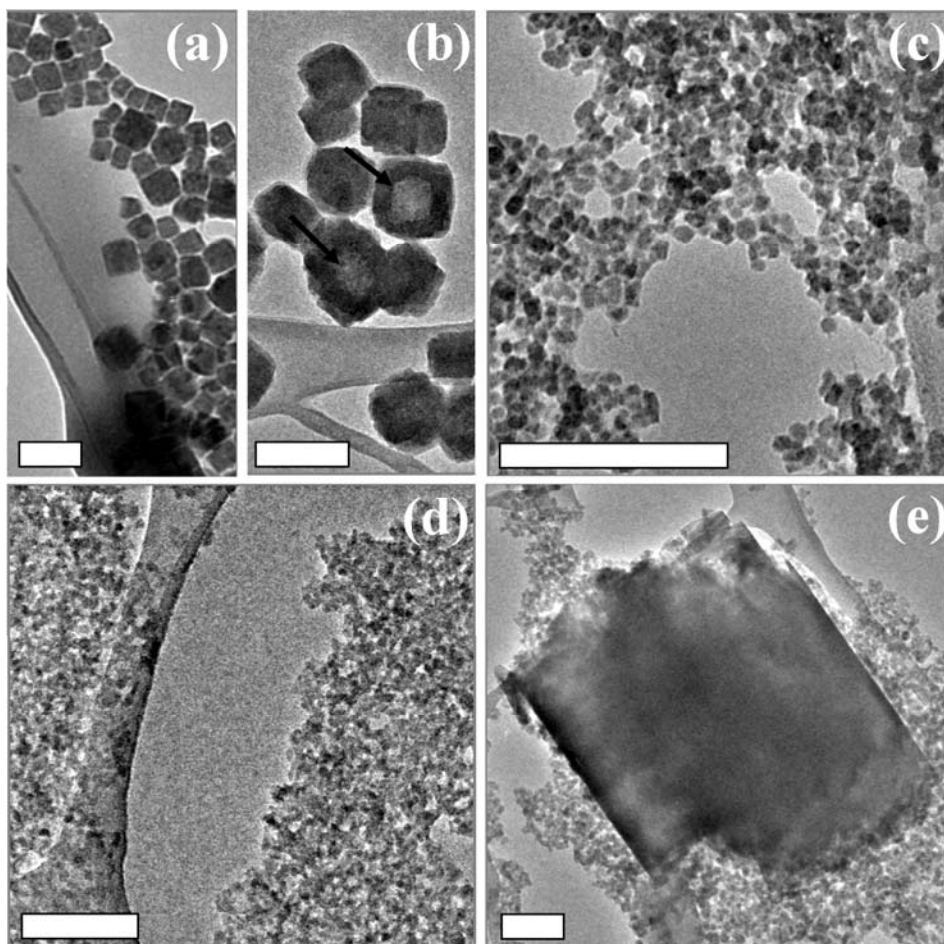


**Figure 4-3.** TEM micrographs of samples Cu-100 (a), Cu-60 (b), Pd-60 (c), Pt-60 (d), and Pt-100 (e) (scale bar = 200 nm in all micrographs).

Completely different crystallization behaviour is observed in the systems containing palladium and platinum amines as templates. In the case of Pd-100, the hydrothermal treatment at 100 °C resulted in the generation of elemental Pd<sup>0</sup> in the form of a black precipitate, while the reaction at 60 °C generates fully crystalline EDI-type phase (Figure 4-1c, d). A similar behaviour is observed for platinum-containing samples. The pure crystalline phase is obtained at a lower temperature in sample Pd-60, while in Pd-100 an unidentified side phase is generated; see new reflection at 20.3 °2 $\theta$  (Figure 4-1e, f). Another remarkable difference to the copper-templated samples is the exceptionally small particle size, which

results in high Bragg peak broadening for all Pd and Pt-containing samples (Figures 4-1c-f). It should be noted that the low angle reflections at  $12.5$  and  $13.5^\circ 2\theta$  of the EDI-type structure visible in the copper samples are present in both the Pd-60 and Pt-60 as well, but greatly reduced due to the high scattering of Pd and Pt. This conclusion was made based on the experimental long-time measurements of the samples and the corresponding simulated XRD patterns of qualitative structure models (see Supporting Information).

Using the Scherrer equation, which is based on the peak broadening of the Bragg reflections, a mean crystalline domain size of  $12$  nm in sample Pd-60 compared to crystallite sizes of  $55$  nm in sample Cu-100 is calculated. These data are confirmed by DLS, which show that the particle size distribution curves are shifted to smaller hydrodynamic diameters in both Pd and Pt samples (Figure 4-2). The copper-based system Cu-100 displays unweighted and number-weighted particle size distribution curves centred at  $200$  nm and  $150$  nm, respectively. The corresponding hydrodynamic diameters are reduced to  $30$  nm and  $20$  nm in sample Pd-60, and to  $35$  nm and  $20$  nm in sample Pt-60 (Figure 4-2a, c, e). Due to the small particle size in these samples, a complete separation from the suspensions by centrifugation became difficult. Moreover, only a partial redispersion of the centrifuge cake was possible after purification of the samples. Therefore isolation of the nanocrystals from the colloidal suspensions by dialysis was applied as an alternative approach (sample Pt-60-dia). This allows separation of the suspended particles while keeping the concentration constant and avoiding further agglomeration due to the close interaction between solid nanoparticles during centrifugation. A good match between the unweighted and number-weighted DLS curves with a peak centred at  $15$  nm and  $20$  nm is observed, thus showing that the amount of agglomerated species is diminished and demonstrating the high monodispersity of the sample (Figure 4-2f). The small sizes of the particles in samples Pd-60 and Pt-60 measured with DLS were also confirmed by TEM (Figure 4-3c, d); nanocrystals with rounded edges and sizes between  $15$  nm and  $20$  nm can be seen. For the platinum-templated system, similar crystals are generated at  $100^\circ\text{C}$

(sample Pt-100), and an unknown side phase is present (Figure 4-1e). The crystalline micrometer-sized particles are detected by DLS and TEM (Figure 4-1e, 4-2d, 4-3e). In conclusion, the type of the metal ammine complex has a pronounced effect on the size of the crystalline colloidal zeolite.

IR/Raman spectroscopy was applied to elucidate the role of the square planar platinum and palladium tetraammine complexes in the formation of zeolites and to investigate the interactions between the complexes and the inorganic framework. Figure 4-4 shows a comparison between samples Pd-60 and Pt-60 and the corresponding free metal ammine complex salts in the region between 360 and 2000  $\text{cm}^{-1}$ . The presence of  $[\text{Pd}(\text{NH}_3)_4]^{2+}$  and  $[\text{Pt}(\text{NH}_3)_4]^{2+}$  complexes inside the zeolite structure can be easily detected by examining the vibrational bands of the complexed ammonia.<sup>[22, 23]</sup> The most prominent band is the symmetric deformation  $\delta_s(\text{NH}_3)$  at 1285  $\text{cm}^{-1}$  and 1326  $\text{cm}^{-1}$  in the Pd and Pt containing materials, respectively. Similarly, the band corresponding to the degenerated deformation  $\delta_d(\text{NH}_3)$  is located at 1560  $\text{cm}^{-1}$  for both Pd and Pt salts, but shifted to higher wavenumbers in sample Pt-60 (1590  $\text{cm}^{-1}$ ). Other typical vibrations of  $\delta_r(\text{NH}_3)$  are located in the region 830 – 900  $\text{cm}^{-1}$ , but they are obstructed by overlapping bands coming from the zeolitic framework. These bands are very weak, and therefore are difficult to be detected inside the zeolite. For the  $\nu(\text{Pd-N})$  and  $\nu(\text{Pt-N})$  stretch vibrations located at 492  $\text{cm}^{-1}$  and 508  $\text{cm}^{-1}$  in the metal salts, respectively, the same tendency is observed.

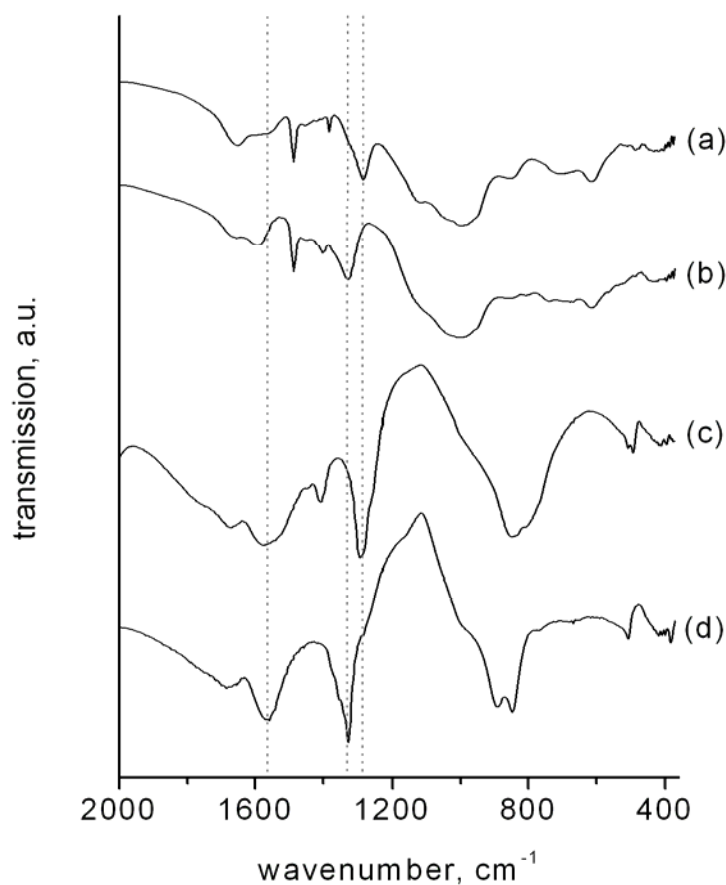


**Figure 4-4.** IR spectra of samples Pd-60 (a), Pt-60 (b), pure tetraamminepalladium(II) nitrate and (c) pure tetraammineplatinum(II) chloride (d).

Raman spectroscopy was used to investigate the occluded metal complexes in the zeolite nanoparticles (Figure 5). In this case the most intense bands associated with the metal ammine complexes are those corresponding to the  $\nu_s(\text{Pd-N})$  ( $A_{1g}$ ) and  $\nu_s(\text{Pt-N})$  ( $A_{1g}$ ) symmetric stretch vibrations which are located at  $505\text{ cm}^{-1}$  and  $550\text{ cm}^{-1}$ , respectively, for the unrestricted complexes in the metal salts.<sup>[23-25]</sup> However, after inclusion of the metal complexes into the zeolite channels, these bands are broadened and strongly shifted to higher energies, i.e.  $539\text{ cm}^{-1}$  and  $576\text{ cm}^{-1}$  in samples Pd-60 and Pt-60, respectively. The position of the less intense



asymmetric stretch vibrations  $\nu(\text{Pd-N})$  ( $B_{1g}$ ) and  $\nu(\text{Pt-N})$  ( $B_{1g}$ ) located at  $469\text{ cm}^{-1}$  and  $530\text{ cm}^{-1}$  in the metal salts are not shifted and can be found at the same positions in samples Pd-60 and Pt-60, correspondingly. The asymmetric stretch vibration appears to have a higher relative intensity in sample Pd-60 due to the overlapping with the zeolitic framework vibration visible as a shoulder located at  $\sim 515\text{ cm}^{-1}$ , which is related to the motion of an oxygen atom in a plane perpendicular to the T-O-T bonds. In contrast, the bending vibrations  $\delta_s(\text{N-Pt-N})$  ( $B_{2g}$ ) and  $\delta_s(\text{N-Pd-N})$  ( $B_{2g}$ ) located at around  $305\text{ cm}^{-1}$  in the metal salts are shifted to lower energies and appear at  $277\text{ cm}^{-1}$  and  $262\text{ cm}^{-1}$  in both samples Pd-60 and Pt-60, respectively (Figure 4-5).

The strong shifts of the metal complex vibrations and their broadening after incorporation into the zeolite matrix are due to the strong interaction between the complex species and the zeolitic framework, i.e. due to hydrogen bonding and sterical restrictions of the templating metal amines inside the zeolite cages.

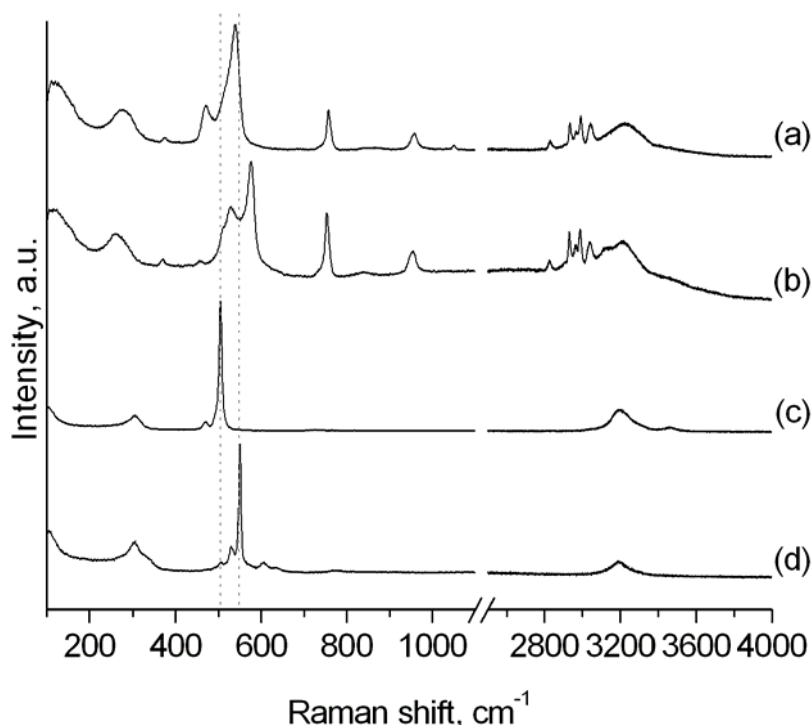


**Figure 4-5.** Raman spectra of samples Pd-60 (a), Pt-60 (b), pure tetraamminepalladium(II) nitrate (d), and pure tetraammineplatinum(II) chloride (e).

The presence of Pt, Pd and Cu in the samples was confirmed by the ICP-AES analysis (Table 4-1). Due to the surplus silica enclosed inside the core-shell type particles in sample Cu-60, a higher Si/Al ratio of 2.19 in comparison to the other samples was determined. All samples Pd-60, Pt-60 and Cu-100 have very similar Si/Al ratios in the range of 1.37 to 1.39, indicating that the composition of the high-alumina EDI-type zeolite framework is not affected by the presence of different templating complexes. However, the amount of incorporated metal seems to be significantly lower for Pd and Pt-samples in comparison to samples synthesized with Cu, indicating that samples Pd-60 and Pt-60 contain a higher amount of tetramethylammonium cations inside the zeolite channels.

**Table 4-1.** Chemical composition of samples as determined by ICP-AES elemental analysis.

Sample	Cu/Al	Pd/Al	Pt/Al	Na/Al	Si/Al
Cu-60	0.42	-	-	0.08	2,19
Cu-100	0.39	-	-	0.08	1.37
Pd-60	-	0.30	-	0.07	1.39
Pt-60	-	-	0.31	0.05	1.37
CuPd-a	0.15	0.18	-	0.08	1.58
CuPd-b	0.31	0.05	-	0.10	1.63

Combined thermogravimetric (TG) and differential scanning calorimetric (DSC) measurements were performed to examine whether the  $[\text{Pd}(\text{NH}_3)_4]^{2+}$  and  $[\text{Pt}(\text{NH}_3)_4]^{2+}$  complexes remain undissociated, and no uncomplexed  $\text{Pd}^{2+}$  and  $\text{Pt}^{2+}$  cations are generated during the hydrothermal synthesis, and subsequently incorporated into the zeolitic materials (Table 4-1, Figure 4-6). The first endothermic peak with the corresponding mass loss at about 100 °C in both samples is attributed to the release of zeolite-type water from the channels of

the materials. The next exothermic peak with a mass loss at 600 °C is attributed to the combined combustion of the tetramethylammonium cations and release of ammonia from the metal complexes.

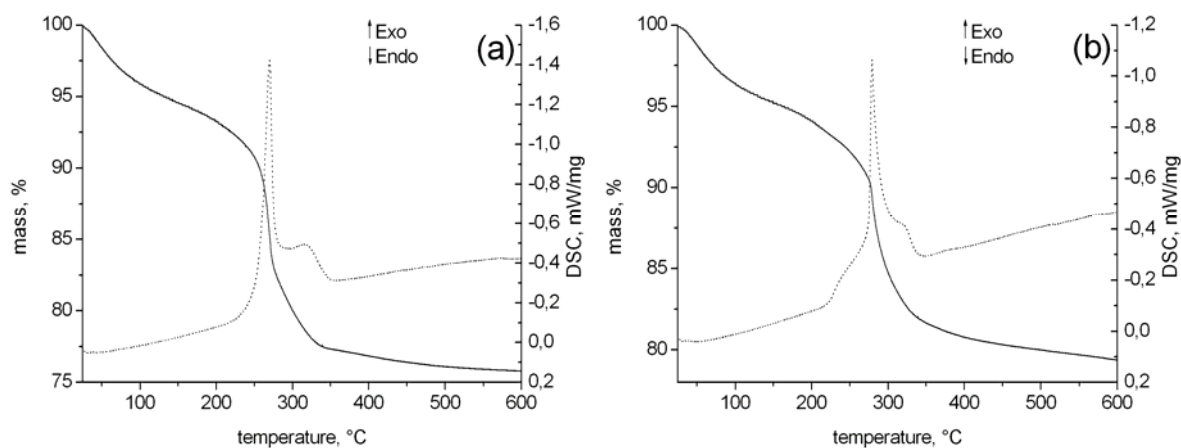


**Figure 4-6.** TGA (full line) and DSC (dotted line) curves for samples Pd-60 (a) and Pt-60 (b).

Two distinct signals are seen in the DSC curves (Figure 4-6). However, the different processes cannot be clearly distinguished based on the DSC curves due to a strong overlapping of the peaks in the temperature range between 200 – 350 °C. Based on the ICP-AES analysis, the amount of tetramethylammonium cations required for charge balancing of the zeolitic framework was calculated. In the case of sample Pd-60, after taking the charges of  $\text{Pd}^{2+}$  and  $\text{Na}^+$  into account, a TMA/Al ratio of 0.33 is needed. With an aluminium content of 4.38 mmol Al per gram zeolite this is equivalent to 1.44 mmol TMA per gram zeolite or a mass loss of 10.7 %. The remaining mass loss in the region between 100 and 600 °C of 9.4 % corresponds to 5.53 mmol  $\text{NH}_3$  per gram zeolite and thus to a molar ratio of  $\text{NH}_3/\text{Pd}$  equal to 4.2, which is in good accordance to the expected stoichiometry of 4. In the same way, the  $\text{NH}_3/\text{Pt}$  ratio of 3.7 for sample Pt-100 and the  $\text{NH}_3/\text{Cu}$  ratio of 3.8 for sample Cu-100 were calculated. In conclusion, the decomposition of Pd/Pt complexes into other species during the hydrothermal treatment is unlikely. The influence of the type of metal ammine template on particle size is related to the presence of the square planar metal complexes in the precursor

solutions. One possible explanation is that the Pd and Pt complexes lead to a faster and enhanced nucleation rate in comparison to the copper species in the precursor aluminosilicate solutions. The latter explains both the smaller particle size and the higher monodispersity in samples Pd-60 and Pt-60 as compared to sample Cu-100 (see Figure 4-3d). In order to confirm this assumption, colloidal crystals were synthesized from precursor solutions by combining copper and palladium at different molar ratios, i.e. sample CuPd-a (50 % Cu, 50 % Pd) and CuPd-b (90% Cu, 10% Pd). The crystallization of EDI-type colloidal zeolite in both samples CuPd-a and CuPd-b was confirmed by XRD, and the incorporation of both types of metal was proven by ICP-AES analysis (Figure 4-7, Table 4-1).

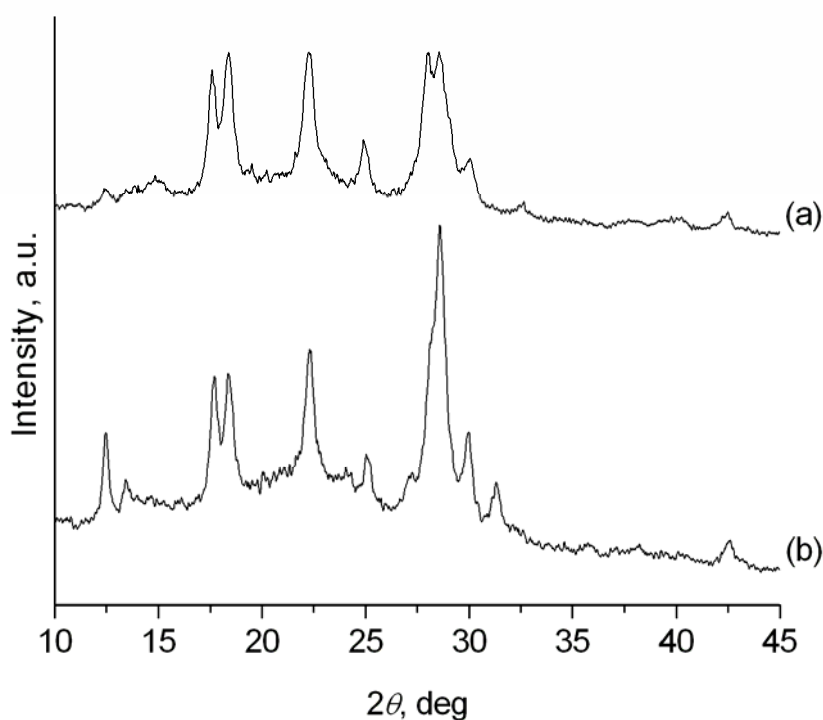


**Figure 4-7.** XRD patterns of samples CuPd-a (a) and CuPd-b (b).

Correspondingly, the intensities of the low angle reflections at 12.5 and 13.5 °2θ increased for samples with lower Pd and higher Cu contents, as expected for the mixed metal systems. While the ratio of incorporated metals in both samples is similar to the amounts employed in

the precursor solutions, a higher relative Pd content is observed, i.e. a Cu/Pd ratio of 0.83 in CuPd-a and 6.2 in CuPd-b instead of the expected values of 1 and 9 found in the respective precursor solutions. This result shows the preferred incorporation of Pd over Cu, as is expected for a higher nucleation rate of the Pd species. Furthermore, DLS data shows that even the relatively low amount of Pd complexes (10 %) in sample CuPd-b leads to a strong decrease in particle size to about 30 nm (Figure 4-8b).

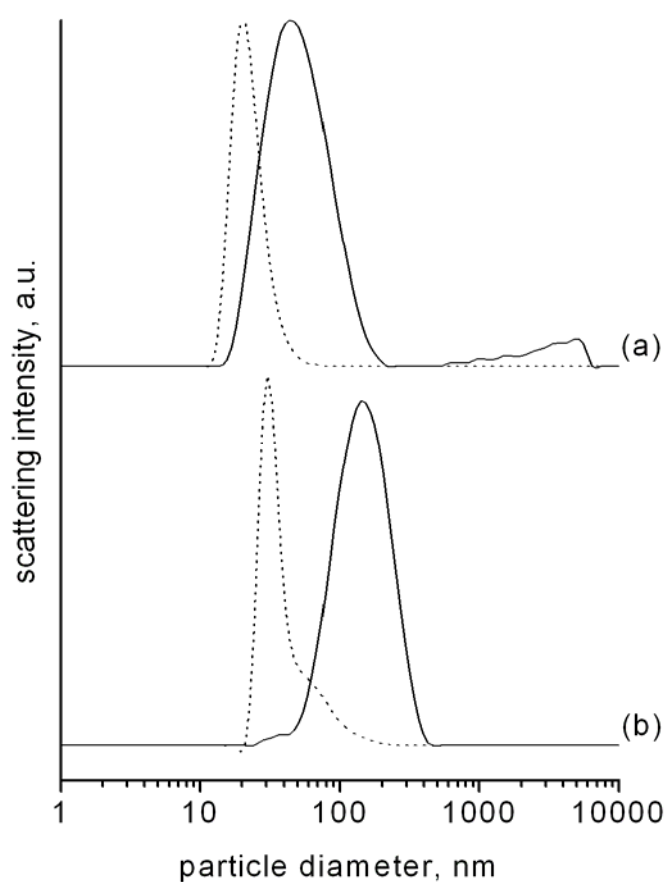


**Figure 4-8.** Unweighted (full line) and number weighted (dotted line) DLS curves of samples CuPd-a (a) and CuPd-b (b).

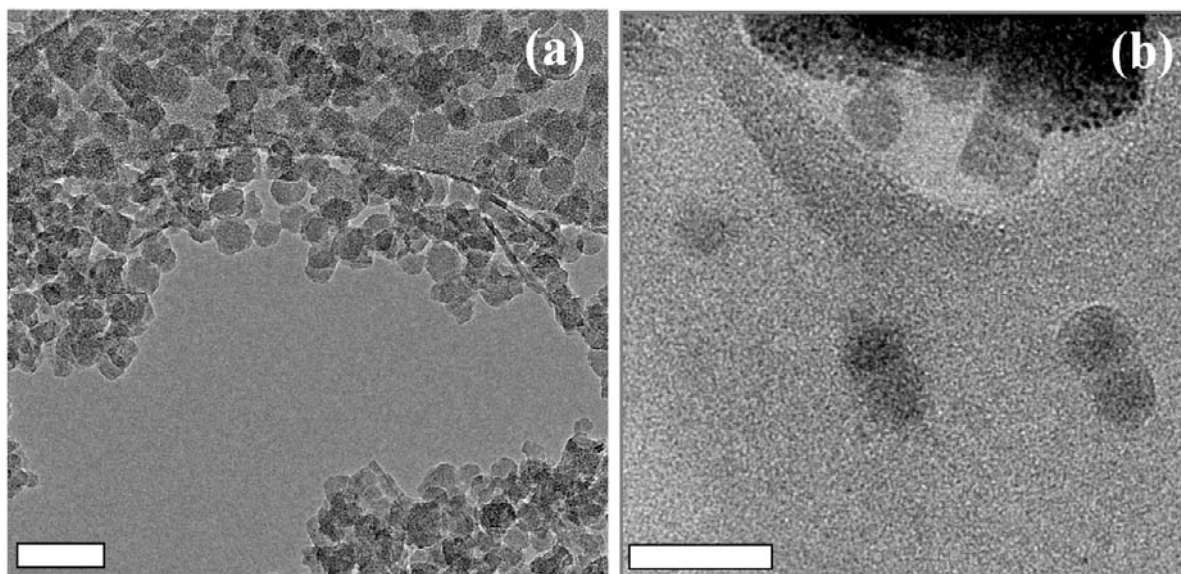


**Figure 4-9.** TEM micrographs of samples CuPd-a (a) and CuPd-b (b) (scale bar = 50 nm in both micrographs).

At higher concentration of Pd (sample CuPd-a, 50 %), the particle size is further reduced to 20 nm, which is comparable to the copper-free system of sample Pd-60. The particle size for both samples was visualized by TEM (Figure 4-9). One can conclude that after generation of initial nuclei by the Pd complexes, further growth of the zeolite particles is possible by incorporation of Cu. Probably the inhomogeneous particle size distribution in these samples is caused by the different rate of nucleation and crystallization of the Cu and Pd systems at low temperatures. While hydrothermal treatment must be performed below 100 °C to avoid reduction of the Pd species, the Cu system tends to incorporate higher amounts of silica at these temperatures, i.e., in the form of core shell particles. This behaviour is responsible for the larger agglomerations seen in DLS data of both samples (Figure 4-8). The incorporation of silica was confirmed by elemental analysis showing increased Si/Al ratios of 1.58 and 1.63 for samples CuPd-a and CuPd-b, respectively. The different crystallization kinetics of zeolite nanoparticles are determined by the type of the metal ammine complex and also by the temperature of crystallization.

## 4.5 Conclusions

Exceptionally small zeolite nanocrystals with sizes below 20 nm were prepared in the form of stable colloidal suspensions with monomodal particle size distributions *via* a Pd and Pt ammine templating approach. In contrast to Pt- and Pd-containing precursor solutions, the Cu-based systems require hydrothermal treatment at temperatures above 100 °C.

The partial substitution of Cu with Pd and Pt ammine complexes is successfully performed, and this leads to the formation of EDI crystals with reduced particle diameter at low temperatures. Furthermore, the successful substitution of  $[\text{Cu}(\text{NH}_3)_4]^{2+}$  by square planar Pd and Pt ammine complexes having the same geometry reinforces the role of these complexes as templates for the formation of EDI zeolite. It was shown that the smaller particle size results from a higher nucleation rate in the systems containing pure Pd or Pt complexes or in mixed systems with  $[\text{Cu}(\text{NH}_3)_4]^{2+}$  and low loadings of  $[\text{Pd}(\text{NH}_3)_4]^{2+}$ . A transfer of the current templating concept to other colloidal systems with less expensive metal complexes would be of interest for the generation of various new nanosized zeolites.

#### 4.6 References

- [1] L. Tosheva, V. P. Valtchev, *Chemistry of Materials* **2005**, *17*, 2494.
- [2] M. A. Snyder, M. Tsapatsis, *Angewandte Chemie, International Edition* **2007**, *46*, 7560.
- [3] H. Wang, L. Huang, Z. Wang, A. Mitra, Y. Yan, *Chemical Communications* **2001**, 1364.
- [4] P. Waller, Z. Shan, L. Marchese, G. Tartaglione, W. Zhou, J. C. Jansen, T. Maschmeyer, *Chemistry--A European Journal* **2004**, *10*, 4970.
- [5] X. D. Wang, W. L. Yang, Y. Tang, Y. J. Wang, S. K. Fu, Z. Gao, *Chemical Communications* **2000**, 2161.
- [6] V. Valtchev, M. Smaïhi, C. Faust, L. Vidal, *Angewandte Chemie, International Edition* **2003**, *42*, 2782.
- [7] J. Kecht, Z. Tahri, V. De Waele, M. Mostafavi, S. Mintova, T. Bein, *Chemistry of Materials* **2006**, *18*, 3373.
- [8] Y. Yan, T. Bein, *Journal of Physical Chemistry* **1992**, *96*, 9387.
- [9] C. Platas-Iglesias, L. Vander Elst, W. Zhou, R. N. Muller, C. F. G. C. Geraldes, T. Maschmeyer, J. A. Peters, *Chemistry--A European Journal* **2002**, *8*, 5121.
- [10] S. Megelski, G. Calzaferri, *Advanced Functional Materials* **2001**, *11*, 277.
- [11] S. Mintova, *Collection of Czechoslovak Chemical Communications* **2003**, *68*, 2032.
- [12] N. B. Castagnola, P. K. Dutta, *Journal of Physical Chemistry B* **1998**, *102*, 1696.
- [13] G. Bonilla, I. Diaz, M. Tsapatsis, H.-K. Jeong, Y. Lee, D. G. Vlachos, *Chemistry of Materials* **2004**, *16*, 5697.
- [14] J. Aguado, D. P. Serrano, J. M. Escola, J. M. Rodriguez, *Microporous and Mesoporous Materials* **2004**, *75*, 41.
- [15] C. C. Freyhardt, M. Tsapatsis, R. F. Lobo, K. J. Balkus, Jr., M. E. Davis, *Nature* **1996**, *381*, 295.
- [16] M. A. Camblor, A. Corma, S. Valencia, *Microporous and Mesoporous Materials* **1998**, *25*, 59.
- [17] I. Schmidt, C. Madsen, C. J. H. Jacobsen, *Inorganic Chemistry* **2000**, *39*, 2279.
- [18] C. J. H. Jacobsen, C. Madsen, T. V. W. Janssens, H. J. Jakobsen, J. Skibsted, *Microporous and Mesoporous Materials* **2000**, *39*, 393.
- [19] S.-S. Kim, J. Shah, T. J. Pinnavaia, *Chemistry of Materials* **2003**, *15*, 1664.
- [20] H. Wang, B. A. Holmberg, Y. Yan, *Journal of the American Chemical Society* **2003**, *125*, 9928.
- [21] M. Treacy, J. Higgins, R. von Ballmoos, *Zeolites* **1996**, *16*, 330.
- [22] R. J. H. Clark, M. Kurmoo, A. M. R. Galas, M. B. Hursthouse, *Journal of the Chemical Society, Dalton Transactions: Inorganic Chemistry (1972-1999)* **1982**, 2505.
- [23] Y. Chen, D. H. Christensen, O. F. Nielsen, *Spectrochimica Acta, Part A: Molecular and Biomolecular Spectroscopy* **1995**, *51A*, 595.
- [24] I. A. Degen, A. J. Rowlands, *Spectrochimica Acta, Part A: Molecular and Biomolecular Spectroscopy* **1991**, *47A*, 1263.
- [25] M. Manfait, A. J. P. Alix, L. Bernard, T. Theophanides, *Journal of Raman Spectroscopy* **1978**, *7*, 143.



## 5 Oxidative removal of template molecules and organic functionalities in mesoporous silica nanoparticles by H<sub>2</sub>O<sub>2</sub> treatment\*

### 5.1 Introduction

Since their discovery in 1992 by Beck et al.,<sup>[1]</sup> ordered mesoporous silica systems have been intensively investigated, thus leading to the discovery of various materials with different pore sizes, pore arrangements and particle morphologies.<sup>[2-4]</sup> Recent examples include the synthesis of stable colloidal suspensions of mesoporous silica nanoparticles with sizes below 100 nm,<sup>[5-7]</sup> which offer many possibilities for new applications in research fields such as sensing, optics and drug delivery.<sup>[8-10]</sup> Nanosized porous silica systems also permit the construction of hierarchical porous materials and the preparation of thin films by spincoating.<sup>[11, 12]</sup>

In order to make the porous network accessible in such systems, the template has to be removed from the mesoporous channels inside the particles. In most cases this is achieved *via* extraction in various media, as direct calcination causes irreversible agglomeration of the colloidal particles during drying and heating. However, depending on the extraction procedure, the template removal can be incomplete, or multiple steps are required for a complete elimination of the template molecules.<sup>[13, 14]</sup>

Therefore, alternative template removal methods based on chemical oxidation have recently been investigated. Various oxidation agents have been employed, including ozone,<sup>[15, 16]</sup> potassium permanganate,<sup>[17]</sup> and hydrogen peroxide.<sup>[18-21]</sup> Application of hydrogen peroxide usually involves the generation of highly reactive hydroxyl radicals by addition of catalysts such as iron(III)<sup>[18, 22]</sup> or irradiation with UV light,<sup>[19]</sup> and in certain cases also involves the addition of acids.<sup>[19, 21]</sup> Depending on template type, reactant concentrations and experimental setup used in the studies, complete oxidation was achieved in a range of conditions, varying from several minutes to days and from room temperature to 250 °C.

The present study first examines suitable conditions, i.e., catalyst, amounts of reactants, reaction time and temperature, for the complete removal of cetyltrimethylammonium

\* J. Kecht, T. Bein, *Micropor. Mesopor. Mater.* **2008**, DOI=10.1016/j.micromeso.2008.03.027.

surfactant from the pore network of MCM-41 and colloidal mesoporous silica (CMS) by oxidation with hydrogen peroxide. The surface properties of CMS samples treated with  $\text{H}_2\text{O}_2$  under these conditions are compared with samples obtained *via* conventional extraction in ethanolic media.

An additional point of interest is the influence of oxidation by  $\text{H}_2\text{O}_2$  on the type and content of functional groups in co-condensed materials. By incorporating organosilanes during the synthesis of CMS, it is possible to influence size and morphology of the resulting particles.<sup>[23]</sup> Removal of these groups by treatment with  $\text{H}_2\text{O}_2$  allows the generation of purely siliceous unfunctionalized materials while retaining the modified particle size and morphology.

## 5.2 Experimental Section

**Reagents.** Tetraethyl orthosilicate (TEOS, Fluka, >98%), ammonia (Aldrich, 25% in  $\text{H}_2\text{O}$ ) phenyltriethoxysilane (PTES, Aldrich, 98%), methyltriethoxysilane (Aldrich, 99%), vinyltriethoxysilane (Aldrich, 97%), mercaptopropyltriethoxysilane (ABCR, 95%), cetyltrimethylammonium bromide (CTAB, Aldrich, 95%), cetyltrimethylammonium chloride (CTAC, Fluka, 25% in  $\text{H}_2\text{O}$ ) and triethanolamine (TEA, Aldrich, 98%) were used as received without further purification. Doubly distilled water from a Millipore system (Milli-Q Academic A10) was used for all synthesis and purification steps.

**Preparation of micrometer-sized MCM-41 mesoporous silica (MS).** MCM-41 material was prepared according to a published procedure.<sup>[24]</sup> To a stirred solution of CTAB (2.39 g, 6.56 mmol), water (125 g, 6.94 mol), ethanol (12.5 g, 271.15 mmol) and aqueous ammonia (25 %wt, 9.18 g, 134.93 mmol) in a 300 mL polypropylene reactor, the amount of 10.03 g TEOS (48.19 mmol) was added. The resulting mixture has a molar composition of 1 TEOS : 0.14 CTAB : 144  $\text{H}_2\text{O}$  : 5.63 ethanol : 2.8  $\text{NH}_3$ . After stirring for 2 hours at room temperature, the reaction mixture was filtered off and washed with 50 mL water. The resulting white

powder was dried at 60°C for 12 h. For the preparation of co-condensed materials, 20 mol% of the TEOS content was replaced by functionalized triethoxysilanes.

**Preparation of colloidal mesoporous silica (CMS) nanoparticles.** Mesoporous silica nanoparticles were prepared according to reference <sup>[25]</sup> from reaction mixtures with a molar composition of 1 TEOS: 0.20 CTAC: 10.37 TEA: 130.15 H<sub>2</sub>O. The combined TEOS (1.92 g, 9.22 mmol) and TEA (14.3 g, 95.6 mmol) were heated for 20 minutes at 90 °C without stirring in a 100 mL polypropylene reactor. A solution of CTAC (25 % in water, 2.41 mL, 1.83 mmol) and water (21.7 g, 1.21 mol) preheated to 60 °C was added, and the resulting mixture was stirred at room temperature for 12 hours. After addition of 100 mL ethanol, the mesoporous silica nanoparticles were separated by centrifugation and redispersed in ethanol. For the preparation of phenyl co-condensed materials, 20 mol% of the TEOS were replaced by PTES.

**Extraction of MCM-41 and CMS.** Extraction of the organic template from the MCM-41 materials was performed by heating the samples (1.0 g) twice under reflux at 90°C for 30 minutes in a solution containing 2 g ammonium nitrate in 100 mL ethanol followed by 30 minutes under reflux in a solution of 4 g concentrated hydrochloric acid in 100 mL ethanol. The MCM-41 material was separated by filtration and the CMS nanoparticles were isolated by centrifugation. Both materials were washed with ethanol after each extraction step. MCM-41 and CMS materials were obtained as white solid powders and as clear ethanolic suspensions, respectively.

**Template oxidation by H<sub>2</sub>O<sub>2</sub> in MCM-41 and CMS.** The amount of 4 mL aqueous hydrogen peroxide solution (30 %) was added to 200 mg template-containing silica material in a 25 mL round-bottom flask equipped with a reflux condenser. In the case of CMS, the ethanolic suspensions were centrifuged and redispersed in a small amount of water prior to the addition of hydrogen peroxide. Selected samples were prepared by further addition of either 4 mL concentrated nitric acid or 8.8 mg iron(III) chloride hexahydrate. The oxidation

reaction was performed at various temperatures and treatment times (see Table 5-1). The MCM-41 materials were separated by filtration and the CMS nanoparticles by centrifugation, respectively, followed by two steps of washing with water. Refluxing in acidified ethanol (4 g HCl per 100 mL EtOH) for 30 minutes was employed for the stabilization of CMS nanoparticles and removal of organic fragments from the pores of functionalized samples after oxidation.

**Table 5-1.** Reaction conditions for the oxidative treatment of unfunctionalized MCM-41.

Sample name	Catalyst	Temperature [°C]	Time [h]
MS 1	Fe(III)	20	18
MS 2	HNO <sub>3</sub>	20	18
MS 3	HNO <sub>3</sub>	50	5
MS 4	HNO <sub>3</sub>	95	5
MS 5	-	95	0.5
MS 6	-	95	1
MS 7	-	95	2
MS 8	-	95	3
MS 9	-	95	5

### 5.3 Characterization

Dynamic light scattering (DLS) measurements were performed on a Malvern Zetasizer-Nano instrument equipped with a 4 mW He-Ne laser (632.8 nm) and avalanche photodiode detector. Thermogravimetric analyses (TGA) of the bulk samples were performed on a Netzsch STA 440 C TG/DSC (heating rate of 10 °C/min in a stream of synthetic air of about 25 mL/min). Raman spectra were recorded on a Jobin Yvon Horiba HR800 UV Raman microscope using a HeNe laser emitting at 632.8 nm. Nitrogen sorption measurements were performed on a Quantachrome Instruments NOVA 4000e at -196 °C (77 K). For calculations of pore sizes the

NLDFT equilibrium model of N<sub>2</sub> on silica was used. Solid state <sup>13</sup>C-MAS-NMR measurements were performed on a Bruker DSX Avance 500 FT (contact time 4 ms, spinning rate 6 kHz, pulse length 2.8 μs, recycle delay 8 s, number of scans 512). Liquid state <sup>13</sup>C-NMR and <sup>13</sup>C-DEPT-NMR spectra were recorded on a JEOL Eclipse-270 NMR spectrometer. Transmission electron microscope (TEM) images of CMS materials were taken with a JEOL JEM 2011 microscope operating at 200 kV, after drying the diluted colloidal suspensions on a carbon-coated copper grid.

## 5.4 Results and Discussion

**Optimizing the conditions for H<sub>2</sub>O<sub>2</sub>-mediated template removal.** The influence of various reaction parameters on the efficiency of the removal of cetyltrimethylammonium (CTA) cations from the pores of mesoporous silica by oxidation with H<sub>2</sub>O<sub>2</sub> was investigated. The degree of template removal was determined by thermogravimetric analysis (TGA) based on published data for the thermal decomposition of CTA in MCM-41.<sup>[26]</sup> In the temperature range up to 110 °C, physisorbed water is released from the pores. From 110 °C to about 395 °C, remaining cetyltrimethylammonium template is successively decomposed by first undergoing Hoffmann elimination followed by combustion and oxidation reactions to CO<sub>2</sub>. At temperatures above 395 °C, weight loss can be attributed to released water from silanol condensation and to the oxidation of small remains of carbonaceous residues from incomplete template combustion. The amount of organic material after oxidation with H<sub>2</sub>O<sub>2</sub> was therefore determined by the weight loss between 110 °C and 395 °C in the case of unfunctionalized materials. In order to take into account the varying amounts of adsorbed water inside the partly filled mesopores, the weight loss is given relative to the amount of residual silica after heating to 900 °C, assuming a complete dehydroxylation and lack of carbonaceous residues at this temperature. Table 5-2 summarizes the content of organic residues thus determined in the

different H<sub>2</sub>O<sub>2</sub>-treated samples; the full TGA/DSC curves for the temperature range of 25 – 900 °C for all samples can be found in the Supporting Information.

**Table 5-2.** Weight loss as determined by TGA of MCM-41 samples treated with H<sub>2</sub>O<sub>2</sub> at different conditions.

Sample name	Normalized weight loss [mg / g(SiO <sub>2</sub> )] <sup>a</sup>
MCM-41 as synthesized	674
MCM-41 extracted	105
MS 1	186
MS 2	79
MS 3	53
MS 4	44
MS 5	355
MS 6	166
MS 7	74
MS 8	34
MS 9	31

<sup>a</sup> weight loss between 110-395 °C, given relative to SiO<sub>2</sub> residue at 900 °C

Removal of the CTA template in the pores of MCM-41 at different temperatures was investigated by treatment with concentrated H<sub>2</sub>O<sub>2</sub> and addition of nitric acid or iron chloride at concentrations similar to those reported in literature.<sup>[18, 21]</sup> The presence of iron cations catalyzes the formation of OH· radicals and thus increases the oxidizing power of hydrogen peroxide, an approach known as Fenton's chemistry.<sup>[27]</sup> As the iron-catalyzed mixture is already strongly reacting and foaming under cooling to 20 °C in sample MS 1, experiments at higher temperatures were not performed. On the other hand, sample MS 2 treated with H<sub>2</sub>O<sub>2</sub> and nitric acid at 20 °C reacted less intensively and did not require additional cooling. Interestingly, decomposition of the template seems to be more effective in the acid-treated sample (Table 2). The high amount of residual organics in MS 1 is possibly related to the fast

decomposition of  $\text{H}_2\text{O}_2$  by the iron cations, leading to a depletion of reactive species before complete template decomposition.

Samples treated with  $\text{H}_2\text{O}_2$  and nitric acid at temperatures of 50 °C (MS 3) and 95 °C (MS 4) reveal that the degree of template removal is increased at higher reaction temperatures (Figure 5-1). This temperature dependency is observed even though no further gas evolution occurs at the end of the treatment time for any of the three samples.

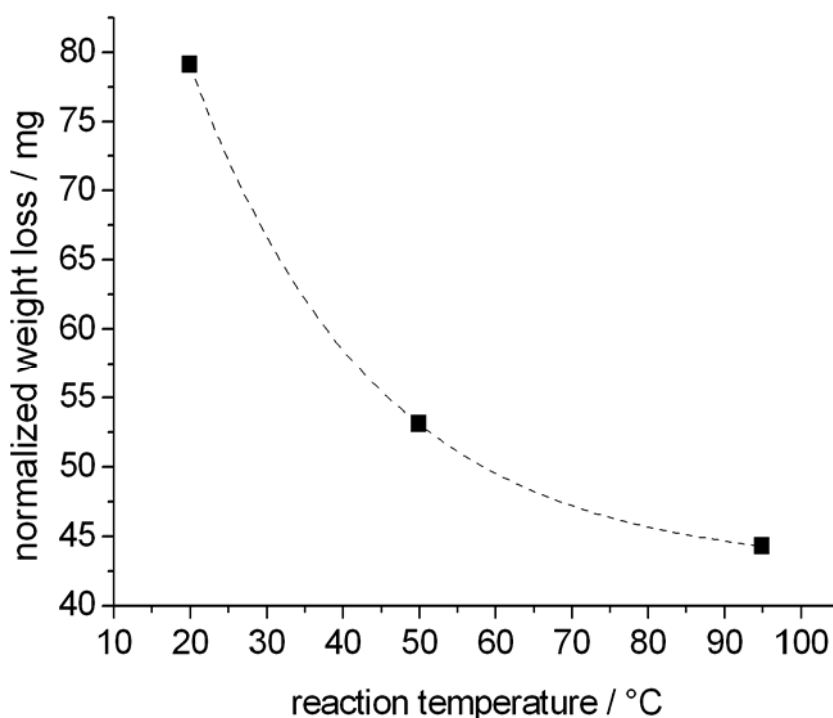


**Figure 5-1.** Temperature-dependence of the  $\text{H}_2\text{O}_2$ -mediated template removal in MCM-41.

Interestingly, similar results regarding the degree of CTA decomposition are obtained when the oxidation reaction is performed in pure aqueous  $\text{H}_2\text{O}_2$  (30 %) without acid addition. In order to optimize the oxidation procedure in this simplified system, several samples were treated at 95 °C for different amounts of time (MS 5 - 9). The decomposition of the template seems to be complete after three hours; after this period no significant change in weight loss is observed (Figure 5-2).

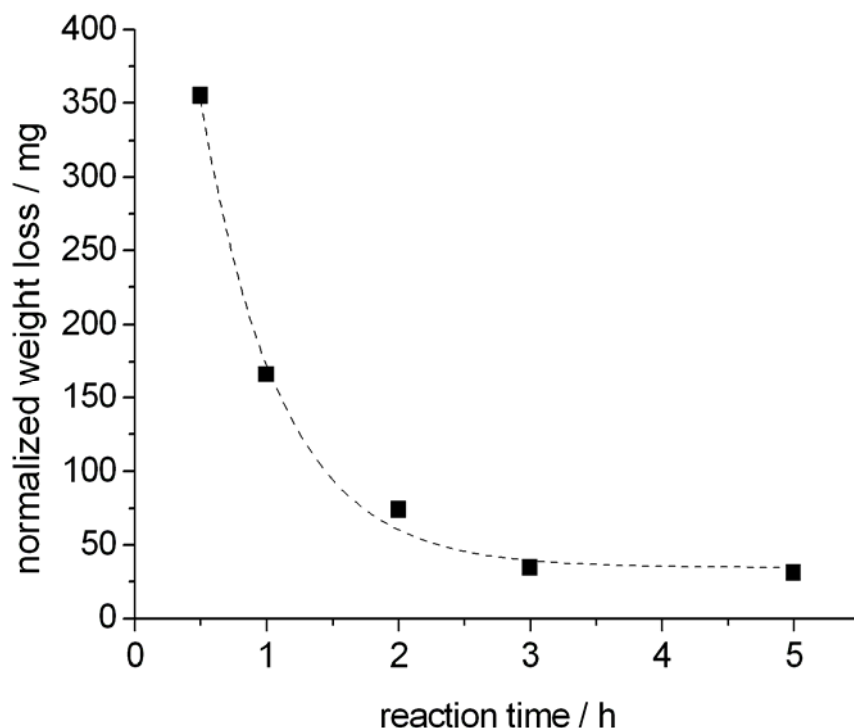


**Figure 5-2.** Time dependence of the  $\text{H}_2\text{O}_2$ -mediated template removal in MCM-41 at 95 °C.

**Comparison of  $\text{H}_2\text{O}_2$ -treated and extracted materials.** Refluxing in ethanolic media containing ammonium nitrate and hydrochloric acid was employed for the extraction of the CTA template from the pores of MCM-41. This approach is commonly used when calcination of the material is impractical in order to avoid effects such as particle agglomeration, structural damage, pore shrinking and loss of organic moieties.<sup>[14]</sup>

While most of the template seems to be removed from the extracted silica material based on thermogravimetric analysis, sample MS **8** still shows a relatively high weight loss compared to a typical  $\text{H}_2\text{O}_2$ -treated sample, indicating the presence of organic residues (Figure 5-3).



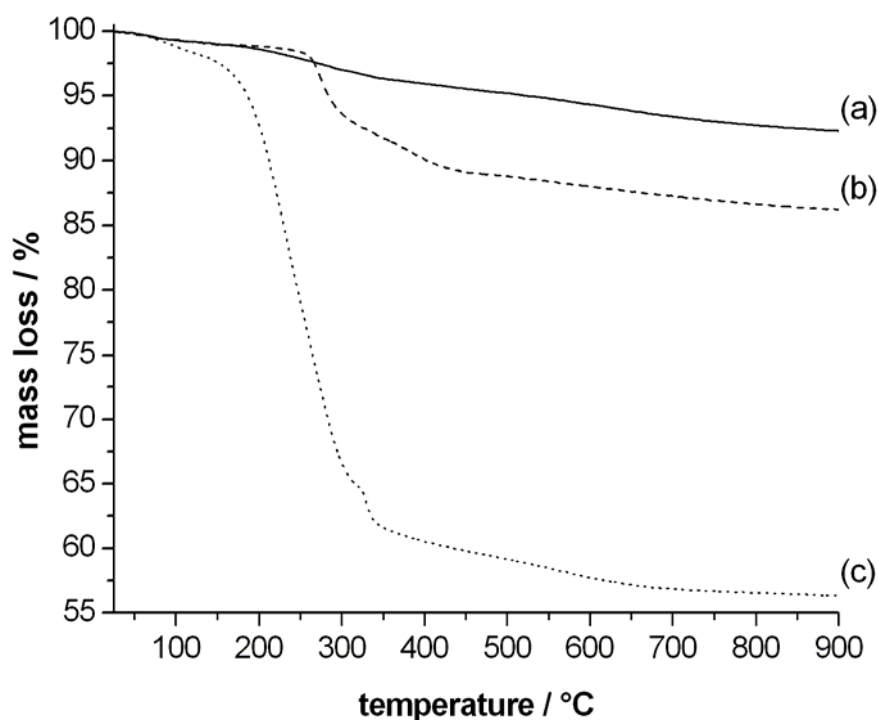


**Figure 5-3.** TGA data for sample MS **8** treated 3 h at 95 °C with H<sub>2</sub>O<sub>2</sub> (a), extracted MCM-41 (b), and as-synthesized MCM-41 (c).

However, this organic content is not associated with residual template molecules as reported for similar extraction methods.<sup>[13]</sup> Instead, <sup>13</sup>C-MAS-NMR spectra show that the signals corresponding to CTA in the parent material are not present following the extraction, and that two new signals emerge at 15 and 59 ppm, respectively. These peaks are attributed to ethoxy groups bound to the silica surface (Figure 5-4b). The H<sub>2</sub>O<sub>2</sub>-treated sample, on the other hand, shows no clearly assignable signals corresponding to either ethoxy moieties or CTA (Figure 5-4c). As shown by <sup>13</sup>C- and <sup>13</sup>C-DEPT liquid NMR spectra of the filtrated aqueous medium after treatment of sample MS **8**, the CTA template was decomposed into different oxidized fragments, in addition to CO<sub>2</sub>. Various signals typical for carboxylic acids as well as methyl and methylene groups adjacent to oxo- and alcohol groups were detected (see supporting information).

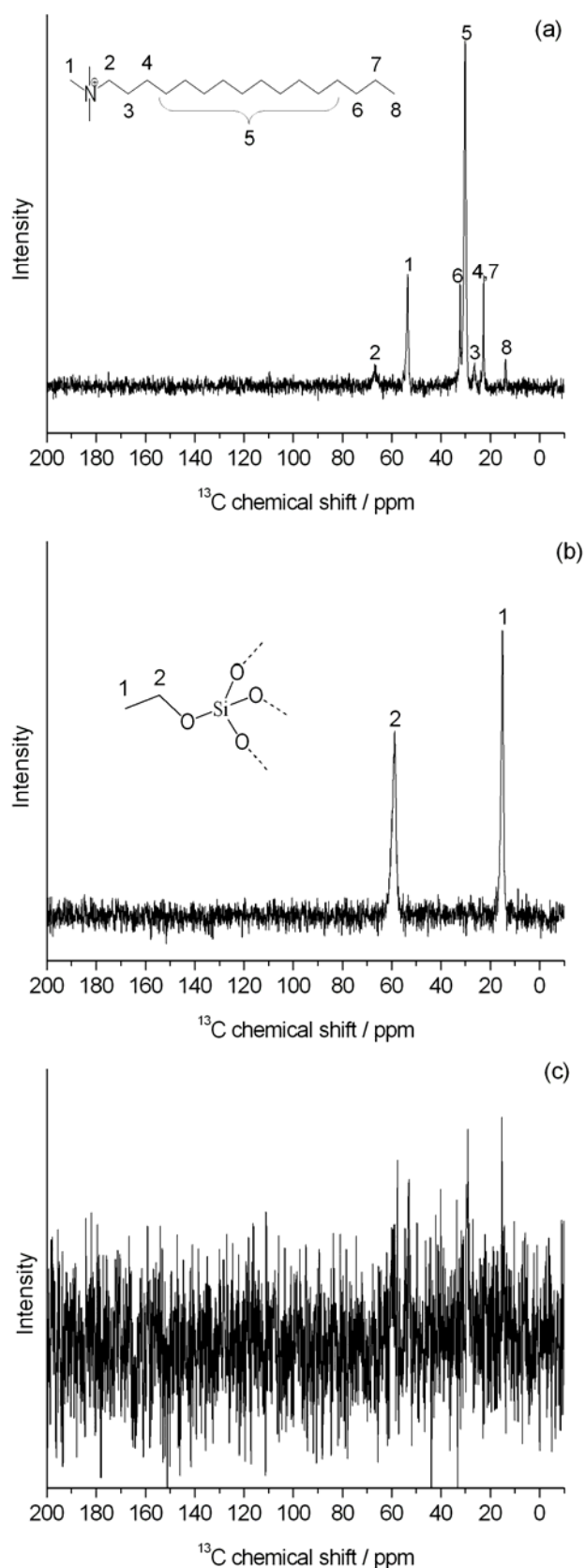


**Figure 5-4.**  $^{13}\text{C}$ -MAS-NMR spectra of as-synthesized MCM-41 (a), extracted MCM-41 (b) and sample MS 8 treated with  $\text{H}_2\text{O}_2$  for 3 h at 95 °C (c).

To the best of our knowledge, the considerable esterification of the silanol surface in MCM-41 materials after extraction in acidified ethanolic media mentioned above has not been reported before, even though numerous publications employ similar procedures for template removal. The underlying chemistry of the reaction between non-porous silica and various alcohols has already been described by Iler in 1953.<sup>[28, 29]</sup> The degree of esterification derived from TG data in combination with the BET surface area of extracted MCM-41 (90 mg  $-\text{CH}_2\text{CH}_3$  and  $813 \text{ m}^2$  per gram dried sample) was found to be 2.4 ethoxy groups per square nanometer. This amount is less than the values of 3.2 - 4.3 reported in the literature for silica treated with ethanol at 225 - 300 °C, which is attributed to the lower treatment temperature.<sup>[29]</sup> It is believed that such extensive esterification of the silica surface brings about drastic changes in the reactivity and affinity of the pore system towards various agents, and is thus of paramount importance for various applications including sorption and host-guest chemistry.

Raman spectroscopy was performed as a further means to characterize the organic species inside the mesoporous hosts (Figure 5-5).

The most prominent features in the spectra of as-synthesized and extracted MCM-41 are the bands corresponding to the C-H and C-C related vibrations of the alkyl chains present in both the CTA template and the ethoxy groups.<sup>[30]</sup> However, some differences in the spectra can be observed based on the nature of the alkyl groups. CTA gives rise to two strong bands centered at 2850 and 2890  $\text{cm}^{-1}$ , corresponding to the symmetric and asymmetric C-H stretch vibrations of the  $-\text{CH}_2-$  subunits in the hexadecyl chain, respectively. After extraction, a series of four distinct signals is observed. The bands emerging at 2882, 2902, 2937 and 2982  $\text{cm}^{-1}$  in the C-H stretch region correspond to the symmetric  $\text{CH}_2$ , symmetric  $\text{CH}_3$ , asymmetric  $\text{CH}_2$  and asymmetric  $\text{CH}_3$  stretch vibrations of the ethoxy group, respectively.<sup>[30]</sup> Other bands corresponding to  $\text{CH}_2$  groups such as the C-H deformation vibrations at 1302 and 1450  $\text{cm}^{-1}$  are also present in the parent material but significantly reduced after extraction. Furthermore,

the band located at  $3040\text{ cm}^{-1}$  in as-synthesized MCM-41 assigned to the  $\text{N-CH}_3$  stretch vibration of the quarternary amine head group in CTA is not present in the extracted material.

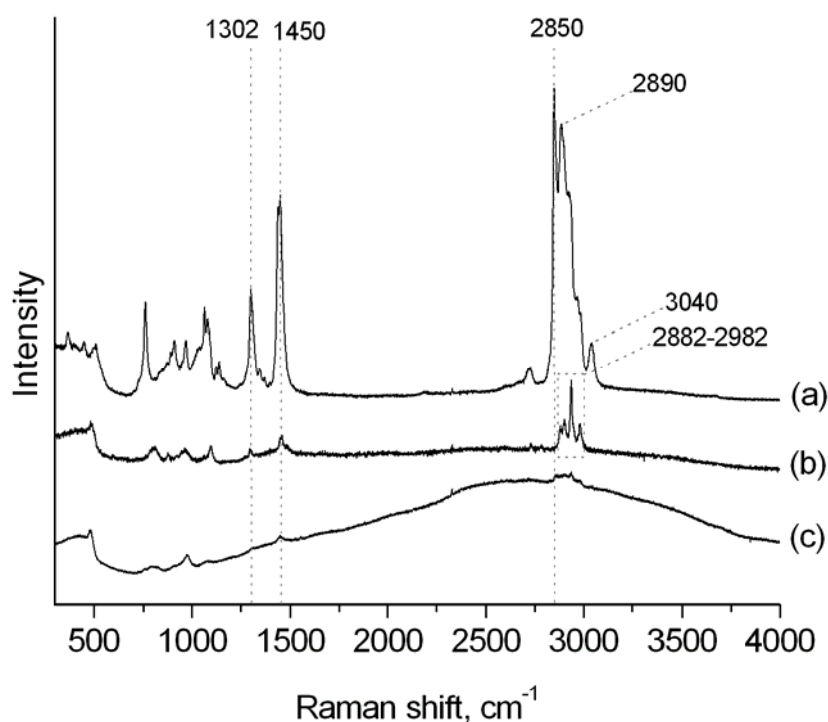


**Figure 5-5.** Raman spectra of as-synthesized MCM-41 (a), extracted MCM-41 (b) and sample MS 8 treated for 3 h at 95 °C with  $\text{H}_2\text{O}_2$  (c).

Surprisingly, the spectra of  $\text{H}_2\text{O}_2$ -treated samples still show traces of organic material (Figure 5-5c). Signals assigned to the vibrations of silica-bound ethoxy groups and CTA were located, although the intensities are very low due to the small amount of organic content. These signals were persistent even if the material was subjected to a second treatment in  $\text{H}_2\text{O}_2$  for 3 hours at 95 °C. Due to the low hydrothermal stability of silanol esters, treatment in aqueous media is supposed to cause fast hydrolysis of surface-bound ethoxy groups. It is therefore assumed that the organic moieties are in some way protected from the aqueous medium, i.e., by being incorporated inside the amorphous siliceous framework instead of being located on the surface. As the samples oxidized by  $\text{H}_2\text{O}_2$  were not previously treated in ethanolic solutions, the small amount of detected ethoxy groups possibly originates from incomplete

hydrolysis of the reactant tetraethylorthosilicate during synthesis of the mesoporous framework. Likewise, it is possible that minor amounts of the CTA template became trapped during the silica condensation.

**Oxidation behaviour of different functionalities.** Functionalized samples were prepared in order to investigate the influence of oxidation with  $\text{H}_2\text{O}_2$  on different organic modifications incorporated by co-condensation. The amount of 20 mol% of different triethoxysilanes was used to replace TEOS in the synthesis of MCM-41, and the template was subsequently removed by either extraction or  $\text{H}_2\text{O}_2$ -treatment. The presence of the organic moieties in the extracted materials and their decomposition after the oxidative treatment were followed by Raman spectroscopy (Figures 5-6 to 5-9, characteristic strong bands for each functional group are marked by asterisks). It should be noted that contrary to unfunctionalized materials, a short refluxing step in  $\text{HCl}/\text{EtOH}$  was necessary to remove the majority of the oxidized organic fragments generated by  $\text{H}_2\text{O}_2$ -treatment in certain co-condensed samples.

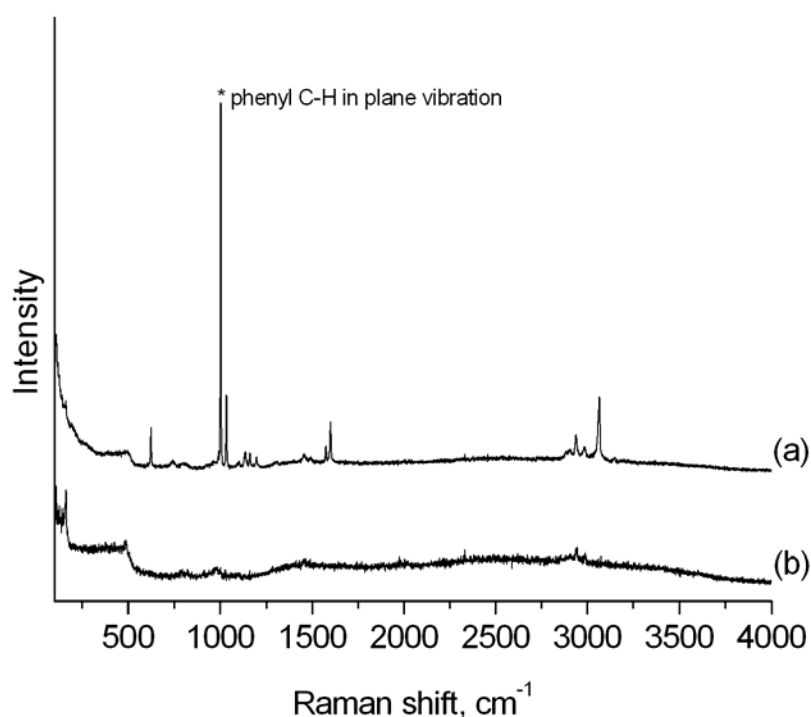


**Figure 5-6.** Raman spectra of phenyl-functionalized MCM-41 after extraction (a) and  $\text{H}_2\text{O}_2$ -treatment (b).

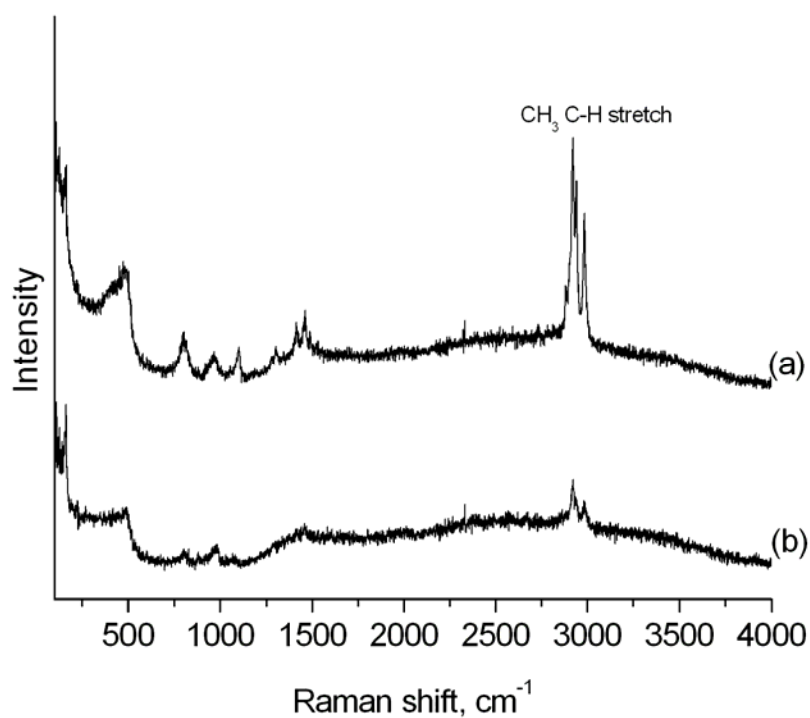


**Figure 5-7.** Raman spectra of methyl-functionalized MCM-41 after extraction (a) and H<sub>2</sub>O<sub>2</sub>-treatment (b).

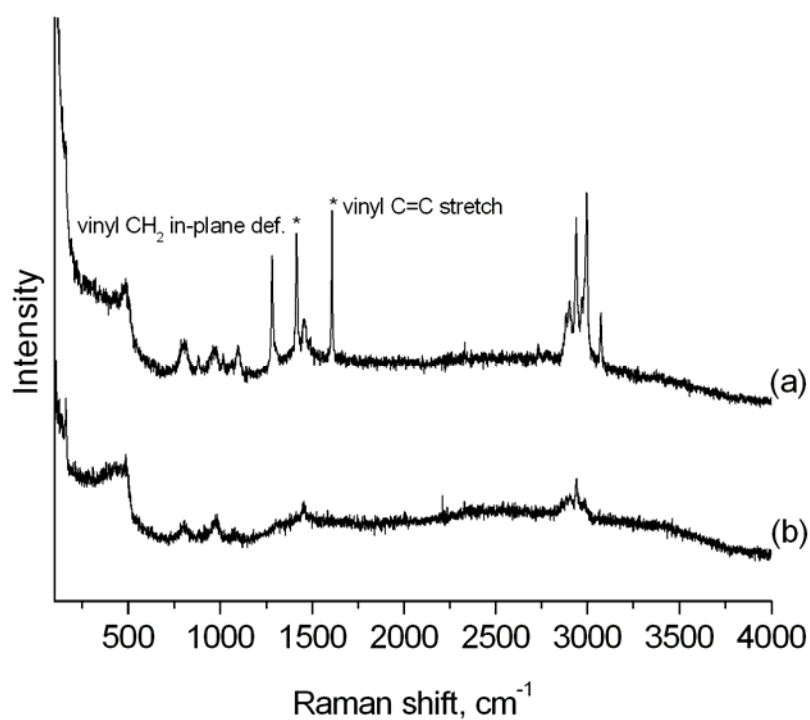


**Figure 5-8.** Raman spectra of vinyl-functionalized MCM-41 after extraction (a) and H<sub>2</sub>O<sub>2</sub>-treatment (b).

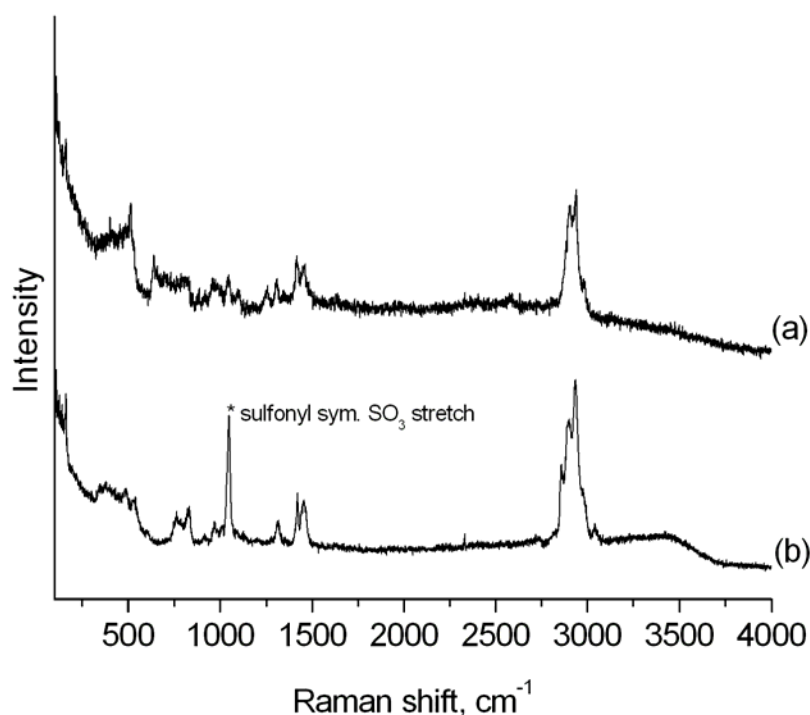


**Figure 5-9.** Raman spectra of mercaptopropyl-functionalized MCM-41 after extraction (a) and H<sub>2</sub>O<sub>2</sub>-treatment (b).

TGA was performed in order to investigate the amounts of remaining organic material after both template removal methods. Due to the different temperatures needed for complete combustion of the various organic moieties (for example, phenyl groups are decomposed at 400-600 °C), the weight loss in all functionalized samples is given for the temperature range between 110-900 °C. As shown in Figure 5-10, aside from mercaptopropyl-modified material all H<sub>2</sub>O<sub>2</sub>-treated samples display similar weight losses after oxidation regardless of functionality, indicating a complete decomposition of the organic moieties. Furthermore, the pore diameters determined by nitrogen sorption are of the same size as in unfunctionalized MCM-41 and similar for all oxidized samples.

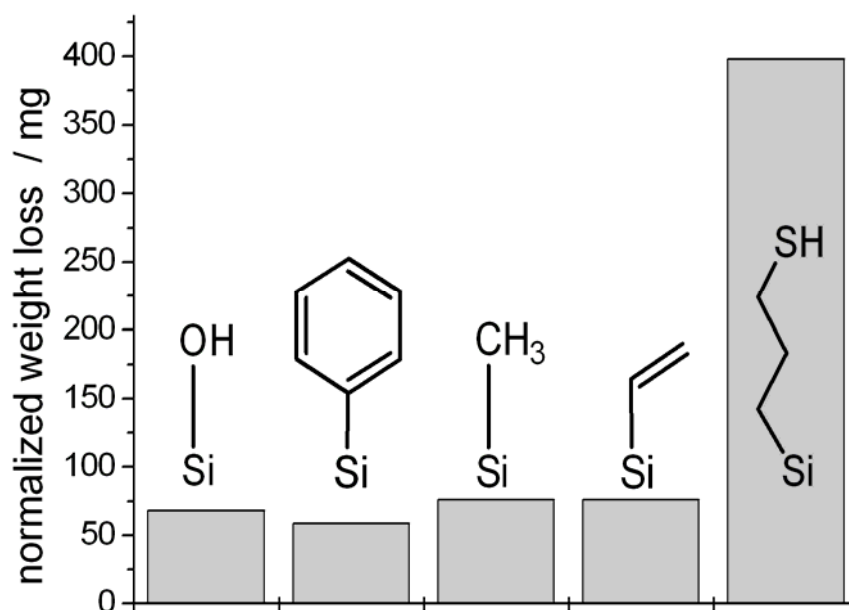


**Figure 5-10.** Normalized weight loss in the range of 110-900 °C for samples functionalized by co-condensation and subsequently treated with H<sub>2</sub>O<sub>2</sub>.

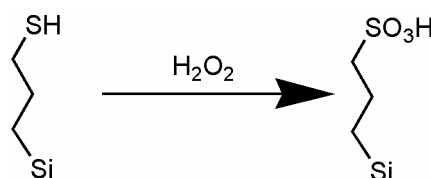
On the other hand, the analogous extracted materials with intact pendent organic groups show different pore diameters and weight losses, depending on the size and type of the functional moieties (Table 5-3). The only exception is the mercaptopropyl functionality, which was oxidized to the bulky sulfonic acid group by H<sub>2</sub>O<sub>2</sub> and thus showed a decreased pore size and increased TGA weight loss after the oxidative treatment (Scheme 5-1).<sup>[31]</sup> Conversion of the thiol moiety to sulfonic acid was also confirmed by Raman spectroscopy (Figure 5-9).



**Table 5-3.** Weight losses and pore diameters for functionalized samples after extraction and after H<sub>2</sub>O<sub>2</sub>-treatment.

Functionality	Template removal	Normalized weight loss	NLDFT pore
	method	[mg / g(SiO <sub>2</sub> )] <sup>a</sup>	diameter [nm]
phenyl	extraction	281	3.18
methyl	extraction	129	3.65
vinyl	extraction	189	3.41
mercaptopropyl	extraction	300	3.33
phenyl	H <sub>2</sub> O <sub>2</sub>	59	3.53
methyl	H <sub>2</sub> O <sub>2</sub>	76	3.53
vinyl	H <sub>2</sub> O <sub>2</sub>	76	3.53
mercaptopropyl	H <sub>2</sub> O <sub>2</sub>	398	3.18

<sup>a</sup> weight loss between 110-900 °C, given relative to SiO<sub>2</sub> residue at 900 °C

**Scheme 5-1.** Oxidation of mercaptopropyl to sulfonic acid by H<sub>2</sub>O<sub>2</sub>.

**Preparation of oxidized CMS with controlled morphology.** After verification of the successful removal of most co-condensed functional groups by H<sub>2</sub>O<sub>2</sub>, the optimized treatment conditions for the CTA decomposition were applied to unfunctionalized and phenyl-functionalized CMS nanoparticles. Phenyl was chosen as exemplary functionality as it showed strong effects in co-condensation synthesis by reducing particle size, increasing monodispersity and resulting in a uniform spherical morphology of the particles in prior

studies.<sup>[32]</sup> However, depending on the desired application, the functionalization with phenyl moieties can also bring disadvantages. The pore size is reduced, and the affinity of the surface towards guest molecules is drastically altered as shown by toluene sorption in phenyl-functionalized CMS thin films on a quartz crystal microbalance.<sup>[33]</sup>

The H<sub>2</sub>O<sub>2</sub>-mediated template removal therefore not only constitutes a quick and effective method to generate pore accessibility without causing particle agglomeration. In combination with selected co-condensation reactions, this method also yields controlled particle morphologies in combination with unfunctionalized silica surfaces which can be further functionalized depending on the desired properties.

CMS and phenyl-functionalized CMS (Ph-CMS), prepared by co-condensation with 20 mol% phenyltriethoxysilane, were synthesized and the template was removed both by extraction and oxidation with H<sub>2</sub>O<sub>2</sub>.

Dynamic light scattering (DLS) measurements were performed in order to investigate the colloidal stability of the nanoparticle suspensions in ethanol (Figure 5-11). The particle size distribution curve of extracted CMS centered at 140 nm is narrowed and shifted to a smaller hydrodynamic mean diameter of 80 nm in the co-condensed sample, which can be attributed to the smaller and more homogeneous particles in Ph-CMS. Treatment with H<sub>2</sub>O<sub>2</sub> causes the appearance of larger agglomerations in the suspensions, resulting in mean hydrodynamic diameters of 500 and 200 nm for CMS and Ph-CMS, respectively. These agglomerations seem to be caused by the interaction of the more polar silanol particle surfaces obtained after oxidation in contrast to the esterified surfaces of extracted materials. Accordingly, agglomeration of the particles can be reversed by subjecting the H<sub>2</sub>O<sub>2</sub>-treated suspensions to the treatment in acidified ethanol used for extraction, thus reducing the interaction between the particles by esterification of the silanol surface.

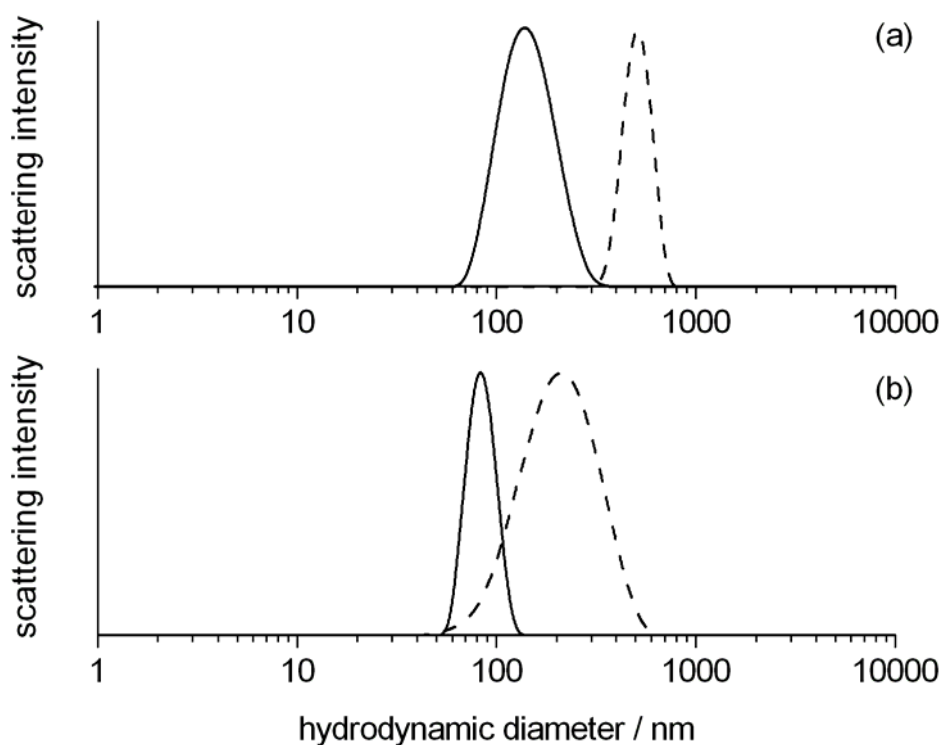


**Figure 5-11.** DLS curves for CMS (a) and Ph-CMS (b) after extraction (full lines) and treatment with H<sub>2</sub>O<sub>2</sub> (dashed lines), respectively.

Transmission electron microscopy (TEM) was performed as a complementary approach for characterization of the H<sub>2</sub>O<sub>2</sub>-treated nanoparticles (Figure 5-12). CMS particles display irregular morphologies and inhomogeneous particle size distributions. In contrast, the co-condensed Ph-CMS particles are smaller and exhibit monomodal particle diameters of about 40 nm with spherical morphologies. No visible changes to the corresponding extracted materials are observed in TEM.

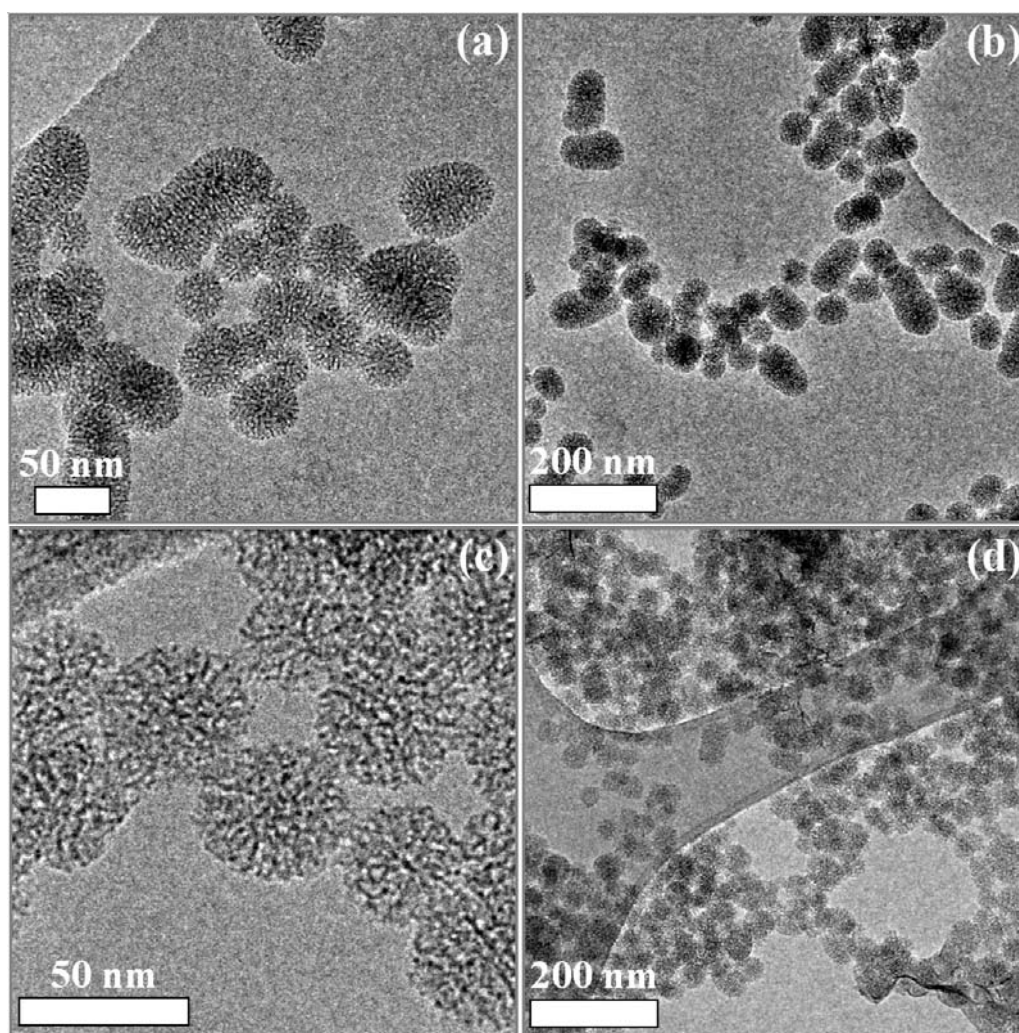


**Figure 5-12.** TEM micrographs of H<sub>2</sub>O<sub>2</sub>-treated CMS (a, b) and Ph-CMS (c, d).

The organic content of extracted and oxidized Ph-CMS was investigated by TGA (Figure 5-13). Extracted Ph-CMS displays a high weight loss coupled with an exothermic DSC signal at about 600 °C corresponding to the combustion of the phenyl moieties. In contrast, Ph-CMS treated with H<sub>2</sub>O<sub>2</sub> displays no significant weight loss or DSC peaks, indicating the removal of both the template and the phenyl functionalities from the pore channels. Correspondingly, nitrogen sorption reveals that while the pore diameter in extracted Ph-CMS is decreased, the pore diameter in oxidized Ph-CMS is similar to unfunctionalized CMS (Table 5-4).

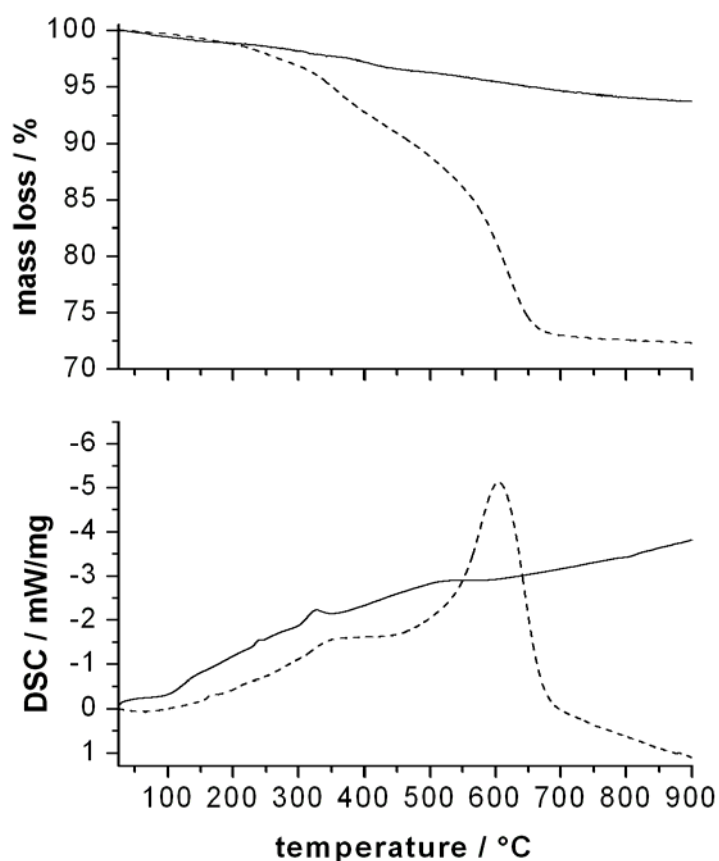


**Figure 5-13.** TGA/DSC data of Ph-CMS after H<sub>2</sub>O<sub>2</sub>-treatment (full lines) and after extraction (dashed lines).

**Table 5-4.** Weight losses and pore diameters for CMS and Ph-CMS after extraction and after H<sub>2</sub>O<sub>2</sub>-treatment

Sample type	Template	Normalized weight loss	NLDFT pore
	removal method	[mg / g(SiO <sub>2</sub> )] <sup>a</sup>	diameter [nm]
CMS	Extraction	191	3.77
CMS	H <sub>2</sub> O <sub>2</sub>	90	3.77
Ph-CMS	Extraction	377	3.53
Ph-CMS	H <sub>2</sub> O <sub>2</sub>	95	3.77

<sup>a</sup> weight loss between 110-900 °C, given relative to SiO<sub>2</sub> residue at 900 °C

Removal of the CTA template and phenyl moieties was also examined by Raman spectroscopy (Figure 5-14). Extracted CMS displays the signals corresponding to surface-bound ethoxy groups as discussed above for MCM-41 materials.  $\text{H}_2\text{O}_2$ -treated CMS that was further treated by short refluxing in acidified ethanol in order to improve colloidal stability shows similar signals, demonstrating the esterification of the silica surface. In the case of extracted Ph-CMS, intense signals corresponding to the in-plane ring deformation vibration ( $624\text{ cm}^{-1}$ ), C-H in-plane vibrations ( $1001$  and  $1033\text{ cm}^{-1}$ ), C=C stretching vibration ( $1601\text{ cm}^{-1}$ ), and C-H stretch vibration ( $3065\text{ cm}^{-1}$ ) of the silicon-bound phenyl group are present.<sup>[30]</sup> In  $\text{H}_2\text{O}_2$ -treated Ph-CMS these signals cannot be detected, demonstrating the removal of the phenyl moieties by oxidation.

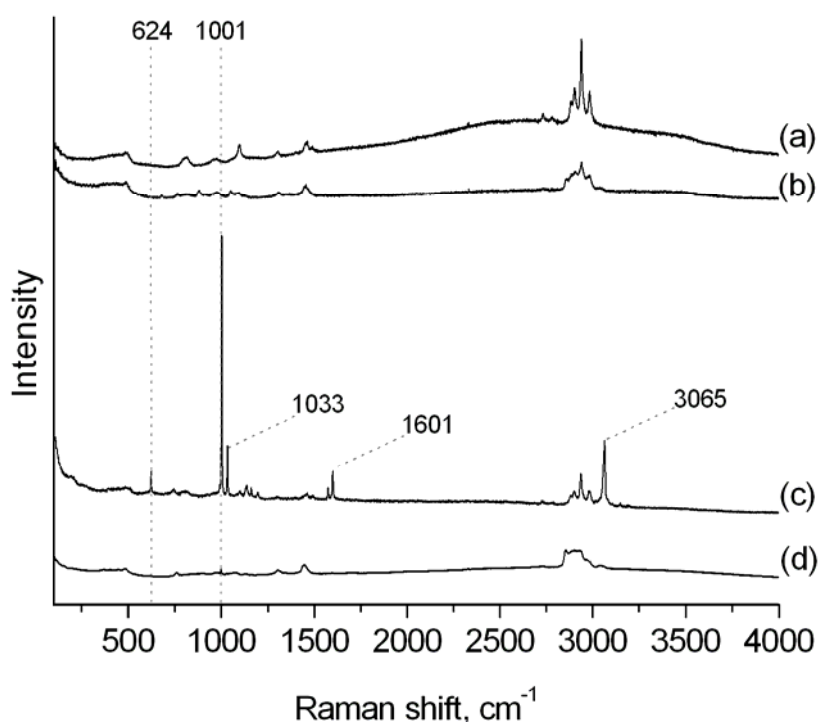


**Figure 5-14.** Raman spectra of extracted CMS (a),  $\text{H}_2\text{O}_2$ -treated CMS refluxed in acidified ethanol (b), extracted Ph-CMS (c), and  $\text{H}_2\text{O}_2$ -treated Ph-CMS (d).

## 5.5 Conclusions

Reaction conditions for the  $\text{H}_2\text{O}_2$ -mediated decomposition of CTA template inside the pores of mesoporous silica were determined. The resulting products are compared to materials obtained by extraction in acid-containing ethanolic media. It is found that extraction produces a significant amount of ethoxy groups by esterification of the silanol surface.

The chosen conditions for  $\text{H}_2\text{O}_2$  treatment are also suitable for the complete removal of various functionalities inserted by co-condensation. The concept of  $\text{H}_2\text{O}_2$ -mediated template decomposition is then transferred to nanosized particles, allowing the removal of organic species from CMS suspensions without producing irreversible agglomeration by drying or calcination. The oxidation process is quick and efficient, allowing template removal in a one-pot reaction within 3 hours, as compared to typical multi-step extraction procedures.

The  $\text{H}_2\text{O}_2$ -treatment allows to easily control particle size and morphology of unfunctionalized mesoporous silica nanoparticles by addition of co-condensation reagents in the synthesis step. The resulting particles with defined sizes and shapes can then be further functionalized by grafting of the free silanol surfaces in order to influence surface properties depending on the requirements of the desired applications.

## 5.6 References

- [1] J. S. Beck, J. C. Vartuli, W. J. Roth, M. E. Leonowicz, C. T. Kresge, K. D. Schmitt, C. T. W. Chu, D. H. Olson, E. W. Sheppard, et al., *Journal of the American Chemical Society* **1992**, *114*, 10834.
- [2] D. Zhao, J. Feng, Q. Huo, N. Melosh, G. H. Frederickson, B. F. Chmelka, G. D. Stucky, *Science* **1998**, *279*, 548.
- [3] S. A. Bagshaw, E. Prouzet, T. J. Pinnavaia, *Science* **1995**, *269*, 1242.
- [4] S. Che, E. Garcia-Bennett Alfonso, T. Yokoi, K. Sakamoto, H. Kunieda, O. Terasaki, T. Tatsumi, *Nature materials* **2003**, *2*, 801.
- [5] K. Möller, J. Kobler, T. Bein, *Advanced Functional Materials* **2007**, *17*, 605.
- [6] G. Trewyn Brian, I. Slowing Igor, S. Giri, H.-T. Chen, S. Y. Lin Victor, *Accounts of chemical research* **2007**, *40*, 846.
- [7] Y. Han, J. Y. Ying, *Angewandte Chemie, International Edition* **2005**, *44*, 288.
- [8] Y.-S. Lin, S.-H. Wu, Y. Hung, Y.-H. Chou, C. Chang, M.-L. Lin, C.-P. Tsai, C.-Y. Mou, *Chemistry of Materials* **2006**, *18*, 5170.
- [9] H. Uchiyama, K. Suzuki, Y. Oaki, H. Imai, *Materials Science & Engineering, B: Solid-State Materials for Advanced Technology* **2005**, *B123*, 248.
- [10] F. Torney, B. G. Trewyn, V. S. Y. Lin, K. Wang, *Nature Nanotechnology* **2007**, *2*, 295.
- [11] S. Mintova, T. Bein, *Advanced Materials* **2001**, *13*, 1880.
- [12] H. Wang, L. Huang, Z. Wang, A. Mitra, Y. Yan, *Chemical Communications* **2001**, 1364.
- [13] S. Hitz, R. Prins, *Journal of Catalysis* **1997**, *168*, 194.
- [14] N. Lang, A. Tuel, *Chemistry of Materials* **2004**, *16*, 1961.
- [15] M. T. J. Keene, R. Denoyel, P. L. Llewellyn, *Chemical Communications* **1998**, 2203.
- [16] G. Buchel, R. Denoyel, P. L. Llewellyn, J. Rouquerol, *Journal of Materials Chemistry* **2001**, *11*, 589.
- [17] A.-H. Lu, W.-C. Li, W. Schmidt, F. Schueth, *Journal of Materials Chemistry* **2006**, *16*, 3396.
- [18] Y. Xia, R. Mokaya, *Journal of Physical Chemistry B* **2006**, *110*, 9122.
- [19] L. Xiao, J. Li, H. Jin, R. Xu, *Microporous and Mesoporous Materials* **2006**, *96*, 413.
- [20] L. M. Yang, Y. J. Wang, G. S. Luo, Y. Y. Dai, *Microporous and Mesoporous Materials* **2005**, *81*, 107.
- [21] B. Tian, X. Liu, C. Yu, F. Gao, Q. Luo, S. Xie, B. Tu, D. Zhao, *Chemical Communications* **2002**, 1186.
- [22] I. Melian-Cabrera, F. Kapteijn, J. A. Moulijn, *Chemical Communications* **2005**, 2744.
- [23] K. Möller, J. Kobler, T. Bein, *Journal of Materials Chemistry* **2007**, *17*, 624.
- [24] M. Grun, K. K. Unger, A. Matsumoto, K. Tsutsumi, *Microporous and Mesoporous Materials* **1999**, *27*, 207.
- [25] K. Möller, J. Kobler, T. Bein, *Advanced Functional Materials* **2007**, *17*, 605.
- [26] F. Kleitz, W. Schmidt, F. Schuth, *Microporous and Mesoporous Materials* **2003**, *65*, 1.
- [27] H. J. H. Fenton, *Journal of the Chemical Society, Transactions* **1894**, *65*, 899.
- [28] R. K. Iler, (E. I. du Pont de Nemours & Co.). US 2657149, **1953**.
- [29] C. C. Ballard, E. C. Broge, R. K. Iler, D. S. St. John, J. R. McWhorter, *Journal of Physical Chemistry* **1961**, *65*, 20.
- [30] G. Socrates, *Infrared and Raman Characteristic Group Frequencies*, 3rd Edition ed., John Wiley & Sons, Chichester, **2005**.
- [31] J. A. Melero, R. Van Grieken, G. Morales, *Chemical Reviews* **2006**, *106*, 3790.
- [32] J. Kobler, K. Möller, T. Bein, *ACS Nano* **2008**, *2*, 791.
- [33] A. Darga, J. Kecht, T. Bein, *Langmuir* **2007**, *23*, 12915-12922.



## 6 Functionalization of colloidal mesoporous silica by metalorganic reagents\*

### 6.1 Introduction

Functionalization of mesoporous silica with organic moieties offers a pathway to control the surface affinity and host-guest chemistry inside the porous network. In this way, tailor-made materials can be synthesized based on the requirements of potential applications in various areas including drug delivery, sensor technology, catalysis, synthesis of nanoparticles and chemisorption.<sup>[1-5]</sup> Conventional approaches for the introduction of functional moieties include the methods of co-condensation, wherein trialkoxy-organosilanes are included in the synthesis mixture, and post-synthesis grafting by attachment of trichloro- or trialkoxy-organosilanes to the silanol surface.<sup>[5]</sup> Some recent grafting methods also employ silazane agents.<sup>[6]</sup>

The use of metalorganic reagents for the functionalization of mesoporous silica frameworks was investigated by Yamamoto and Tatsumi in 2000.<sup>[7, 8]</sup> A simplified and efficient one-pot reaction for direct conversion of MCM-41 with Grignard and organolithium reagents was independently developed by J. M. Kim et al. and our group.<sup>[9, 10]</sup>

In these versatile metalorganic reactions the linkage to the silica walls is achieved via Si-C bonds by direct attachment of the nucleophile to a framework silicon atom. The use of metalorganic reagents offers several advantages compared to conventional functionalization methods, e.g., pore blocking by condensed oligomeric silane species can be avoided. Furthermore, the limited spectrum of functionalities found in commercially available organosilanes is drastically increased due to the access to numerous Grignard and lithiated reagents in organic chemistry. A variety of metalorganic reagents can either be directly purchased or easily generated from the respective halogenated compounds, allowing a higher control and variety for the surface decoration in mesoporous silica materials. Recent examples from work in our group include the incorporation of nitrogen functionalities and different

\* J. Kecht, T. Bein, manuscript in preparation.

multibonded systems such as alkyne derivatives into the pores of MCM-41 by metalorganic modification.<sup>[10,11]</sup>

In the case of colloidal mesoporous silica (CMS) nanoparticles, the use of metalorganic reagents would permit the introduction of elaborate organic moieties in order to generate sophisticated nanosized systems. Colloidal suspensions of porous nanoparticles are particularly interesting for applications in sensing, controlled release and drug delivery.<sup>[3, 4, 12, 13]</sup>

The present work demonstrates the application of metalorganic reagents for the functionalization of CMS nanoparticles. However, as will be shown, the reaction conditions suitable for the modification of micrometer-sized MCM-41 particles cannot be simply transferred to the nanosized systems. Due to the small size and corresponding high surface energy, sintering of the nanoparticles is observed at the high temperatures commonly used for the calcination and dehydration of the mesoporous hosts. Furthermore, complete removal of solvents is not feasible while retaining the colloidal nature of the suspensions, due to the irreversible agglomeration caused by attractive forces in the drying material. At the same time, removal of remaining water from the silica mesopores is required to avoid hydrolysis of the metalorganic reagents. In the following, different strategies are compared in order to generate anhydrous synthesis conditions without causing irreversible agglomeration in the CMS suspensions, and to investigate their subsequent reactions with lithiated model compounds. The methods developed here give insights into the complexity of transferring well-known preparative methods from bulk materials to nanosized systems, and demonstrate suitable pathways for the potential preparation of non-agglomerated anhydrous systems with other colloidal porous media, i.e., nanosized zeolites.

## 6.2 Experimental Section

**Reagents.** Tetraethyl orthosilicate (TEOS, Fluka, >98%), ammonia (Aldrich, 25% in H<sub>2</sub>O), cetyltrimethylammonium bromide (CTAB, Aldrich, 95%), cetyltrimethylammonium chloride (CTAC, Fluka, 25% in H<sub>2</sub>O), triethanolamine (TEA, Aldrich, 98%), molecular sieve (Merck, 0.5 nm, ~2 mm beads), toluene (Fluka, 99.7%, over molecular sieve), triethyl orthoformate (Aldrich, 98%), phenyllithium (Fluka, 1.9 M in butyl ether), and *tert*-butyllithium (Fluka, 1.7 M in pentane) were used as received without further purification. Doubly distilled water from a Millipore system (Milli-Q Academic A10) was used for all synthesis and purification steps.

**Preparation of micrometer-sized MCM-41 mesoporous silica (MS).** MCM-41 material was prepared according to a published procedure.<sup>[14]</sup> To a stirred solution of CTAB (2.39 g, 6.56 mmol), water (125 g, 6.94 mol), ethanol (12.5 g, 271.15 mmol), and aqueous ammonia (25 %wt, 9.18 g, 134.93 mmol) in a 300 mL polypropylene reactor, the amount of 10.03 g TEOS (48.19 mmol) was added. The resulting mixture has a molar composition of 1 TEOS : 0.14 CTAB : 144 H<sub>2</sub>O : 5.63 ethanol : 2.8 NH<sub>3</sub>. After stirring for 2 hours at room temperature, the reaction mixture was filtered off and washed with 50 mL water. The resulting white powder was dried at 60°C for 12 h.

**Preparation of colloidal mesoporous silica (CMS) nanoparticles.** Mesoporous silica nanoparticles were prepared according to reference <sup>[15]</sup> from reaction mixtures with a molar composition of 1 TEOS: 0.20 CTAC: 10.37 TEA: 130.15 H<sub>2</sub>O. The combined TEOS (1.92 g, 9.22 mmol) and TEA (14.3 g, 95.6 mmol) were heated for 20 minutes at 90 °C without stirring in a 100 mL polypropylene reactor. A solution of CTAC (25 % in water, 2.41 mL, 1.83 mmol) and water (21.7 g, 1.21 mol) preheated to 60 °C was added, and the resulting mixture was stirred at room temperature for 12 hours. After addition of 50 mL of ethanol, the mesoporous silica nanoparticles were separated by centrifugation and redispersed in ethanol.

**Extraction of MCM-41 and CMS.** Extraction of the organic template from the MCM-41 materials was performed by heating the samples (1.0 g) twice under reflux at 90°C for 30

minutes in a solution containing 2 g ammonium nitrate in 100 mL ethanol followed by 30 minutes under reflux in a solution of 4 g concentrated hydrochloric acid in 100 mL ethanol. The MCM-41 material was separated by filtration and the CMS nanoparticles were isolated by centrifugation. Both materials were washed with ethanol after each extraction step. MCM-41 and CMS materials were obtained as white solid powders and as clear ethanolic suspensions, respectively.

#### **Pretreatment of MCM-41 and CMS for water removal.**

- **Conversion of dried MCM-41 (A1).** The amount of 250 mg calcined or extracted MCM-41 was dried at 150 °C for 4 h under vacuum. After cooling, 5 mL anhydrous THF were added under nitrogen atmosphere.
- **Direct conversion of CMS (A2).** The amount of 250 mg CMS in the form of an ethanolic suspension was centrifuged and washed with dry toluene three times.
- **Drying in a Dean-Stark apparatus (A3).** The amount of 250 mg CMS was suspended in 8 mL dry toluene. A Dean-Stark apparatus (water separator) was used to collect the released water under heating at reflux conditions for 30 minutes.
- **Direct addition of desiccants (A4).** The amount of 250 mg CMS suspended in toluene was mixed with 3 g molecular sieve beads. After storing for 12 hours at room temperature, the beads were separated by sieving and the resulting suspension was filtered off under nitrogen atmosphere.
- **Hydrolysis of orthoformate (A5).** The amount of 250 mg CMS suspended in 8 mL dry toluene was mixed with 0.5 mL triethyl orthoformate. The reaction mixture was stirred at 90 °C for 2 hours. The ethanol resulting from the hydrolysis reaction was removed by distillation.
- **Vapor absorption with desiccants (A6).** The amount of 250 mg CMS suspended in 8 mL dry toluene was heated to 90 °C for 3 hours. Water was removed from the gas phase by a Soxhlet extractor filled with molecular sieve.

**Metalorganic conversion with lithiated reagents.** The suspensions obtained after the various water-removal treatments described above were cooled to 25 °C. All reactions were performed under nitrogen atmosphere. The amount of 0.60 mL (1.14 mmol) of a 1.9 M solution of phenyllithium in *n*-butylether was added dropwise. The reaction mixture was stirred at 25 °C for 3 hours and subsequently quenched with 40 mL of an ethanolic ammonium nitrate solution (20 g / L) or hydrochloric acid in ethanol. After stirring at room temperature for 30 minutes, the products were isolated and thoroughly washed with water and ethanol (Table 6-1).

**Table 6-1.** Summary of all samples and their respective reaction conditions.

Sample name	Material	Drying method	Reagent
MS-1-cal	MCM-41 <sup>[a]</sup>	A1	PhLi
MS-1-ex	MCM-41	A1	PhLi
CMS-2	CMS	A2	PhLi
CMS-3	CMS	A3	PhLi
CMS-4	CMS	A4	PhLi
CMS-5	CMS	A5	PhLi
CMS-6	CMS	A6	PhLi

<sup>[a]</sup> calcined material, in all other samples the template was removed by extraction

### 6.3 Characterization

Dynamic light scattering (DLS) measurements were performed on a Malvern Zetasizer-Nano instrument equipped with a 4 mW He-Ne laser (632.8 nm) and avalanche photodiode detector. Thermogravimetric analyses (TGA) of the bulk samples were performed on a Netzsch STA

440 °C TG/DSC (heating rate of 10 K/min in a stream of synthetic air of about 25 mL/min). Raman spectra were recorded on a Jobin Yvon Horiba HR800 UV Raman microscope using a HeNe laser emitting at 632.8 nm. Nitrogen sorption measurements were performed on a Quantachrome Instruments NOVA 4000e at 77 K. Samples were degassed for 12 h at 60 °C. Note: it was found that the extracted samples showed a strong effect of outgassing conditions on the remaining pore volume and surface area, presumably due to continued consolidation of the wall structure. Therefore these conditions have to be carefully controlled. For calculations of pore sizes the NLDFT equilibrium model of N<sub>2</sub> on silica was used. Solid state <sup>13</sup>C-MAS-NMR measurements were performed on a Bruker DSX Avance 500 FT (contact time 4 ms, spinning rate 6 kHz, pulse length 2.8 μs, recycle delay 8 s, number of scans 512). Transmission electron microscope (TEM) images of CMS materials were taken with a JEOL JEM 2011 microscope operating at 200 kV, after drying the diluted colloidal suspensions on a carbon-coated copper grid.

## 6.4 Results and Discussion

Metalorganic functionalization of mesoporous silica is a powerful means to generate novel organic-inorganic hybrid materials, as demonstrated in previous work.<sup>[10, 11]</sup> The procedures developed thus far were optimized for powders consisting of micrometer-sized particles dried at 150 °C, by performing the metalorganic reaction in typical reaction media such as tetrahydrofurane. However, new challenges for advanced applications of such materials, i.e. in the area of drug delivery, require nanoscale particles in the form of stable colloidal suspensions. The specific properties of nanomaterials, such as increased sensitivity to the reaction conditions, may in turn demand more sophisticated preparative techniques and render classical procedures inefficient.

Such a behavior was also observed in this study, as the different features of colloidal mesoporous silica (CMS) in comparison to bulk MCM-41 required the development of a set of alternative techniques for the removal of residual water from the porous network without causing irreversible agglomeration of the nanoparticles.

**Metalorganic conversion of extracted materials.** One of the first issues to be resolved is the aspect of template extraction. While bulk MCM-41 can be simply calcined, this procedure is not transferable to CMS without drying, followed by inevitable agglomeration of the nanoparticles due to strong capillary forces. Extraction in ethanolic media has been shown to be an effective alternative in this case.<sup>[16, 17]</sup> However, extraction leads to a higher density of silanol groups on the silica surface as well as partial esterification by the reaction between silanol groups and ethanol. This altered surface functionality is a potential disruptive factor for the metalorganic conversion, i.e., the higher silanol concentration could lead to protonation of the lithiated carbanions.

Therefore the metalorganic conversion reaction of calcined and extracted MCM-41 samples (MS-1-cal and MS-1-ex) was compared after drying at 150 °C. Phenyllithium was chosen as a model compound due to the easy distinction of signals corresponding to silicon-bound aromatic groups by Raman, NMR and TGA in the presence of aliphatic moieties.

As can be seen in the Raman spectra, phenyl groups were incorporated in both calcined and extracted materials (Figure 6-1). After metalorganic conversion, several new signals corresponding to the in-plane ring deformation vibration ( $623\text{ cm}^{-1}$ ), C-H in-plane vibrations ( $1002$  and  $1034\text{ cm}^{-1}$ ), C=C stretching vibration ( $1600\text{ cm}^{-1}$ ), and C-H stretch vibration ( $3066\text{ cm}^{-1}$ ) of the silicon-bound phenyl groups are present.

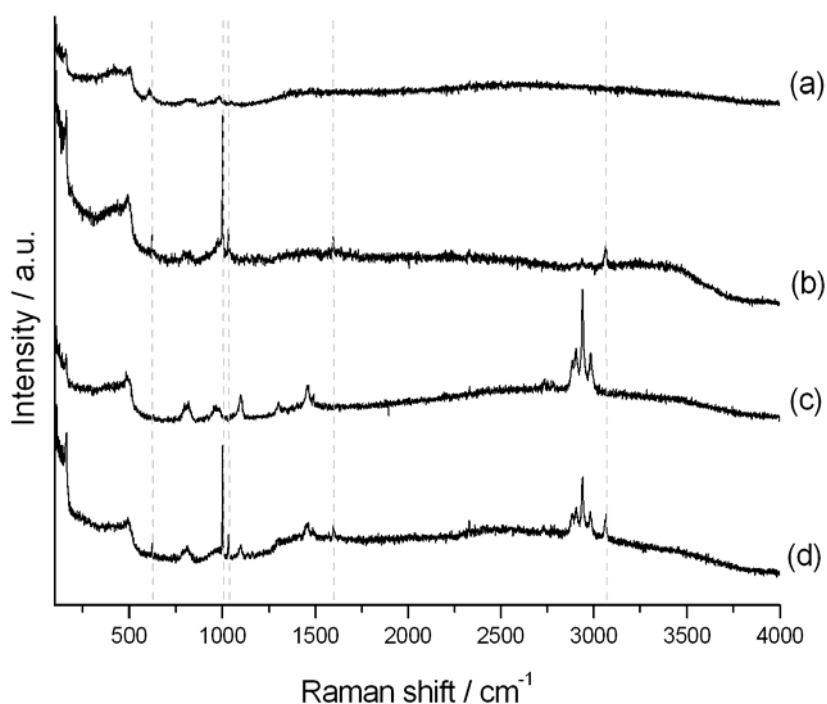


**Figure 6-1.** Raman spectra of calcined MCM-41 (a), sample MS-1-cal (b), extracted MCM-41 (c) and sample MS-1-ex (d).

Quantification of the amount of incorporated phenyl is possible by thermogravimetric analysis, as most aliphatic compounds combust in the temperature range between 110-395 °C, while silicon-bound phenyl is mainly decomposed between 400-600 °C. It should be noted that dehydroxylation of the siliceous framework also contributes to the mass loss in this high temperature range. The relevant data are summarized in Table 6-2, and curves for the temperature range of 20-900 °C for all samples can be found in the supplemental information. Interestingly, it is found that the relative additional weight loss after metalorganic functionalization is higher for extracted material (+64 mg; 111 mg/g(SiO<sub>2</sub>) - 47 mg/g(SiO<sub>2</sub>), see Table 6-2) than for calcined material (+42 mg). This could be related to the lower silica framework condensation in extracted MCM-41 as compared to the highly condensed state obtained after calcination, which is possibly less reactive towards nucleophilic attacks of the metalorganic reagent.



**Table 6-2.** Data derived from thermogravimetric analysis

Sample name	Normalized weight loss
	[mg / g(SiO <sub>2</sub> )] <sup>a</sup>
calcined MCM-41	13
MS-1-cal	55
extracted MCM-41	47
MS-1-ex	111

<sup>a</sup> weight loss between 395-900 °C, given relative to SiO<sub>2</sub> residue at 900 °C

Similar observations are made based on the nitrogen sorption data (Figure 6-2, Table 6-3). It should be noted that calcined MCM-41 silica materials show considerable pore shrinkage after calcination due to condensation of framework silanol groups at high temperature, and thus the extracted samples display significantly larger pore sizes. For both calcined and extracted MCM-41, a reduction of the surface area, pore volume and pore diameter is observed after metalorganic conversion.

**Table 6-3.** Nitrogen sorption data for MCM-41 samples

Sample name	Surface area [m <sup>2</sup> /g]	Pore volume [cc/g]	Pore diameter [nm]
calcined MCM-41	1099	0.775	3.5
MS-1-cal	867	0.543	3.1
extracted MCM-41	813	0.694	4.0
MS-1-ex	760	0.628	3.8

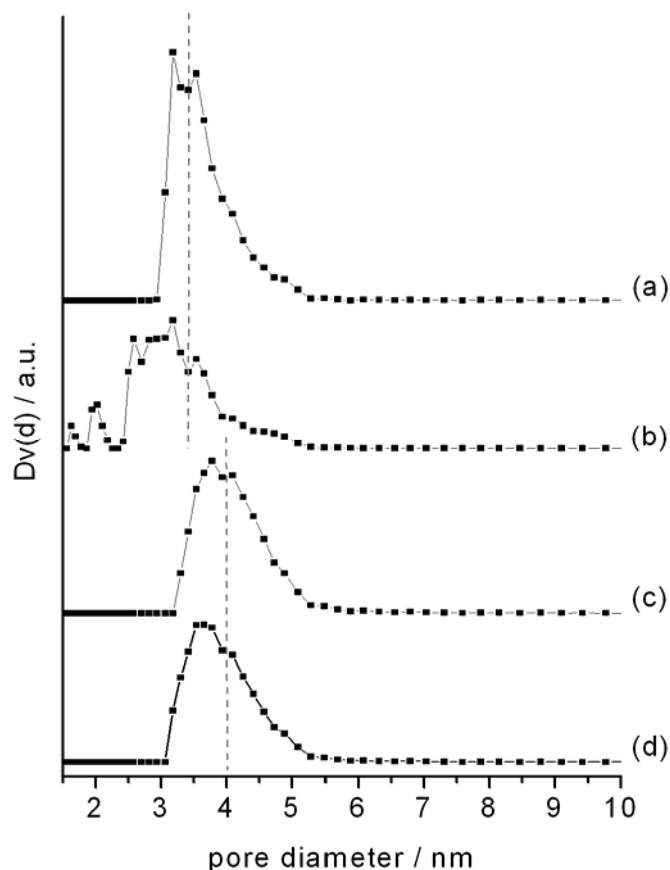


**Figure 6-2.** Pore diameters of calcined MCM-41 (a), sample MS-1-cal (b), extracted MCM-41 (c) and sample MS-1-ex (d).

In contrast to the results obtained from thermogravimetric data, the impact of metalorganic functionalization on pore size and pore volume seems less pronounced in the case of extracted material as compared to calcined MCM-41. This behavior can be explained by considering the different surface functionalities prevalent on both material types, i.e., a low surface silanol concentration in calcined MCM-41 versus a high silanol concentration and abundant ethoxy groups due to esterification in the case of extracted samples (Figure 6-3). As can be seen, the decrease in pore diameter by attachment of phenyl groups to framework silicon atoms is expected to be smaller in the case of ethoxy-functionalized surfaces ( $\Delta_{\text{extracted}}$ ), and higher for unfunctionalized samples ( $\Delta_{\text{calcined}}$ ).

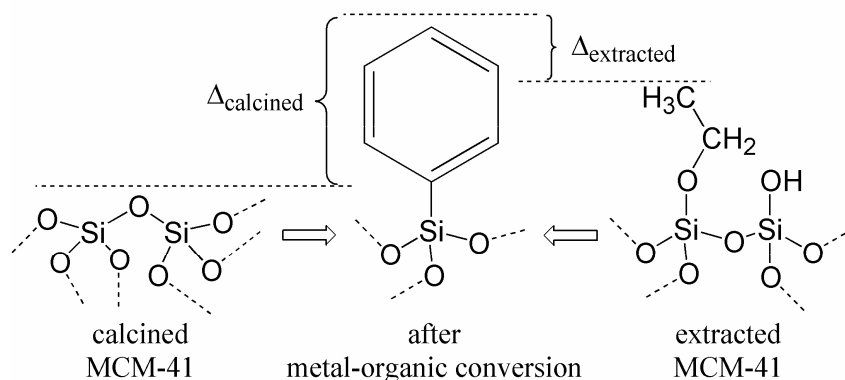


**Figure 6-3.** Schematic representation of the influence of metalorganic functionalization on the pore diameter of extracted and calcined materials.

By combining the results from Raman, TGA and sorption data it can therefore be concluded that it is possible to perform the metalorganic conversion in extracted samples despite their different surface structure.

**Choosing a suitable solvent.** Choosing the right reaction solvent is an important issue. While the metalorganic reagents require aprotic solvents, CMS nanoparticles are most stable as aqueous or ethanolic suspensions. Typical solvents used for metalorganic reactions such as tetrahydrofuran and diethyl ether, as well as most other common aprotic solvents including isohexane and dioxane lead to strong agglomeration and flocculation of the particles. It was found that toluene combines both requirements of stability against metalorganic reagents and good dispersion properties for CMS. Only minor agglomeration of the particles was observed and thus the stabilization of homogeneous suspensions was possible. In order to ensure that toluene does not influence the metalorganic conversion, preliminary tests were performed by functionalizing bulk MCM-41 with phenyllithium and tert-butyllithium in THF and toluene under otherwise identical conditions. No significant differences were observed in the Raman, TGA and nitrogen sorption data.

**Comparison of drying methods.** One of the most simple conceivable approaches to retain colloidal stability under anhydrous conditions is a solvent exchange with dry solvents (sample CMS-2). However, the mesopores are able to strongly bind and retain significant amounts of water which are not removed by this method even after multiple washing cycles. The high remaining water content thus prevents any functionalization by hydrolysis of the lithiated reagents. This was also confirmed by Raman spectroscopy, as none of the characteristic vibrations for phenyl moieties are present in sample CMS-2 (Figure 6-4a).

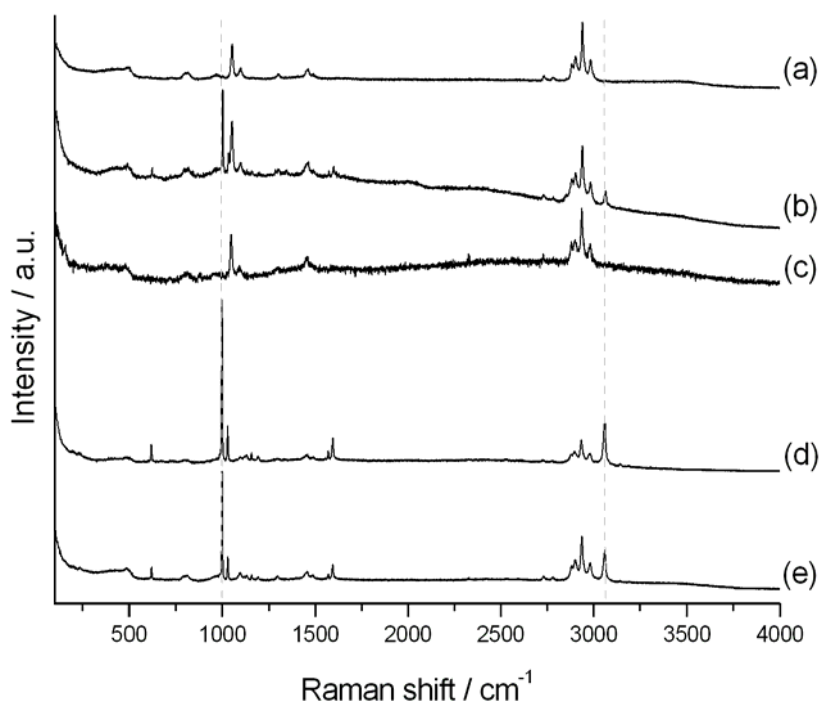


**Figure 6-4.** Raman spectra of samples CMS-2 (a), CMS-3 (b), CMS-4 (c), CMS-5 (d), and CMS-6 (e). For clarity, only two prominent bands corresponding to phenyl moieties are marked by dashed lines.

In order to remove this residual water a strong driving force is necessary. Due to the very low miscibility of toluene and water, the azeotropic distillation in a Dean Stark trap is a viable option (sample CMS-3). By heating to reflux, water-rich vapour is removed from the reaction

mixture and subsequently undergoes a phase separation after condensation. While the water phase is collected in the trap and removed from the reaction mixture, the toluene is recycled. This gradual shift in equilibrium leads to water being drawn out from inside the mesopores. Consequentially, signals corresponding to phenyl groups were detected in the Raman spectrum of sample CMS-3 after metalorganic conversion indicating a successful functionalization (Figure 6-4b).

However, investigation of the particle morphology by TEM showed unexpected results (Figure 6-5). The majority of the particles were found to have coalesced into large clots or elongated structures. Generation of agglomerates was also confirmed by DLS data. It was found that the formation process is temperature-induced, as similar results were obtained by hydrothermal treatment of nanoparticle suspensions at 130 °C without addition of further reagents.

This behavior was attributed to the high surface energy of the nanoparticles, which renders them prone to coalescence processes in order to minimize their outer surface area. Interestingly, the inner surface of the pore system is unaffected by this process and does not collapse, as demonstrated by nitrogen sorption (Figure 6-6, Table 6-4). Probably condensation occurs preferentially at the silanol-rich interface of two touching particles, while the silica framework is rigid enough to keep the channel walls stabilized and thus prevent condensation processes between opposing pore walls. Similar observations made for conformationally fluctuating template-containing mesoporous silicas showing phase transformations above 100 °C have been published.<sup>[18, 19]</sup>

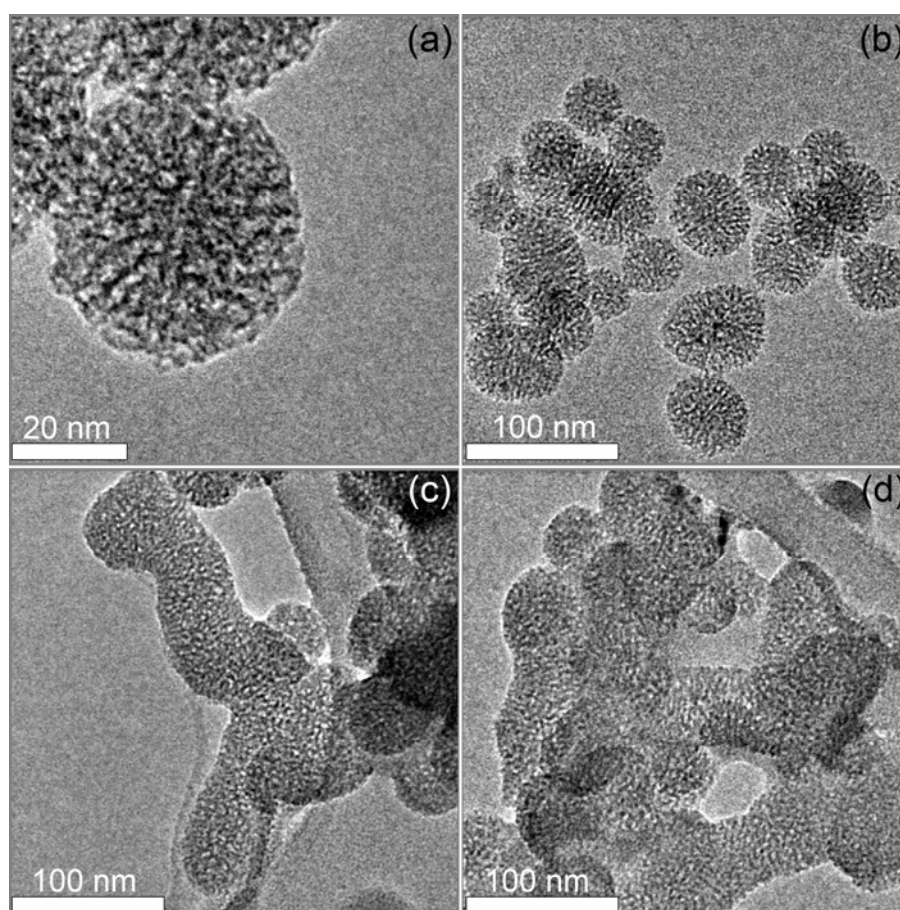


**Figure 6-5.** TEM micrographs of extracted unfunctionalized CMS (a,b) and sample CMS-3 (c,d).

**Table 6-4.** Nitrogen sorption data for CMS samples

Sample name	Surface area [ $\text{m}^2/\text{g}$ ]	Pore volume <sup>a</sup> [ $\text{cc/g}$ ]	Pore size [nm]
extracted CMS	1190	0.821	3.80
CMS-3	1136	0.752	3.65
CMS-5	961	0.529	3.68
CMS-6	970	0.678	3.63

<sup>a</sup> only cumulative pore volumes for pores < 8 nm are specified here due to the considerable textural porosity of CMS samples

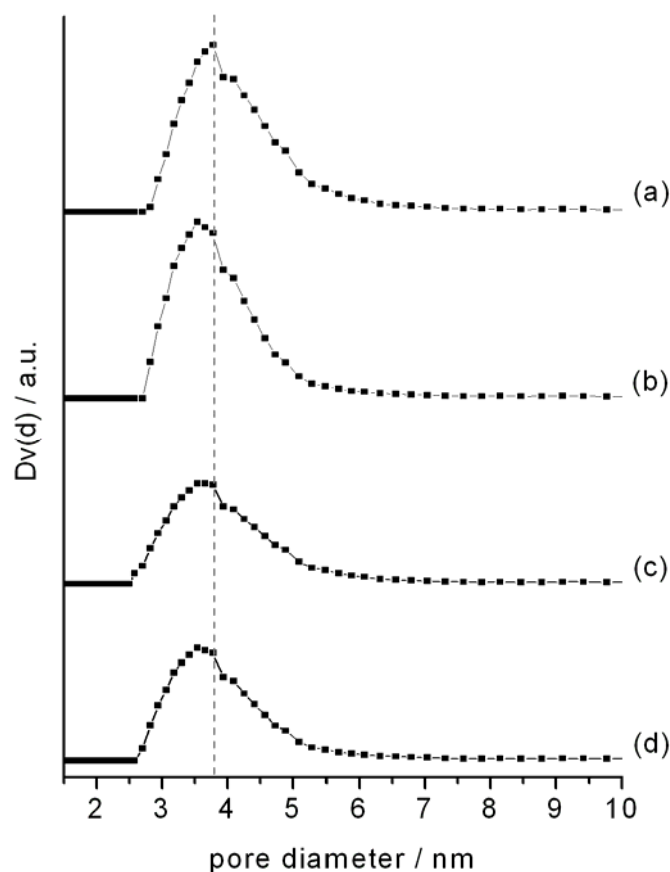


**Figure 6-6.** Pore diameters of extracted CMS (a) and samples CMS-3 (b), CMS-5 (c) and CMS-6 (d).

It is therefore of paramount importance to perform the water removal at low temperatures in order to retain the monomodal and small particle size distributions necessary for the preparation of stable colloidal suspensions.

Direct additions of desiccants, i.e., molecular sieve beads, was found to be ineffective (sample CMS-4). Due to the high water retention capacity of the mesopores and the low concentration of free water molecules in the solvent phase, equilibration of the system was found to be very slow. Furthermore, separation of the molecular sieve is difficult without contamination of the system or loss of CMS nanoparticles by adhesion to the desiccant particles.

Therefore two alternate pathways were developed which allow the removal of water at mild conditions (90 °C) while retaining colloidal stability. Preliminary tests confirmed that CMS

suspensions are stable below 100 °C without showing any signs of temperature-induced coalescence.

In the first approach, the hydrolysis of triethyl orthoformate was applied as a chemical driving force (sample CMS-5). Orthoformates are common reagents for removal of water in organic syntheses, i.e., for the shifting of reaction equilibria during preparation of acetals and ketals.<sup>[20]</sup>

The side products resulting from hydrolysis, i.e. ethanol and ethyl formate, have to be completely removed from the reaction mixture by distillation in order to avoid their subsequent reaction with the metalorganic reagent.

In the second approach, water was continuously removed from the gas phase by a desiccant reservoir, i.e., a Soxhlet extractor filled with molecular sieve beads (sample CMS-6). It should be noted that in contrast to classical Soxhlet extraction the reservoir is kept dry and at the chosen reaction conditions no refluxing of the solvent takes place. Due to the inherent vapor pressure of water, small amounts are always present in the gas phase. Continuous vapor removal from the gas phase results in a shift in equilibrium thus extracting the water from the mesopores. As the desiccant is physically separated from the liquid phase, no sample contamination occurs. The absorption of water from the gas phase was highly efficient and anhydrous conditions were reached after heating 3 hours at 90 °C.

Raman spectroscopy confirms the presence of phenyl moieties in both samples CMS-5 and CMS-6 after metalorganic conversion (Figure 6-4de).

Furthermore, a decrease in pore diameter, pore volume, and surface area compared to unfunctionalized material was detected in both samples (Table 6-4, Figure 6-6cd).

The relative amount of incorporated phenyl groups was investigated by TGA. The weight loss above 395 °C, i.e., the temperature range corresponding to the combustion of aromatic groups and silanol condensation, is strongly increased after metalorganic conversion (Table 6-5). The samples CMS-5 and CMS-6 display similar weight losses, indicating that both the orthoformate hydrolysis and vapor adsorption approach are efficient tools for the removal of



water from the mesopores. On the other hand, the azeotropic distillation at high temperatures applied for sample CMS-3 shows a lower functionalization degree in addition to causing particle coalescence, implying that the water removal was incomplete in this case.

**Table 6-5.** Data derived from thermogravimetric analysis

<b>Sample name</b>	<b>Normalized weight loss [mg / g(SiO<sub>2</sub>)]<sup>a</sup></b>
extracted CMS	60
CMS-3	164
CMS-5	299
CMS-6	267

<sup>a</sup> weight loss between 395-900 °C, given relative to SiO<sub>2</sub> residue at 900 °C

DLS curves of the colloidal suspensions obtained after drying treatment and metalorganic conversion confirm the absence of agglomerations in both samples CMS-5 and CMS-6 (Figure 6-7). Modification of the outer particle surface with phenyl groups seems to influence the colloidal characteristics of the suspensions. The particle size distributions appear broader and extend to smaller particle sizes, which could be related to the altered interparticle surface interactions.

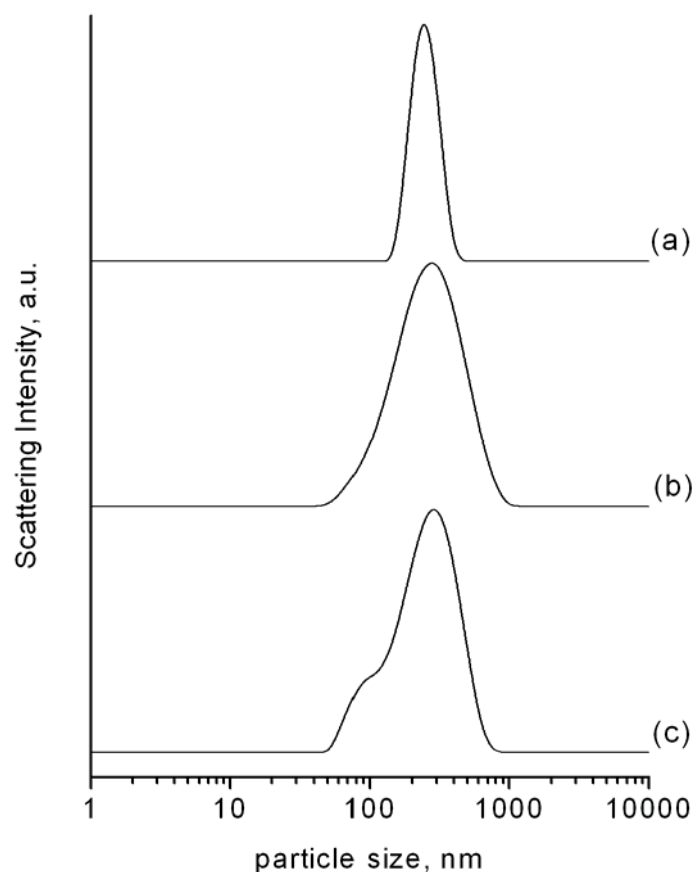


**Figure 6-7.** Unweighted DLS curves for unfunctionalized CMS (a), sample CMS-5 (b), and sample CMS-6 (c).

Furthermore, no differences in particle morphology of samples CMS-5 and CMS-6 in comparison to unfunctionalized CMS were observed by TEM (Figure 6-8). These data confirm that the applied drying methods are capable of creating anhydrous conditions in nanosized mesoporous systems without inducing irreversible particle agglomerations or coalescence phenomena.

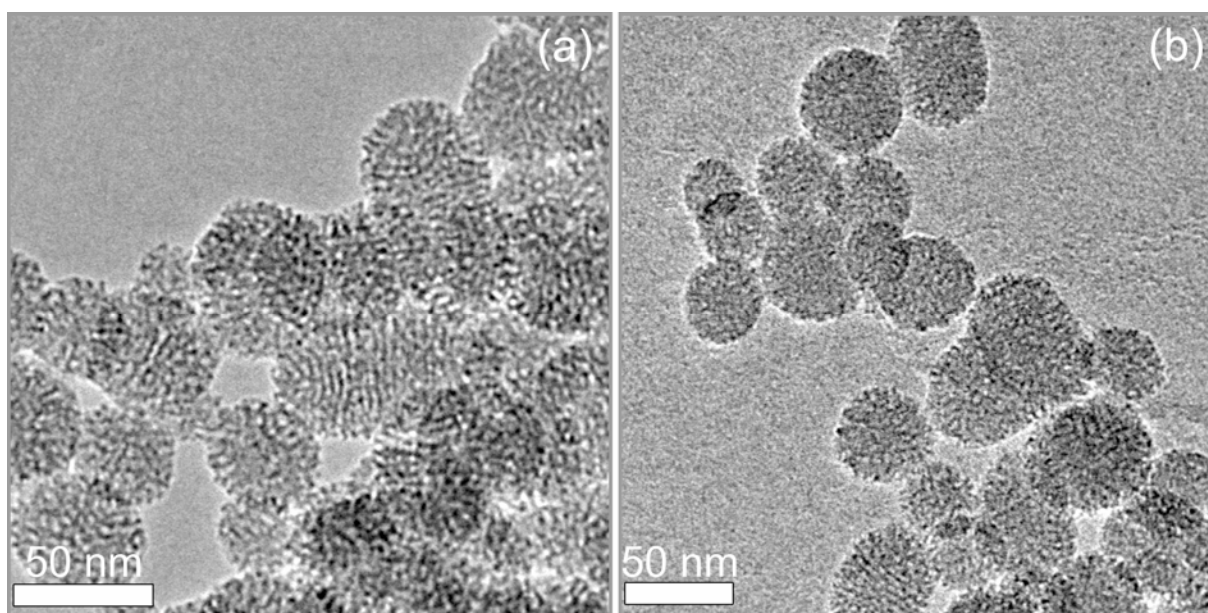


**Figure 6-8.** TEM micrographs of samples CMS-5 (a) and CMS-6 (b).

## 6.5 Conclusion

The concept of mesoporous silica functionalization via metalorganic reagents was transferred from micrometer-sized MCM-41 materials to colloidal suspensions containing mesoporous silica nanoparticles. The influence of the different surface chemistries resulting from template removal via calcination or extraction on the outcome of metalorganic conversion with phenyllithium has been investigated. Furthermore, different drying methods have been compared for their suitability to remove water from the mesopores without causing agglomeration of the colloidal suspensions. Elevated temperatures above 100 °C lead to coalescence of the mesoporous silica nanoparticles. However, two approaches for water removal from the mesopores at mild conditions were developed: triethyl orthoformate hydrolysis and vapor adsorption. Both methods allowed us to perform metalorganic conversions while retaining colloidal stability.

## 6.6 References

- [1] D. M. Ford, E. E. Simanek, D. F. Shantz, *Nanotechnology* **2005**, *16*, 458.
- [2] A. Stein, B. J. Melde, R. C. Schroden, *Advanced Materials* **2000**, *12*, 1403.
- [3] I. I. Slowing, B. G. Trewyn, S. Giri, V. S. Y. Lin, *Advanced Functional Materials* **2007**, *17*, 1225.
- [4] S. Giri, B. G. Trewyn, V. S. Y. Lin, *Nanomedicine* **2007**, *2*, 99.
- [5] F. Hoffmann, M. Cornelius, J. Morell, M. Froeba, *Angewandte Chemie, International Edition* **2006**, *45*, 3216.
- [6] R. Anwender, I. Nagl, M. Widenmeyer, G. Engelhardt, O. Groeger, C. Palm, T. Roeser, *Journal of Physical Chemistry B* **2000**, *104*, 3532.
- [7] K. Yamamoto, T. Tatsumi, *Chemistry Letters* **2000**, 624.
- [8] K. Yamamoto, T. Tatsumi, *Microporous and Mesoporous Materials* **2001**, *44-45*, 459.
- [9] J. E. Lim, C. B. Shim, J. M. Kim, B. Y. Lee, J. E. Yie, *Angewandte Chemie, International Edition* **2004**, *43*, 3839.
- [10] S. Angloher, J. Kecht, T. Bein, *Chemistry of Materials* **2007**, *19*, 3568.
- [11] S. Angloher, J. Kecht, T. Bein, *Chemistry of Materials* **2007**, *19*, 5797.
- [12] G. Trewyn Brian, I. Slowing Igor, S. Giri, H.-T. Chen, S. Y. Lin Victor, *Accounts of chemical research* **2007**, *40*, 846.
- [13] Y.-S. Lin, S.-H. Wu, Y. Hung, Y.-H. Chou, C. Chang, M.-L. Lin, C.-P. Tsai, C.-Y. Mou, *Chemistry of Materials* **2006**, *18*, 5170.
- [14] M. Grun, K. K. Unger, A. Matsumoto, K. Tsutsumi, *Microporous and Mesoporous Materials* **1999**, *27*, 207.
- [15] K. Möller, J. Kobler, T. Bein, *Advanced Functional Materials* **2007**, *17*, 605.
- [16] S. Hitz, R. Prins, *Journal of Catalysis* **1997**, *168*, 194.
- [17] N. Lang, A. Tuel, *Chemistry of Materials* **2004**, *16*, 1961.
- [18] S. H. Tolbert, C. C. Landry, G. D. Stucky, B. F. Chmelka, P. Norby, J. C. Hanson, A. Monnier, *Chem. Mater.* **2001**, *13*, 2247.
- [19] C. C. Landry, S. H. Tolbert, K. W. Gallis, A. Monnier, G. D. Stucky, P. Norby, J. C. Hanson, *Chem. Mater.* **2001**, *13*, 1600.
- [20] C. A. MacKenzie, J. H. Stocker, *Journal of Organic Chemistry* **1955**, *20*, 1695.

## **7 Probing the intrapore surface of phenyl-substituted nanoscale mesoporous silica – piezoelectric sorption measurements in thin films (joint project)\***

### **7.1 Introduction**

The sorption or diffusion of volatile compounds in porous materials has been the subject of numerous studies.<sup>[1-5]</sup> However, surprisingly little information is available on the heat of adsorption of volatile compounds on empty and functionalized periodic mesoporous materials, e.g., MCM-41 silica.

MCM type materials feature high surface areas of up to  $1500 \text{ m}^2 \text{ g}^{-1}$  and tunable pore sizes and pore volumes. Such high surface area materials are ideal candidates for many sorption-related applications. The knowledge of sorption behavior is critical in the case of catalytic and sensor applications as well as membrane separations.<sup>[6-8]</sup> Well-known methods for the determination of the heat of adsorption include calorimetric measurements,<sup>[9]</sup> temperature programmed desorption (TPD) processes<sup>[1]</sup> and calculations from equilibrium adsorption data.<sup>[10-12]</sup>

The acquisition of sorption heats by calorimetric methods or TPD are usually relatively time consuming experiments with measuring times in the range of several hours or even days. Common approaches require sample amounts of several milligrams or grams to determine the desired thermodynamic values. In contrast, the quartz crystal microbalance technique permits gravimetric recording of sorption isotherms with microgram quantities of material, hence offering several advantages, such as fast diffusion times and less consumption of valuable sample material. The method further benefits from the high measuring accuracy of industry-standard quartz resonators and electronic equipment as well as the possibility to perform a parallel evaluation of isosteric adsorption heats with several samples.

The quartz crystal microbalance (QCM) technique is based on the proportionality of the frequency of an oscillating QCM to additional adsorbed mass density. Provided the porous material can be deposited in an acoustically coupled thin film on the surface of the device, one

\* A. Darga, J. Kecht, T. Bein, *Langmuir* **2007**, 23, 12915-12922.

can measure the uptake of adsorbate molecules as a function of partial pressure and temperature *via* the frequency changes of the QCM.

By applying an electric field on a piezoelectric crystal, e.g. quartz, a mechanical deformation or stress is detectable which is known as the inverse piezoelectric effect. The resonance frequency of the QCM device is strongly affected by various parameters of the surrounding medium, such as temperature, density and viscosity.

In 1959 *Sauerbrey*<sup>[13]</sup> demonstrated the physical relationship between additional mass loading on quartz plates and their frequency changes (see equation 7-1).

$$\Delta m = \frac{A\sqrt{\mu_q\rho_q}}{-2f_0^2}\Delta f \quad (7-1)$$

$\Delta m$ : mass change

$A$  : piezo-active area of the electrode

$\mu_q$  : shear-modulus of quartz

$\rho_q$  : density of quartz

$f_0$  : resonant frequency of the fundamental mode of the crystal

$\Delta f$  : frequency change

The sensitivity of this gravimetric measurement method lies in the range of nanograms and is therefore enhanced by a factor of approximately 100 compared to commercially available electro-mechanical microbalances. As a result, the application of QCM techniques with very small amounts of sample in the range of 5 - 30  $\mu\text{g}$  becomes possible, thus leading to short diffusion times in adsorbents and short overall measurement times for adsorption isotherms.

The present work utilizes the QCM technique supported by a fully automated dosing and measurement system, which is described in detail in the supporting information, to determine the sorption isotherms of unfunctionalized and phenyl-functionalized periodic mesoporous

silica. The thin mesoporous films used in this study fulfill the preconditions of the *Sauerbrey* equation<sup>[14]</sup> of limited thickness and homogeneity of the deposited material. *C.-S. Lu and O. Lewis*<sup>[15]</sup> investigated the impact of film thickness on the validity of the *Sauerbrey* equation. The authors report a linear correlation between additional deposited mass and frequency changes up to a 2 % decrease of the fundamental frequency of the quartz resonator. In case of a 10 MHz QCM device the linearity can be assumed for frequency changes up to 20.000 Hz. Periodic mesoporous silica materials offer rich opportunities in sorption-related fields due to the possibility to control their pore diameters in a wide range (about 2 - 15 nm) as well as their facile functionalization, leading to adjustable surface properties. Although some alternative techniques including the functionalization by metalorganic reagents<sup>[16]</sup> and by silazanes<sup>[17]</sup> have been reported recently, the two common primary methods for functionalization of mesoporous silica materials are the grafting and co-condensation approaches. In the former method, trialkoxy- or trichlorosilanes bearing the desired functionalities are attached to the surface silanol groups of the mesoporous structure by a post-synthesis treatment step. In the co-condensation approach, the functionalization takes place *in situ* by adding the appropriate amount of functionalized trialkoxysilanes to the reaction mixture. While both methods are adequate to introduce high amounts of organic moieties into the material, they can result in significantly different surface properties. In this work, both functionalization approaches, the co-condensation and grafting of phenyltriethoxysilane, are applied in the synthesis of colloidal suspensions of non-functionalized and phenyl-containing mesoporous silica nanoparticles (MSN in the sample codes). The materials are thoroughly characterized by various standard techniques and subsequently applied in the preparation of homogeneous layers on the surface of QCM devices *via* spin-coating. For each sample, toluene sorption isotherms were recorded at four different temperatures, thus allowing the calculation of the respective heats of adsorption via the Clausius-Clapeyron equation (see equation 7-2).<sup>[10]</sup>

$$\frac{d(\ln p)}{d(1/T)} = -\frac{\Delta H_{ads}^0}{R} \quad (7-2)$$

$p$ : pressure

$T$ : temperature

$\Delta H_{ads}^0$ : isosteric heat of adsorption

$R$ : gas constant

The relevant data were taken at isosteric conditions (at constant loading) from the adsorption branch of the corresponding isotherms.<sup>[18]</sup> The resulting heats of adsorption yield information about the affinity of the adsorbate towards the modified mesoporous materials. It is thus demonstrated that QCM measurements can be applied for the efficient characterization of mesoporous silica materials, which is a valuable approach due to the rapidly achieved equilibrium conditions and short diffusion times obtained by using small amounts of sample in thin films.

The following investigation was performed as a joint project between coworkers Alexander Darga and Johann Kecht in the group of Professor Thomas Bein. The responsibilities were shared as follows: Alexander Darga was responsible for measurement and interpretation of all QCM and SEM data, as well as preparation of the QCM chips and SEM samples. Johann Kecht was responsible for the synthesis of the colloidal mesoporous silica samples, interpretation of the TEM and NMR data, as well as measurement and interpretation of the DLS, N<sub>2</sub> sorption, TGA, NMR, and Raman data.



## 7.2 Experimental Section

Tetraethyl orthosilicate (TEOS, Fluka, >98%), phenyltriethoxysilane (PTES, Aldrich, 98%), cetyltrimethylammonium chloride (CTAC, Fluka, 25% in H<sub>2</sub>O) and triethanolamine (TEA, Aldrich, 98%) were used as received without further purification. Doubly distilled water from a Millipore system (Milli-Q Academic A10) was used for all synthesis and purification steps. Unfunctionalized mesoporous silica nanoparticles were prepared according to reference <sup>[19]</sup> from reaction mixtures with a molar composition of 1 TEOS : 9.6 TEA : 0.22 CTAC : 145 H<sub>2</sub>O (sample MSN-I). TEOS (10.4 g) and TEA (71.5 g) were heated for 25 minutes at 363 K (90 °C) without stirring in a 250 mL polypropylene reactor. An aqueous CTAC-solution (133.6 g, 2.58 %wt) preheated to 333 K (60 °C) was added and the resulting mixture stirred at room temperature for 3 hours. After addition of 100 mL ethanol, the mesoporous silica nanoparticles were separated by centrifugation and redispersed in ethanol. Extraction of the organic template was performed by heating under reflux at 368 K (95 °C) for 30 minutes in two solutions containing 2 g ammonium nitrate in 100 mL ethanol and 4 g concentrated hydrochloric acid in 100 mL ethanol, respectively. The nanoparticles were washed by centrifugation after each extraction step, resulting in clear ethanolic suspensions.

For preparation of phenyl-grafted material (sample MSN-II), 400 mg PTES were added to 6.5 g of an ethanolic suspension containing 3.0 wt% unfunctionalized extracted nanoparticles. The suspension was heated under reflux for 3 hours and purified by two steps of centrifugation (40000 rcf, 30 min) and redispersion in ethanol.

For the preparation of phenyl-containing samples by the co-condensation route, the synthesis for mesoporous silica nanoparticles was performed starting from a reaction mixture with a molar composition of 0.9 TEOS : 0.1 PTES : 9.6 TEA : 0.22 CTAC : 145 H<sub>2</sub>O (sample MSN III).

All samples were stabilized as ethanolic suspensions with a solid concentration of about 3 wt% and repeatedly spin-coated (3000 rpm) onto a QCM device featuring gold electrodes,

thus obtaining deposited sample amounts on the electrodes varying from  $14.6 \mu\text{g cm}^{-2}$  up to  $36.2 \mu\text{g cm}^{-2}$ . The resulting QCM devices were heated in a furnace at 623 K (350 °C) in air for 10 hours with a prior heating ramp of 0.5 K / min in order to decompose any residual template molecules inside the silica mesopores.

Prior to any recording of isotherms the QCM device was heated up to 403 K (130 °C) inside the measurement cell under nitrogen at a constant flow of 2000 ml / min for at least 20 minutes until frequency stability was reached. After the heating and purging period at 403 K (130 °C), a deviation of less than  $\pm 10$  Hz within a 240 seconds period was accepted as sufficiently stable to indicate the absence of water in the mesopores, subsequently enabling the next temperature step.

### 7.3 Characterization

Dynamic light scattering (DLS) measurements to determine the hydrodynamic particle diameter in colloidal suspensions were performed with a Malvern Zetasizer-Nano instrument equipped with a 4 mW He-Ne laser (633 nm) and avalanche photodiode detector. Thermogravimetric analyses (TGA) of the bulk samples were performed on a Netzsch STA 440 C TG/DSC (heating rate of 10 K/min in a stream of synthetic air of about 25 mL/min). Solid state  $^1\text{H}$ - $^{29}\text{Si}$ -CP-NMR measurements were performed on a Bruker DSX Avance 500 FT (contact time 10 ms, spinning rate 5.5 kHz, pulse delay 2.8  $\mu\text{s}$ , recycle delay 2 s, number of scans between 2600 and 5600). Raman spectra of the coated QCM devices were recorded on a Jobin Yvon Horiba HR800 UV Raman microscope using a HeNe laser emitting at 632.8 nm. Transmission electron microscope (TEM) images were taken with a JEOL JEM 2011 microscope operating at 200 kV, by drying the diluted colloidal suspensions on a carbon-coated copper grid.

In order to evaluate the smoothness and overall sample thickness and to validate the applicability of the Sauerbrey equation, the mesoporous silica layer on top of the quartz crystal was investigated with a JEOL JSM 6500F scanning electron microscope (Figure 7-1). As an example, Figure 7-1a shows the surface of the QCM device spin-coated with sample MSN-III, which does not contain any large agglomerations. Figure 7-1b also demonstrates the low thickness of about 800 nm of the removed particle layer observed after scratching the silica surface with a scalpel.

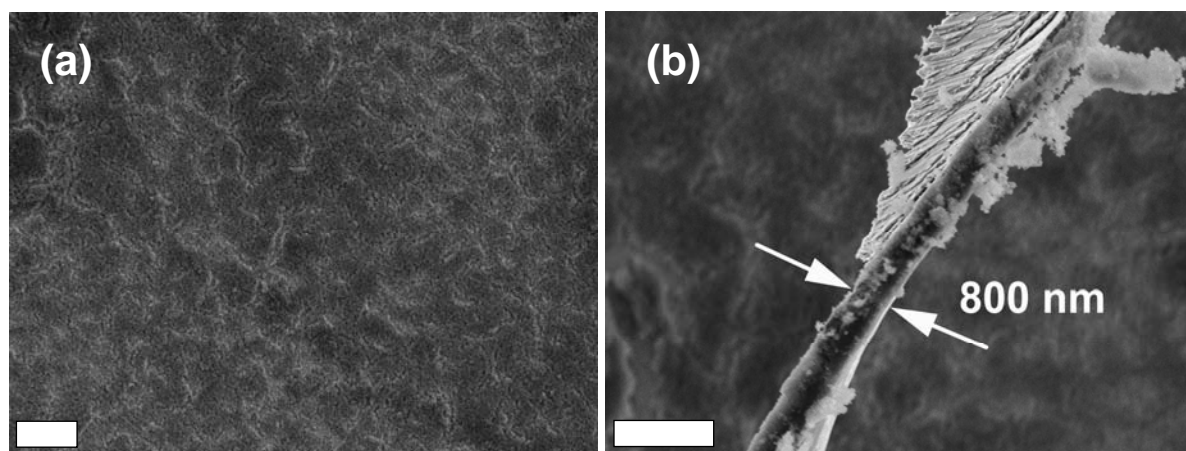


**Figure 7-1.** SEM micrographs of a QCM-device spincoated with sample MSN-III (a) and the corresponding film removed from the surface (b) (scale bar = 2  $\mu\text{m}$ ).

Nitrogen sorption measurements were performed on a Quantachrome Instruments NOVA 4000e at 77 K. For calculations of pore sizes and volumes a NLDFT equilibrium model of  $\text{N}_2$  on silica was used. Pore diameters based on the BJH model are also given for better comparison with literature data. A BET model was applied to evaluate the surface areas.

The recording of isotherms was performed on a QCM experimental setup described in detail in the supporting information. Digital mass flow controllers (W-101A-110-P, F-201C, Bronkhorst High-Tech) ensured the accurate dosing of the carrier gas nitrogen and the analyte liquid toluene, which was vaporized in a controlled evaporation and mixing element (W-101A,

Bronkhorst High-Tech). A 10 MHz QCM device (XA 1600 AT-cut, KVG Quartz Crystal Technology) was used to measure frequency changes due to additional adsorbed mass.

Some parameters of the Sauerbrey equation, such as the density  $\rho_q = 2.648 \text{ g}\cdot\text{cm}^{-3}$  and the shear-modulus  $v_q = 2.947 \cdot 10^{11} \text{ g}\cdot\text{cm}^{-1}\cdot\text{s}^{-2}$  are characteristics of the piezoelectric material quartz.

The Sauerbrey equation is usually normalized to  $1 \text{ cm}^2$  sensing area on the QCM-chip, thus a frequency change of 1 Hz corresponds to a mass-loading of  $4.42 \cdot 10^{-9} \text{ g}$ . The overall frequency fluctuation of the system is  $\pm 1 - 2 \text{ Hz}$  at room temperature.

Concerning the sorption of the vaporized liquid toluene, partial pressures were calculated using the van-der-Waals equation (see equation 7-3) with real gas state assumptions. Van-der-Waals parameters for toluene ( $a = 24.86$ ,  $b = 0.1497$ ) were taken from reference [20].

$$\left( p + a \frac{n^2}{V^2} \right) (V - nb) = nRT \quad (7-3)$$

$p$ : pressure

$a$ : constant to correct for intermolecular attractive forces

$n$ : quantity of gas in moles

$V$ : volume

$b$ : constant to correct for volume of individual gas molecules

$R$ : gas constant

$T$ : temperature

## 7.4 Results and Discussion

Mesoporous silica samples were prepared using different functionalization approaches and subsequently characterized. Solutions without PTES as an additive yielded unfunctionalized silica nanoparticles (sample MSN-I). After removal of the template by extraction, a functionalization *via* post-synthesis treatment with PTES was performed, thus obtaining the grafted sample MSN-II. For the preparation of co-condensed material, PTES was included in the initial synthesis mixture leading to an *in-situ* functionalization (sample MSN-III). After extraction of the template, the samples were obtained as stable colloidal solutions in ethanol. DLS measurements reveal that all samples possess narrow particle size distributions with hydrodynamic diameters in the range of 100 - 200 nm (Figure 7-2). Corresponding TEM investigations show round and elongated mesoporous particles with diameters below 100 nm (Figure 7-3).

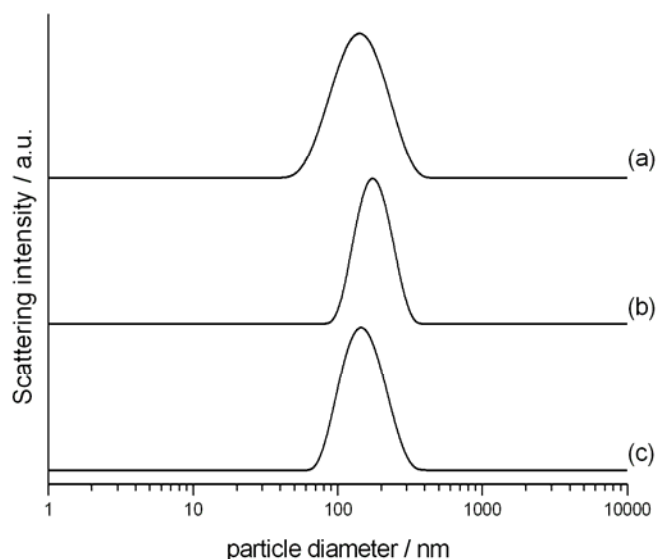


**Figure 7-2.** Unweighted DLS curves (A) for ethanolic suspensions of samples MSN-I (a), MSN-II (b) and MSN-III (c).

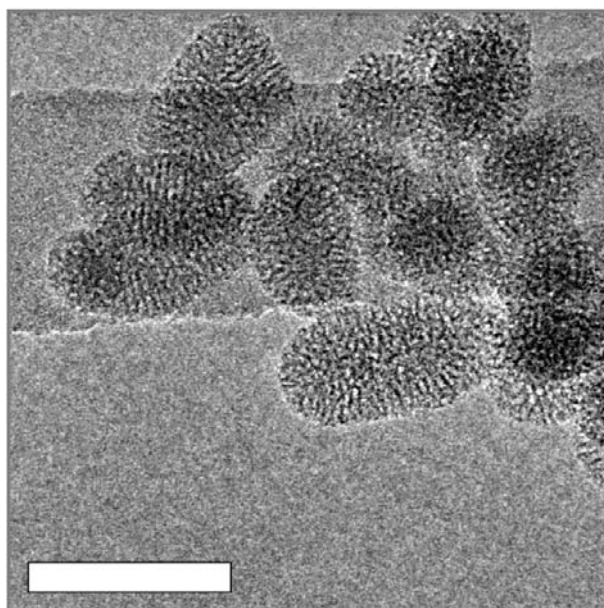


**Figure 7-3.** TEM micrograph of sample MSN-I (scale bar = 100 nm).

Parts of the solutions were dried for further characterization of powder samples. Nitrogen sorption measurements were applied to investigate the porous nature of the products (Figure 7-4). All samples show the expected IUPAC classified Type IV shape isotherm, typical for mesoporous systems, indicating mesopore filling as well as a pronounced hysteresis loop at higher  $p/p_0$ -values due to external textural porosity of the nanoparticles. BET calculations reveal high surface areas for all three samples due to the large internal surface of the mesoporous channel system. NLDFT calculations show that the pore diameter of 3.7 nm in the unfunctionalized material is decreased by about 0.3 nm by incorporation of phenyl groups (Figure 7-5) which is less than twice the molecular dimension (about  $2 \times 0.3$  nm for two single phenyl groups), thus suggesting a tilted arrangement and/or a low density of the phenyl groups coating the walls.<sup>[21]</sup> The reduced pore diameter is also reflected in the decreased pore volume (Table 7-1).

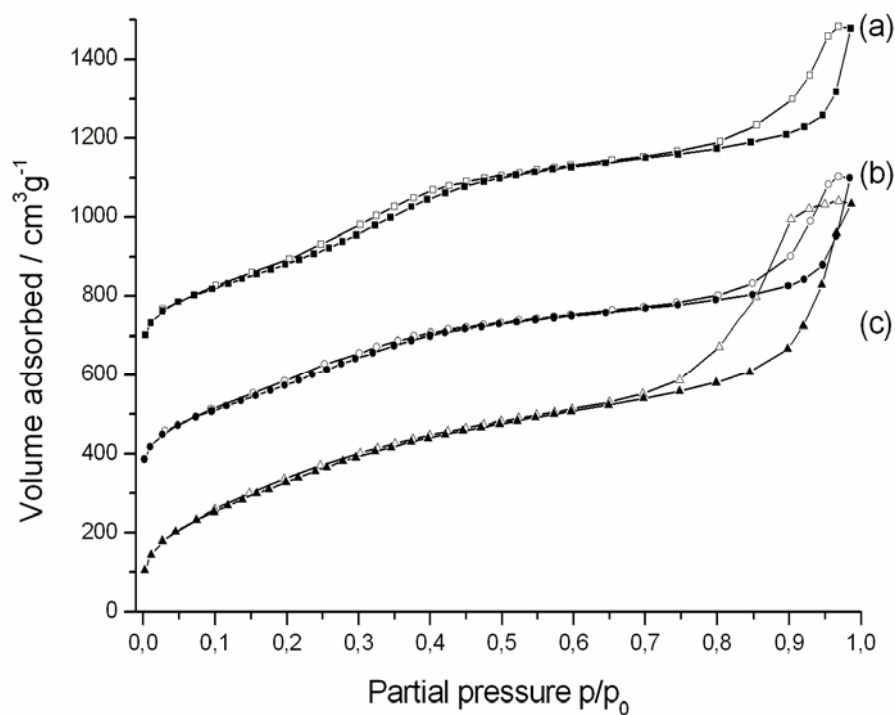


**Figure 7-3.** Nitrogen sorption measurements of the dried bulk samples MSN-I (a), MSN-II (b) and MSN-III (c). Curves (a) and (b) are offset by 300 and 600, respectively.

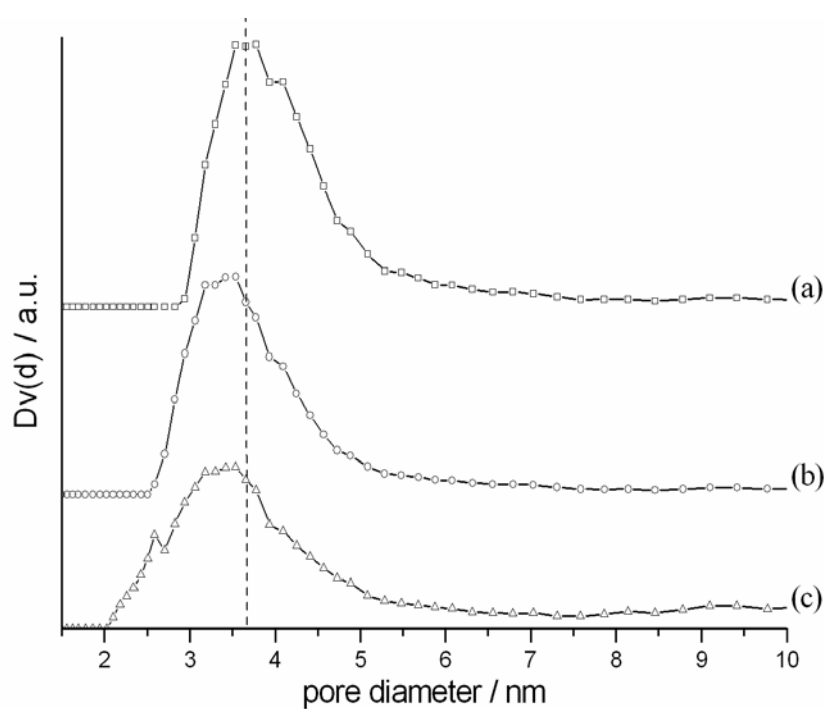


**Figure 7-4.** Pore diameters of the dried bulk samples MSN-I (a), MSN-II (b) and MSN-III (c) as calculated from N<sub>2</sub> isotherms by a NLDFIT equilibrium model.

**Table 7-1.** N<sub>2</sub> sorption data

sample	functionalization method	BJH pore diameter [nm]	DFT pore diameter [nm]	DFT pore volume* [cm <sup>3</sup> g <sup>-1</sup> ]	BET surface area [m <sup>2</sup> g <sup>-1</sup> ]
MSN-I	unfunctionalized	2.6	3.7	0.82	1187
MSN-II	grafting	2.2	3.4	0.62	1104
MSN-III	co-condensation	2.1	3.4	0.61	1275

\* for pores under 8 nm

A complete coverage of the silica surface with densely packed and vertical phenyl groups would result in a decrease of the pore diameter by about 0.6 nm, by assuming a layer of phenyl groups facing each other on both sides of a pore wall. However, such a scenario would be highly unlikely considering the respective mechanisms of phenyl incorporation. During grafting, the density of the phenyl groups on the silica surface is determined by the availability of binding sites and remaining free space between previously grafted molecules, which will prevent a close packing of the phenyl groups. During co-condensation, the relevant phenyl groups are placed on the hydrophilic-hydrophobic interface of the micelles and will arrange themselves in such a way that they are pointing inside the hydrophobic part of the micelles during self-assembly. Since the pore walls can therefore only be partially functionalized, the observed pore size reduction is smaller than expected from a densely packed monolayer of phenyl groups.

In order to determine the extent of phenyl functionalization, thermogravimetric analysis was performed on all samples (Figure 7-5). It is assumed that the thermal decomposition of the template in the MSN-samples is similar to the mechanism reported for CTAB-containing MCM-41 described in the literature.<sup>[22]</sup> In the temperature range up to 383 K (110 °C), physisorbed water is released from the pores. From 383 K (110 °C) to about 668 K (395 °C), remaining cetyltrimethylammonium template is decomposed by first undergoing Hoffmann



elimination followed by oxidation to  $\text{CO}_2$ .<sup>[22]</sup> In the range of about 668 K (395 °C) to 1173 K (900 °C), three reactions can take place. In all three samples, water is released by condensation of framework silanol groups, and small amounts of carbonaceous residues from incomplete template combustion are oxidized. In the case of phenyl-containing samples, the aromatic groups are also decomposed within this temperature range. While the TG curves of all samples are similar for temperatures up to 668 K (395 °C), the extent of functionalization is clearly visible by comparison of the weight loss between 668 and 1173 K (395 and 900 °C) for sample MSN-I (2.6 %) in contrast to samples MSN-II (11.3 %) and MSN-III (13.7 %).

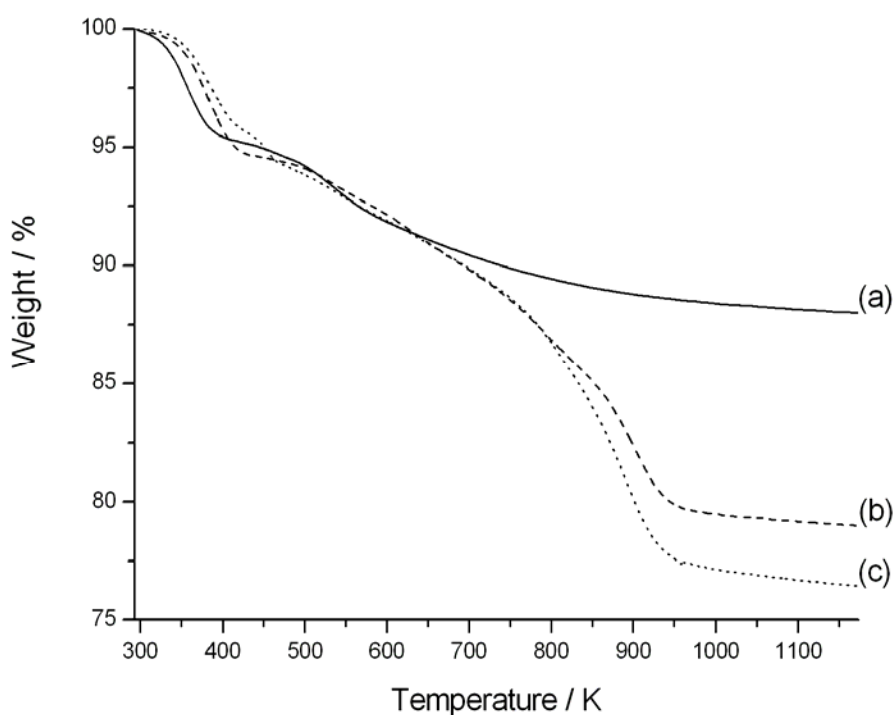


**Figure 7-5.** Thermogravimetric data for samples MSN-I (a), MSN-II (b) and MSN-III (c).

While both MSN-II and MSN-III contain a comparable mass-loading of phenyl-groups, there should be major differences in the nature of the framework attachment.  $^1\text{H}$ - $^{29}\text{Si}$ -CP-MAS-NMR was used to investigate the different connectivity of the functionalized silicon atoms to the mesoporous framework prior to the calcination step at 623 K (350 °C) in air (Figure 7-6A).

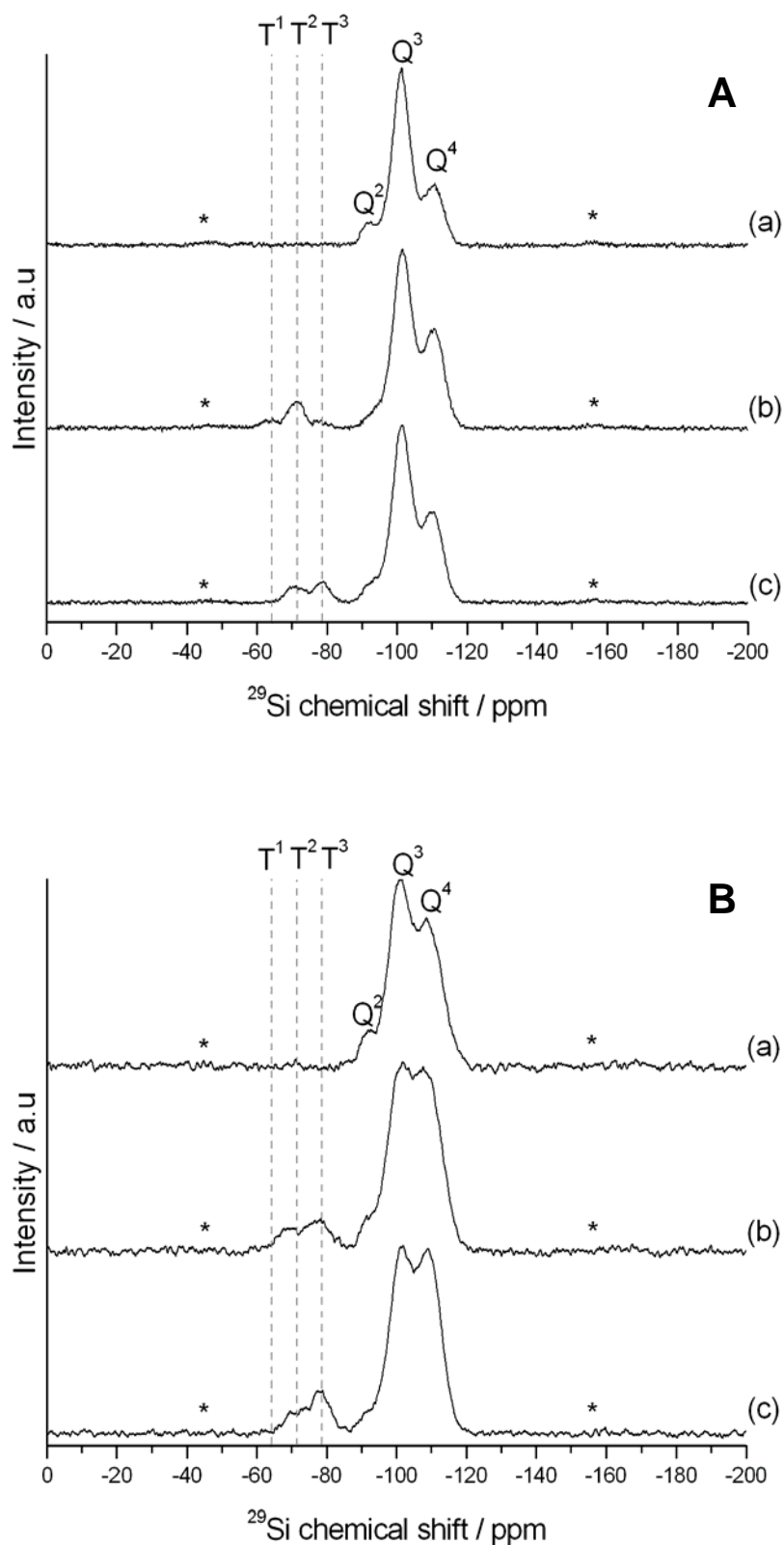


**Figure 7-6.**  $^1\text{H}$ - $^{29}\text{Si}$  CP/MAS NMR spectra of samples MSN-I (a), MSN-II (b) and MSN-III (c) before (A) and after (B) calcination at 623 K (350 °C) for 10 h. Dashed lines mark the signals corresponding to T<sup>1</sup>, T<sup>2</sup> and T<sup>3</sup> sites. The asterisks mark rotation side bands.

All three samples show  $Q^4$ ,  $Q^3$  and to a lesser extent  $Q^2$  resonances at -110, -100 and -90 ppm, respectively, arising from the incompletely condensed silica framework ( $Q^4 = \text{Si}(\text{OSi})_4$ ,  $Q^3 = \text{Si}(\text{OSi})_3\text{OH}$ ,  $Q^2 = \text{Si}(\text{OSi})_2(\text{OH})_2$ ). However, the  $Q^2$  species seem to be reduced in sample MSN-II due to further condensation at higher temperatures during the grafting treatment. For the co-condensed sample MSN-III, signals corresponding to  $T^3$  and  $T^2$  sites can be found at 80 and 70 ppm, respectively. They are caused by the phenyl-bearing silicon atoms that were co-condensed into the mesoporous silica framework ( $T^3 = \text{Si}(\text{OSi})_3\text{R}$ ,  $T^2 = \text{Si}(\text{OSi})_2(\text{OH})\text{R}$ ,  $T^1 = \text{Si}(\text{OSi})(\text{OH})_2\text{R}$ ).<sup>[23]</sup>

In contrast, the phenyl-groups in sample MSN-II were grafted onto the silica surface of the sample by a post-synthesis treatment. Here,  $T^3$  sites are less prominent compared to the co-condensed sample. However, a higher concentration of  $T^2$  sites and a signal corresponding to  $T^1$  sites at about 63 ppm is detected. This indicates that the grafted silyl species bearing phenyl groups are mainly connected to the silica framework by two siloxane bonds. As the framework is already pre-formed, phenyltriethoxysilane moieties attaching to the surface are not always able to find a silanol group in a suitable location for further condensation. After attachment of two groups, as is the case in a  $T^2$  site, the flexibility and rotation of the group is hindered, thereby reducing the possibility of finding a third opportunity for condensation and thus explaining the prominence of  $T^2$  sites in sample MSN-II.

A different picture is obtained after heating treatment. In order to evaluate the influence of the calcination step at 623K (350 °C) on the degree of silanol condensation and connectivity of the phenyl-groups, the  $^1\text{H}$ - $^{29}\text{Si}$ -CP-MAS-NMR measurements were repeated on calcined samples (Figure 7-6B). As is to be expected, framework condensation was significantly increased during heating, resulting in a higher degree of  $Q^4$  species by annealing of free silanol groups in the material. In all three samples the relative intensity of the  $Q^4$  signals versus  $Q^3$  signals was increased, and similar observations can be made for signals corresponding to  $T^3$  and  $T^2$  species. It should also be noted that the high degree of  $T^2$  sites

detected earlier in grafted sample MSN-II was drastically lowered by the calcination treatment. This was probably caused by the increased mobility of the phenyl-bearing silyl groups at higher temperatures, thus enabling the final condensation step of the remaining silanol group on the  $T^2$  species to the framework surface. It can therefore be stated that based on NMR analysis the connectivities of phenyl-bearing silyl groups in the grafted and cocondensed samples after calcination are rather similar.

Raman spectroscopic studies on the QCM device were performed in order to elucidate the fate of the attached phenyl groups after heating the film at 623 K (350 °C) (Figure 7-7).

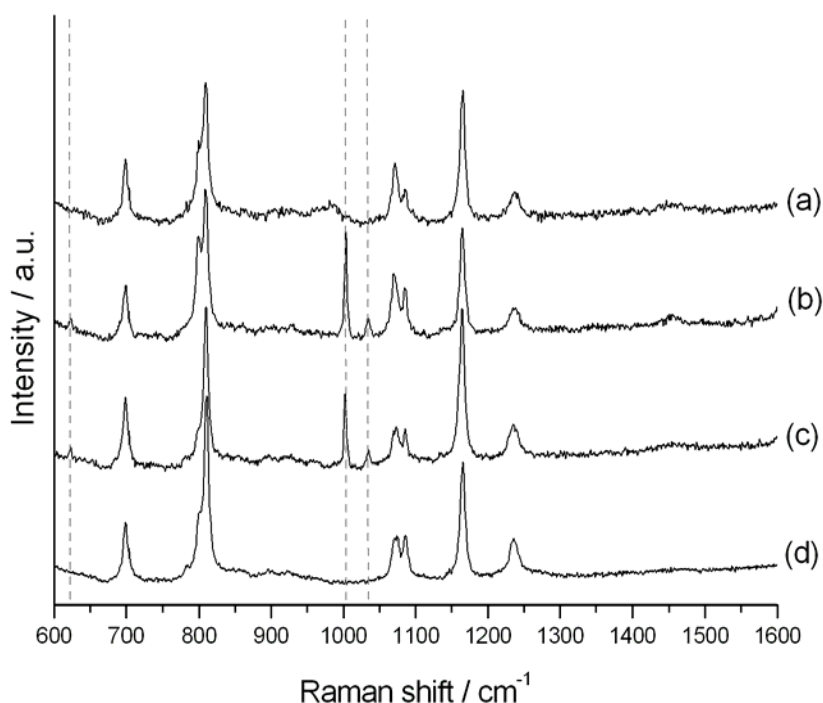
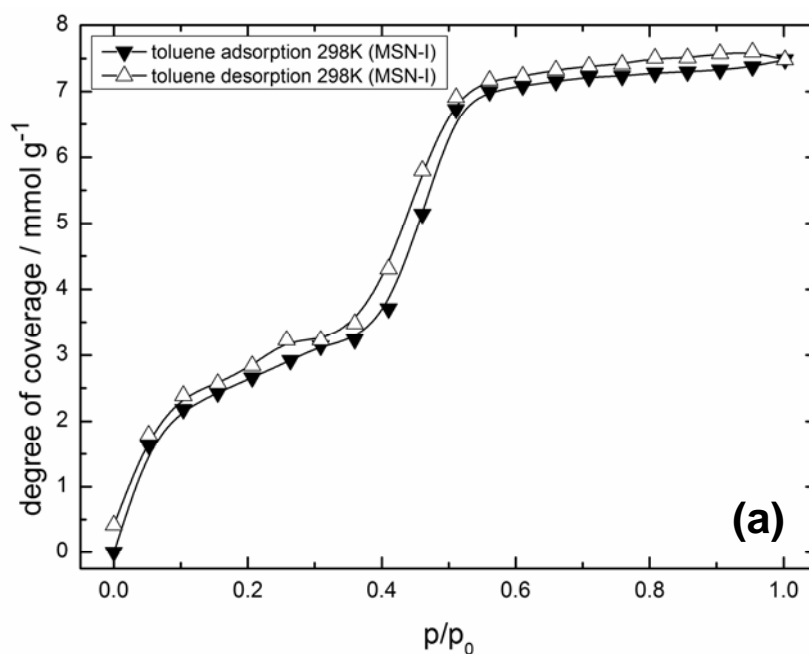


**Figure 7-7.** Raman spectra of the surface of QMC-chips coated with samples MSN-I (a), MSN-II (b), MSN-III (c) and of an uncoated QCM-device (d). Dashed lines mark the additional vibrations corresponding to the presence of phenyl groups.

Samples MSN-II and MSN-III show three additional bands emerging at 622, 1002 and 1032  $\text{cm}^{-1}$ , which can be assigned to the in-plane ring deformation (622) and C-H in-plane

vibrations (1002, 1032) of the phenyl group, respectively. The other bands belong to vibrations of the quartz plate, as can be seen by comparison with an uncoated QCM-chip. It is therefore concluded that the phenyl groups remain intact in the calcined films, which is also to be expected based on the thermal stability shown during TG analysis.

Toluene sorption isotherms at 298 K recorded with QCM-devices coated with the 3 samples are illustrated in Figure 7-8. The sorption of toluene on MSN-I shows a steep Type IV isotherm, and samples MSN-II and MSN-III exhibit Type IV isotherms as well. Type IV classified isotherms represent a high affinity of the gaseous molecules towards the adsorbent which is shown by the steep increase of toluene-loading at low relative pressures in all three samples. The determination of the heat of adsorption based upon sorption isotherms provides a quantitative refinement of the affinity of toluene during physisorption towards the three different types of sample surfaces.



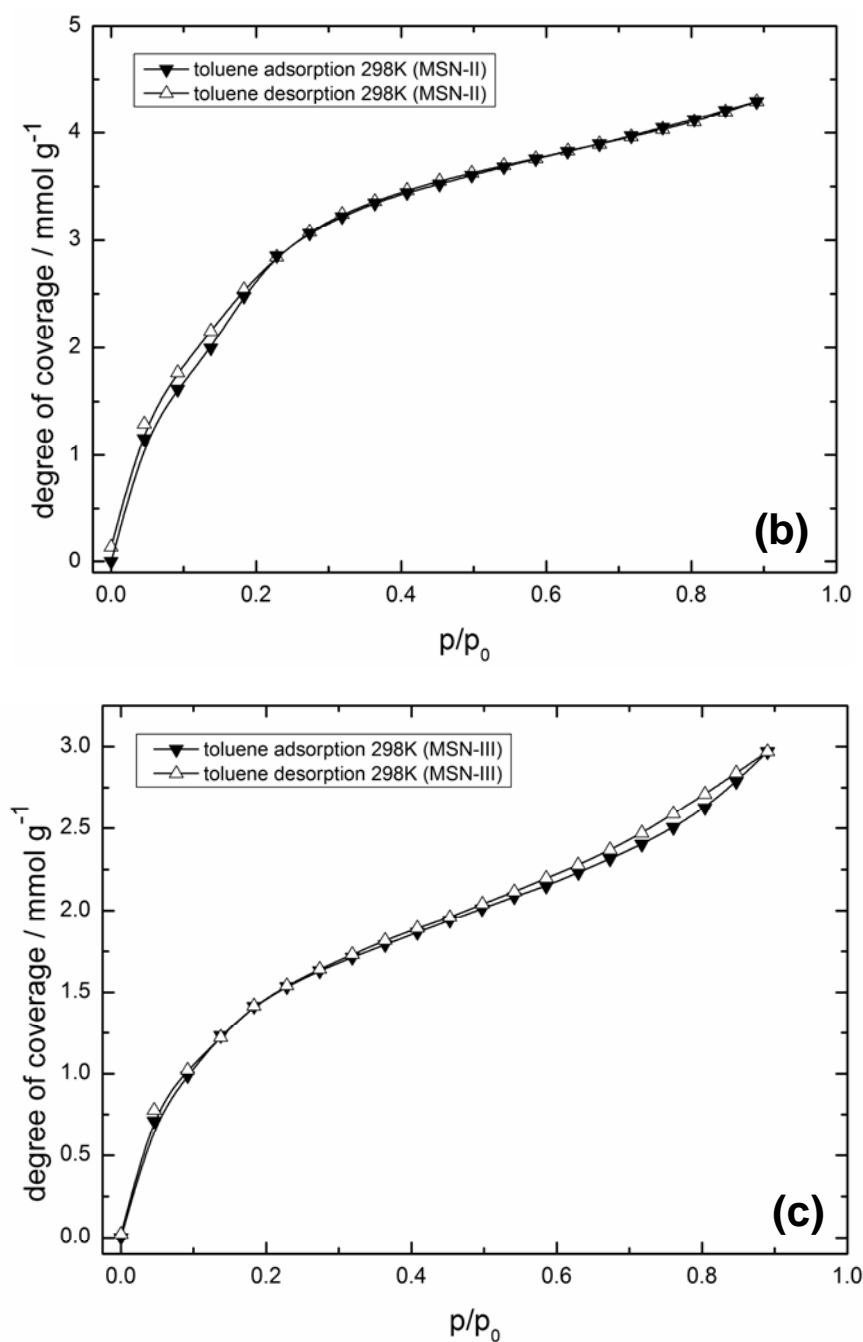


**Figure 7-8.** QCM toluene sorption isotherms at 298 K for samples MSN-I (a), MSN-II (b), and MSN-III (c).

Table 7-2 illustrates the isosteric heats of adsorption calculated at different degrees of coverage for all three samples. It should be mentioned that the determination of  $\Delta H_{\text{ads}}$  at isosteric conditions is not recommended in the isotherm region of adsorbate-adsorbate

adsorption as it would generate erroneous values which would be influenced by the adsorption of toluene on toluene. To overcome that problem the heats of adsorption were calculated according to the individual break point at which we still can assume sub-monolayer coverage of toluene adsorbing on each individual sample. Therefore, the heat of adsorption on sample MSN-III was evaluated at coverages of 0.75, 1.0 and 1.5 mmol·g<sup>-1</sup> (Table 7-2).

**Table 7-2.** Isosteric heats of adsorption in kJ·mol<sup>-1</sup> obtained from the sorption isotherms

$\theta$ mmol / g	MSN-I	MSN-II	MSN-III
0.75	-	-	23.9 ± 1.4
1.0	-	-	24.2 ± 0.6
1.5	17.8 ± 1.6	28.1 ± 1.2	24.1 ± 0.8
2.0	17.9 ± 1.6	32.2 ± 1.1	-
2.5	18.3 ± 1.5	31.6 ± 1.2	-
3.0	-	30.3 ± 1.2	-
<i>average</i>	<i>18.0 ± 1.6</i>	<i>30.5 ± 1.2</i>	<i>24.1 ± 1.0</i>

The lowest expected monolayer coverage of toluene is calculated assuming a space requirement of 116 Å<sup>2</sup> per molecule toluene (COSMO surface in the MoPac package of reference [21]) occupying all sorption sites with the  $\pi$ -electron system parallel to the surface (which is unlikely). In this case, a monolayer of toluene molecules would be present at a coverage of about 1.7 mmol·g<sup>-1</sup> (MSN-I), 1.7 mmol·g<sup>-1</sup> (MSN-II) and 1.8 mmol·g<sup>-1</sup> (MSN-III) (these values vary because of the different surface areas of the samples). Thus, determining the heats of adsorption at loadings below these values will ensure the desired sub-monolayer coverages. A closer look at the sorption isotherms of sample MSN-I and MSN-II shows that an almost linear correlation of relative pressure and coverage can be observed up to 2.5 mmol

$\text{g}^{-1}$  and  $3.0 \text{ mmol g}^{-1}$ , respectively. It is therefore assumed that toluene-toluene adsorption will only have a minor influence on the results within this data range. This is further supported by the fact that all variations of the loading parameter in this data range lead only to minimal variations in the calculated heat of adsorption.

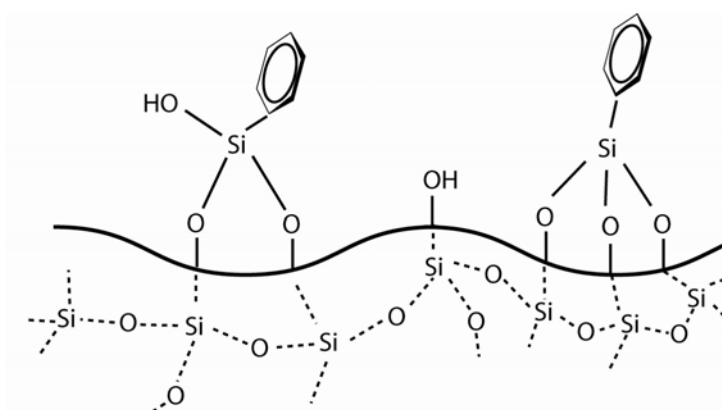
The unfunctionalized silica sample MSN-I exhibits the lowest heat of adsorption for toluene ( $18.0 \pm 1.6 \text{ kJ mol}^{-1}$ ). This is attributed to the relatively small affinity of the non-polar solvent vapor of toluene ( $0.375 \pm 0.01 \text{ Debye}$ )<sup>[20]</sup> to the relatively polar, silanol-rich internal surface of the silica material. This behavior is also reflected in the higher heats of adsorption of the samples bearing a phenyl-substituted surface. The post-synthesis grafted sample MSN-II shows a distinctive high affinity to toluene vapor which results in an average value for the heat of adsorption of  $30.5 \pm 1.2 \text{ kJ mol}^{-1}$  calculated from four different loadings ( $1.5, 2.0, 2.5$  and  $3.0 \text{ mmol g}^{-1}$ , see Table 7-2). The heat of adsorption for the phenyl-grafted sample MSN-II is the highest of all three, but still noticeably lower than the heat of vaporization of toluene ( $38.01 \text{ kJ mol}^{-1}$  at  $298 \text{ K}$ ).<sup>[20]</sup>

In contrast, the sample MSN-III which was phenyl-functionalized *via* co-condensation only reveals an average isosteric heat of adsorption of  $24.1 \pm 1.0 \text{ kJ mol}^{-1}$ , indicating a lower affinity of toluene molecules towards the co-condensed surface, although TGA data indicate a slightly higher concentration of phenyl groups (by  $2.5 \text{ \%wt}$ ). Reproducibility of the measurements was confirmed by a second set of samples prepared at identical conditions. The obtained values for the toluene heat of adsorption were  $18.6 \pm 1.4 \text{ kJ mol}^{-1}$ ,  $30.8 \pm 1.1 \text{ kJ mol}^{-1}$  and  $24.5 \pm 1.2 \text{ kJ mol}^{-1}$  for the unmodified, grafted and co-condensed sample, respectively. The heat of adsorption on these reproduced samples is thus matching the values obtained for MSN-I, MSN-II and MSN-III within the calculated error limits.

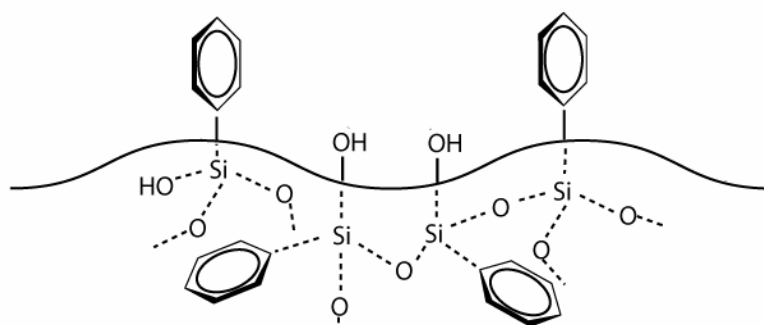
The observed differences between samples MSN-II and MSN-III regarding their heats of adsorption can be explained by taking into account the different localization of phenyl groups at the internal pore surface. The grafted sample offers the highest amount of freely available



phenyl groups that are accessible at the internal pore surface. By nature of the grafting procedure, all phenylsilane groups are concentrated at the internal and external sample surface where they replace up to three hydroxyl groups by condensation reactions (Scheme 7-1). Even though the co-condensed sample MSN-III contains somewhat more phenyl groups according to TGA data, this attachment scheme will not result in a significant capping of silanols, due to steric requirements, and will lead to possible incorporation of phenyl groups in the silica walls. This would result in a surface that could be considered, in terms of interaction forces, as an intermediate between the unfunctionalized and the grafted surface with respect to silanol concentration. The outer surface therefore still bears a large number of free hydroxyl groups and fewer phenyl groups than the grafted sample (Scheme 7-2). This results in a lower affinity and decreased heat of adsorption for the non-polar toluene molecules.



**Scheme 7-1.** Silica surface of phenyl-grafted sample MSN-II.



**Scheme 7-2.** Silica surface of co-condensed sample MSN-III.

The isotherms of all three samples confirm the good reversibility of the adsorption at 298 K, 313 K, 328 K and 343 K. Minor differences between the adsorption and sorption branches in terms of sorption capacity at identical relative pressures are attributed to possible drift of the experimental system. The isotherms at higher temperatures for samples MSN-I, MSN-II and MSN-III are available as supplemental information.

In order to demonstrate equilibration behavior of the system, one raw data set is illustrated in Figure 7-9 showing the decrease in frequency caused by increasing relative pressure (adsorption) and vice versa (desorption). The automated experimental setup records frequency changes at 4 temperatures, including a purging and heating step at a flow rate of 2000 ml N<sub>2</sub> per minute at 403 K (130 °C) before adjusting each new experimental temperature, to ensure the complete removal of residual toluene molecules.

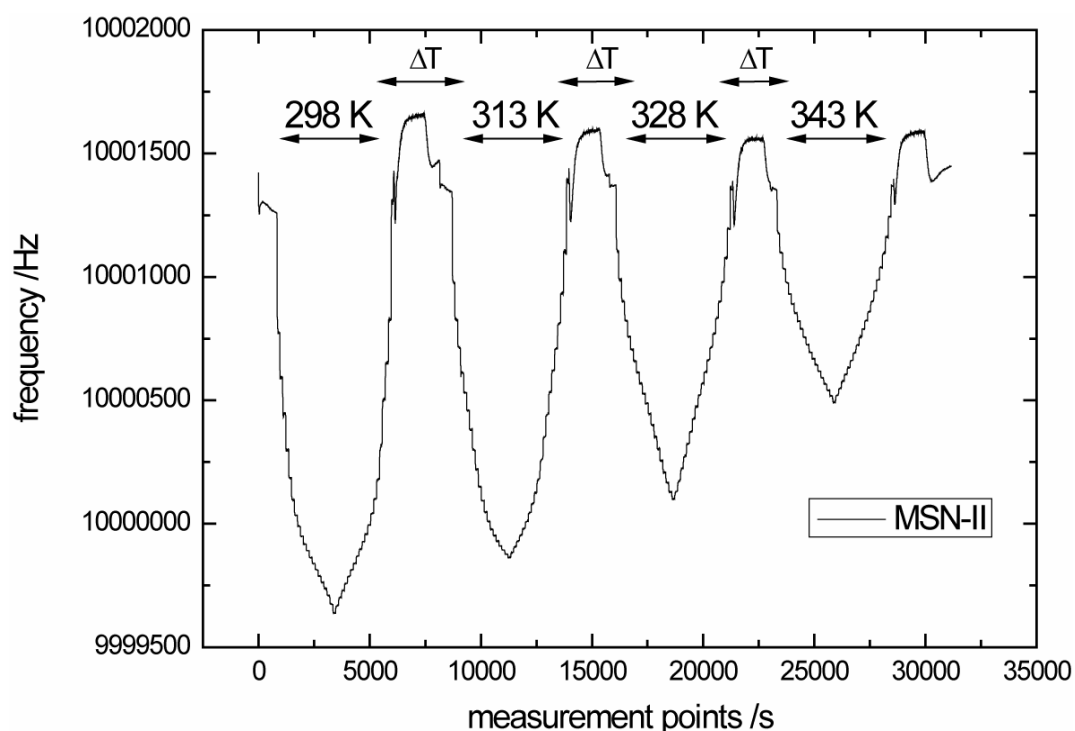


**Figure 7-9.** QCM raw data set for sample MSN-II acquired at 298 K, 313 K, 328 K and 343 K. The “ $\Delta T$ ” label indicates the heating and purging period at 403 K.

A magnified graph (see Figure 7-10) shows that equilibrium is reached during the experimental conditions for adsorption: within 100 s no measurable frequency changes are observed, while the initial partial pressure increase step (or decrease step) is very fast and completed within 5 seconds.

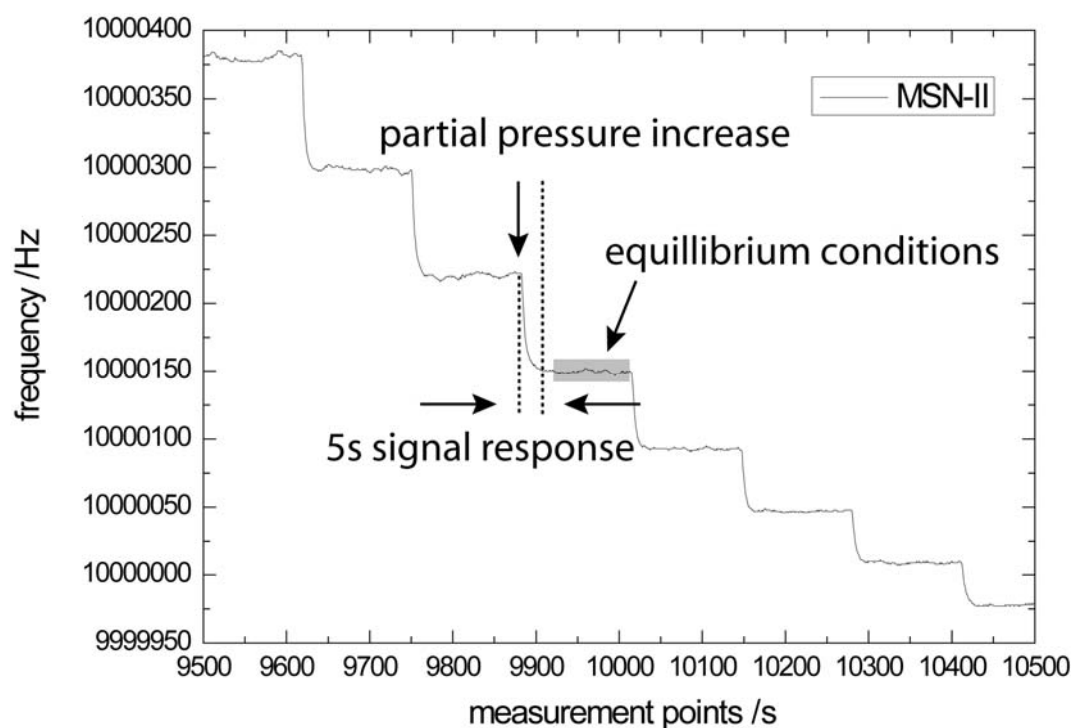


**Figure 7-10.** Magnified raw data set of the measurement for sample MSN-II recorded at 313 K.

## 7.5 Conclusions

A convenient and fast method for determining heats of adsorption in porous nanoparticles was demonstrated for the case of unfunctionalized and phenyl-functionalized mesoporous silica synthesized by co-condensation and grafting routes. Although both samples incorporate comparable amounts of phenyl groups, the resulting surface functionalization differs significantly with respect to the affinity of the pores towards toluene. The effect of surface functionalization on the heat of adsorption of toluene has been quantified using QCM measurements at different temperatures. While co-condensed material shows only a 33 % increase of the heat of adsorption, with respect to the unfunctionalized host, the increase is more than doubled for grafted material. It is thus demonstrated that QCM sorption studies can distinguish and quantify the differences between a sample where most phenyl groups are placed on the silica surface by post-synthesis treatment and a sample where phenyl groups are partially dispersed in the silica framework during synthesis.

The QCM-based sorption method offers the capability to acquire isotherms of volatile vapors and the corresponding heats of adsorption at the same time, while using very small sample amounts in the range of about 5 to 30  $\mu\text{g}$ . The small amounts of sample, presented in the form of a thin film, additionally result in a very fast sensor response due to the short diffusion times, thus allowing the measurements in this study to be completed in 4 - 6 hours. On the other hand, standard gravimetric or volumetric determination of sorption isotherms utilizes sample masses in the range of milligrams, thus requiring significantly more time to reach equilibrium conditions.<sup>[24]</sup> Possible applications of such QCM-based techniques include the screening of potential catalytically active materials in terms of affinity for different gaseous species, development of sensors for volatile compounds, and evaluation of membrane materials. The method is capable, with statistical significance because it averages over the entire sample, of giving more insights into the nature of surface modifications and their influence on sorption properties.

## 7.6 References

- [1] D. P. Serrano, G. Calleja, J. A. Botas, F. J. Gutierrez, *Industrial & Engineering Chemistry Research* **2004**, 43, 7010.
- [2] M. Thommes, R. Koehn, M. Froeba, *Journal of Physical Chemistry B* **2000**, 104, 7932.
- [3] J. P. Fox, S. P. Bates, *Langmuir* **2005**, 21, 4746.
- [4] C. Nguyen, C. G. Sonwane, S. K. Bhatia, D. D. Do, *Langmuir* **1998**, 14, 4950.
- [5] S. Z. Qiao, S. K. Bhatia, *Microporous and Mesoporous Materials* **2005**, 86, 112.
- [6] T. Nassivera, A. G. Eklund, C. C. Landry, *Journal of Chromatography, A* **2002**, 973, 97.
- [7] T. F. Narbeshuber, H. Vinek, J. A. Lercher, *Journal of Catalysis* **1995**, 157, 388.
- [8] B. A. Williams, S. M. Babitz, J. T. Miller, R. Q. Snurr, H. H. Kung, *Applied Catalysis, A: General* **1999**, 177, 161.
- [9] C. E. Ramachandran, B. A. Williams, J. A. van Bokhoven, J. T. Miller, *Journal of Catalysis* **2005**, 233, 100.
- [10] D. Ramirez, S. Qi, M. J. Rood, K. J. Hay, *Environmental Science and Technology* **2005**, 39, 5864.
- [11] H. Vinh-Thang, Q. Huang, M. Eic, D. Trong-On, S. Kaliaguine, *Langmuir* **2005**, 21, 5094.
- [12] Y. He, N. A. Seaton, *Langmuir* **2006**, 22, 1150.
- [13] G. Sauerbrey, *Zeitschrift fuer Physik* **1959**, 155, 206.
- [14] D. R. Denison, *Journal of Vacuum Science and Technology* **1973**, 10, 126.
- [15] C.-S. Lu, O. Lewis, *Journal of Applied Physics* **1972**, 43, 4385.
- [16] S. Angloher, J. Kecht, T. Bein, *Chemistry of Materials* **2007**, 19, 3568.
- [17] C. Zapilko, M. Widenmeyer, I. Nagl, F. Estler, R. Anwender, G. Raudaschl-Sieber, O. Groeger, G. Engelhardt, *Journal of the American Chemical Society* **2006**, 128, 16266.
- [18] D. Do, *Adsorption analysis: Equilibria and kinetics*, Imperial College Press, **1998**.
- [19] K. Möller, J. Kobler, T. Bein, *Advanced Functional Materials* **2007**, 17, 605.
- [20] D. Lide, *Handbook of Chemistry and Physics*, CRC Press, **2004-2005**.
- [21] Calculated with *Chem3D*; Cambridgesoft, 100 CambridgePark Drive, Cambridge, MA 02140.
- [22] F. Kleitz, W. Schmidt, F. Schuth, *Microporous and Mesoporous Materials* **2003**, 65, 1.
- [23] M. C. Burleigh, S. Jayasundera, C. W. Thomas, M. S. Spector, M. A. Markowitz, B. P. Gaber, *Colloid and Polymer Science* **2004**, 282, 728.
- [24] L. Huang, Q. Huang, H. Xiao, M. Eic, *Microporous and Mesoporous Materials* **2007**, 98, 330.



## 8 Selective functionalization of the outer and inner surfaces in mesoporous silica nanoparticles\*

### 8.1 Introduction

Mesoporous structured materials have attracted a great deal of interest in recent years due to their ordered porosity and high internal surface area.<sup>[1, 2]</sup> If additional molecular functionality can be introduced in a controlled way, it is possible to control many key properties, including hydrothermal stability, surface polarity, and the density of attached organic moieties, which are crucial for applications in sorption, catalysis, templating and host-guest chemistry.<sup>[3, 4]</sup> Within these growing fields, new advanced applications begin to emerge that require more sophisticated materials, i.e., drug delivery systems with multiple functionalities.<sup>[5, 6]</sup> Thus, the selective functionalization of specific locations inside mesoporous materials becomes a point of interest in order to gain greater control over the surface properties.

A recent example of such work includes the separate functionalization of the inner surface in micropores and mesopores of SBA-15 silica.<sup>[7]</sup> By partial cleavage of the P123 surfactant, the mesopore surface could be functionalized with trimethylchlorosilane while the micropores remained inaccessible until a subsequent heating treatment removed the remaining surfactant. The micropore surface was then functionalized with trivinylchlorosilane and reacted with a palladium complex in order to generate a final product with fully accessible mesopores and Pd nanoparticles located inside the micropores.

Other examples of site-selective functionalization include the generation of Janus particles, in which the surfaces located on both hemispheres of a round particle are of different types.<sup>[8]</sup> Such particles were produced from non-porous fused silica spheres with diameters of 800 nm and 1.5  $\mu\text{m}$ , respectively. The selectivity was achieved by fixating the particles at the liquid-liquid interface of emulsified molten wax in water, followed by solidification of the wax and subsequent functionalization of the half-embedded silica.<sup>[9]</sup> This approach allowed production

\* J. Kecht, A. Schloßbauer, T. Bein, submitted.

of bipolar (cationic-anionic) and surfactant-like (cationic-hydrophobic) silica Janus particles in gram-scale quantities.

Recent investigations center on the selective functionalization of the outer and inner surface in mesoporous silica systems.<sup>[10-12]</sup> These locations are especially relevant for mesoporous silica nanoparticles with sizes below 100 nm, which possess a high external surface area in addition to the inner surface of the mesopores. Mesoporous silica nanoparticles can be prepared as stable colloidal suspensions and can subsequently be used for the construction of hierarchical porous materials and thin films, thus offering many possibilities for new applications in research fields such as sensing, optics and drug delivery.<sup>[5, 13]</sup> Functionalization of the external nanoparticle surface is of paramount importance for colloidal stability and interaction with the environment, i.e., with living cells and other biological substrates, and allows the attachment of large molecular moieties and nanoscale building blocks without reducing pore size and available free pore volume. On the other hand, functionalization of the internal pore system is needed in order to control and fine-tune the host-guest chemistry, i.e., for drug delivery, catalysis and sorption applications.

Recently, Fmoc (9-fluorenylmethyloxycarbonyl) protected alkylamines grafted on mesoporous silica spheres were differentially functionalized by diffusion-based cleavage with piperidine solution.<sup>[12]</sup> Moreover, it was shown that during grafting reactions the external surface is more accessible and grafted preferentially to the inner pore system even in empty calcined MCM-41.<sup>[10]</sup> Functional groups deposited at the channel opening may also slow down the diffusion of further grafting reagents, thus resulting in an inhomogeneous distribution of attached groups.<sup>[14]</sup> Similar results were obtained for template-filled as-synthesized MCM-41 which upon exposure to trimethylsilylchloride was functionalized mainly on the external surface.<sup>[11]</sup> However, several publications demonstrate that grafting reagents including various chloro- and trialkoxysilanes can easily and efficiently enter the template-filled channels and functionalize the inner pore systems, in some cases even



producing extracted materials by completely replacing the surfactant molecules.<sup>[15-18]</sup> In fact, results of the present work reveal that functionalization inside template-filled pores already occurs at very mild conditions, i.e. after reaction for 4 h at room temperature.

In view of these challenges we present a new approach for the highly selective control of the outer versus the internal pore surface in colloidal mesoporous silica nanoparticles. By using a site-selective co-condensation approach, the particle is functionalized *in situ* either during or after the growth process. In comparison to grafting approaches, much greater control over the amount and density of the functional groups is achieved. By choosing suitable reaction conditions, unwanted functionalization of the inner pore surface can be completely inhibited. Furthermore, functionalization by co-condensation is known to produce a more homogeneous surface functionalization than grafting.

## 8.2 Experimental Section

**Reagents.** Tetraethyl orthosilicate (TEOS, Fluka, >98%), ammonia (Aldrich, 25% in H<sub>2</sub>O) phenyltriethoxysilane (PTES, Aldrich, 98%), aminopropyltriethoxysilane (APTES, ABCR, 96 %), 11-bromo-undecyltrimethoxysilane (BUTMS, ABCR, 95%), cetyltrimethylammonium bromide (CTAB, Aldrich, 95%), cetyltrimethylammonium chloride (CTAC, Fluka, 25% in H<sub>2</sub>O) and triethanolamine (TEA, Aldrich, 98%) were used as received without further purification. Doubly distilled water from a Millipore system (Milli-Q Academic A10) was used for all synthesis and purification steps.

**Preparation of micrometer-sized MCM-41 particles.** MCM-41 was prepared according to a published procedure.<sup>[19]</sup> To a stirred solution of CTAB (2.39 g, 6.56 mmol), water (125 g, 6.94 mol), ethanol (12.5 g, 271 mmol) and aqueous ammonia (25 %wt, 9.18 g, 135 mmol) in a 300 mL polypropylene reactor, the amount of 10.03 g TEOS (48.19 mmol) was added. The resulting mixture has a molar composition of 1 TEOS : 0.14 CTAB : 144 H<sub>2</sub>O : 5.63 ethanol :

2.8 NH<sub>3</sub>. After stirring for 2 hours at room temperature, the reaction mixture was filtered off and washed with 50 mL water. The resulting white powder was dried at 60 °C for 12 h.

**Preparation of colloidal mesoporous silica (CMS) nanoparticles.** Mesoporous silica nanoparticles were prepared according to reference <sup>[20]</sup> from reaction mixtures with a molar composition of 1 TEOS: 0.20 CTAC: 10.37 TEA: 130.15 H<sub>2</sub>O. The combined TEOS (1.92 g, 9.22 mmol) and TEA (14.3 g, 95.6 mmol) were heated for 20 minutes at 90 °C without stirring in a 100 mL polypropylene reactor. A solution of CTAC (25 % in water, 2.41 mL, 1.83 mmol) and water (21.7 g, 1.21 mol) preheated to 60 °C was added, and the resulting mixture was stirred at room temperature for 12 hours. After addition of 100 mL ethanol, the mesoporous silica nanoparticles were separated by centrifugation, redispersed in ethanol and extracted according to the procedure described below.

**General procedure for the selective functionalization by grafting of template-containing MCM-41.** As-synthesized MCM-41 (360 mg) was added to dry toluene (5 mL) in a dry flask under nitrogen atmosphere. After addition of 1 mmol of the respective functionalized trialkoxysilane, the reaction mixture was stirred for 4 hours at room temperature or under reflux conditions (see table 1). The functionalized MCM-41 was filtered off and washed with 20 mL each of toluene, methanol, and water before being exposed to the MCM-41 extraction procedure. In the case of CMS materials, the grafting was performed by direct reaction of the ethanolic suspensions (~3 wt%) with the triethoxysilanes and purification of the resulting suspensions via multi-step centrifugation (see Table 8-1).

**Table 8-1.** Samples functionalized by post-synthesis grafting of template-containing mesoporous silica.

sample name	material	grafting agent (RTES)	reaction temperature
Ph-MS 1	MCM-41	PTES	25 °C
Ph-MS 2	MCM-41	PTES	reflux
AP-MS 3	MCM-41	APTES	25 °C
BU-MS 4	MCM-41	BUTMS	25 °C
Ph-CMS 5	CMS	PTES	25 °C
AP-CMS 6	CMS	APTES	25 °C

**General procedure for the selective functionalization of CMS by co-condensation.** The reactants are mixed following the synthesis procedure for CMS. However, a second set of reactants is added at specific time periods after combination of the initial TEOS/TEA and CTAC solutions (see Table 8-2). The reactants were added to the stirred reaction mixture with an Eppendorf micropipette and consist of TEOS and a functionalized triethoxysilane (RTES) in varying ratios. The combined amount of both silanes was 185  $\mu\text{mol}$  in all samples, i.e., 2 % of the total amount of “Si” in the initial CMS synthesis. The resulting mixture was stirred at room temperature for 12 hours followed by purification and extraction as described for CMS.

**Table 8-2.** Samples obtained via *in situ* functionalization by co-condensation.

sample name	triethoxysilane (RTES)	TEOS : RTES relative molar ratio <sup>a</sup>	TEOS : RTES volumes [ $\mu\text{L}$ : $\mu\text{L}$ ]	addition time [min]
AP-CMS 7	APTES	0.5 : 0.5	20.5 : 21.5	5
AP-CMS 8	APTES	0.5 : 0.5	20.5 : 21.5	10
AP-CMS 9	APTES	0.5 : 0.5	20.5 : 21.5	30
AP-CMS 10	APTES	0.5 : 0.5	20.5 : 21.5	60
AP-CMS 11	APTES	0 : 1	0 : 43.0	30
AP-CMS 12	APTES	0.8 : 0.2	32.8 : 8.6	30
AP-CMS 13	APTES	0.95 : 0.05	39.25 : 2.1	30
Ph-CMS 14	PTES	0.5 : 0.5	20.5 : 22.3	30
Ph-CMS 15	PTES	0 : 1	0 : 44.6	30

<sup>a</sup> total silane amount = 185  $\mu\text{mol}$

**Extraction of MCM-41 and CMS.** Extraction of the organic template from the MCM-41 and CMS materials was performed by heating 1 g twice under reflux at 90°C for 30 minutes of in a solution containing 2 g ammonium nitrate in 100 mL ethanol, followed by 30 minutes under reflux in a solution of 4 g concentrated hydrochloric acid in 100 mL ethanol. The MCM-41 material was separated by filtration and the CMS nanoparticles were purified by centrifugation. Both types of materials were washed with ethanol after each extraction step. MCM-41 and CMS materials were obtained as white solid powders and as clear ethanolic suspensions, respectively.

### 8.3 Characterization

Dynamic light scattering (DLS) and zeta potential measurements were performed on a Malvern Zetasizer-Nano instrument equipped with a 4 mW He-Ne laser (632.8 nm) and avalanche photodiode detector. DLS measurements were directly recorded in ethanolic colloidal suspensions. For determination of the zeta potential curves, one drop of the ethanolic suspension (~3 %wt.) was mixed with 1 mL commercial Hydrion Buffer solution of the appropriate pH prior to measurement. This approach allowed fast and reproducible zeta potential measurements which are comparable to the respective curves obtained by pH adjustment via addition of hydrochloric acid (see supporting information). Thermogravimetric analyses (TGA) of the bulk samples were performed on a Netzsch STA 440 C TG/DSC (heating rate of 10 K/min in a stream of synthetic air of about 25 mL/min). Raman spectra were recorded on a Jobin Yvon Horiba HR800 UV Raman microscope using a HeNe laser emitting at 632.8 nm. IR spectra were recorded on a Bruker Equinox 55 under diffuse reflectance conditions (samples were mixed with KBr, spectra are background subtracted). Scanning transmission electron microscopy (STEM) was performed on a Titan 80-300 kV microscope operating at 300 kV equipped with a high-angle annular dark field detector. STEM samples stained with iridium were prepared by adding 3 drops of an aqueous 1 M solution of  $\text{IrCl}_3$  to 3 mL of an ethanolic/aqueous CMS suspension (~3 wt%), followed by two steps of centrifugation, washing with ethanol, and subsequent drying of a drop of the resulting diluted colloidal suspension on a carbon-coated copper grid. Nitrogen sorption measurements were performed on a Quantachrome Instruments NOVA 4000e at 77 K. For calculations of pore sizes and volumes a NLDFT equilibrium model of  $\text{N}_2$  on silica was used. The BET model was applied to evaluate the surface areas.

## 8.4 Results and Discussion

In order to selectively functionalize the inner and outer surface of mesoporous silica nanoparticles two different approaches based on grafting and co-condensation reactions were investigated and compared.

The first approach is based on the grafting of template-containing mesoporous materials. Micrometer-sized MCM-41 type silica particles were employed as a model system with a high ratio of inner to outer surface. By performing the grafting while the mesopore channels are occupied by template molecules, diffusion of the grafting reactant into the porous structure is limited thus leading to a preferential functionalization of the outer particle surface. As-synthesized samples were grafted with phenyltriethoxysilane (PTES) and aminopropyltriethoxysilane (APTES) at different temperatures before extraction of the organic template (see Table 8-1). After the grafting procedure, the template was removed by extraction prior to further characterization. Thermogravimetric analysis was performed in order to determine the amount of incorporated phenyl groups (Figure 8-1).

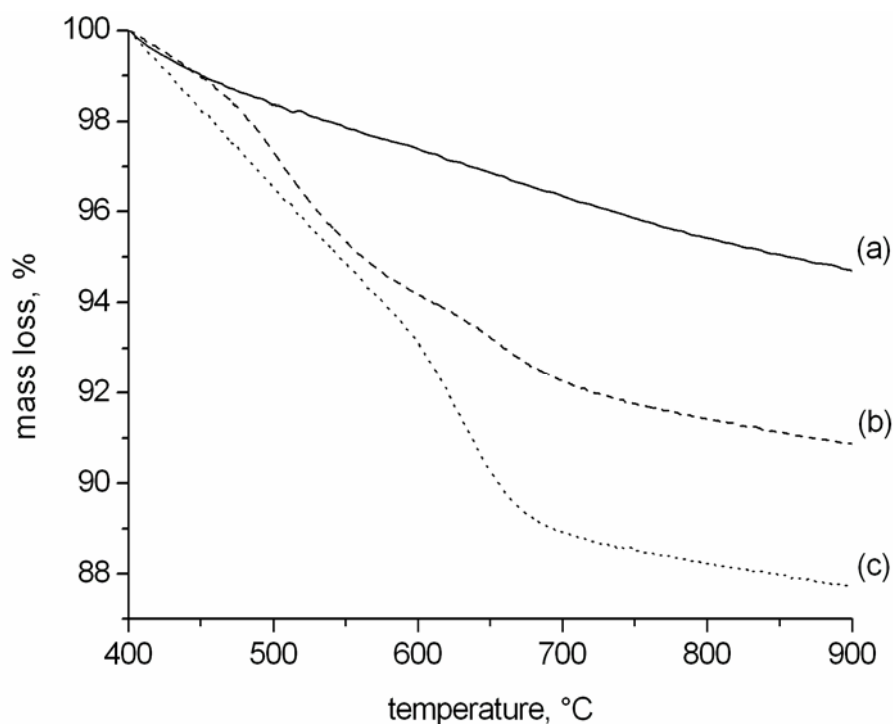


**Figure 8-1.** Thermogravimetric data for unfunctionalized MCM-41 (a), and phenyl-functionalized samples Ph-MS 1 (b) and Ph-MS 2 (c).

Due to the thermal stability of the aromatic ring, combustion of grafted phenyl occurs at elevated temperatures over 400°C, in contrast to most aliphatic groups which decompose in a temperature range between 110 °C and 400 °C.<sup>[21]</sup> Extracted mesoporous silica without additional grafting shows only a minor weight loss over 400 °C which can be attributed to silanol condensation (Figure 8-1a). Template-containing materials grafted with PTES at room temperature and under reflux conditions display a significantly higher weight loss in this temperature range due to the incorporated phenyl groups (Figure 8-1bc; TG data for the temperature range 25-900 °C can be found in the supporting information). As can be seen, the phenyl content inside the mesoporous materials strongly depends on the grafting temperature, and a lower amount is incorporated at room temperature as compared to reflux conditions. These observations were confirmed by nitrogen sorption. Correspondingly, samples with higher phenyl contents in TGA display smaller pore diameters (Figure 8-2; Table 8-3; the corresponding isotherms can be found in the supporting information). However, a minor reduction of the pore diameter is observed in samples obtained by grafting of template-containing materials even at mild conditions (Figure 8-2).

**Table 8-3.** Surface areas and pore volumes determined from nitrogen sorption.

sample name	surface area [m <sup>2</sup> /g]	pore volume [cc/g]
MCM-41	1022	0.772
Ph-MS 1	1103	0.714
Ph-MS 2	1142	0.597
AP-MS 3	990	0.669
BU-MS 4	989	0.672
CMS	1152	0.852 <sup>a</sup>
Ph-CMS 5	886	0.606 <sup>a</sup>
AP-CMS 6	597	0.299 <sup>a</sup>

<sup>a</sup> only cumulative pore volumes for pores < 8 nm are specified here due to the considerable textural porosity of CMS samples

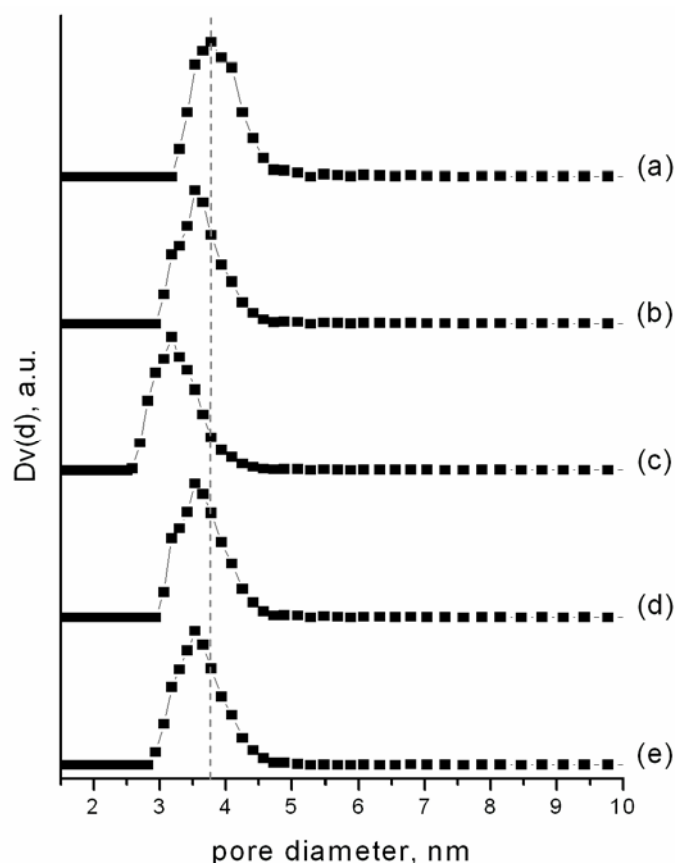


**Figure 8-2.** Pore diameters derived from nitrogen sorption isotherms of unfunctionalized MCM-41 (a) and samples Ph-MS **1** (b), Ph-MS **2** (c), AP-MS **3** (d), and BU-MS **4** (e).

It can therefore be concluded that 4 hours at room temperature are sufficient to at least partially functionalize the inside of the filled mesopores, and that at higher temperatures it is possible to replace a major part of the template with the grafting reagent. Similar observations were made for template-containing MCM-41 grafted with APTES and BUTMS (Figure 8-2) and for colloidal mesoporous silica (CMS) samples grafted with APTES and PTES (Figure 8-3). In case of the nanoscale particles with shorter diffusion paths, the functionalization by expulsion of template molecules can be observed even more clearly, especially by grafting with APTES (Figure 8-3c). The presence of the corresponding organic moieties in the materials was also confirmed by Raman spectroscopy (Figure 8-4).



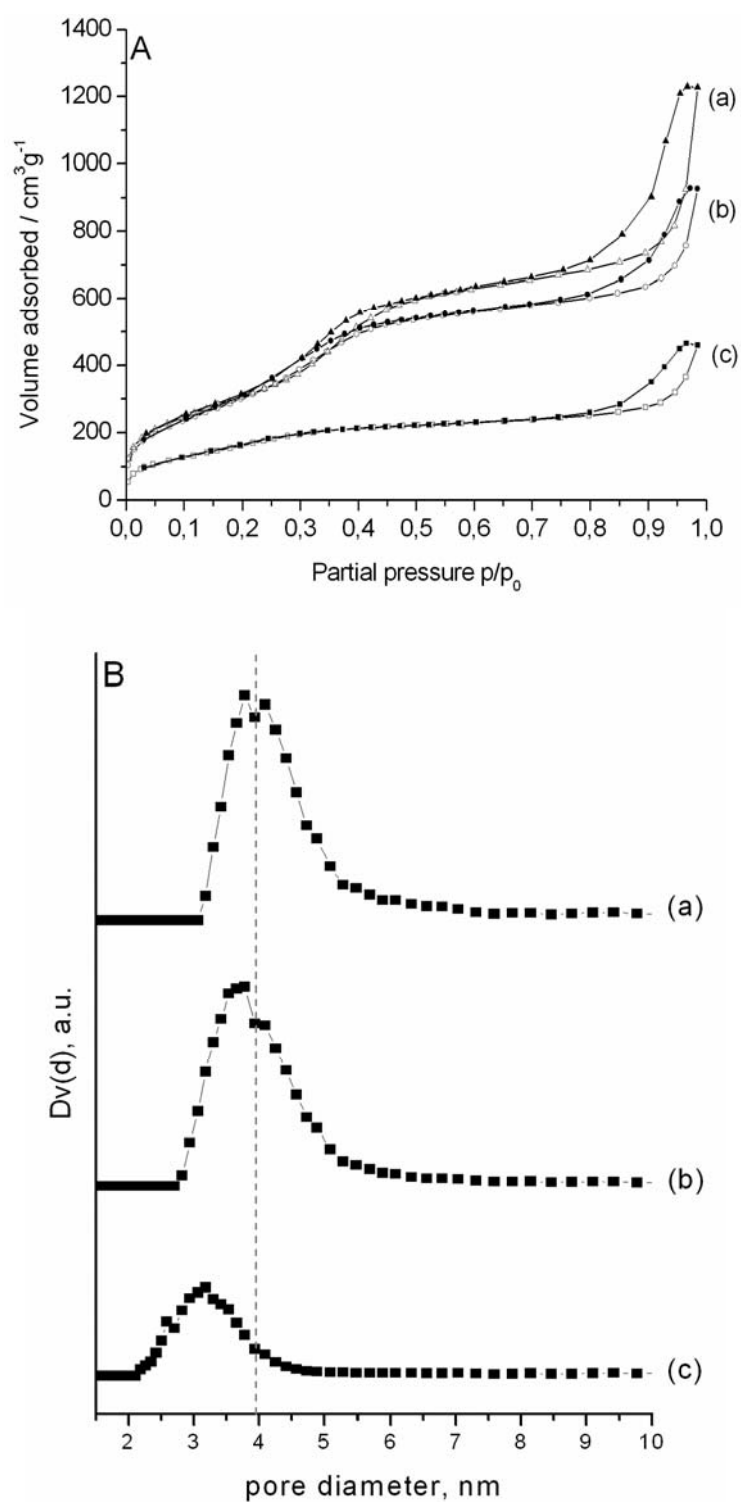


**Figure 8-3.** Nitrogen sorption isotherms (A) and pore size distributions (B) of unfunctionalized CMS (a) and samples Ph-CMS 5 (b) and AP-CMS 6 (c).

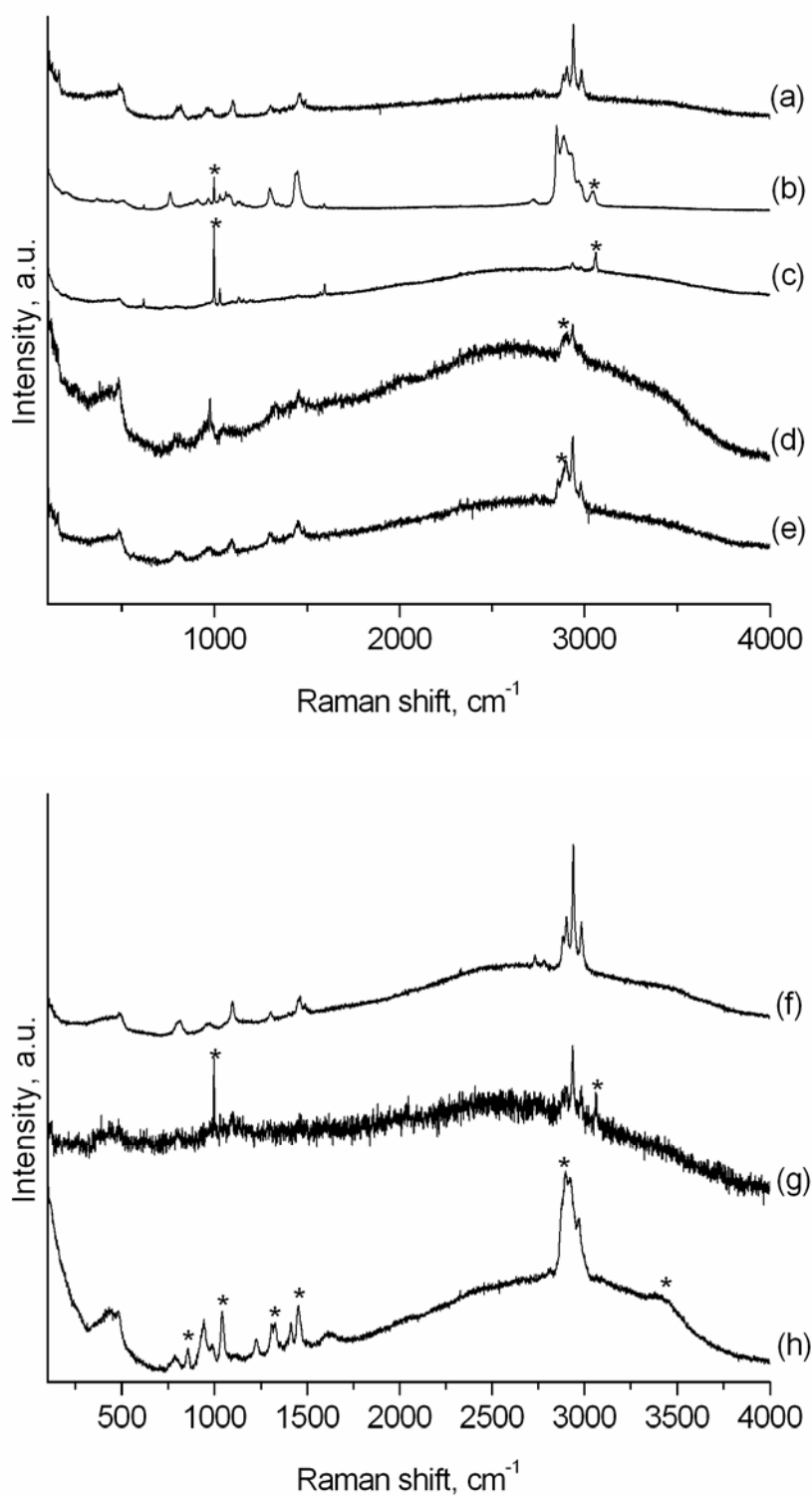


**Figure 8-4.** Raman spectra of extracted MCM-41 (a) and samples Ph-MS **1** (b), Ph-MS **2** (c), AP-MS **3** (d), and BU-MS **4** (e), as well as extracted CMS (f) and samples Ph-CMS **5** (g) and AP-CMS **6** (h). Bands marked with asterisks are assigned below.

## Bands corresponding to phenyl groups

998 $\text{cm}^{-1}$	aromatic C-H in plane deformation vibration
3063 $\text{cm}^{-1}$	aromatic C-H stretching vibration

## Bands corresponding to aminopropyl groups

856 $\text{cm}^{-1}$	R- <u>CH<sub>2</sub></u> -NH <sub>2</sub> rocking
1043 $\text{cm}^{-1}$	C-N stretch
1311 $\text{cm}^{-1}$	R- <u>CH<sub>2</sub></u> -NH <sub>2</sub> twisting
1328 $\text{cm}^{-1}$	R- <u>CH<sub>2</sub></u> -NH <sub>2</sub> wagging
1452 $\text{cm}^{-1}$	R- <u>CH<sub>2</sub></u> -NH <sub>2</sub> def.
2850-2900 $\text{cm}^{-1}$	R- <u>CH<sub>2</sub></u> -NH <sub>2</sub> sym. and asym. stretch
~3400 $\text{cm}^{-1}$	N-H stretch

## Bands corresponding to 11-bromoundecyl groups

2850-2900 $\text{cm}^{-1}$	chain CH <sub>2</sub> sym. and asym. stretch
----------------------------	--

Occluded template slows the diffusion of the grafting reactant into the pores, therefore favoring the preferential functionalization at the outer surface. As demonstrated above, diffusion into the pores can be further limited by lowering of the grafting temperature. However, even at mild conditions a small part of the reactants diffuses into the structure and functionalizes the inner pore surface to a significant degree. This behavior is problematic for certain applications, for example, the attachment of large moieties is not possible without causing pore blocking. Furthermore, a precise control over the amount and location of functional groups is not possible by this grafting-based method.

In our novel approach addressing these issues, colloidal mesoporous silica (CMS) nanoparticles were functionalized *in situ* during their growth process by site-selective co-condensation instead of post-synthesis grafting.

CMS materials were synthesized according to our previously published procedures.<sup>[20]</sup> TEOS was hydrolyzed in a reaction mixture containing CTAC and triethanolamine, resulting in high nucleation rates and slow subsequent growth of the generated seeds. By using this method, stable ethanolic suspensions of mesoporous nanoparticles with sizes below 100 nm were obtained after extraction. Co-condensed CMS can be obtained by incorporation of organosilanes in the batch composition as described in previous studies.<sup>[22]</sup>

By the addition of small amounts (2 mol% of total silane content) of a mixture of functionalized triethoxysilanes (RTES) and TEOS at specific times during synthesis, it is possible to control the location of the organic moieties. Depending on the addition time, the functionalized groups are either dispersed more homogeneously throughout the particle or concentrated inside a shell in the outer regions (Figure 8-5).

As demonstrated in the following, the concentration of functional groups on the external surface increases at later addition times due to particle growth. If the addition takes place after complete growth of the particle, the functionalized silanes condense only on the last layer, i.e. on the outer particle surface.

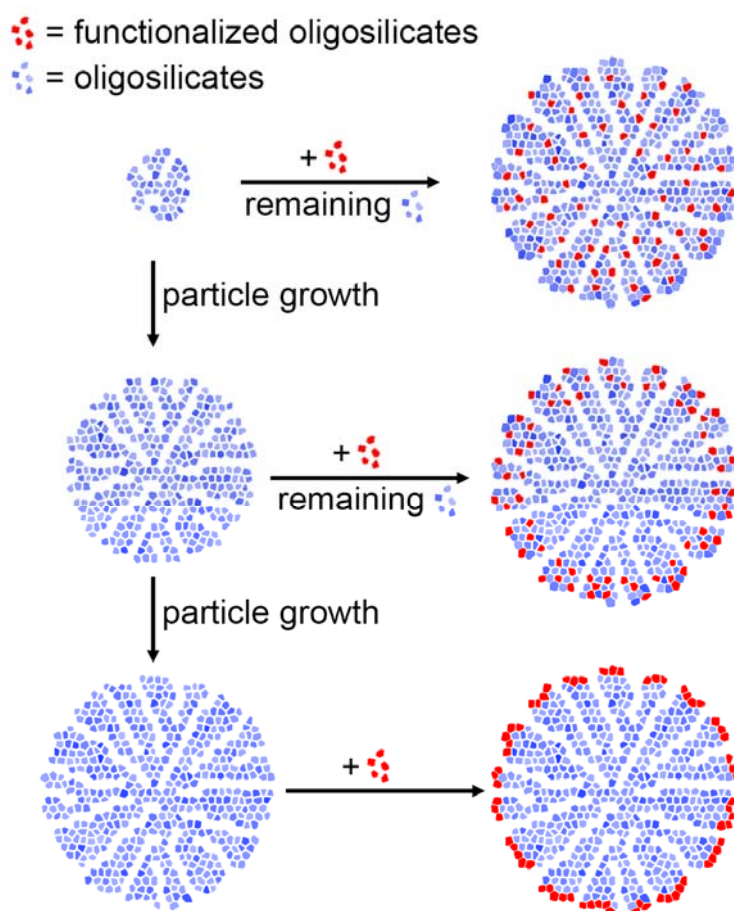


**Figure 8-5.** Distribution of functional groups depending on the addition time of the organosilane component during synthesis.

In order to monitor this change in density of functional groups on the external surface, zeta potential measurements were performed at pH values between two and six on samples prepared by addition of an APTES/TEOS mixture (molar ratio 1:1) at different stages of particle growth (Figure 8-6). The use of zeta potential measurements for the determination of the amount and location of amine functionalities in mesoporous silica has been reported in the literature.<sup>[23, 24]</sup>

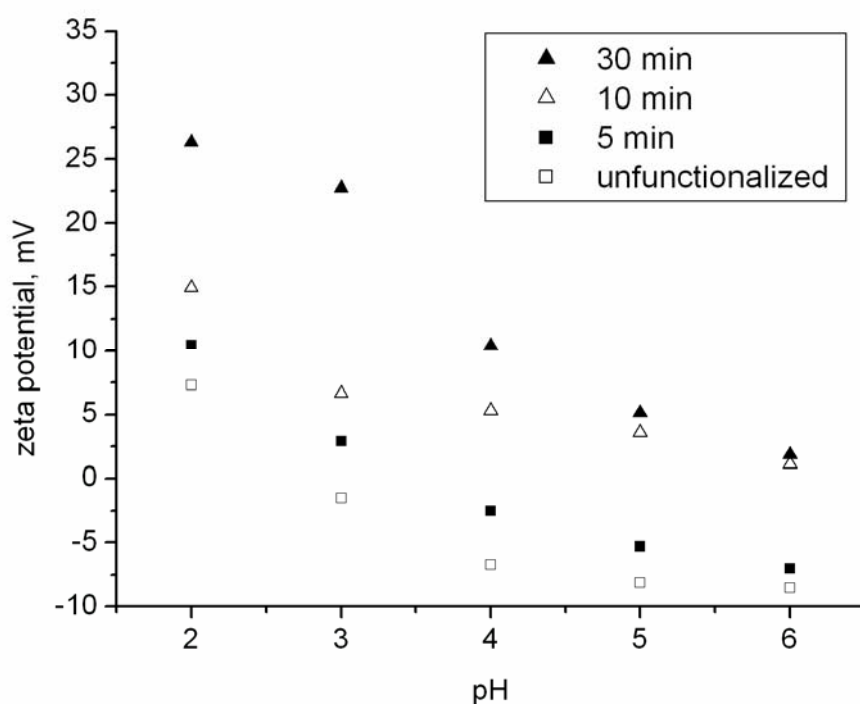


**Figure 8-6.** Zeta potential of samples prepared by variation of the addition time of the APTES/TEOS mixture: samples AP-CMS 9 (filled triangles), AP-CMS 8 (empty triangles), AP-CMS 7 (filled squares), and unfunctionalized CMS (empty squares).

The incorporated aminopropyl moieties are protonated at acidic pH values and carry a positive charge. A higher density of such groups on the outer particle layer thus leads to increased zeta potential curves as they affect the overall surface charge. Correspondingly, functional groups located at the interior surface, i.e. the channel walls of the mesopores, do not contribute to the zeta potential.

As can be seen, the zeta potential and thus the concentration of aminopropyl groups on the outer surface is strongly dependent upon the time of addition. Early APTES/TEOS addition, for example after 5 minutes, only leads to a minor increase of the zeta potential curve as the organic groups are dispersed throughout a large volume of the particle and only a few are located on the external surface. However, addition of the same APTES/TEOS amount at later times, i.e. after 10 and 30 minutes, generates more positive surface charges (Figure 8-6).

Interestingly, increasing the addition time above 30 minutes does not lead to significantly higher zeta potentials, as the particles are fully grown at this point. The observed zeta potential obtained after an addition delay of 30 minutes is about half that of a completely APTES-saturated surface. This observation is in accordance with the employed APTES/TEOS ratio of 1:1 and proves the high concentration of positively charged functional groups at the outer interface. Despite the small amounts of employed organosilane (2%), the organosilane groups are concentrated at the densely functionalized outer surface. The outer layer thus possesses a high positive charge, which is only partially compensated by the negative charge of the silanol groups.

Transmission electron microscopy was performed as a complementary approach for determining the location of the aminopropyl groups in the mesoporous silica nanoparticles. In order to distinguish between functionalized and unfunctionalized surfaces, iridium(III) chloride was added as a contrast agent and uncomplexed iridium cations were removed by two steps of washing and centrifugation. Scanning Transmission Electron Microscopy in High Angle Annular Dark Field mode (STEM-HAADF) was performed in order to visualize the heavy metal content in the stained CMS particles of samples prepared with addition times of 10 min (AP-CMS **8**) and 30 minutes (AP-CMS **9**), respectively (Figure 8-7).

This technique allows Z-contrast imaging with an intensity proportional to  $Z^2$ , the squared atomic number of the elements present, resulting in clearly visible bright spots corresponding to clustered heavy iridium atoms. As STEM shows a two-dimensional projection, these spots are positioned over the whole imaged particle, but with different radial distributions depending on the location of the functional groups.

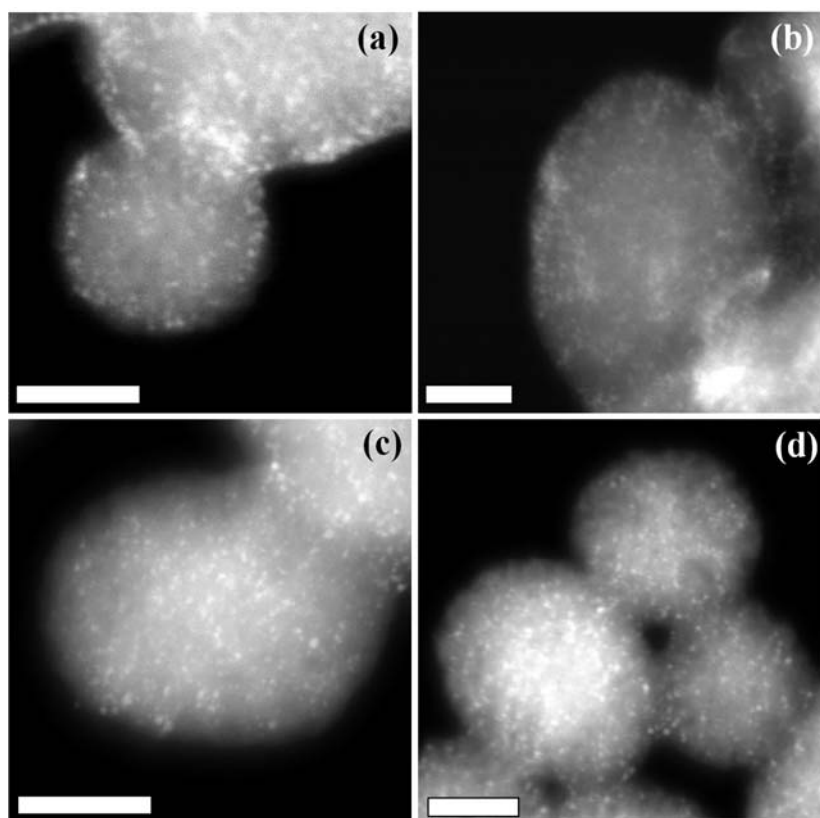


**Figure 8-7.** STEM-HAADF micrographs of samples AP-CMS **9** (a,b) and AP-CMS **8** (c,d) (scale bar = 20 nm).

Depending on the addition time in the selective functionalization procedure, the resulting materials can attain any state between two extreme cases, that is, either the aminopropyl groups and thus the iridium clusters are homogeneously distributed over the whole particle volume, or they are solely located on the outer particle surface. For statistical analysis each investigated particle was divided into two radial segments corresponding to equal volumes transmitted by the electron beam, i.e., an “inner part” and “outer part”, by placing a circle or ellipsoid with a relative diameter of 60.8 % in the center of each particle projection (Figure 8-8a).



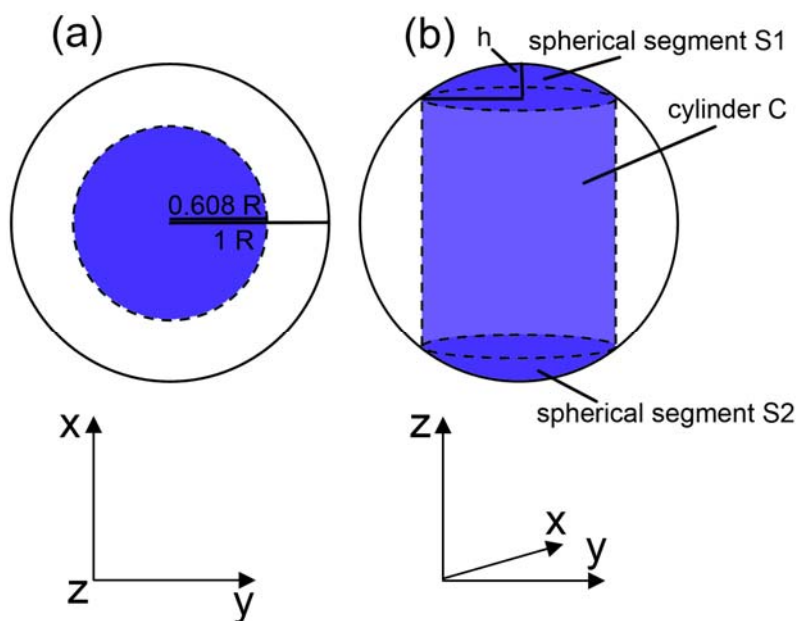


**Figure 8-8.** Scheme of a CMS particle with divided into “inner part” (darkened area with radius 0.608 R) and “outer part” (white area with radius 1 R) seen along the z-axis parallel to the STEM electron beam (a). The same particle oriented sideways shows the corresponding volumes transmitted by the STEM electron beam (b).

The volume corresponding to the “inner” darkened area traversed by the electron beam can be divided into two identical spherical segments (S1 and S2) and a cylinder. The volume of a sphere and spherical segment with radius  $r$  and height  $h$ , and cylinder with radius  $r_2$  and height  $h_2$  are described in equations (8-1) to (8-3).

$$V_{\text{sphere}} = \frac{4}{3} r^3 \pi \quad (8-1)$$

$$V_{\text{segment}} = \frac{h^2 \pi}{3} (3r - h) \quad (8-2)$$

$$V_{\text{cylinder}} = r_2^2 \pi h_2 \quad (8-3)$$

The radius of the spherical CMS particle was defined as  $R$ . The smaller radius of the “inner part” corresponding to the cylinder was defined as  $R_2$ . The equation (8-4) was then solved in

Mathematica 5.0 (Wolfram research, Inc.) yielding  $R_2 = 0.608309 R$ . The corresponding heights of the spherical segment and the cylinder are  $0.20629 R$  and  $1.5874 R$ , respectively.

$$\frac{1}{2}V_{\text{sphere}} = 2 \cdot V_{\text{segment}} + V_{\text{cylinder}} \quad (8-4)$$

The volumes corresponding to the inside and outside of the darkened area in Figure 8-8a each constitute half of the total particle volume. Metal atoms dispersed homogeneously throughout the whole spherical particle are therefore contained in both areas in a 1:1 ratio.

On the other hand, metal atoms present solely on the external particle surface will be dispersed according to the ratio of the external surface in both spherical segments (“inner part”) relative to the remaining sphere surface (“outer part”). The surface area of a sphere and a spherical segment are given in equations (8-5) and (8-6).

$$S_{\text{sphere}} = 4r^2\pi \quad (8-5)$$

$$S_{\text{segment}} = h\pi(4r - h) \quad (8-6)$$

By inserting  $R$  as the radius of the sphere and of the spherical segment with the height  $h = 0.20629 R$ , the ratio  $2 \cdot S_{\text{segment}} : (S_{\text{sphere}} - 2 \cdot S_{\text{segment}})$  of  $0.642 : 1$  is obtained for metal atoms dispersed on the inner and outer part, respectively.

In summary, the corresponding volumes transmitted by the electron beam in both areas are equal, and thus the number distribution of iridium clusters in those to areas is expected to be 1:1 in the case of a homogeneous distribution over the whole particle volume (assuming similar nucleation and growth rates for the clusters throughout the particles). On the other hand, a relative distribution of  $0.642 : 1$  for the inner and outer parts is expected if iridium clusters are present solely on the external surface, i.e. the ratio corresponding to the external particle surfaces traversed by the electron beam. While it is expected that the organosilanes were completely incorporated in both samples during co-condensation based on the obtained data, it should be noted that these calculations are still valid even for different total amounts of functional groups. The calculated distribution values are relative ratios of the number of

clusters in two volume parts of each particle and thus independent of the total amount of functional groups in each sample. A total of 1568 iridium clusters in 19 different CMS particles of both samples were evaluated, yielding a relative distribution and standard deviation of  $0.986 \pm 0.097$  in sample AP-CMS **8** and  $0.636 \pm 0.045$  in sample AP-CMS **9**. Both values are in good accordance with the calculated theoretical results for a selective functionalization of the external surface and a more homogeneous distribution inside the particle channels (assuming similar nucleation and growth rates for the clusters throughout the particles), and thus support the observations made by zeta potential measurements.

Using this selective co-condensation approach, a phenyl-functionalized sample (Ph-CMS **14**) was prepared by addition of a PTES/TEOS mixture with a molar ratio of 1:1 after 30 minutes. The presence of the attached functional groups in the externally functionalized silica material was shown by Raman spectroscopy (Figure 8-9a). Due to the small amount of employed organosilane only the strongest band at  $998\text{ cm}^{-1}$  (aromatic C-H in-plane deformation vibration) is clearly visible, while the second strongest band located at  $3063\text{ cm}^{-1}$  (aromatic C-H stretching vibration) already displays a very low intensity in comparison to the non-phenyl signals.

Nitrogen sorption measurements were performed in order to investigate the impact of the introduced functional groups on the porous network. As expected, no pore size reduction was observed in the externally functionalized samples (Figure 8-10, Table 8-4, the corresponding isotherms can be found in the supporting information).

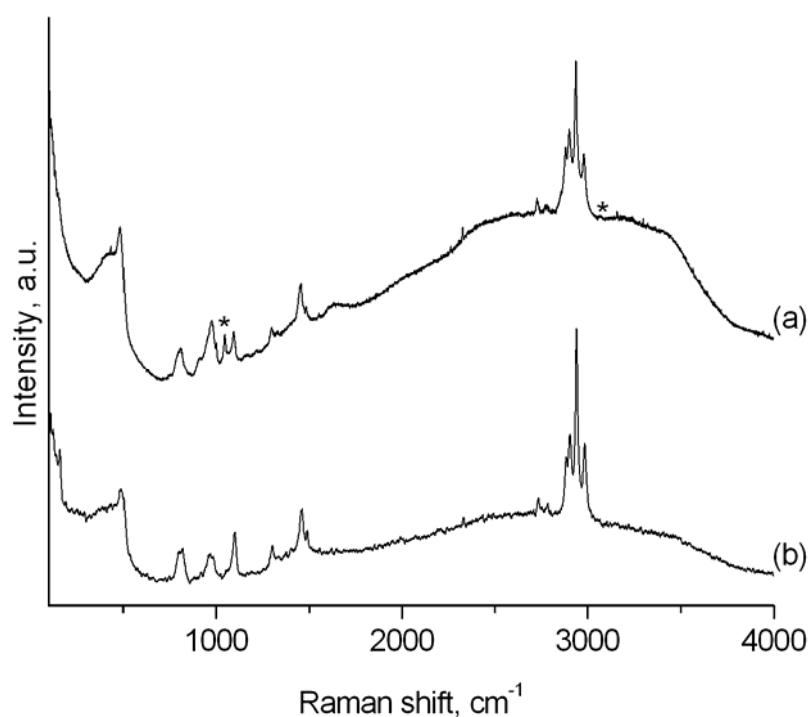


**Figure 8-9.** Raman spectra of samples Ph-CMS **14** (a) and Ph-CMS **15** (b).

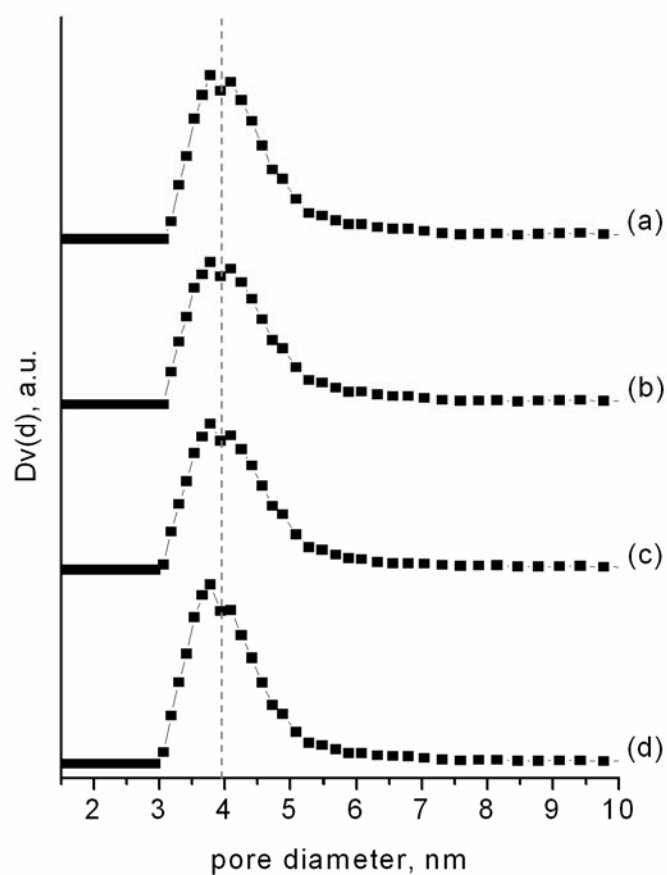


**Figure 8-10.** Pore diameters derived from nitrogen sorption isotherms of unfunctionalized CMS (a) and samples AP-CMS **9** (b), AP-CMS **8** (c) and Ph-CMS **14** (d).

**Table 8-4.** Surface areas and pore volumes of samples obtained by selective functionalization via co-condensation

sample name	surface area [m <sup>2</sup> /g]	pore volume <sup>a</sup> [cc/g]
CMS	1152	0.852
AP-CMS 8	1114	0.775
AP-CMS 9	1158	0.782
Ph-CMS 14	1182	0.857

<sup>a</sup> only cumulative pore volumes for pores < 8 nm are specified here due to the considerable textural porosity of CMS samples

However, it should be noted that these data do not provide clear evidence for the location of the functional groups considering the small amounts of incorporated organosilane. Due to the high internal surface area of the mesopores, dispersed groups cannot significantly influence the pore size due to their small concentration on the channel walls. However, the presence and location of these dispersed functional groups can be determined by combined zeta potential and STEM measurements even at very low concentrations, as has been demonstrated.

We propose a site-selective co-condensation mechanism for our new approach (Figures 8-5 and 8-11).

The generation of mesoporous silica by hydrolysis of alkoxysilanes proceeds *via* formation of small anionic oligosilicates, which subsequently build up the inorganic framework by cooperative self-assembly with the surfactant micelles.<sup>[25, 26]</sup> As the organic moieties are introduced by in situ co-condensation in aqueous basic media (pH > 9), the trialkoxysilanes are rapidly hydrolyzed to give anionic species. This prevents entry into the nonpolar interior of the micelles inside the channels and subsequent exchange of template molecules, as observed for grafted nanoscale CMS (Figure 8-11). In this way, a locally selective functionalization becomes possible by co-condensation of the oligosilicates during framework-formation of the growing particle. Depending on the time of addition of the

organosilanes, three cases can be distinguished. A, the entire channel wall is functionalized in a classic co-condensation reaction, B, a part of the mesopore channels is functionalized during growth from an initially formed nucleus, or C, the oligosilicates attach themselves on the last layer of the outer surface of a fully grown particle.

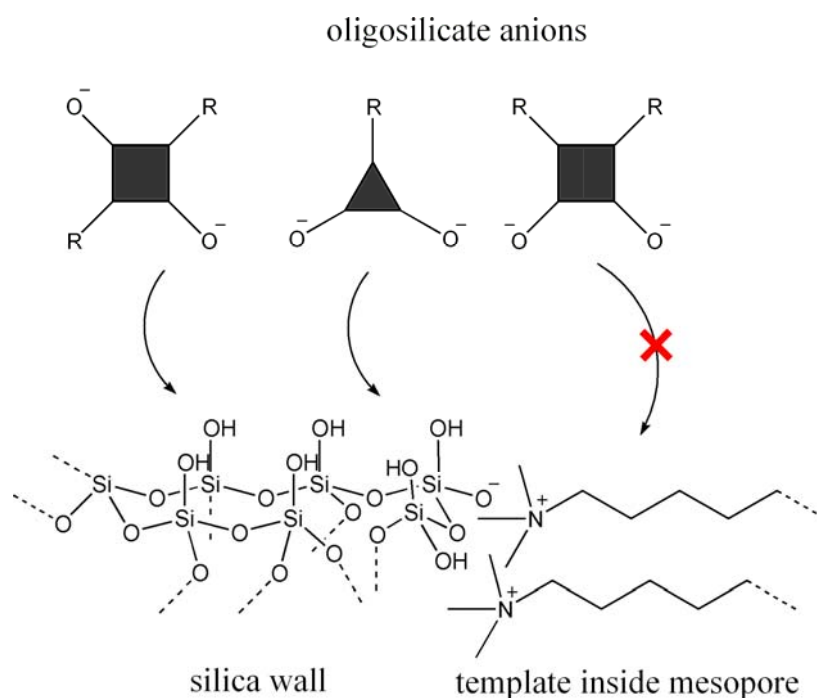


**Figure 8-11.** Formation mechanism of the outer layer during external functionalization of a mesoporous particle. Oligomeric organosilicate anions condense with the silica framework but cannot enter the hydrophobic interior of the micellar structure.

Apart from allowing a precise control over the location of the functionalized groups, this co-condensation strategy also offers further advantages. Grafting methods are generally faced with the difficulty to accurately adjust functionalization density due to the various controlling factors such as reaction time, temperature and reactant species, which determine the surface concentration of attached groups. However, by variation of the silane ratios in a co-condensation reaction it is possible to control the amount of incorporated functionalities. This

was shown by zeta potential measurements of samples functionalized by aminopropyl on the outer particle surface. Samples AP-CMS **9**, **11**, **12** and **13** were prepared by addition of a silane mixture with different APTES/TEOS ratios after 30 minutes of particle growth. As can be seen, increasing amounts of incorporated aminopropyl groups lead to higher positive surface charges, thus demonstrating the successful adjustment of organic group densities on the particle surface (Figure 8-12).

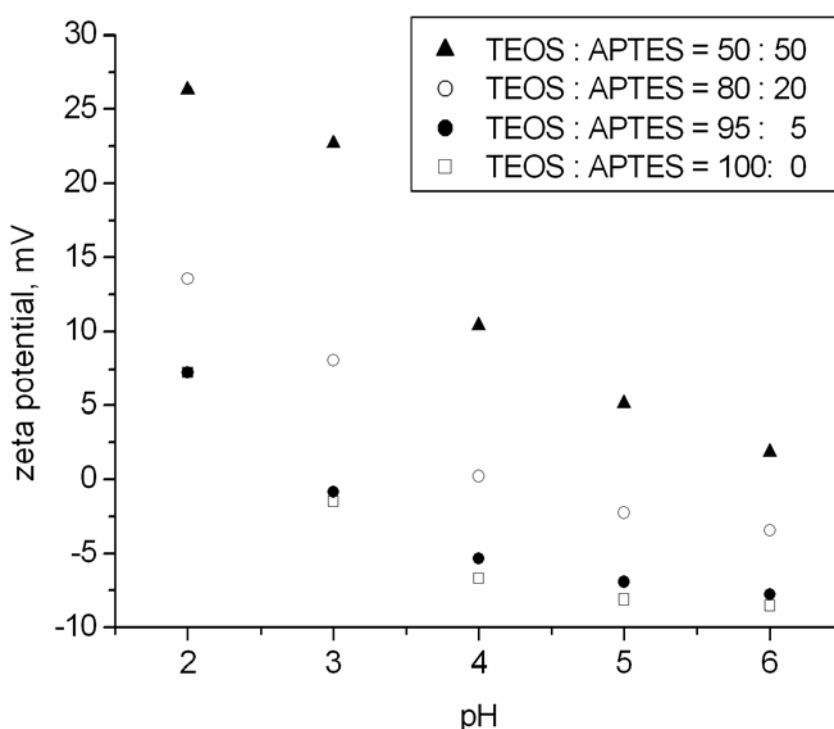


**Figure 8-12.** Zeta potential of samples with different APTES/TEOS ratios: samples AP-CMS **9** (filled triangles), AP-CMS **12** (empty circles), AP-CMS **13** (filled circles), and unfunctionalized CMS (empty squares).

However, a contrasting behavior is observed at very high ratios, i.e., addition of the pure functionalized organosilane without additional TEOS in samples AP-CMS **11** and Ph-CMS **15**: In the case of pure APTES, the recorded zeta potential curves of AP-CMS **11** showed a lower surface charge than samples prepared with a 1:1 mixture of APTES and TEOS (Figure

8-13). Moreover, in contrast to the other samples, irreproducible fluctuations of the zeta potential occurred during measurement (i.e. at pH = 4 in Figure 8-13).

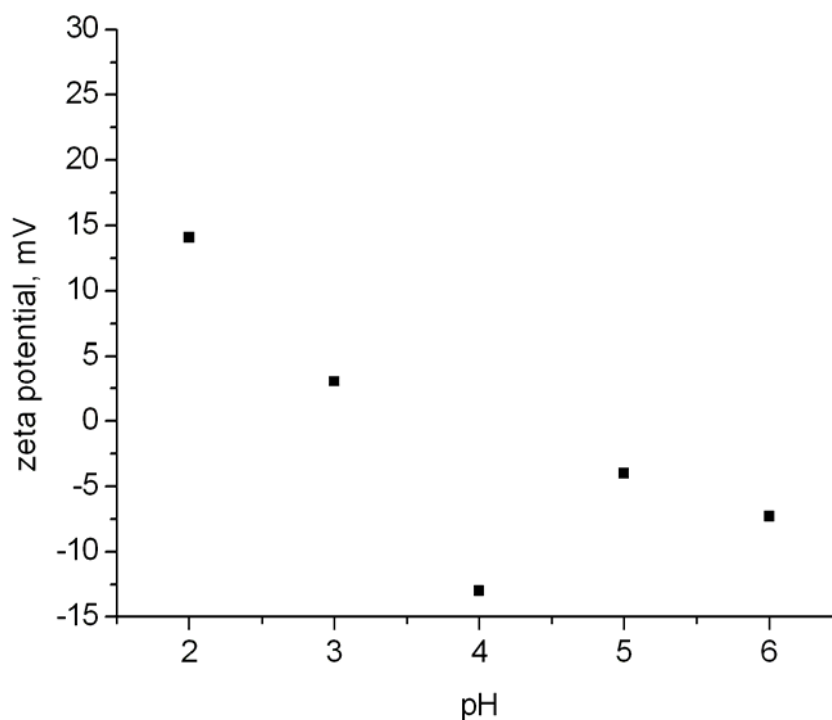


**Figure 8-13.** Zeta potential of sample AP-CMS **11**.

Furthermore, after addition of pure PTES in sample Ph-CMS **15** no phenyl groups were detected by Raman spectroscopy (Figure 8-9b). The observed results can be explained by taking into account the different oligosilicates prepared by pure organosilane addition as compared to a mixture with TEOS during the formation mechanism of the functionalized outer layer (Figure 8-14).

In the case of pure functionalized triethoxysilanes, the oligosilicates resulting from hydrolysis and condensation have few or no free silanol groups, which are necessary for attachment and further condensation to the inorganic framework. DLS measurements confirm the bimodal particle size distribution in sample AP-CMS **11** (Figure 8-15d).



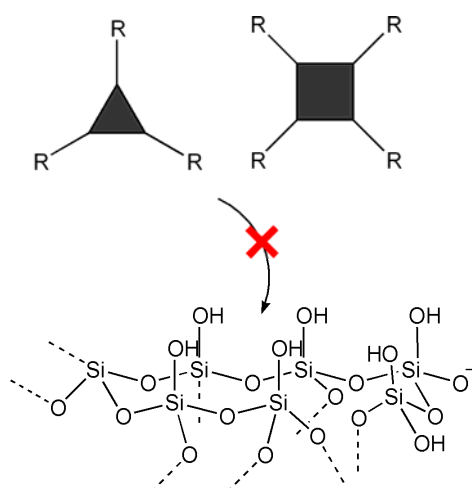


**Figure 8-14.** Organosilane oligomers lacking free silanol groups cannot condense with the silica framework during the external functionalization step.

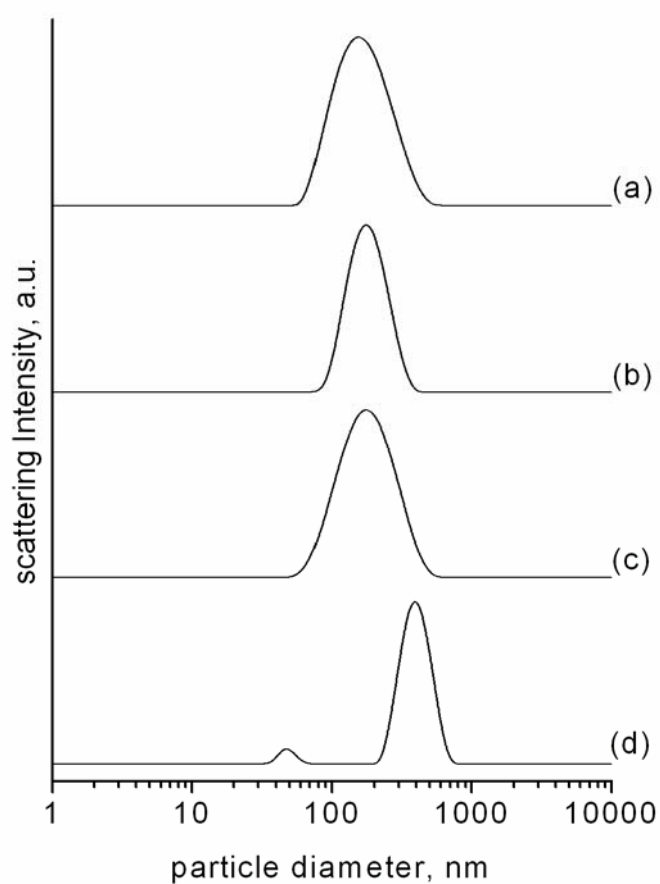


**Figure 8-15.** Unweighted DLS curves for ethanolic suspensions of unfunctionalized CMS (a) and samples Ph-CMS **14** (b), AP-CMS **9** (c), and AP-CMS **11** (d).

While samples coated with an APTES/TEOS mixture showed no significant difference in particle diameter with respect to uncoated samples, addition of pure APTES resulted in small particles which are attributed to agglomerations of aminopropyl-functionalized oligosilicates as well as larger agglomerates of such oligosilicates with the CMS particles. The zeta potential fluctuations are thus assigned to the heterogeneity of this sample containing both negatively charged CMS particles and positively charged APTES oligomers.

In the case of PTES, the resulting phenyl-functionalized oligomers were too small to be recovered by centrifugation and thus were removed from the sample, resulting in unfunctionalized material. It should be noted that this behavior was only observed for late addition times, i.e. after 30 minutes or more. As expected, materials synthesized by addition of pure organosilanes during early stages of particle growth show no differences to samples prepared by addition of TEOS-containing mixtures, as excess TEOS is still present in the reaction mixture at early particle growth stages.

## 8. 5 Conclusion

A versatile approach for the selective functionalization of mesoporous silica nanoparticles has been developed. By using an *in-situ* co-condensation approach during the growth of the particles, functional groups can be completely dispersed inside the channels, concentrated in parts of the mesopores, or exclusively placed on the external surface, depending on the time of addition. In this way, several disadvantages associated with post-synthesis grafting can be avoided, such as the unwanted partial functionalization of the internal surface by diffusion of grafting reactants into the mesopores. Furthermore, the functional group density on the outer particle surface can be easily adjusted by variation of the organosilane-to-TEOS ratio.

The resulting nanoparticles are promising candidates for the generation of sophisticated multifunctional systems, for example in drug delivery applications. External functionalization allows for the attachment of bulky groups and other nanoparticles without reducing pore volume and causing excessive pore blocking. Moreover, selective functionalization of the outer particle surface does not influence the interactions of guest molecules with the internal pore walls, and diffusion of the guest molecules inside the mesopores, which is an important aspect in drug delivery. By alteration of the internal surface in subsequent functionalization steps, such as post-synthesis grafting, the generation of materials with tailor-made properties becomes possible for which interactions with the environment and with guest species can be completely controlled.

## 8.6 References

- [1] F. Hoffmann, M. Cornelius, J. Morell, M. Froeba, *Angewandte Chemie, International Edition* **2006**, *45*, 3216.
- [2] Y. Wan, D. Zhao, *Chemical reviews* **2007**, *107*, 2821.
- [3] D. M. Ford, E. E. Simanek, D. F. Shantz, *Nanotechnology* **2005**, *16*, 458.
- [4] A. Stein, B. J. Melde, R. C. Schroden, *Advanced Materials* **2000**, *12*, 1403.
- [5] I. I. Slowing, B. G. Trewyn, S. Giri, V. S. Y. Lin, *Advanced Functional Materials* **2007**, *17*, 1225.
- [6] S. Giri, B. G. Trewyn, V. S. Y. Lin, *Nanomedicine* **2007**, *2*, 99.
- [7] C.-M. Yang, H.-A. Lin, B. Zibrowius, B. Spliethoff, F. Schueth, S.-C. Liou, M.-W. Chu, C.-H. Chen, *Chemistry of Materials* **2007**, *19*, 3205.
- [8] A. Perro, S. Reculosa, S. Ravaine, E. Bourgeat-Lami, E. Duguet, *Journal of Materials Chemistry* **2005**, *15*, 3745.
- [9] L. Hong, S. Jiang, S. Granick, *Langmuir* **2006**, *22*, 9495.
- [10] D. S. Shephard, W. Zhou, T. Maschmeyer, J. M. Matters, C. L. Roper, S. Parsons, B. F. G. Johnson, M. J. Duer, *Angewandte Chemie, International Edition* **1998**, *37*, 2719.
- [11] F. De Juan, E. Ruiz-Hitzky, *Advanced Materials* **2000**, *12*, 430.
- [12] K. Cheng, C. C. Landry, *Journal of the American Chemical Society* **2007**, *129*, 9674.
- [13] Y.-S. Lin, S.-H. Wu, Y. Hung, Y.-H. Chou, C. Chang, M.-L. Lin, C.-P. Tsai, C.-Y. Mou, *Chemistry of Materials* **2006**, *18*, 5170.
- [14] M. H. Lim, A. Stein, *Chemistry of Materials* **1999**, *11*, 3285.
- [15] A. B. Bourlinos, T. Karakostas, D. Petridis, *Journal of Physical Chemistry B* **2003**, *107*, 920.
- [16] V. Antochshuk, M. Jaroniec, *Chemical Communications* **1999**, 2373.
- [17] V. Antochshuk, M. Jaroniec, *Chemistry of Materials* **2000**, *12*, 2496.
- [18] V. Antochshuk, A. S. Araujo, M. Jaroniec, *Journal of Physical Chemistry B* **2000**, *104*, 9713.
- [19] M. Grun, K. K. Unger, A. Matsumoto, K. Tsutsumi, *Microporous and Mesoporous Materials* **1999**, *27*, 207.
- [20] K. Möller, J. Kobler, T. Bein, *Advanced Functional Materials* **2007**, *17*, 605.
- [21] F. Kleitz, W. Schmidt, F. Schuth, *Microporous and Mesoporous Materials* **2003**, *65*, 1.
- [22] K. Moller, J. Kobler, T. Bein, *Journal of Materials Chemistry* **2007**, *17*, 624.
- [23] J. M. Rosenholm, M. Linden, *Chemistry of Materials* **2007**, *19*, 5023.
- [24] J. M. Rosenholm, A. Duchanoy, M. Linden, *Chemistry of Materials* **2008**, *20*, 1126.
- [25] J. Frasc, B. Lebeau, M. Soulard, J. Patarin, R. Zana, *Langmuir* **2000**, *16*, 9049.
- [26] X. S. Zhao, G. Q. Lu, G. J. Millar, *Industrial & Engineering Chemistry Research* **1996**, *35*, 2075.

## 9 Conclusion

### 9.1 Summary

During the course of this work several new concepts for the synthesis and functionalization of colloidal porous hosts were developed.

It was demonstrated that metal ammine complexes can be applied as a novel class of zeolite templates for the synthesis of colloidal molecular sieves. The crystallization of nanosized EDI-type zeolite was shown to be directed by square planar  $[\text{Cu}(\text{NH}_3)_4]^{2+}$  complexes used as co-templating species in addition to tetramethylammonium cations. Various factors including aging treatment, composition of the reaction mixture, time and temperature of hydrothermal treatment were investigated in order to elucidate the role of the complexes in the crystallization pathway. It was found that  $[\text{Cu}(\text{NH}_3)_4]^{2+}$  acts as the main templating species and that it is necessary for crystallization and growth of the EDI-type nanoparticles. Stabilization of the complexes by incorporation into the aluminosilicate matrix during aging is one of the key steps in order to avoid decomposition inside the alkaline reaction media at elevated temperatures. Substitution of the copper complexes by isostructural palladium and platinum species results in drastically decreased particle sizes by increasing nucleation rates, yielding colloidal suspensions of zeolite nanocrystals with sizes below 20 nm and monomodal size distributions. Variation of the hydrothermal treatment temperature leads to different results based on the complex used. While palladium and platinum species decompose above 100 °C, the copper species were found to be stable up to 150°C but to yield core-shell particles at lower temperatures, i.e. 60 °C.

Colloidal mesoporous silica created by cooperative self-assembly of surfactant templates and silica precursors was the second theme of this work. A simple one-pot reaction for the oxidative removal of template molecules and functional groups by reaction with hydrogen peroxide was developed. In this way, the size and morphology of colloidal mesoporous silica

nanoparticles could be controlled by addition of phenyltriethoxysilane during synthesis without affecting surface functionalization.

The functionalization of colloidal mesoporous silica systems with metalorganic reagents was demonstrated, i.e., by reaction with phenyllithium. The key step for avoiding particle agglomeration and coalescence processes was the removal of water from the mesopores at temperatures below 90 °C either by hydrolysis of triethyl orthoformate or by vapour adsorption from the gas phase.

It was shown that toluene sorption measurements in thin films of functionalized mesoporous silica nanoparticles on quartz crystal microbalance chips are a powerful means of surface characterization for these nanosized systems. This technique offers the capability to acquire isotherms of volatile vapors and the corresponding heats of adsorption at the same time, while using very small amounts of sample in the range of about 5 to 30 µg.

Finally, a versatile approach for the selective functionalization of mesoporous silica nanoparticles was developed. By using an *in-situ* co-condensation approach during the growth of the particles, functional groups can be completely dispersed inside the channels, concentrated in parts of the mesopores, or exclusively placed on the external surface depending on the time of addition. In this way, several disadvantages associated with post-synthesis grafting can be avoided, such as the unwanted partial functionalization of the internal surface by diffusion of grafting reactants into the mesopores. Furthermore, the functional group density on the outer particle surface can be easily adjusted by variation of the organosilane to silane ratio.

## 9.2 Outlook

The applicability of square planar metal ammine complexes as templates for the synthesis of colloidal zeolites has been demonstrated. The next step should be the extension of the concept to different complexes with varied geometries, sizes, and charge densities, with the goal of discovering previously unknown zeolite frameworks. For example, the use of functionalized amines permits the generation of a large number of metal amine complexes with different structures. Depending on the complex used, several parameters may have to be adjusted, i.e., the silicon-to-alumina ratio will have to be increased for incorporation of large complexes and consequently co-templates with lower charge densities may be necessary for the adjustment of the pH. High-throughput methods are a suitable tool for the investigation of large ranges of composition parameters. First preliminary experiments in this area have already been performed, and it was found that the zeolite syntheses presented in this work can be downscaled to reaction volumes of about 1.5 mL inside high throughput autoclave systems, without any alteration of the particle size or crystallinity of the products.

Furthermore, several of the concepts developed in this work have already been successfully applied in cooperations and further studies inside our group. Metalorganic conversions have been used for the functionalization of colloidal mesoporous silicas with moieties that are not commercially available in the form of triethoxysilanes, i.e., protected alkyne moieties. Furthermore, the selective functionalization of colloidal mesoporous silicas with various anchor groups allowed the attachment of large molecules without blocking of the internal pore system. One example of such studies includes the successful attachment of DNA oligomers on the outer particle surface via click chemistry recently performed by Axel Schloßbauer in our group.

Prospective future projects also include the attachment of stimuli-responsive caps and polymers, as well as biological markers and other functionalities by fully exploiting the high versatility of the functionalization concepts devised in this work.





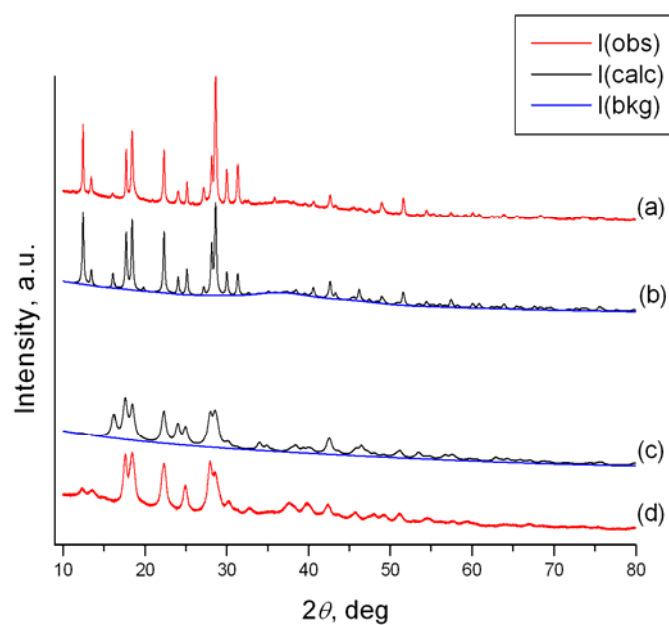
## 10 Supporting Information

### 10.1 Supplemental Data for Chapter 4 - Structural models for Cu-EDI and Pt-EDI

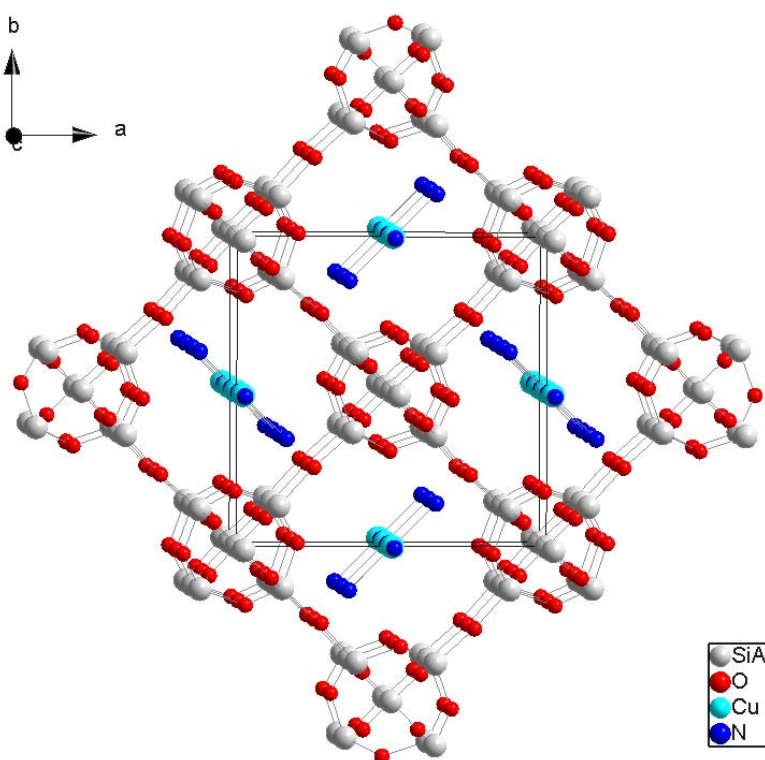
The full Rietveld refinement of both zeolite structures from XRD powder patterns is very challenging due to several factors, i.e., the partial occupancies of water, TMA, sodium, and the metal complexes, combined with some degree of disorder of these species due to multiple possible orientations inside the zeolite structure, as well as partial occupancies in the cage system. Furthermore, the significant peak broadening due to the small size of the nanocrystallites is problematic, especially for evaluation of the high-angle reflections. However, the underlying EDI-type framework structure is well known, and the metal complexes are supposed to be the most strongly scattering species inside the pores. Therefore it becomes possible to develop a qualitative structure model from which some basic conclusions can be drawn, i.e., concerning the effects of metal substitution.

Based on the XRD pattern of sample Cu-100, a simple model for the metal complex-containing EDI-type zeolite was constructed (Figure 10-1, 10-2). Starting with the empty EDI framework in the space group  $P-42_1m$ , the Cu positions were located by DELF (difference electron Fourier mapping) in the program GSAS/EXPGUI. Nitrogen atoms were manually placed at a Cu-N distance of 2 Å. The Cu and N fractions were set to the values determined from elemental analysis and TGA data. The resulting calculated powder pattern of this model system is similar to that of Cu-100 (Figure 10-1b). By exchanging all Cu atoms in the model for Pt atoms and adjusting the particle size related peak broadening, a calculated powder pattern with low intensity of the reflections at 12.5 and 13.5 °2 $\theta$  is obtained (Figure 10-1c). A similar pattern is observed for sample Pt-60 (Figure 10-1d). One can therefore conclude that the low intensity of these reflections in sample Pt-60 is due to the high scattering of the Pt atoms. It should be noted that the simulated powder patterns of the models, especially of the Pt-model, are not identical to the experimental powder patterns and are not meant to be a structure solution. In order to keep the model simple many factors including the correct space

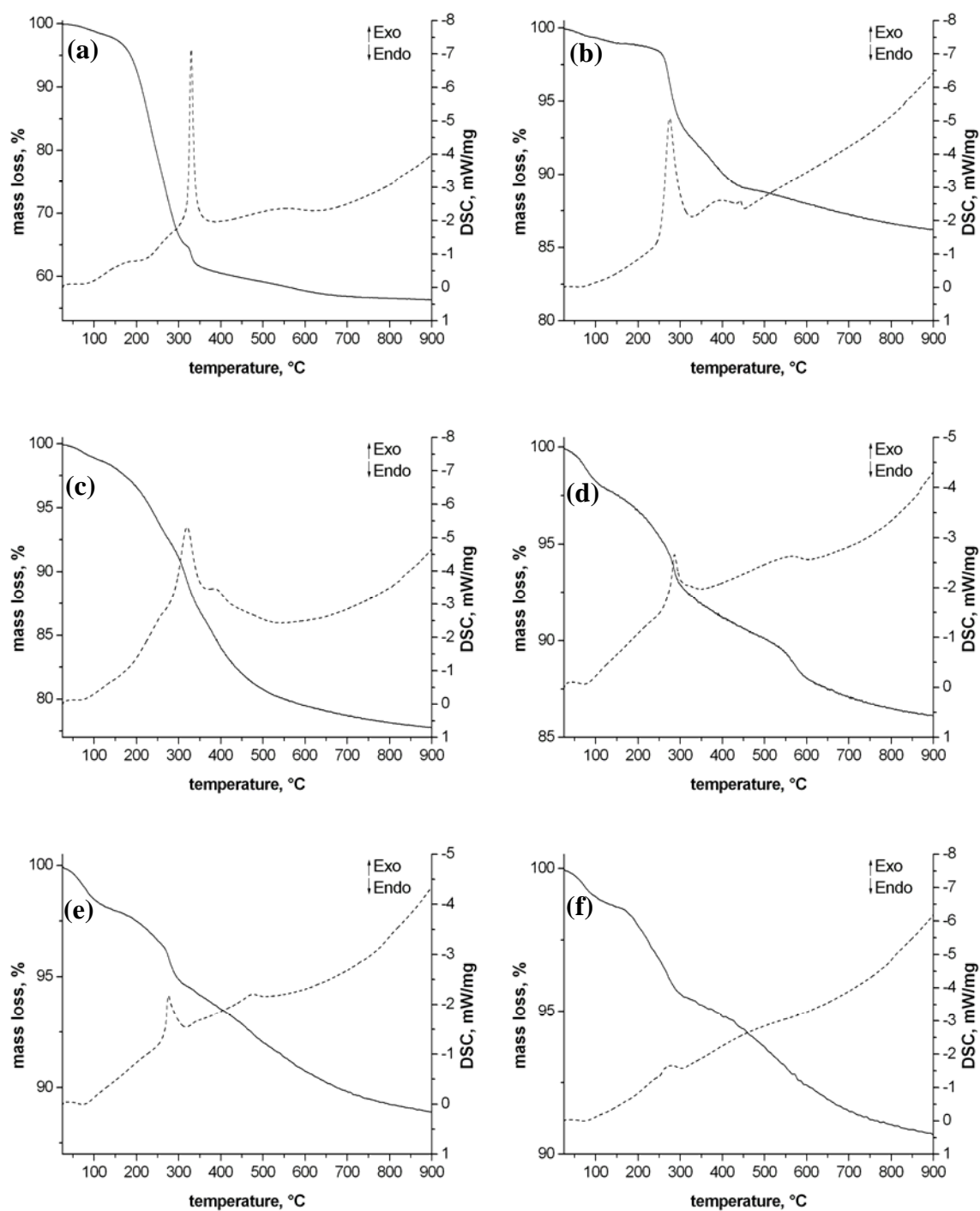
group and the presence of TMA, sodium and zeolitic water in the structure are not accounted for.



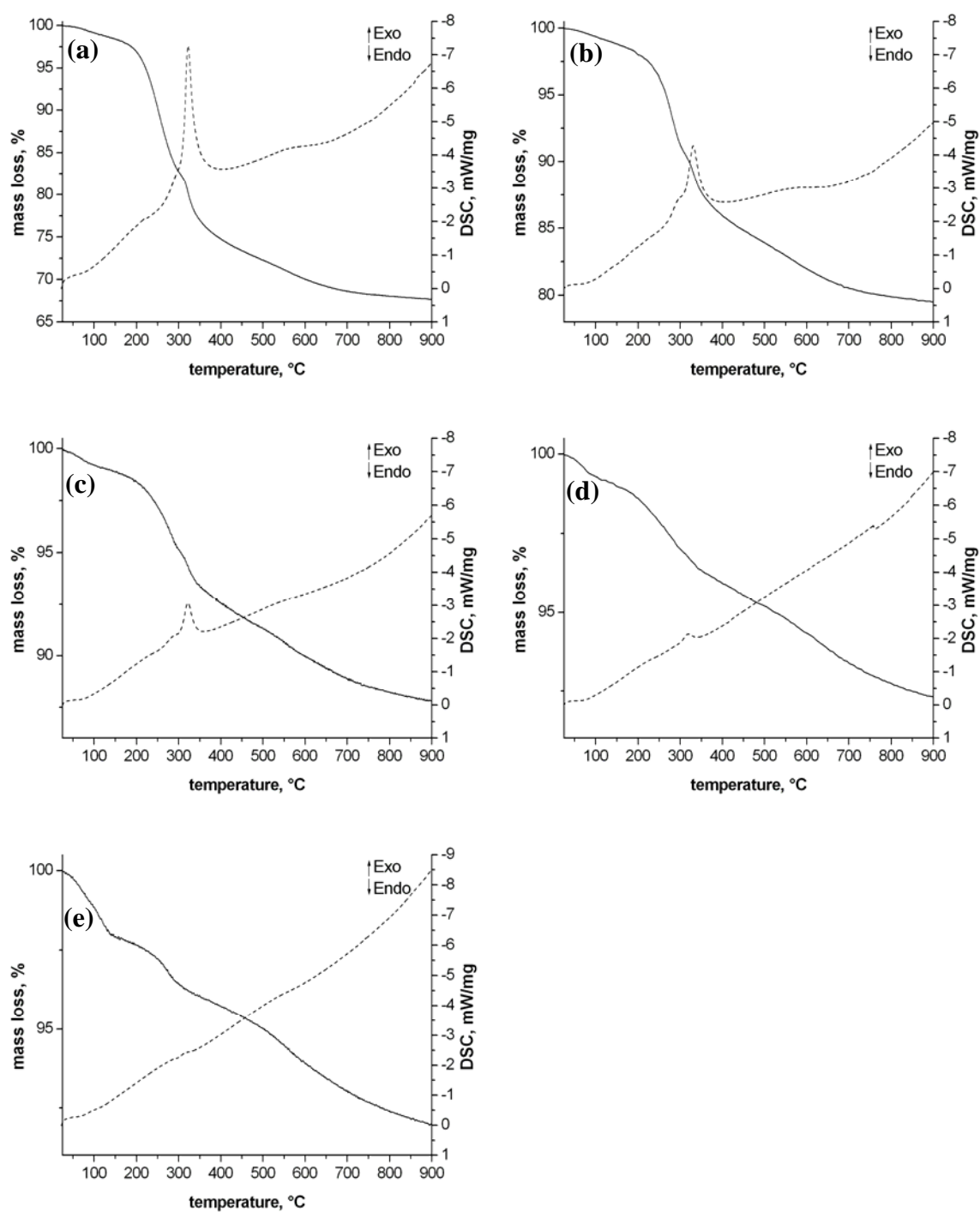
**Figure 10-1.** XRD powder patterns of sample Cu-100 (a, experimental), the Cu-model (b, simulated), the Pt-model (c, simulated) and sample Pt-60 (d, experimental).



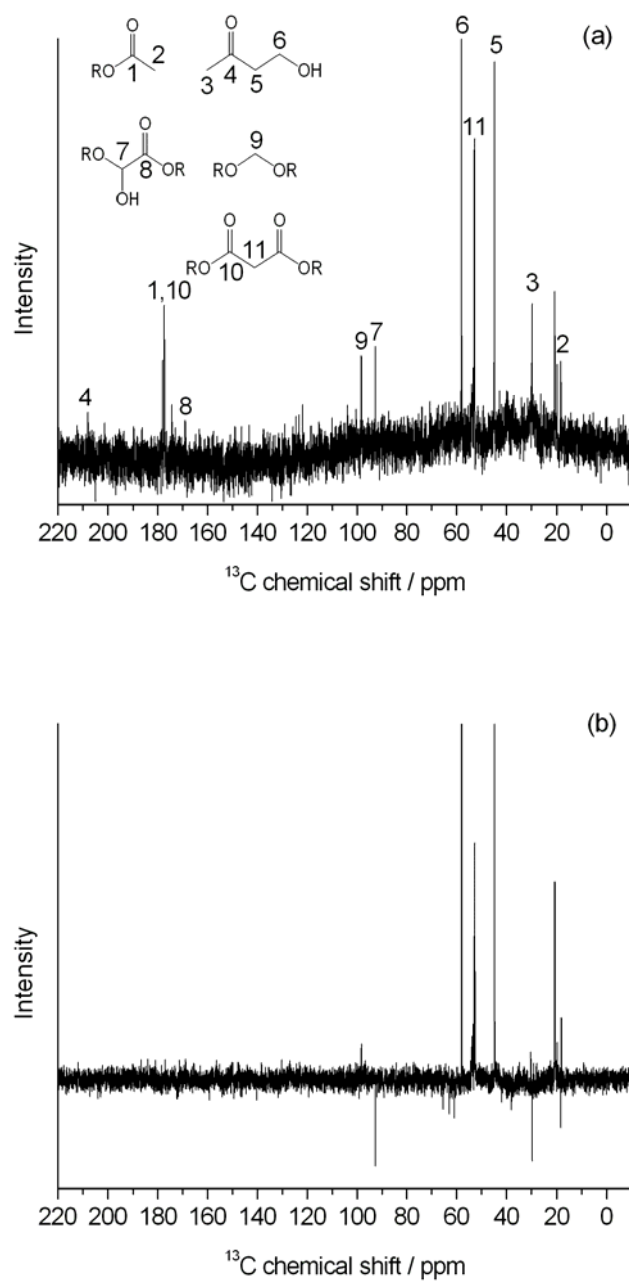
**Figure 10-2.** Graphical representation of the Cu-model along the c axis.

10.2 Supplemental Data for Chapter 5 – TGA data and  $^{13}\text{C}$  liquid state NMR

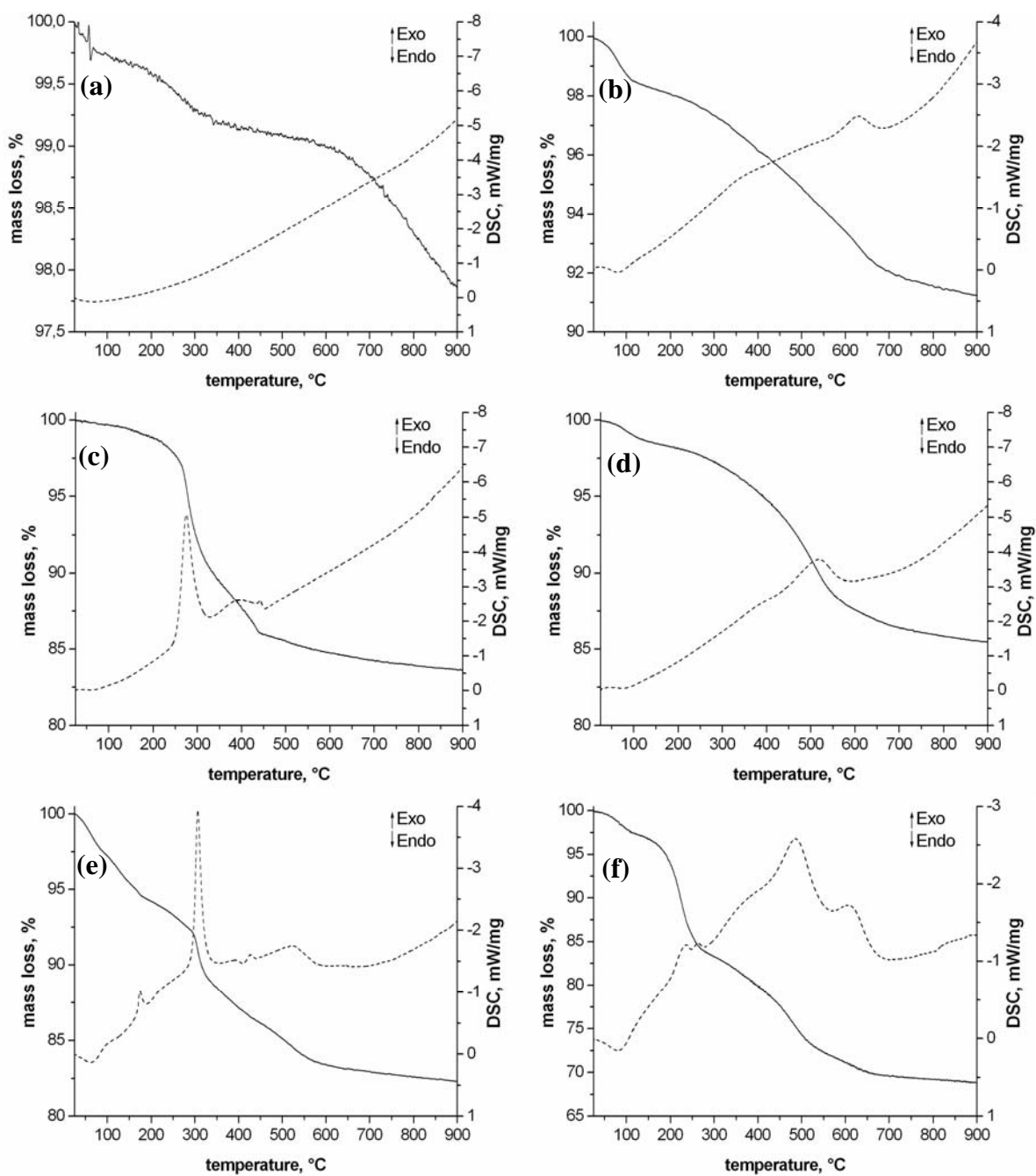
**Figure 10-3.** TGA/DSC data of as-synthesized MCM-41 (a), extracted MCM-41 (b), and samples MS 1 (c), MS 2 (d), MS 3 (e), and MS 4 (f).



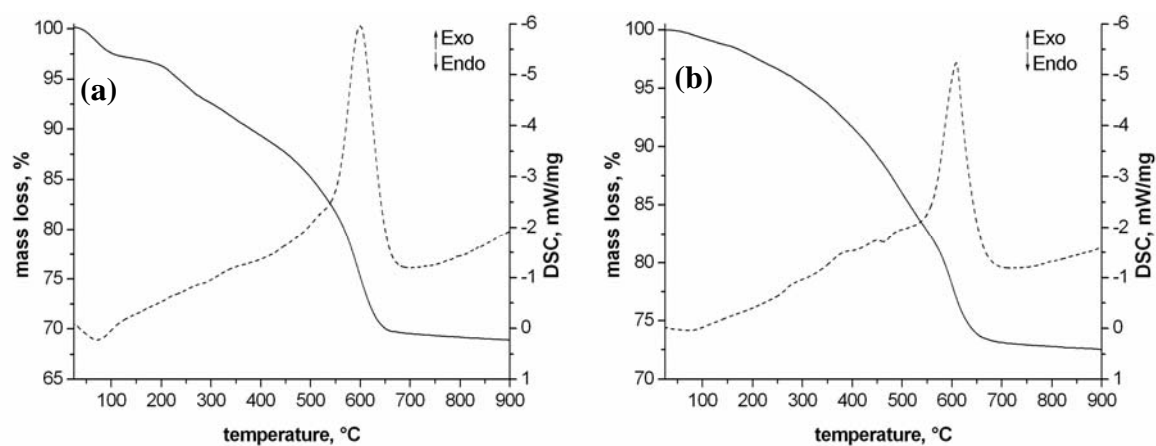
**Figure 10-3.** TGA/DSC data of samples MS 5 (a), MS 6 (b), MS 7 (c), MS 8 (d), and MS 9 (e).



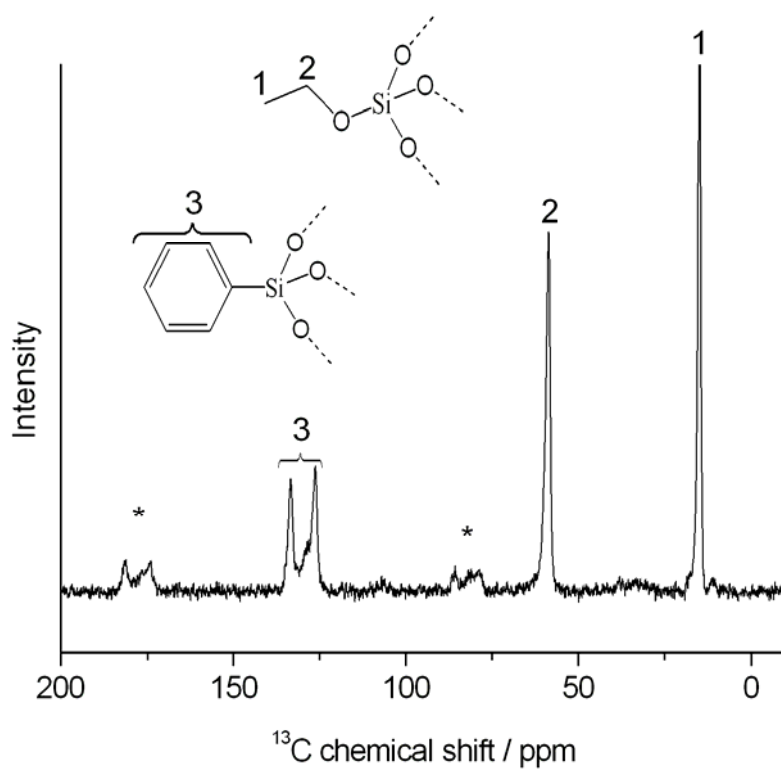
**Figure 10-4.**  $^{13}\text{C}$ - (a) and  $^{13}\text{C}$ -DEPT- (b) liquid state NMR spectra of the aqueous medium after treatment of sample MS **8** with  $\text{H}_2\text{O}_2$ .

**10.3 Supplemental Data for Chapter 6 - TGA data and  $^{13}\text{C}$  solid state NMR**

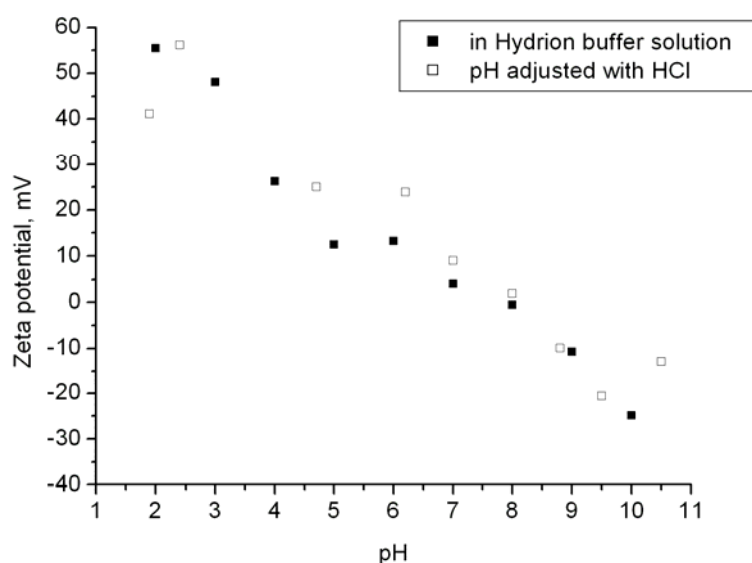
**Figure 10-5.** TGA/DSC data for calcined MCM-41 (a), sample MS-1-cal (b), extracted MCM-41 (c), sample MS-1-ex (d), extracted CMS (e), and samples CMS-3 (f).



**Figure 10-6.** TGA/DSC data for samples CMS-5 (a) and CMS-6 (b).



**Figure 10-7.**  $^{13}\text{C}$  MAS-NMR spectrum of sample CMS-6. The asterisks denote spinning sidebands.

**10.4 Supplemental Data for Chapter 7 – zeta potential curves, TG data, N<sub>2</sub> isotherms**

**Figure 10-8.** Comparison of zeta potential curves obtained by pH adjustment using Hydrion buffer solutions (filled squares) or addition of diluted hydrochloric acid (empty squares) for aminopropyl-functionalized CMS. The sample was obtained by grafting of extracted CMS with APTES in toluene under reflux conditions.

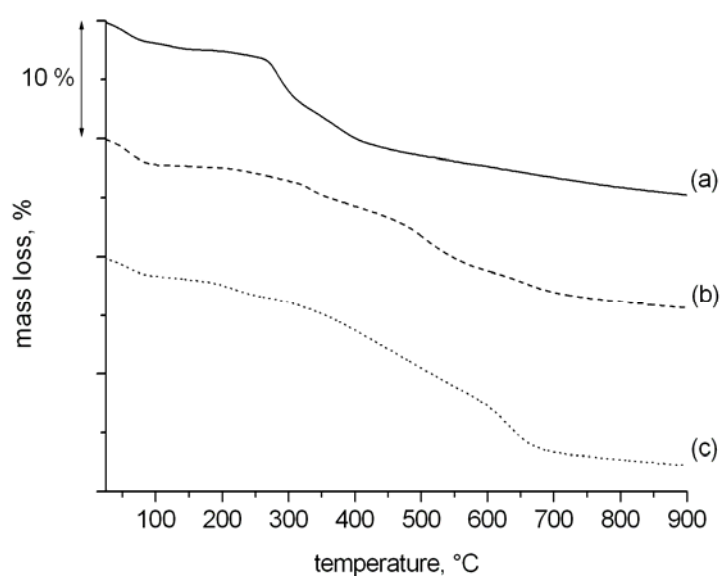


**Figure 10-9.** Thermogravimetric data for unfunctionalized MCM-41 (a), and phenyl-functionalized samples Ph-MS 1 (b) and Ph-MS 2 (c).



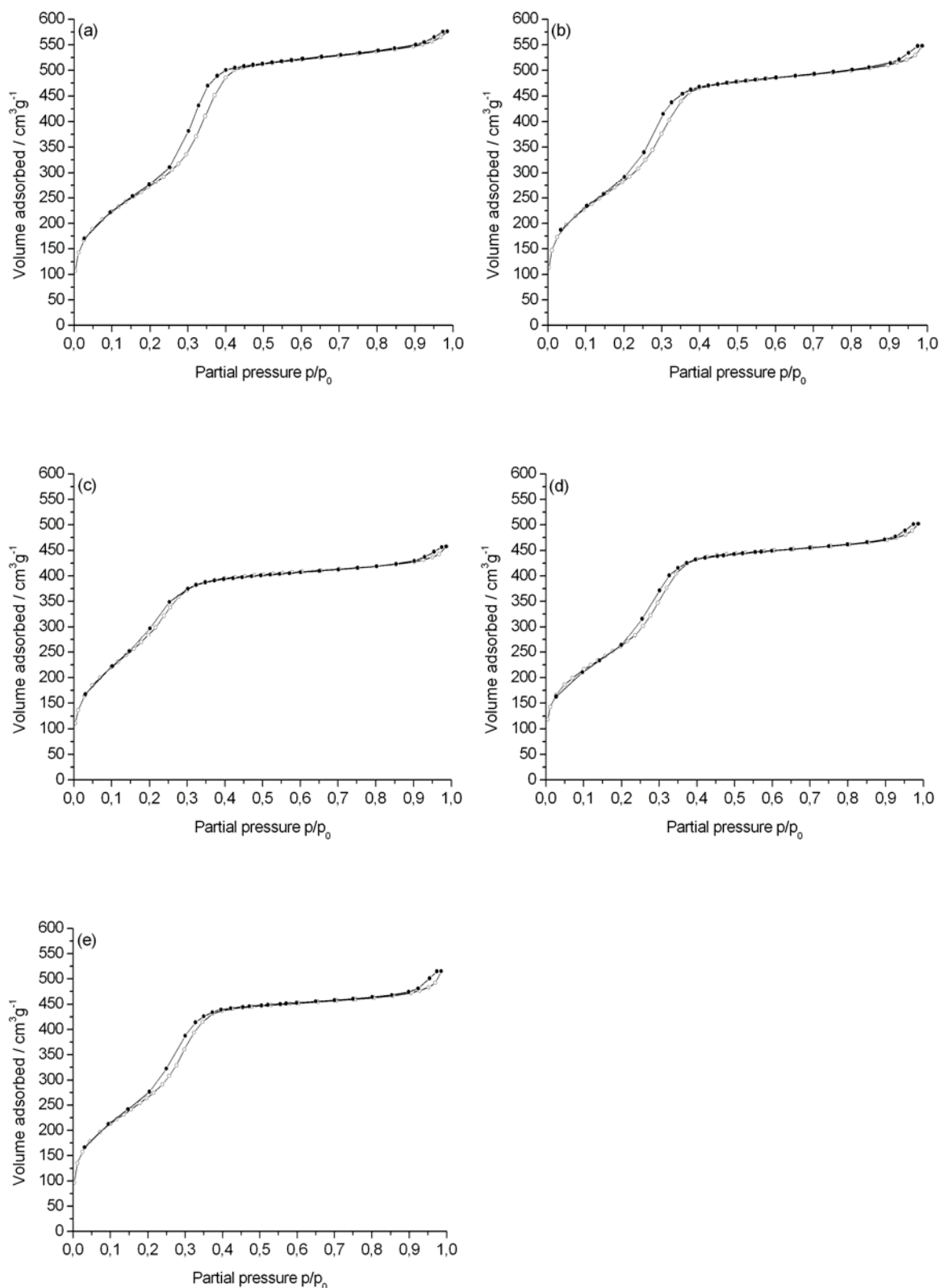


**Figure 10-10.** Nitrogen sorption isotherms of unfunctionalized MCM-41 (a) and samples Ph-MS 1 (b), Ph-MS 2 (c), AP-MS 3 (d), and BU-MS 4 (e).

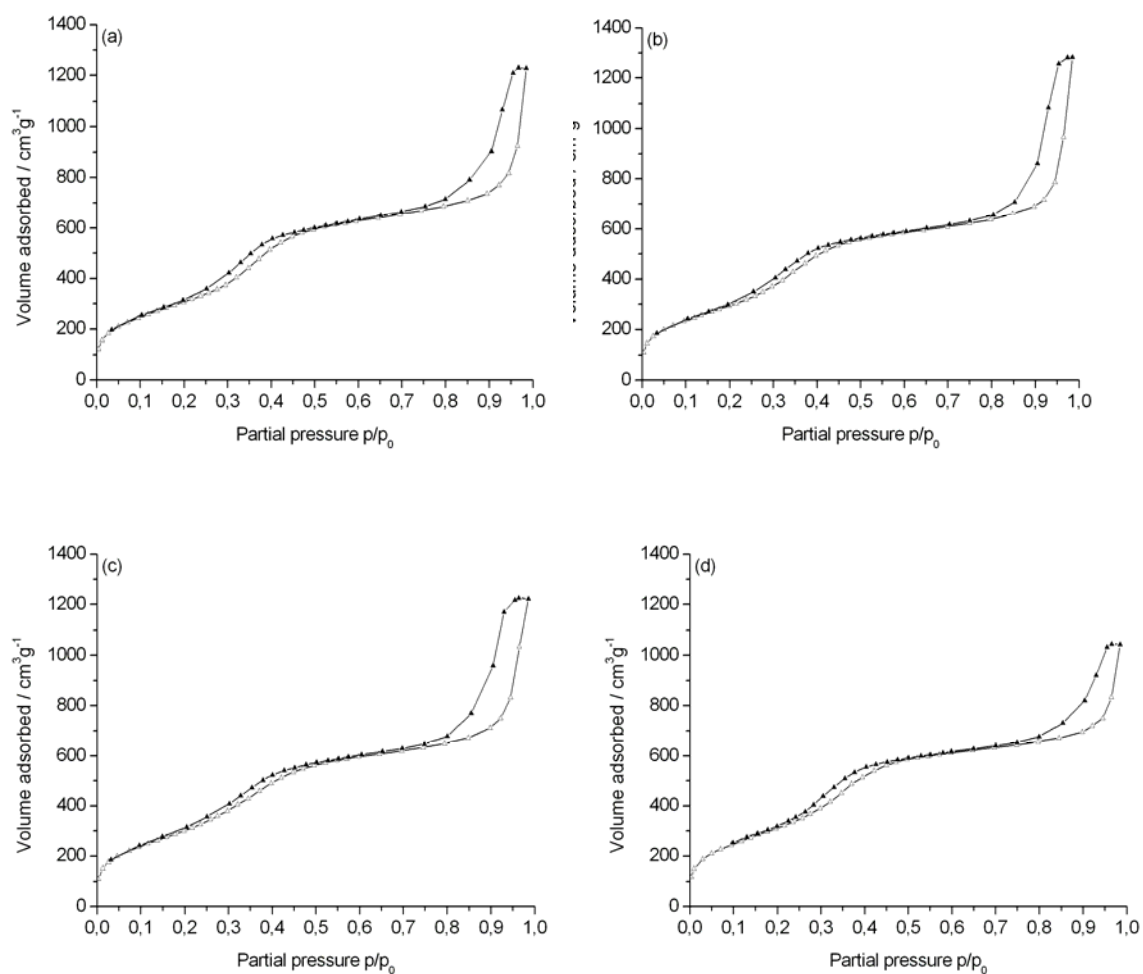


**Figure 10-11.** Nitrogen sorption isotherms of unfunctionalized CMS (a) and samples AP-CMS **8** (b), AP-CMS **9** (c) and Ph-CMS **14** (d).

## 11 Curriculum vitae

### Persönliche Daten

---

Geb. am 22.01.1981 in München  
Familienstand: ledig  
Staatsangehörigkeit: österreichisch

### Schule

---

30.06.2000            Abitur am Wilhelm-Hausenstein-Gymnasium München  
(Note 1,7)

### Studium und Promotion

---

09/2000-05/2005    Studium der Chemie an der Ludwig-Maximilians-Universität München  
(Schwerpunkte: Anorganische Festkörperchemie, nanostrukturierte  
Materialien, Wirkstoffsynthese, Polymere)

09/2000-11/2002    Grundstudium

07.11.2002           Vordiplom (Note 1,1)

12/2002-10/2004    Hauptstudium

11/2004-05/2005    Diplomarbeit: „*Preparation of transition metal containing nanoscale  
zeolites for the generation of metal clusters by gamma irradiation*“,  
Einsatz von Suspensionen poröser Nanopartikel zur Aufklärung  
räumlich begrenzter Wachstumsprozesse nach radioaktiver Bestrahlung,  
im Arbeitskreis Prof. Bein an der LMU in Zusammenarbeit mit  
Arbeitskreis Prof. Mostafavi an der Université Paris-Sud 11 in  
Frankreich (Note 1,0)

24.05.2005           Diplom-Chemiker (Note 1,0)

07/2005-06/2008    Promotion im Arbeitskreis Prof. Bein, Physikalische Chemie, LMU,  
Thema: Synthese und Funktionalisierung kolloidaler Nanopartikel aus  
mesoporösem Silika und auf Zeolithbasis, u. a. zur Anwendung im  
gezielten Arzneimitteltransport, Einsatz von Metall-Amin-Komplexen  
als neue Zeolithtemplate

**Industriepraktika, berufliche Tätigkeiten**

---

- 07/2002-09/2002     Nucleotide Analog Design AG, München, Praktikant: mehrstufige organische Synthesen, Ergebnispräsentation
- 10/2005-05/2008     NanoScape AG, München, Nebentätigkeit als freier Mitarbeiter: Synthese und Charakterisierung nanoskaliger oxidischer Materialien, Projektabwicklungen im F&E-Bereich
- 01/2006-04/2008     Fachliche Anleitung und Ausbildung von Diplomanden und Studenten im Hauptstudium, Betreuung von Praktika in der Anorganischen und Physikalischen Chemie
- 06/2006-01/2008     Verantwortlicher wissenschaftlicher Angestellter für die Infrarot- und Raman-Spektrometer im AK Bein: Wartung, Fehlerbehebung, Einweisung, Firmenkontakt

**Sonstiges**

---

- 02/2003-05/2005     Stipendiat der Studienstiftung des deutschen Volkes
- 07/2003                Herbert-Marcinek-Preis für besondere Leistungen in der Diplom-Vorprüfung
- 06/2006                Participation Award - 18th Meeting of Nobel Prize Winners in Chemistry

**Zusatzqualifikationen**

---

- Sprachen:             Englisch (verhandlungssicher)  
                             Spanisch (sehr gut)  
                             Japanisch (gut, Japanese Language Proficiency Test Level II)  
                             Französisch (gut)
- EDV-Kenntnisse:     Word, Excel, Origin, Powerpoint, Adobe Photoshop (sehr gut)  
                             Programmiersprache Pascal (gut)  
                             Mathematica (Grundkenntnisse)



München, 13.06.2008

## 12 Publications and presentations

### 12.1 Publications

1. J. Kecht, B. Mihailova, K. Karaghiosoff, S. Mintova, T. Bein, "Nanosized Gismondine Grown in Colloidal Precursor Solutions", *Langmuir* **2004**, *20*, 5271-5276.
2. J. Kecht, Z. Tahri, V. De Waele, M. Mostafavi, S. Mintova, T. Bein, "Colloidal Zeolites as Host Matrix for Copper Nanoclusters", *Chem. Mater.* **2006**, *18*, 3373-3380.
3. S. Angloher, J. Kecht, T. Bein, "Optimization of Reaction Conditions for the Metalorganic Modification of MCM-41", *Chem. Mater.* **2007**, *19*, 3568-3574.
4. S. Angloher, J. Kecht, T. Bein, "Metal-Organic Modification of Periodic Mesoporous Silica: Multiply Bonded Systems", *Chem. Mater.* **2007**, *19*, 5797-5802.
5. J. Kecht, S. Mintova, T. Bein, "Nanosized Zeolites Templated by Metal-Amine Complexes", *Chem. Mater.* **2007**, *19*, 1203-1205.
6. V. De Waele, J. Kecht, Z. Tahri, M. Mostafavi, T. Bein, S. Mintova, "Diverse Copper Clusters Confined in Microporous Nanocrystals", *Sensors and Actuators B* **2007**, *126*, 338-343.
7. A. Darga, J. Kecht, T. Bein, "Probing the Intrapore Surface of Phenyl-Substituted Nanoscale Mesoporous Silica – Piezoelectric Sorption Measurements in Thin Films", *Langmuir* **2007**, *23*, 12915-12922.
8. J. Kecht, S. Mintova, T. Bein, "Exceptionally small colloidal zeolites templated by Pd and Pt amines", *Langmuir* **2008**, *24*, 4310-4315.
9. S. Angloher, J. Kecht, T. Bein, "Sequential Transformations of Organic Nitrogen Functionalities in Periodic Mesoporous Silica", *J. Mater. Chem.* **2008**, *18*, 3103-3108.
10. J. Kecht, T. Bein, "Oxidative Removal of Template Molecules and Organic Functionalities in Mesoporous Silica Nanoparticles by H<sub>2</sub>O<sub>2</sub> Treatment", *Micropor. Mesopor. Mater.* **2008**, DOI=10.1016/j.micromeso.2008.03.027.
11. J. Kecht, S. Mintova, T. Bein, "Nanosized EDI-type molecular sieve", *Micropor. Mesopor. Mater.* **2008**, DOI=10.1016/j.micromeso.2008.04.010.
12. L. Lakiss, J. Kecht, V. de Waele, S. Mintova, "Copper-Containing Nanoporous Films", *Superlattices Microstruct.* **2008**, DOI=10.1016/j.spmi.2007.10.009.
13. S. Angloher, J. Kecht, T. Bein, "Mesoporous Ordered Silica Structures Modified by Metal-Organic Reagents and their Application in Catalytic Michael-Additions", *Micropor. Mesopor. Mater.* **2008**, DOI=10.1016/j.micromeso.2008.02.019.
14. J. Kecht, A. Schloßbauer, T. Bein, "Selective Functionalization of the Outer and Inner Surfaces in Mesoporous Silica Nanoparticles", submitted.

15. A. Schloßbauer, D. Schaffert, J. Kecht, E. Wagner, T. Bein, "Click chemistry for high-density biofunctionalization of mesoporous silica", submitted.
16. J. Kecht, T. Bein, "Functionalization of Colloidal Mesoporous Silica by Metalorganic Reagents", submitted.

### 12.2 Poster presentations

1. C. Hecht, J. Kecht, V. De Waele, M. Mostafavi, S. Mintova, T. Bein, "*Study of metal clustering process in colloidal zeolite hosts*", 17. Deutsche Zeolithtagung, **2005**, Gießen, Germany.
2. J. Kecht, Z. Thari, V. De Waele, M. Mostafavi, S. Mintova, T. Bein, "*Copper clusters inside zeolites formed by gamma radiolysis*", International Symposium "Catalytic processes on advanced micro- and mesoporous materials", **2005**, Nessebar, Bulgaria.
3. J. Kecht, A. Darga, T. Bein, "*Determining vapor-surface interactions of functionalized mesoporous silica nanoparticles with a quartz-crystal microbalance*", 19. Deutsche Zeolithtagung, **2007**, Leipzig, Germany.
4. J. Kecht, T. Bein, „*Template removal by uncatalyzed oxidation with hydrogen peroxide*“, **2007**, CeNS Winterschool, Mauterndorf, Austria.

### 12.3 Oral presentations

1. J. Kecht, S. Mintova, T. Bein, "*Exceptionally small metal-amine templated zeolite nanocrystals*", Second International Symposium "Advanced micro- and meso-porous materials", **2007**, Varna, Bulgarien.